Beyond the Light:

A Study on the Nanophotocatalytic Degradation of Gas-Phase Contaminants

by

Giacomo Edi Canciani

A thesis presented for the degree of

Doctor of Philosophy

School of Life Sciences

University of Sussex

July 2016

Declaration

I hereby declare that the thesis presented herein has not been submitted in any substance to another university for the award of any other degree as well as any other academic or professional distinction.

Signed: .....

Giacomo Edi Canciani

Per Mamma, Papà, ed Ans

"...C'è fra noi chi ha legato il suo destino, indelebilmente, al bromo o al propilene o al gruppo −NCO o all'acido glutammico; ed ogni studente in chimica, davanti ad un qualsiasi trattato, dovrebbe essere consapevole che in una di quelle pagine, forse in una sola riga o formula o parola, sta scritto il suo avvenire, in caratteri indecifrabili, ma che diventeranno chiari «poi»: dopo il successo o l'errore o la colpa, la vittoria o la disfatta."

– Primo Levi, *Il sistema periodico*

University of Sussex

Giacomo Edi Canciani

Submitted for the degree of Doctor of Philosophy

Beyond the Light: a Study on the Nanophotocatalytic Degradation of Gas-Phase Contaminants

Abstract

The present study focuses on the development of high surface area nanostructures and their applications in the removal of gas-phase contaminants through both photocatalytic and adsorptive techniques. Particular importance was given to ensure the commercial viability of the developed technologies. Due to its industrial importance, the elimination of siloxanes from biogas was investigated with major interest.

Through electrospinning techniques it was possible to synthesise a large number of nanostructures: TiO_2, SiO_2, WO_3, and WO_3 doped TiO_2 nanofibres. These structures were further enhanced through templating techniques in order to make core/shell SiO_2/TiO_2 nanofibres, hollow TiO_2 nanofibres, and porous TiO_2 nanofibres. Additionally, the synthesis of SiO_2 aerogel granules under ambient conditions was performed through a novel, commercially facile, technique.

The created nanostructures were initially employed as adsorptive materials for the removal of gaseous siloxanes from static environments. The adsorption kinetics and total siloxane loadings of the created structures were compared to those of P25, commercial silica gel, and the industrial PpTek siloxane removal standard. Although the commercial adsorbents were shown to perform better than the created nanostructures, the nanostructure surface areas were seen to lead to enhanced adsorptive properties with respect to P25.

TiO_2 nanofibres, porous TiO_2 nanofibres, WO_3 doped TiO_2 nanofibres, and P25 were further used to study the photodecomposition of siloxanes in a static environment. Through kinetic studies it was possible to establish that 1 mol% WO_3 doped TiO_2 nanofibres were an ideal candidate for the photodecomposition of gaseous siloxanes, with a decomposition rate 126.5 % larger than that of simple P25.

P25 was coated on glass beads through a novel technique in order to photocatalytically degrade

contaminants in gas flows. Through the decomposition of both siloxanes and VOCs it was possible to study the turnover numbers and conversion levels of the reactions. The poisoning of the catalysts was identified and countered through industrially viable recoating techniques. From these studies it was possible to develop a prototype reactor for the photodecomposition of siloxanes in biogas.

Finally, the synthetic properties of the flow reactors were studied by carrying out the photoepoxidation of hexene over P25. These studies were further enhanced by reacting the partial photoepoxidation products of the reactor's exhaust in order to create rare and complex organic species.

Acknowledgements

" On The Shoulders of Giants..."

As much as this thesis is the work of my own hands, brain, and eyes, it would have never seen the light of day without the support of an army of people. Many are the personal giants upon whose shoulders I have built to get this far and, unfortunately, I cannot take the space required to thank each and every one. Nonetheless, amongst these giants there are some which deserve particular gratitude for their part in this chapter of my life.

First and foremost, I don't think I would be able to write these words if it was not for the love, support, energy and strength that my family have given me. My parents, Simona and Egidio Canciani have helped me in every way they could think of. Thanks to their constant encouragements I was always able to push forward with smiles and determination, they have given me much more than a thesis, they have helped me become the person I am today. For this, and for so much more, I am proud that they are my parents... these are debts which I will never be able to repay.

My brother, Anselmo Canciani, deserves an incredible thanks. It has been a pleasure sharing scientific discourse on the most disparate topics we could think of. I have fond memories of the evenings spent talking of comic books, films, and video games as we battled over the control of corporations in Netrunner. It will be a pleasure to come back to it all. Without Anselmo's support and ideas I most certainly wouldn't be here, I am proud to have him as my favourite brother.

To Katy Kirzynowski I owe an incredible debt. Her support, strength, and love throughout the long months behind this thesis have been more than one could have ever wished for. Without her I do not think I'd have been able to finish this thesis, and if I had, I would most certainly not have done so as a sane human being. I could not have asked for a better companion.

The Nanogroup has been a beacon of knowledge, sanity, and mirth in these last four years! In particular I would not be here without the wisdom and good company of Brnyia Omar and the Fangward collective (also known as Fang Yanxing and Wei Cheat Lee) with whom I have shared many things best left untold... Talking of invaluable friendships, I will forever be grateful to Thomas Draper for his company during this Stygian journey! We have shared drinks, discussions, hobbies, stress, and anguish... Tom has been a worthy accomplice, A+, would recommend.

Of the Nanogroup, I fondly remember my awesome posse of MChem students. With Samuel Pearce it was a pleasure to learn the ropes of supervising whilst with the energy of Charlie Readman we achieved incredible things! Further thanks goes to Ed Hills, Josh Fellowes, Ben Fry, Jone-him Tsang, Thomas Samuels, and Anna Crosby for their company in the long winter nights. I am proud to have seen you guys through the Nanolab!

With Vicki, Fang, and JK I share an incredible bond. We are the old guard who have, for the last 8 years, laughed and smiled together through Sussex University. Now we are old, tired, and jaded, but I am happy to have shared this journey with you.

A further mention goes to the new recruits! For the Nanolab, I look at Daniel, Munirah, and Emmanuel and rest assured that they will accomplish great and wonderful things. For lab 14, the torch passes to Matt Leech and Matt Molloy, provided they do not blow up the department, they should achieve some quite funky chemical things of the inorganic type.

From Sussex University I want to give my thanks to to Mick Henry and Fran Chick of the teaching labs. I know that it wasn't always easy to host the Nanolab during our exodus but for their hard work I will be forever grateful. Of the teaching lab team, I also need to thank Shane Lo Fan Hin and Chris Dadswell for their help and experience in both the undergraduate demonstrations and the analysis of complicated samples. I have deep gratitude towards Sussex's Mac Guyver team; Alex Burns and Paul Andrews have been the oft unsung backbone of the Nanolab.

My supervisors, Dr Qiao Chen and Dr John Turner need to be thanked for their leading roles in the Faustian pact which was this PhD. Qiao's constant support and ideas deserve particular mention. Kicking and screaming, he has brought me this far, it will be hard to make do without his fantastic metaphors.

In addition to all these people I must also give my deepest thanks to my great proofreaders: Anselmo Canciani, Matt Leech, Andrew Stella, Jamie McKinven, Egidio Canciani and of course Dr Qiao Chen. Their eyes and minds have poured over this text, allowing me to polish the roughness and cracks out of the thesis.

Finally, the time has come to thank the institutions who have played an essential role towards this thesis. PpTek ltd. and Innovate UK (the entity formerly known as TSB) have taught me just how rewarding, complicated, and exhausting an industrial/academic cooperation can become, as well as providing their (non negligible) financial support. I must also thank the European Union for its financial support as well as for an ideal towards which it is worth dreaming. The Papons bank also deserves recognition, it would be impossible to get such a versatile and convenient service from any other institution. Lastly, I need to acknowledge "Il Consorzio Dei Moccioamici" without which, I am certain, the world would be overflowing with port!

Contents

Abstract **iv**

Acknowledgements **vi**

List of Figures **xii**

List of Tables **xviii**

List of Abbreviations **xix**

1 Introduction **1**

1.1 Photoexcited Phenomena 3

1.1.1 Electron Photoexcitation 4

1.1.2 Common Photostimulated Reactions 6

1.2 Semiconductors as Photocatalysts 14

1.2.1 TiO_2 Photocatalysis 17

1.2.2 Nanostructured Semiconductors as Photocatalysts 22

1.3 Biogas 29

1.3.1 Biogas as an Energy Source 29

1.3.2 Sources of Biogas Contamination 29

1.3.3 Elimination of Siloxanes in Biogas 31

1.4 Kinetic Factors in TiO_2 Purification Reactors 34

1.4.1 The Effects of Surface Area on Reaction Kinetics 34

1.4.2 The Influence of Light Intensity on Reaction Kinetics 37

1.4.3 Catalyst Concentration Effects on Reaction Kinetics 38

1.5 Thesis Overview 39

2 Instrumentation **41**

2.1 Scanning Electron Microscopy 41

2.1.1 Energy Dispersive X-Ray Spectroscopy 44

2.2 X-Ray Diffraction 44

2.3 Diffuse Reflectance Spectroscopy 48

2.4 Gas Chromatography 51

2.4.1 Flame Ionisation Detection 54

2.4.2 Mass Spectrometry 55

2.5 Fourier Transform Infrared Spectroscopy 58

3 Nanoarchitecture Synthesis **63**

3.1 Introduction 63

3.2 Experimental 65

3.2.1 Chemicals and Characterisation Techniques 65

3.2.2 Semiconductor Nanofibre Synthesis 66

3.2.3 Core/Shell Nanofibre Synthesis Through Dip-Coating 68

3.2.4 Hollow TiO_2 Nanofibre Synthesis Through Templating 69

3.2.5 Template-Assisted Nanofibres With Controlled Porosity 70

3.3 Results and Discussion 71

3.3.1 Electrospun Semiconductor Nanofibre Characterisation 71

3.3.2 Characterisation of SiO_2/TiO_2 Core/Shell Nanofibres 82

3.3.3 Characterisation of Hollow TiO_2 Nanofibres 87

3.3.4 Characterisation of Nanofibres with Controlled Porosity 89

3.4 Conclusions 93

4 Siloxane Adsorption Studies **95**

4.1 Introduction 96

4.2 Experimental 97

4.2.1 Chemicals and Characterisation Techniques 97

4.2.2 Silica Aerogel Synthesis at Ambient Conditions 98

4.2.3 Surface Modification of Commercial SiO_2 Gels 100

4.2.4 Nanofibre Synthesis Through Electrospinning 101

4.2.5 Siloxane Adsorption Onto High Surface Area Structures 101

4.3 Results and Discussion . . . 102
4.3.1 Silica Aerogel Characterisation . . . 102
4.3.2 L2 Adsorption Studies on Enhanced Adsorbents . . . 110
4.4 Conclusions . . . 120

5 Static Photodegradation of Siloxanes 122
5.1 Introduction . . . 123
5.2 Experimental . . . 124
5.2.1 Chemicals and Characterisation Techniques . . . 124
5.2.2 Synthesis of Electrospun WO_3 Doped TiO_2 Nanofibres . . . 125
5.2.3 Siloxane Photodegradation in Static Systems . . . 125
5.3 Results and Discussion . . . 127
5.3.1 WO_3 Doped TiO_2 Nanofibre Characterisation . . . 127
5.3.2 Static Siloxane Photodecomposition . . . 130
5.4 Conclusions . . . 141

6 Siloxane Decomposition in Gas Streams 144
6.1 Introduction . . . 145
6.2 Experimental . . . 146
6.2.1 Chemicals and Characterisation Techniques . . . 146
6.2.2 General Flow Reactor Design . . . 147
6.2.3 Siloxane Loading in the Gas Streams . . . 148
6.2.4 TiO_2 Photocatalyst Immobilisation on Glass Substrates . . . 149
6.2.5 TiO_2 Photocatalyst Regeneration Techniques . . . 150
6.3 Results and Discussion . . . 152
6.3.1 Rod Supported TiO_2 Photocatalyst Efficiency . . . 153
6.3.2 Bead Supported TiO_2 Photocatalyst Efficiency . . . 158
6.4 Conclusions . . . 165

7 Volatile Organic Molecule Degradation 167
7.1 Introduction . . . 168
7.2 Experimental . . . 169
7.2.1 Chemicals and Characterisation Techniques . . . 169

7.2.2 P25 Immobilisation on Glass Beads 170
7.2.3 VOC Photodegradation Reactor Design 171
7.2.4 Exhaust trapping Technique 173
7.3 Results and Discussion 173
7.3.1 Effectiveness of Acetone Photodegradation 173
7.3.2 Effectiveness of IPA Photodegradation 182
7.3.3 Effectiveness of Styrene Photodegradation 184
7.4 Conclusions 192

8 Hexene Photoepoxidation in Gas Flows 194
8.1 Introduction 194
8.2 Experimental Procedure 197
8.2.1 Chemicals and Characterisation Techniques 197
8.2.2 P25 Immobilisation on Glass Beads 197
8.2.3 Epoxidation Reactor Design 198
8.2.4 Synthetic Trapping 200
8.3 Results and Discussion 201
8.3.1 1-Hexene Photoepoxidation Product Analysis 201
8.3.2 Tandem Reaction of Diisopropylamine With the Photoreactor Exhaust . . 204
8.4 Conclusions 210

9 Conclusions and Future Developments 212
9.1 Conclusions 212
9.2 Future Developments 216

10 Bibliography 219

List of Figures

1.1 Jabłoński diagram showing the relaxation of photoexcited electrons. 5

1.2 Representation of the linear combination of the AO of two hydrogen atoms. . . . 8

1.3 Mechanistic pathway for the selective photoisomerisation of stillbene. 9

1.4 General mechanistic pathway for the photocycloaddition of alkenes. 10

1.5 Scheme showing the photodimerisation of *cis*-butene 10

1.6 Mechanistic pathway for the photostimulated homolytic fission of σ bonds. . . . 11

1.7 Scheme showing the three different phases of radical mediated synthesis of chloromethane. 12

1.8 Formation of orbital bands in bulk materials from the merging of AO. 14

1.9 Diagram showing the band transition occurring during the electronic excitation in semiconductors. 16

1.10 Ball and stick crystal structures of the three main polymorphs of TiO_2. 17

1.11 The main phases of the TiO_2 mediated photocatalytic activation of molecules. . . 18

1.12 Diagram showing the main phases leading to the formation of an aerogel monolith. 23

1.13 Schematic diagram of the formation of electrospun nanofibres. 25

1.14 Band alignment in a rutile/anatase TiO_2 composite. 28

1.15 General molecular structure of siloxanes. 30

1.16 The specific molecular structures of L2 and D5, two common siloxanes in biogas. 31

2.1 Diagram showing the main components of a scanning electron microscope. . . . 42

2.2 Schematic representation of Bragg's law. 45

2.3 Tauc plot showing the band gap of P25 from its diffuse reflectance spectrum. . . . 49

2.4 Diagram showing the operation of an integrating sphere. 51

2.5 Schematic representation of a gas chromatograph. 52

2.6 Schematic representation of a FID detector. 54

2.7 Schematic representation of a MS detector. 56
2.8 Schematic representation of a FTIR spectrometer. 59
2.9 FTIR interferogram of L2. 61
2.10 FTIR absorption spectrum of L2. 62

3.1 Experimental set up for the electrospinning of nanofibres. 67
3.2 Diagram showing the main steps in the experimental procedure for the synthesis of SiO_2/TiO_2 core/shell nanofibres. 69
3.3 Schematic representation of the principal steps for the template-assisted synthesis of hollow TiO_2 nanofibres. 69
3.4 Schematic representation showing the SiO_2 nanosphere removal process from the templated TiO_2 nanofibres. 71
3.5 EDX scan of the electrospun TiO_2 nanofibres. 72
3.6 XRD pattern for the electrospun TiO_2 nanofibres. 73
3.7 SEM images showing the structures of the electrospun TiO_2 nanofibre mat and the individual TiO_2 nanofibres. 74
3.8 Tauc plot derived from the reflectance spectrum of TiO_2 nanofibres. 75
3.9 XRD pattern of the electrospun WO_3 nanofibres. 76
3.10 SEM images showing the fibre mat and individual fibre structures of the electrospun WO_3 nanofibres 77
3.11 Tauc plot derived from the reflectance spectrum of WO_3 nanofibres. 78
3.12 EDX scan of the electrospun SiO_2 nanostructures. 79
3.13 XRD pattern of the electrospun SiO_2 nanofibres. 80
3.14 SEM images showing the SiO_2 nanofibre mat and the surface of SiO_2 nanofibres. 81
3.15 EDX scan of the created SiO_2/TiO_2 core/shell nanostructures. 82
3.16 XRD patterns of the created SiO_2/TiO_2 core/shell nanostructures. 82
3.17 SEM images of the SiO_2/TiO_2 core/shell nanostructures at different TiO_2 loadings. 83
3.18 SEM images showing the evolution of the SiO_2 nanofibre mat morphology through six dip coating cycles. 85
3.19 Thickness of the TiO_2 shell coating on the core/shell nanostructures in relation to the dip coating cycles. 86

3.20 SEM images showing the fibre mat and individual fibre morphologies of the created hollow TiO_2 nanofibres. 87
3.21 SEM image showing the damage on the general hollow nanofibre structure following mechanical stress. 88
3.22 SEM images showing low and high magnifications of the synthesised SiO_2 nanospheres 89
3.23 SEM images showing the SiO_2 nanosphere templated TiO_2 nanofibres. 90
3.24 SEM image showing the embedded SiO_2 templates in the TiO_2 nanofibres 91
3.25 SEM images showing the synthesised porous nanofibres. 91
3.26 Diagram showing the relationship between the observed pore diameter and its true radius in the porous TiO_2 nanofibres. 92

4.1 Diagram showing the drop-wise formation of spherical SiO_2 hydrogel beads. . . 99
4.2 Diagram showing the main steps of the experiments performed to investigate the siloxane absorption properties of studied materials. 102
4.3 Scheme showing the polymerisation of silicic acid from sodium silicate. 103
4.4 Scheme showing the steps in the condensation reaction of silicic acid. 104
4.5 Graph showing the effect of changing reagent molar ratios on the gelation time of silicic acid solutions. 105
4.6 SEM images of the external and internal surface morphologies of the created SiO_2 aerogels 107
4.7 Graph showing the contraction of the synthesised aerogel granules during drying. 108
4.8 Scheme showing the capping of surface silanol groups by TMCS. 108
4.9 Photograph of the contraction of the synthesised aerogel granules. 109
4.10 Evolution of L2 concentration and adsorption constants over two subsequent siloxane injections in relation to time. 112
4.11 Evolution of L2 concentration over time in silica gel samples with varying surface treatments. 114
4.12 Silica gel surface functional groups after TMCS and ODPA modification. 116
4.13 Evolution of L2 concentration over time in SiO_2 and TiO_2 nanofibres. 117
4.14 SEM images comparing the surface morphologies of electrospun SiO_2 and TiO_2 nanofibres. 118

5.1 Diagram showing the experimental set up for the static photodecomposition reactions. 126
5.2 SEM images contrasting the surface morphologies of pure and WO_3 doped TiO_2 nanofibres. 127
5.3 XRD patterns showing the effect of WO_3 doping on TiO_2 nanofibre crystal structure. 128
5.4 Calculated band gaps for the doped TiO_2 nanofibres in relation to WO_3 doping concentration. 129
5.5 Graph showing the photodecomposition of L2 in a static reactor showing the three key events of siloxane elimination. 131
5.6 Graph showing the photodecomposition of L2 in a static reactor during extended reaction periods. 132
5.7 Graphs showing the first order reaction behaviour observed during the photodecomposition of L2 on a clean catalyst and on reused catalysts. 134
5.8 Graph showing the evolution of TiO_2 nanofibre reaction kinetics in relation to the decomposition of L2. 135
5.9 L2 concentration in a static reactor during thermal treatment of the photocatalyst after extended photodecomposition reactions. 137
5.10 Photodecomposition of L2 on WO_3 doped TiO_2 nanofibres. 137
5.11 L2 photodecomposition kinetics of WO_3 doped TiO_2 nanofibres in relation to dopant concentration. 138

6.1 Diagram showing the experimental set up used for the photodecomposition of siloxanes in gas streams. 147
6.2 Schematic diagram showing the methods used in order to load gas streams with the studied siloxanes. 148
6.3 Schematic diagram of the placement of TiO_2 coated glass beads in the quartz photoreactor tubes. 150
6.4 Initial evolution of D5 concentration in a gas flow reactor in relation to UV illumination. 154
6.5 Graphs depicting the poisoning of the TiO_2 photocatalysts in a D5 spiked methane stream as well as the determination of the TON of the studied catalysts. 155
6.6 Graphs showing the effect of thermal regeneration of poisoned photocatalysts. . . 157

6.7 Photographs showing the loss of catalyst from the substrate after the base treatment of TiO_2 dip coated glass rods. 158
6.8 Flow dynamics simulations of the gas flow through the two different catalyst supports investigated. 159
6.9 Graph showing the effect of contact time on the total decomposition of D4. . . . 161
6.10 Graph showing the decomposition profiles of D4 and L4 during gas flow experiments. 162
6.11 Photographs showing the coloration of poisoned catalyst beads following the extended use of TiO_2 photocatalysts. 163

7.1 Experimental set up used for the photodecomposition of VOCs. 172
7.2 Schematic diagram showing the chemical trapping of the photoreactor exhaust. . 173
7.3 Evolution of CO_2 concentration during the photodecomposition of acetone 174
7.4 Evolution of CO_2 production rate with respect to catalyst loading. 175
7.5 SEM images of specific and general morphologies of TiO_2 coated glass beads with different catalyst loadings. 176
7.6 Photographs showing the effect of mechanical abrasion on different bead coatings. 177
7.7 Graph showing the photodecomposition of acetone in a gas stream. 178
7.8 Graph showing the evolution of CO_2 concentration during the photodecomposition of acetone. 179
7.9 Graph showing the emission of CO_2 arising from the photodecomposition of carbonaceous residues. 181
7.10 Evolution of the concentrations of different chemicals present in the exhaust during the photodecomposition of IPA in relation to flow time. 183
7.11 Evolution of the concentrations of different chemicals present in the exhaust during the photodecomposition of styrene in relation to flow time.. 185
7.12 Gas chromatogram of the secondary products of the photodecomposition to styrene. 188
7.13 Chemical scheme showing the conversion of styrene into benzaldehyde. 189
7.14 Chemical scheme showing the conversion of styrene into ethylbenzene. 190
7.15 Chemical scheme showing the conversion of styrene into phenylacetylene. 191
7.16 Chemical scheme showing the conversion of styrene into cumene. 191

8.1 Experimental set up used for the photoepoxidation of hexene. 199

8.2 Schematic diagram showing the chemical trapping of the photoepoxidation reactor exhaust. 200
8.3 Gas chromatogram of the toluene trap used for the collection of the partial photooxidation products of 1-hexene after 24 h of reaction time. 201
8.4 Mass spectrum of epoxyhexane. 202
8.5 Mass spectrum of an unknown product from the partial photoxidation of 1-hexene. 203
8.6 Gas chromatogram of the diisopropylamine/toluene trap used for the reaction of the partial photooxidation products of 1-hexene after 72 h of reaction time. 204
8.7 Mass spectrum of an unknown product formed from the reaction of diisopropylamine with the partial photoxidation products of 1-hexene. 206
8.8 Mass spectrum of a major unknown product (unknown A) formed from the reaction of diisopropylamine with the partial photoxidation products of 1-hexene. 207
8.9 Mass spectrum of a major unknown product (unknown B) formed from the reaction of diisopropylamine with the partial photoxidation products of 1-hexene. 208
8.10 Proposed molecular structure for the two major unknown products formed during the reaction of the partial photodecomposition products of 1-hexene with diisopropylamine. 208
8.11 Proposed reaction schemes for the formation of unknown products A and B. . . . 209
8.12 Proposed reaction schemes for the formation of the epoxide precursors to unknown A and unknown B. 210

9.1 Photograph of the prototype photoreactor developed for the industrial photodecomposition of siloxanes in biogas. 217

List of Tables

4.1 Kinetic data for the adsorption of L2 onto silica aerogel granules over two consecutive injections. 112
4.2 Kinetic data for the adsorption of L2 onto silica gel with varying surface modifications. 115
4.3 Kinetic data for the adsorption of L2 onto TiO_2 and SiO_2 nanofibres. 117
4.4 Comparison of the L2 kinetic adsorption data of the synthesised adsorbents and PpTek's ion exchange resin. 119

5.1 Evolution of photodecomposition kinetics of TiO_2 nanofibres in relation to increasing siloxane injections and L2 decomposition. 136
5.2 Comparison of the photodecomposition constants for different TiO_2 nanostructures. 140

6.1 Effects of thermal regeneration of poisoned catalysts at different temperatures. . . 157
6.2 TON for the photocatalytic degradation of D4 on TiO_2 regenerated through a variety of techniques. 164

8.1 Overview of the main GC-MS signals observed after the reaction of the 1-hexene photodecomposition products with diisopropylamine. 205

List of Abbreviations

°C	Degrees Celsius
K	Degrees Kelvin
M	Moles per litre
wt%	Percentage weight
α	Absorption coefficient of a material
γ	Initial adsorption velocity
ϵ	Photonic efficiency
λ	Wavelength
ν	Rate of a chemical reaction
	Frequency of light
σ_{CO_2}	Rate of CO_2 production
τ	Global adsorption time
ϕ	Quantum yield
A	Acceptor molecule
AO	Atomic orbitals
ATR	Attenuated total reflectance
$C_{\%}$	Percent Conversion
CBM	Conduction band minimum
D	Donor molecule
$\overline{d}$	Average diameter
D4	Octamethylcyclotetrasiloxane
D5	Decamethylcyclopentasiloxane
D_{avg}	Mean crystallite dimension of a crystal plane
DC	Direct current

DMF	Dimethylformamide
e^-	Electron
EDX	Energy dispersive x-ray
E_g	Band gap
FID	Flame ionisation detector
FMO	Frontier molecular orbital
FTIR	Fourier transform infrared
G	Gaseous chemical species
GC	Gas chromatography
GIAC	Gyration induced adhesive coating
h	Plank constant
h^+	Hole
HOMO	Highest occupied molecular orbital
ICDD	International centre for diffraction data
IPA	Isopropyl alcohol
IQE	Internal quantum efficiency
ISC	Intersystem crossing
k	Reaction rate constant
k’	Rate of gas adsorption
	Modified photodecomposition rate constant
L2	Hexamethydisiloxane
L4	Decamethyltetrasiloxane
LCAO	Linear combination of atomic orbitals
L-H	Langmuir Hinshelwood
LUMO	Lowest unoccupied molecular orbital
MO	Molecular orbital
MS	Mass spectroscopy
$\overline{MW}$	Average molecular weight
NIST	National institute of statistics
NS	Nanosphere
ODPA	Octadecylphosphonic acid
OPD	Optical path difference
P25	Aeroxide P25
PMMA	Polymethylmethacrylate

PVA	Polyvinyl alcohol
QE	Quantum efficiency
q_e	Adsorption capacity at equilibrium
q_{max}	Maximum adsorption capacity
S	Substrate
S_{CO_2}	Reaction selectivity for CO_2
SEM	Scanning electron microscopy
TEOS	Tetraethyl orthosilicate
TMCS	Trichloromethylsilane
TOF	Turnover frequency
TON	Turnover number
TT^iP	Titanium tetraisopropoxide
TUFT	Tubes by fibre templates
UV	Ultraviolet
UV_a	Ultraviolet light ($315 \leq \lambda \leq 400$ nm)
VBM	Valence band maximum
Vis	Visible
VOCs	Volatile organic compounds
XRD	X-ray diffraction

1. Introduction

The second decade of the 21st century has established energy as a pillar of modern human existence. This importance of energy has been highlighted by the rising geopolitical instability caused by a desperate control for primary resources in petroleum exporting countries.[1,2] In 2013, the International Energy Agency outlined a shift in the global energy demands towards developing countries in combination with alarming levels of global CO_2 production as a result of energy consumption.[3] The importance of CO_2 production, and global warming in general, was further shown in 2014 when the Intergovernmental Panel on Climate Change highlighted the drastic humanitarian and economic consequences of unmitigated climate change.[4] Public concern for anthropogenic climate change resulting from the consumption of energy eventually reached its paroxysm in 2015, where, at the United Nations climate change conference, 195 nations drafted a global agreement *"to pursue efforts to limit the temperature increase to 1.5 °C above pre-industrial levels"*.[5]

In this historical landscape, academic and industrial research in the fields of renewable and green energies has garnered a large amount of interest. This growing interest has focused on the production of sustainable energies and the elimination of anthropogenic greenhouse gases. As such, a number of different technologies have been developed in order to generate energy from renewable, carbon neutral, sources.[6] Amongst these resources, the combustion of biomatter and biofuels has an essential role to play as it is one of the few sources of renewable energy which can be used to supplant the consumption of fossil fuels whilst avoiding the costs of extensive technological overhauls. Indeed, the share of biofuels used for transport is expected to rise by 11 % by the year 2035.[3] Furthermore, the combustion of biofuels such as biogas can often be beneficial to the environment by converting often toxic and noxious gases into inert CO_2. Although CO_2 is well known for it's important effects on global warming,[4] the combustion of biogas can nonetheless be considered climatically favourable as it allows to convert methane into CO_2, effectively decreasing the global warming potential of the gas by a factor of 28.[4]

The combustion of biogas in spark engines does, nonetheless, present a number of problems, the most important of which is the presence of a large number of impurities. As biogas originates from the decomposition of organic matter, it is known to contain a large number of secondary compounds in varying concentrations depending on the original source of the gas (landfill sites, animal waste, etc.).[7,8] Amongst the different impurities present in biogas, two are particularly problematic: hydrogen sulfide and the family of organosilicon compounds known as siloxanes. Siloxanes, in particular, have received a large amount of industrial[9] and academic[10,11] interest due to their tendency to convert to SiO_2 microcrystallites and fatally damage spark engines during combustion.[12,13]

As a result of the damaging nature of siloxanes, their removal from biogas has received a lot of interest.[10,14–16] A number of different techniques have thus been developed in order to remove siloxanes from biogas. The most common of these purification techniques rely on the capture of siloxanes prior to the combustion of the gas. At a commercial level, this is achieved by using high surface area adsorbents (such as activated carbon) as filters[9,17] although the cryogenic capture of siloxanes has also shown promising potential at an academic level.[16]

Unfortunately, the capture of siloxanes as a method of purifying biogas remains far from ideal. Indeed, as the siloxanes are concentrated and captured into the high surface area adsorbents, the problem of their ultimate fate arises since they cannot be returned into their original landfill sites or released into the atmosphere unchanged as siloxanes are known to lead to bioaccumulation.[18] Industrially, this setback is overcome by causing the desorption of the siloxanes from the andsorbents and combusting them in a waste gas stream. Although effective, this technique is not ideal as it is considerably energy intensive. As such, two different methods have been studied to carry out the direct decomposition of siloxanes in gas streams: reactive liquid extraction and photodecomposition. Reactive liquid extraction focuses on chemically converting siloxanes by passing the biogas through a liquid, whilst photodecomposition uses heterogeneous catalysts for the removal of siloxanes *in-situ*.[7,14,15] Current studies using the photodecomposition technique have focused on using TiO_2 as a photocatalyst and studied its applications for the elimination of siloxanes in ambient air.[14,15] However, the studied technologies displayed relatively limited efficiencies due to their use of macrostructured TiO_2. During the present study TiO_2 was used in a nanostructured form in order to decompose siloxanes in the gas phase with the ultimate goal of approaching the developed technologies towards the indsutrial photodecomposition of siloxanes in gas streams. Initial studies

focused on the development of high surface area TiO_2 nanostructures and the quantification of their adsorptive properties. Once this was preformed, the photodecomposition potential of the created nanostructures was studied by decomposing gas-phase siloxanes in static environments. The studied photocatalysts were then used to decompose siloxanes in gas streams in order to approach the industrial requirements of the technique. As such, the present research aimed to develop industrially applicable technologies for second generation biogas filters based on the photodecomposition of gas phase contaminants through nanostructured photocatalysts. The development of such technologies would be an important asset in the use and application of biofuels in the modern world.

Although biofuels are a suitable renewable alternative energy source for transport and combustion engines, different technologies are required for the production of electricity. Of the many renewable sources used for this purpose, wind and solar power generation have gained the most traction, with an estimated combined global electricity production of 3750 TWh, corresponding to 11 % of the global electricity supply, by the year 2035.[3] Amongst these two renewable resources, solar power has gathered the largest interest in the chemical sciences due to its potential as a vector for low-energy reaction pathways.

Due to the crucial importance of solar power, it becomes essential to gain an in-depth understanding to the interaction of light with different materials and molecules.

1.1 Photoexcited Phenomena

The use of solar energy in chemistry arises as a natural extension from the field of photochemistry. Photochemistry studies the use and effects of light in chemical reactions with a particular focus on the differences from the more conventional thermally driven chemical reactions. Historically, photochemistry gained traction as a chemical discipline in the early 1900s with the establishment of the law of photochemical equivalence by Albert Einstein[19] and Johannes Stark,[20] which applied quantum theory to the effects of photons on chemical reactions. Since then, the understanding of the molecular adsorption of photons and its effects have greatly improved with the ever growing expansion of photochemistry.

1.1.1 Electron Photoexcitation

The primary principle governing photochemical reactions is known as the Grotthuss-Draper law.[21] This principle states that in order for light to have an effect on a system, it must be absorbed.[21] This basic concept has since been developed and expanded, leading to the present understanding of photonic excitation of electrons in molecular systems.

It is now known that the absorption of photons by a molecule leads to an electronic excitation within the molecule. The electrons within the molecule are excited from a low energy ground state, S_0, to a higher energy state, depending on the energy of the absorbed photon. From this excited state, the electron can undergo a large variety of processes, eventually resulting in its relaxation back to the lower energy state. These different processes and their relative energetic positions were schematically represented for the first time in 1933 by Alexander Jabłoǹski.[22] Figure 1.1 shows an adaptation of the Jabłoǹski diagram.

As a photon is absorbed by a molecule, a single electron is excited from a ground state in the Highest Occupied Molecular Orbital (MO), the HOMO, to an excited state (process A in Figure 1.1). Kasha's rule[23] stipulates that electrons excited to higher energy states will rapidly undergo non-radiative internal conversion to the Lowest Unoccupied MO (LUMO, S_1), represented as process B in Figure 1.1. Due to the Franck-Condon principle, if the photoexcited electron transitions directly to the LUMO, it will not be transferred directly to the lowest vibrational level within this excited state; this electron will undertake non-radiative decay in order to reach the lowest vibrational energy level within the LUMO, prior to undergoing further electronic transitions (process C in Figure 1.1).

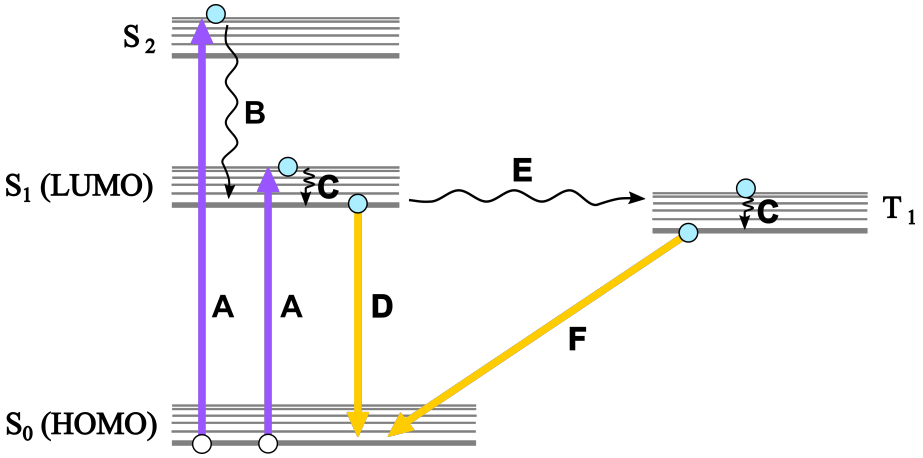

Fig. 1.1 Jabłoǹski diagram showing the different relaxation pathways of photoexcited electrons. The diagram depicts photoexcitation (A), non radiative internal conversion (B), non radiative decay (C), fluorescence (D), intersystem crossing (E) and phosphorescence (F). The straight arrows depict the radiative pathways whilst the curly arrows depict non radiative transitions.

From the LUMO the excited electron can undergo relaxation to the HOMO through two different pathways. The most facile pathway is for the electron to undergo a radiative decay from S_1 to S_0, and emit its excess energy as a photon through fluorescence (process D in Figure 1.1). The second process occurs as a consequence of the electron in S_1 undergoing a change in spin from a singlet to a triplet state (T_1) through InterSystem Crossing (ISC) (process E in Figure 1.1). The electron in T_1 will then lose its energy and return to S_0 by emitting photons through the process of phosphorescence shown as pathway F in Figure 1.1. Due to the higher difficulty of the intersystem crossing, the population of excited electrons undergoing phosphorescence will be significantly inferior to that undergoing fluorescence.[24]

However, in photochemistry, the relative lifetimes of phosphorescence and fluorescence remain much less important than the overall population of excited electrons present in the LUMO. As such, in order to quantify the efficiency of photochemical reactions, a mathematical relation between the amount of incident light and the amount of photogenerated electrons over a given unit of time, was defined as the Quantum Efficiency (QE). The QE is expressed as shown in Equation (1.1).

$$QE = \frac{Photogenerated\ electrons}{Incident\ photons} \tag{1.1}$$

Equation (1.1) is particularly useful when considering systems wherein light irradiation is used

to achieve the direct generation of electric currents, such as photovoltaic cells. Additionally, as photovoltaic cells will only absorb at specific wavelengths, the Internal Quantum Efficiency (IQE, shown in Equation (1.2)) is also calculated. The measurement of a system's IQE is often preferred at academic levels as it only takes into account the photons absorbed by a given material rather than all of the photons in the incident flux. However, it is important to remember that as the IQE only considers the photogenerated electrons, it effectively results in an artificial boost in a device's efficiency which is unlikely to be observed once the material becomes used for commercial or industrial applications.

$$IQE = \frac{Photogenerated\ electrons}{Absorbed\ photons} \tag{1.2}$$

Although Equations (1.1) and (1.2) have been developed to study photovoltaic systems, it is important to remember that the excited state population is also an essential element in photochemical reactions. Indeed, it is only through the effective use of the photoexcited electrons that it is possible to carry out chemical reactions such as organic photosynthesis and photocatalysis.

1.1.2 Common Photostimulated Reactions

Even though light stimulated species can undergo many different reactions, their chemical interactions are of particular importance during the present work. This importance arises with the necessity of transforming toxic chemical species into inert molecules through the use of suitable light.

Although photochemical reactions can be seen as an extension of photovoltaic reactions, they require the interaction of multiple chemical species. This means that the efficiency of a photochemical species could be limited by the rate of reagent interaction rather than by the population of photogenerated electrons. As such, the efficiency of photochemical systems is usually defined as the ratio between the number of molecules undergoing the studied photoreaction and the number of absorbed photons. This ratio, known as the quantum yield (Φ), is calculated as shown in Equation (1.3).

$$\Phi = \frac{Molecules\ undergoing\ reactions}{Absorbed\ photons} \tag{1.3}$$

Experimentally, it is often difficult to calculate the exact amount of species undergoing chemical reactions. As such, the photonic efficiency of reactions, ξ, is usually preferentially considered. ξ is defined as the ratio between the number product molecules formed and the number of photons absorbed, as shown in Equation (1.4).

$$\xi = \frac{Reaction\ products}{Absorbed\ photons} \tag{1.4}$$

Due to its simplicity, Equation (1.4) can be used to quantify the effects of photonic excitation in chemical reactions. Although vastly numerous, these photochemical reactions can be separated into two broad subjects: photosynthesis and photocatalysis.

Organic Photosynthesis

Photosynthesis is a chemical procedure commonly used to perform reactions through thermally prohibited pathways. Many reviews and studies have been carried out on photosynthetic organic chemistry since its initial academic applications in the late 1960s.[20,25–27] From these studies it is possible to observe three principal photoreaction types: isomerisation, C−C bond formation, and radical generation.[27]

In order to gain an understanding of the processes governing organic photosynthesis, it becomes important to consider the excited systems in terms not only of Atomic Orbitals (AO) but also of MOs. Upon the formation of a covalent bond, the AO of the component molecules combine to form a pair of MOs containing the bonding electrons, one with higher energy, and one with lower energy than the constituent AO. The pair of created MOs are referred to as the bonding and antibonding MOs for the low and high energy systems, respectively. Figure 1.2 shows a representation of the placement of the two MOs arising from the Linear Combination of AO (LCAO) in the H_2 molecule. In simple terms, the types of MO created from LCAO can be described either as symmetrical orbitals around the molecular axis (denoted as σ) or as orbitals that are antisymmetric along a plane that contains the intermolecular bond (denoted as π). As the MOs exist in pairs, the low energy bonding orbitals are denoted σ and π whilst their high energy antibonding counterparts are denoted as σ* and π*. During the photonic excitation of an organic molecule, electrons are promoted from the bonding orbitals to the antibonding orbitals.

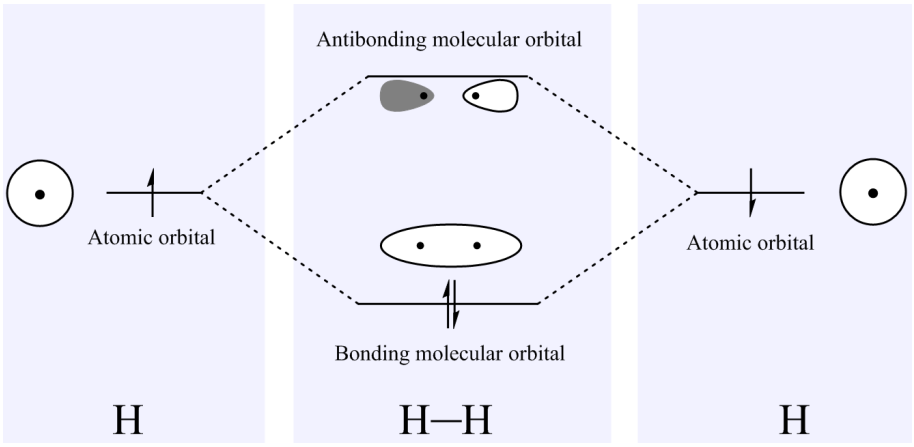

Fig. 1.2 Representation of the linear combination of the AO of two hydrogen atoms. The formation of the bonding and antibonding MOs as well as the relative energies of each orbital can be seen.

Once promoted to these antibonding orbitals, high energy electrons can lead to a large variety of chemical reactions.[25,26] Of these reactions, the photoisomerisation of alkenes is one of the most useful as it allows for the synthesis of thermodynamically unstable chemical species. During photoisomerisation, the excited electrons can undergo a transition from the excited state, S_1, to a triplet state, T_1, which leads to a loss of stereochemical rigidity across the excited bond.[28,29] During the electronic decay from T_1 to S_0 the molecule can relax into either the *cis* or *trans* conformation. As the *cis* and *trans* conformations of molecules have different absorption spectra, it becomes possible to selectively excite one molecular isomer and thus promote the formation of the other. This technique has been applied successfully in a large number of organic reactions. Most notably, the sterically hindered *cis*-stillbene was photosynthesised by irradiating the thermodynamically stable *trans*-stillbene with UV light (λ = 313 nm).[28] The energetic positions of the electrons during this isomerisation are shown in Figure 1.3.

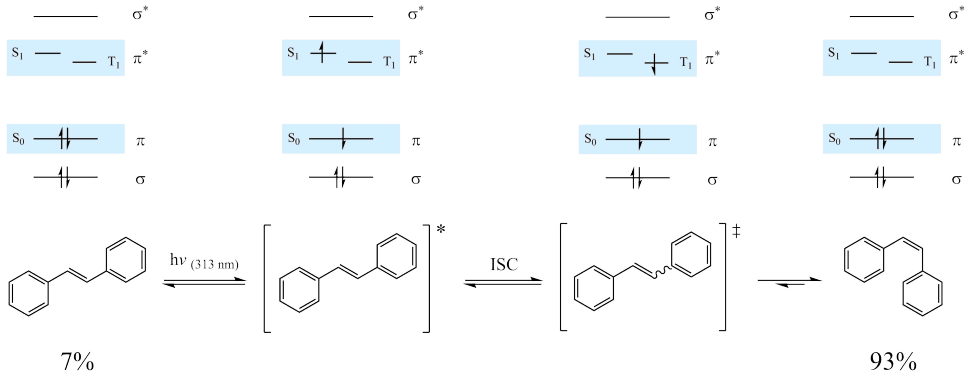

Fig. 1.3 Mechanistic pathway showing the selective photoisomerisation of stillbene. The electronic configuration of the C=C bond during each step of the photoisomerisation process is shown above the reaction scheme.

It is important to note that such *cis-trans* photoisomerisation are not unique to C=C bonds but have also been observed in N=N bonds.[30] The most common example of an N=N photoisomerisation is that which is known to occur in azobenzene wherein the more thermodynamically stable *trans* isomer can be converted into the *cis* conformation through UV irradiation at wavelengths between 320 and 380 nm.[30] Conversely, the *trans* conformation of azobenzene can be favoured by irradiation with light at wavelengths of 400 to 450 nm.[30] From this isomerisation it becomes clear that although photochemical phenomena are studied primarily through carbon species, they are not limited to this element.

Photoactivated reactions can be further used for the photomediated formation of C−C bonds. Of the many different photoactivated C−C bond formation reactions, the [2+2] cycloaddition of unsaturated molecules remains one of the most useful photoreactions. Two properties of these cycloaddition reactions render them particularly important. Firstly, the thermodynamic barrier for the formation of cyclobutane systems makes their thermal synthesis highly difficult, the use of photonic excitation allows to overcome this barrier.[27] Secondly, the products of [2+2] photocycloaddition reactions are often less absorbing than the synthetic reagents, effectively minimising the occurrence of reverse reactions.[26]

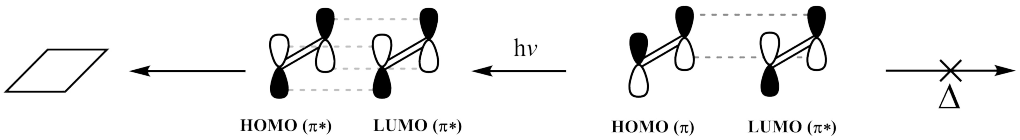

Fig. 1.4 General mechanistic pathway for the [2+2] photocycloaddition of alkenes. The different orbital configurations of the alkene molecules are shown in order to highlight the orbital mismatch when both alkene species are in their ground state.

The electronic mechanism of [2+2] photocycloadditions can be understood based on applying Frontier Molecular Orbital (FMO) theory. The main attractive interaction between two molecules and the formation of new chemical bonds arise from the successful overlap between the HOMO of one molecule and the LUMO of the other. As shown in Figure 1.4, no overlap exists between the π orbital (HOMO) and the π* orbital (LUMO) of alkenes, rendering the formation of two covalent bonds impossible. However, when one of the molecules absorbs a photon, an electron within the molecule is excited from the π to the π* orbitals, effectively making π* the HOMO of the photoexcited system. From this photoexcitation, the formation of an effective HOMO-LUMO overlap between the two molecules becomes possible. This overlap allows to create two covalent bonds, as shown in Figure 1.4.

Although the use of photoexcited molecules allows to form C−C bonds through thermally unattainable pathways, it is important to note that [2+2] photocycloaddition reactions will be stereochemically selective. Indeed, during [2+2] cycloaddition the excited electron does not need to transition to a triplet state which causes the loss of stereochemical configurations within the molecule. As such, the stereochemistry of the final product will be dependent of the stereochemistry of the reactants. This effect was observed by Yamazaki and Cvetanović during their studies on the photodimerisation of *cis*-butene wherein only two diastereoisomers were observed, as shown in Figure 1.5.[31]

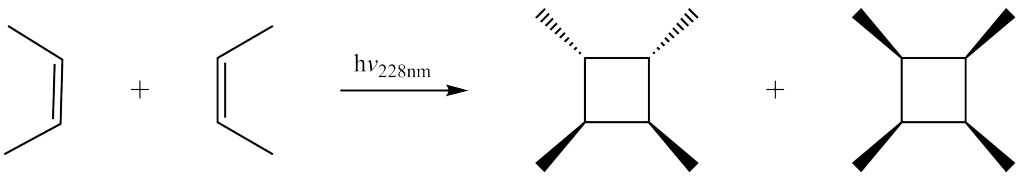

Fig. 1.5 Photodimerisation of *cis*-butene carried out by Yamazaki and Cvetanović.[31] The retention of the individual stereochemistry of the butene molecules was observed.

Even though photocycloaddition allows to create thermodynamically unfavourable products, the requirement of C=C bonds limits the applicability of this technique. The photostimulated formation of radical species can be used as a more effective and versatile alternative to the excitation of C=C bonds.

Radicals are species which possess an unpaired electron in their HOMO. The formation of radicals occurs through the homolytic fission of molecular bonds resulting from the absorption of either thermal or photonic energy as shown in Figure 1.6. Even though this homolytic fission of molecular bonds can be achieved through thermal excitation, the photoexcitation process remains more energetically efficient.[27,32]

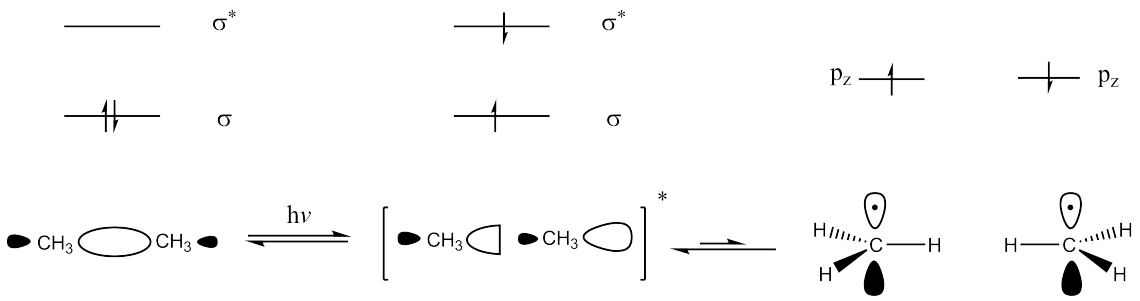

Fig. 1.6 Scheme showing the changes in electronic configuration (above) and orbital geometry (below) during the photostimulated homolytic fission which leads to the formation of radical species.

Due to the unpaired electrons, the created radical species are highly reactive and play an essential role in a large part of photosynthetic procedures.[27,33–35] Radical reactions proceed through three different phases: initiation, propagation, and termination. During initiation, free radicals are generated through the homolytic fission of a molecule with a relatively low activation energy. These radicals can proceed to react with non-radical species through H abstraction or bond formation. The reaction of a radical with a non-radical species will lead to the formation of another radical. This is the propagation process, as shown in Figure 1.7. Finally, the radicals (either generated through the initiation step or the propagation step) can react with other radicals in the system, effectively achieving complete electron pairing and leading to the loss of active species in the reaction through the termination process. These three different phases can be seen clearly during the photoinitiated chlorination of methane as shown in Figure 1.7.

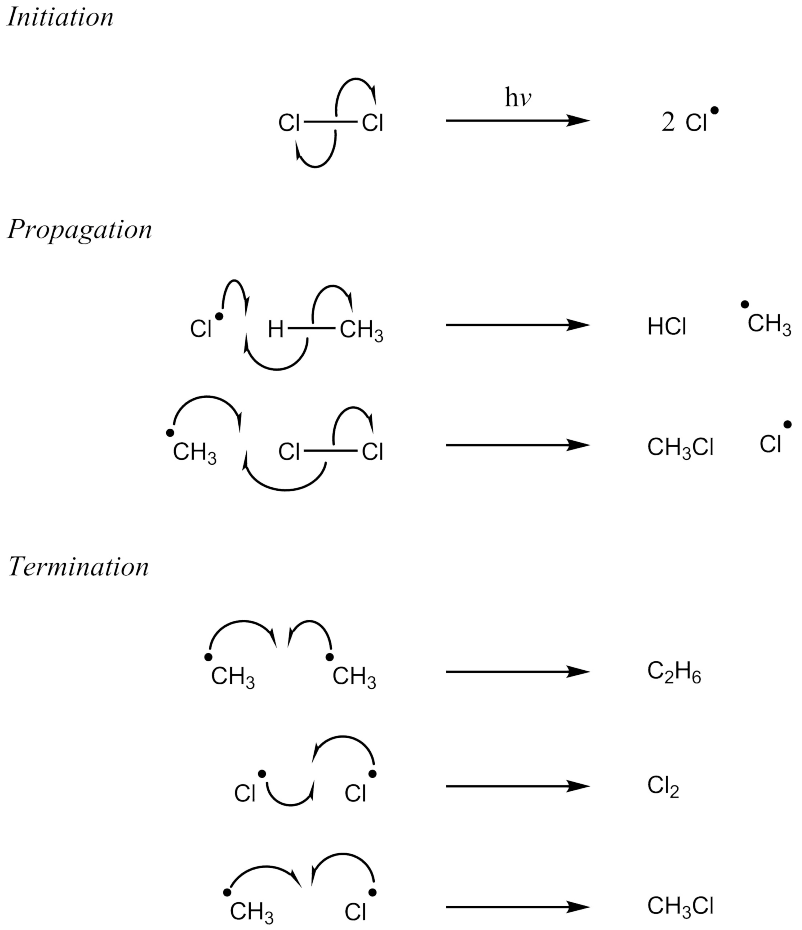

Fig. 1.7 Scheme showing the three different phases of radical reactions in the chlorination of methane from photogenerated chlorine radicals.

The versatility of the propagation step has rendered the use of radicals an invaluable asset for both organic and polymer synthetic reactions.[36] Furthermore, due to their high reactivity, radicals have been extensively used to carry out reactions involving energetically stable molecules.[37,38] One such class of reactions, that of organic decompositions, forms the foundation of the purification techniques developed during the present study as described in Chapters 5 to 7. Organic decomposition reactions take advantage of the high reactivity of radical species generated from photocatalytic materials in order to convert toxic molecules into valuable chemical species.

Photocatalysis

Although the direct interaction of light with molecules allows for the actuation of complex chemical reactions, the energy requirement for direct photosynthetic phenomena remains very high, often

requiring illumination of wavelengths below 300 nm.[39,40] As such, in order to make photochemical reactions more energetically efficient and sustainable, the eye was turned to natural photosynthetic chemistry. In a large feat of biomimetics, a series of photocatalysts have been developed in order to perform photochemical reactions through the use of solar light.[41–43]

Photocatalysts are photoactivated species which can be introduced to chemical reactions in order to reduce the required activation energies or increase the rate of product formation. By absorbing light, photocatalysts can supply an additional source of energy to chemical reactions, thus allowing to overcome the reaction barriers of a wide variety of such reactions. Most photocatalytic processes hinge on the formation of free radicals which supply a lower energy alternative reaction pathway for chemical syntheses due to their highly reactive nature. Two main families of photocatalysts exist: homogeneous and heterogeneous catalysts.

Homogeneous photocatalysis focuses on the use of photocatalytic species in the same phase as the reagents. These reactions are normally restricted to liquid systems. Although organic homogeneous photocatalysts have been used successfully in many photosynthetic reactions,[40] the most commonly used homogeneous photocatalysts are transition metal complexes.[44] The advantages of using inorganic complexes as homogeneous photocatalysts are clearly displayed by the cation of tris(bipyridine)ruthenium(II) chloride ($[Ru(bpy)_3]Cl_2$), $Ru(bpy)_3^{2+}$. Only mild photon energies ($\lambda \approx 450$ nm) are required in order to generate high energy electrons through a metal to ligand charge transfer.[44] This low energetic requirement as well as a high QE and long excited state lifetimes have rendered $Ru(bpy)_3^{2+}$ one of the most important homogeneous photocatalysts for the exploitation of solar energy.[45]

Although the presence of photocatalysts in the same phase as the reagents allows to maximise the contact between the reagent and the catalysts, it can often be difficult to separate and recover the catalysts. This difficulty effectively hinders the industrial applicability of homogeneous photocatalysts. Furthermore, organometallic complexes often have to be synthesised through difficult procedures involving expensive reagents. As such, the commercialisation of homogeneous photocatalysis remains limited to special chemical syntheses.

Heterogeneous photocatalysts can, in general, be used to overcome the problems of homogeneous photocatalysis. Although the phase discrepancy of heterogeneous photocatalysis reduces the contact between the catalysts and the reagent species, the advantages gained by the ease of cata-

lyst/product separation have led to a heightened interest in these systems. Furthermore, many solid state photocatalysts are based on low cost transition metal oxides due to their natural abundance.[46] Such advantages have allowed the effective use of photochemistry at commercial scales.[47,48] In particular, heterogeneous photocatalysts have received significant interest as agents for the photodecomposition of toxic pollutants.[49–52] During the present study on the purification of gas streams, semiconductor heterogeneous photocatalysts were used for the photodegradation of contaminant species.

1.2 Semiconductors as Photocatalysts

In order to understand the particular effectiveness of solid state catalysts, it is important to establish the electronic structures of bulk solids. Figure 1.8 shows the effects on orbital structures as increasing numbers of AO are combined in solids. For clarity reasons, Figure 1.8 only displays the combination of atomic s orbitals although all of the AO in a given species will undergo the described process.

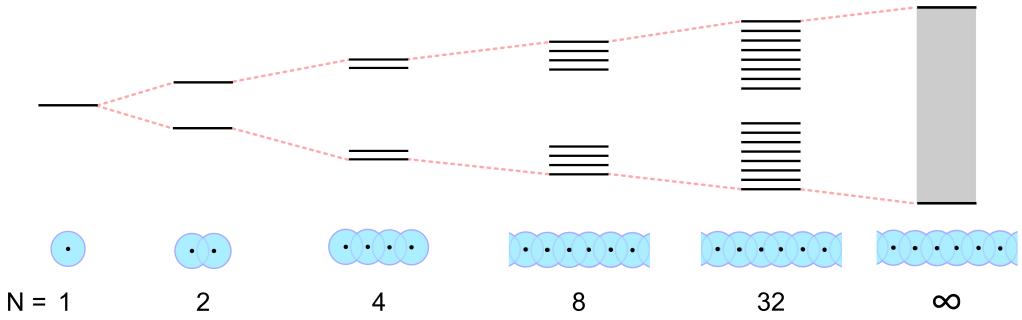

Fig. 1.8 Scheme showing the formation of band orbital structures in bulk solids from the LCAO of N orbitals. As N tends to infinity, the width of the band remains finite whilst its component orbitals tend to infinity.

It can clearly be seen in Figure 1.8 that as the amount of component atoms (N) tends to infinity, the energy between the highest antibonding orbital and the lowest bonding orbital remains finite. This can be expressed mathematically by considering the energy levels according to Hückel theory. From the Hückel secular determinant of a series of N overlapping s orbitals, the energy level of any given MO (E_R) can be expressed as reported in Equation (1.5) where α and β are two energy terms for the electrons in the MOs, N is the total number of AO and k is a positive integer relating to the energy levels of the specific MOs studied.

$$E_R = \alpha + 2\beta cos(\frac{k\pi}{N+1}) \tag{1.5}$$

It can be seen from Equation (1.5) that for the lowest energy MO (k=1) and the highest energy MO (k=N) for a system with N orbitals, will have fixed energies as shown in Equation (1.6) and Equation (1.7).

$$E_1 = \alpha + 2\beta cos(\frac{\pi}{N+1}) \tag{1.6}$$

$$E_N = \alpha + 2\beta cos(\frac{N\pi}{N+1}) \tag{1.7}$$

As N tends to infinity, Equations (1.6) and (1.7) can be reduced to simpler terms, as shown in Equations (1.8) and (1.9), respectively.

$$E_1 = \alpha + 2\beta \tag{1.8}$$

$$E_N = \alpha - 2\beta \tag{1.9}$$

From Equations (1.8) and (1.9), it can be seen that the energy difference between the highest and the lowest MOs in a system composed by the LCAO of *s* orbitals, corresponds to 4β.

This fixed energy difference between MOs signifies that when the number of AO approaches infinity, the difference between individual MO energy levels becomes infinitesimally small. This, in turn, leads to the formation of a continuous energy band (as shown in Figure 1.8). Nonetheless, it remains important to note that as MOs can only be created by the effective overlap of similar AO, different orbital bands, corresponding to different overlapping orbitals (s band, p band, etc.), will be generated in bulk materials.

In semiconductors, electrons can be promoted from the energetically highest occupied band, the valence band, to the energetically lowest unoccupied orbital band, the conduction band. However,

electronic excitation can only occur if the energy supplied to the system is equal to or greater than the energy gap between the valence band maximum, VBM, and the conduction band minimum, CBM. This energy is defined as the band gap, E_g. Figure 1.9 shows the band transition occurring in a semiconductor during electronic excitation.

As electrons transition to the conduction band through photonic (or thermal) excitation, they leave a positively charged hole in in the valence band. Both the created hole and the excited electron are mobile. However there is an energy barrier to overcome in order to separate these charges. As such, the electron-hole pair can often be considered as a single particle, an exciton. The high mobility of the exciton in semiconductors has allowed for the use of semiconductors in a wide variety of applications such as photovoltaics, photoelectrolysis and photodegradation.[46,49,53]

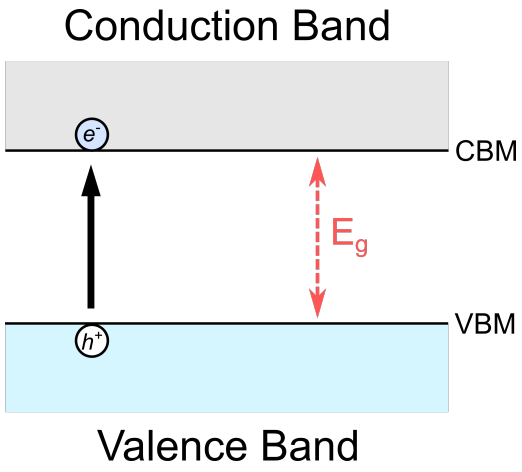

Fig. 1.9 Diagram showing the band transition occurring in semiconductors during electronic excitation. Electrons, e^-, are promoted from the VBM to the CBM, leaving a positively charged hole, h^+. The energetic difference between the VBM and CBM is the band gap, E_g, this is the minimum energy required by electrons in order to undergo photoexcitation.

Nonetheless, it is important to note that not all semiconductors can be photoexcited in a useful manner. This limitation can be attributed to two intrinsic properties of the semiconductors: band gap energy and chemical stability. As discussed previously, in order to achieve the photoexcitation, a photon of energy equal to or larger than E_g needs to be absorbed. Whilst this means that semiconductors with small band gaps such as Fe_2O_3 and CdO (E_g = 2.3 and 2.1 eV, respectively)[54] can be easily photoexcited by the solar spectrum ($\lambda \leq 590$ nm), wide band gap semiconductors such as ZrO_2 ($E_g \approx 5.0$ eV)[55] require dedicated photon sources. It becomes readily apparent that in order for semiconductors to be energetically and financially efficient photocatalysts, the choice of available materials is limited to those which have band gaps that allow solar photoexcitation.

The second limitation of photoexcited semiconductors is that of chemical stability. Due to the high reactivity of the photogenerated radicals, it is important for photocatalysts to be relatively chemically inert. This, unfortunately, is not the case for many semiconductors with small band gaps (such as Fe_2O_3) which are known to be highly reactive not only to photogenerated radicals but also to a very large variety of chemical conditions.[54,56] This chemical instability can result very problematic for industrial applications as photocatalytic devices often need to operate in harsh environments.[57,58]

During the present study, TiO_2 was chosen as a semiconducting catalyst for the purification of gas streams due to a number of particular properties amongst which a good chemical stability and an appropriately sized band gap.[46] Indeed, TiO_2 is known to possess a band gap which allows to achieve photoexcitation from the solar spectrum in addition to being chemically inert,[46,59] signifying that the semiconductor can be used as a photocatalyst without it being decomposed by any photogenerated radicals.

1.2.1 TiO_2 Photocatalysis

TiO_2 is a semiconducting metal oxide that can be readily found in nature in three crystalline phases: rutile, anatase and brookite. Due to their crystal structure differences, (as seen in Figure 1.10) the three natural polymorphs of TiO_2 possess different chemical and electronic properties which affect their suitability in photocatalytic applications.

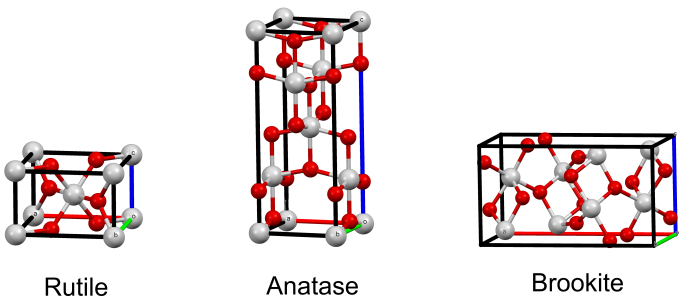

Fig. 1.10 Ball and stick crystal structures of the three main polymorphs of TiO_2. Titanium is represented as white whilst Oxygen is shown as red.

Zhang and Banfield have shown that with TiO_2 particle sizes of less than 11 nm the anatase crystal phase was favoured, with particle sizes ranging from 11 to 35 nm, brookite is preferentially formed, and above 35 nm, the rutile crystal phase will be the most thermodynamically stable.[60]

However, once formed, the anatase crystal phase is kinetically stable at room temperatures due to a slow phase transition to the more thermodynamically stable rutile.[46] This kinetic stability can be overcome by high temperatures, allowing for the formation of pure rutile crystals from anatase annealed at temperatures exceeding 600°C for large periods of time.[61] As such, the presence of both the anatase and rutile TiO_2 phases can be observed in samples processed at mild temperatures.

Electronically, different crystal structures possess slightly different band gaps. The band gaps of rutile and anatase were calculated by Tang *et al.* to be 3.0 eV and 3.2 eV, respectively.[62] Whilst the band gap of brookite was calculated to be 3.14 eV by Grätzel and Rotzinger.[63,64] This signifies that photons of energy above 3.0 eV ($\lambda \leq 413$nm) will promote the formation of excitons in TiO_2. The process for the photogeneration of electrons (e^-) and holes (h^+) on TiO_2 can be summarised as shown in Equation (1.10)

$$TiO_2 \xrightarrow{h\nu} TiO_2 + h^+_{vb} + e^-_{cb} \tag{1.10}$$

The photogenerated exciton can migrate to the surface of the TiO_2 in order to undergo redox reactions with molecules adsorbed on the semiconductor. During these redox processes the photoexcited electron will undergo intermolecular transition onto an acceptor molecule (A). Concurrently, a donor molecule (D) will transfer an electron into the positively charged vacancy of the photogenerated hole. This process leads to the formation of two excited species (A^- and D^+) which will undergo chemical reactions with neighbouring molecules. This photocatalytic molecular activation is represented schematically in Figure 1.11.[65,66]

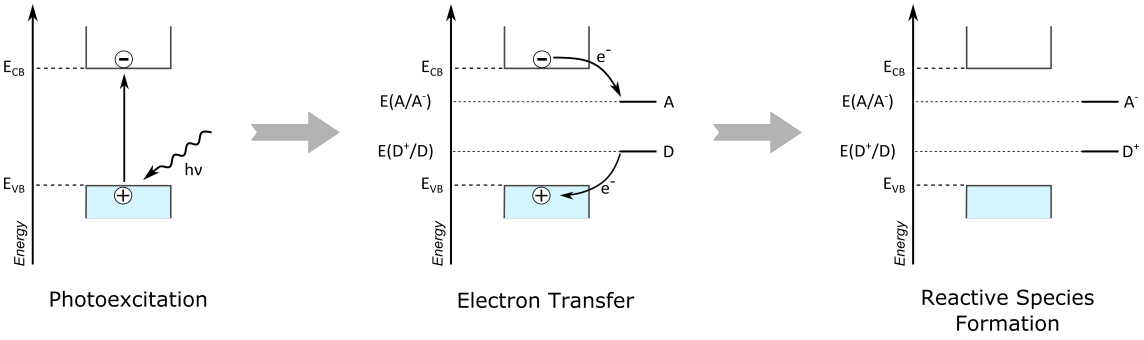

Fig. 1.11 Schematic representation of the electronic transitions during the main steps involved in the photocatalytic activation of acceptor (A) and donor (D) by TiO_2. The energy levels of the conduction and valence bands of TiO_2 are labelled as E_{CB} and E_{VB}, respectively, whilst the energy levels of the acceptor and donor redox pairs are labelled as $E(A/A^-)$ and $E(D/D^+)$, respectively.

It can be further seen in Figure 1.11, that the energy level of the acceptor species must lie below that of the conduction band of TiO_2 in order to achieve a successful electronic transition. In addition to this, the energy level of the donor species must lie above that of the valence band in order to supply an electron to the depleted band of TiO_2. As such, TiO_2 photochemical reactions are limited to specific acceptor and donor molecules. Although this limitation can be overcome through a number of processes such as the use of multiple photons to achieve electronic excitation (as reported in multiphoton processes)[67] or the combination of thermal excitation with photonic excitation (as seen in light enhanced thermal catalysis),[68] TiO_2 photocatalysis performed through single photon photoexcitation has the highest efficiency.

In TiO_2 photocatalysis, the most common acceptor and donor molecules adsorbed onto the semiconductor surface are O_2 and H_2O, respectively. The O_2 molecules adsorbed onto the TiO_2 will react with the photogenerated electrons to form the highly reactive superoxide radical, $O_2^{-\cdot}$, as shown in Equation (1.11).[69] Similarly, the OH^- ions generated from the water adsorbed on the TiO_2 surface react with the photogenerated holes to create $OH^\cdot$ radicals, as shown in Equation (1.12).[62] These photogenerated $OH^\cdot$ possess a strong oxidation potential of +2.80 V, this potential is only exceeded by elemental fluorine.[46] Due to this tremendous oxidising power, the $OH^\cdot$ radicals can react indiscriminately, often leading to the complete mineralisation of organic compounds into CO_2 and H_2O.[69]

$$O_2 + e^- \longrightarrow O_2^{-\cdot} \tag{1.11}$$

$$OH^- + h^+ \longrightarrow OH^\cdot \tag{1.12}$$

The high oxidative potential of TiO_2 in combination with its chemical stability, photoefficiency, low toxicity, and low costs effectively render it the “perfect” catalyst for the photodecomposition of organic contaminants. In addition to this, these advantages have led to the use of TiO_2 in controlled photosynthetic techniques. These techniques focus not on the complete mineralisation of chemical species but rather on the use of photoactivated TiO_2 to catalyse synthetic reactions.

TiO_2 catalysed photosynthetic reactions

Photoexcited TiO_2 has been used in synthetic reactions since 1977 when Schrauzer and Guth observed the formation of ammonia whist reducing acetylene.[70] This observed reduction of N_2 is of particular importance as the reductive potential of the electrons created by photoexcited TiO_2 is insufficient to carry out the reaction due to the stability of the bond within the nitrogen molecules.[71] Further studies carried out by Soria *et al.* proposed that the reduction of N_2 proceeds through the formation of a reactive complex with the photogenerated $OH^{\cdot}$ radicals (as shown in Equation (1.13)).[71] During these studies, the yield of the reaction was further increased by inserting Fe^{3+} into the TiO_2 matrix.[71] These ions were observed to act as electron scavengers (as shown in Equation (1.14)), effectively increasing the population of photogenerated $OH^{\cdot}$. However, as the Fe^{2+} ions formed during these reactions were comparatively more stable than their oxidised counterparts, the enhancement effect caused by the Fe ions was non-catalytic.[71]

$$N_2 + OH^{\cdot} \longrightarrow [N_2 \cdots OH]^* \tag{1.13}$$

$$Fe^{3+} + e^- \longrightarrow Fe^{2+} \tag{1.14}$$

Further photocatalytic reductions of N containing species were reported by Mahdavi *et al.* in 1993 with the successful photoreduction of nitroorganic molecules to amines.[72] Mahdavi *et al.* used ethanol as the reducing agent which reacted with the nitroorganic molecules.[72] This procedure was of particular importance as it presented an alternative technique for the formation of amines.[72] Indeed, previous amine formation techniques relied on the use of Sn or Pd catalysts through non-selective and complex procedures.[72] Mahdavi's studies were further pursued by Ferry and Glaze who demonstrated the direct reduction by the electrons photogenerated on TiO_2, as well as an improved functional group selectivity for the reactions.[73]

The photocatalytic reductive potential of TiO_2 has been recently studied for the elimination of CO_2. The reduction of CO_2 has become an important research subject due to its crucial role in global climate change.[4,74–76] The photocatalytic reduction of CO_2 by TiO_2 catalysts was demonstrated in 1979 by Inoue *et al.* with the conversion of CO_2 into formic acid, formaldehyde and methanol

through the use of H_2O.[77] This was further improved by Thampi *et al.* for the reduction of CO_2 under standard conditions with Ru doped TiO_2.[76] However, the direct reduction of CO_2 is difficult as, due to the high bond strength of the molecules, the reducing electrons need to have an incredibly high energy.[78,79]

Although the reduction of CO_2 remains technically complicated, TiO_2 can be used to catalyse alternative synthetic reactions. The formation of C−C bonds by photoactivated TiO_2 was shown by Yanagida *et al.*[80] as well Cermenati *et al.*[43] Yanagida *et al.* used photoactivated H_2O as an oxidant species for the formation of carbon bonds. A separate reaction pathway was developed by Cermenati *et al.* where the formation of carbon bonds was carried out by the radical alkylation of electron deficient alkenes.[43]

The interaction of alkenes with photoactivated TiO_2 is known to lead to the formation of a variety partial photooxidation products.[81–83] Amongst these products, the formation of epoxides from alkenes is particularly important due to the role of epoxides within synthetic chemistry.[32,84] Such TiO_2 catalysed epoxidations were reported by Murcia-López *et al.* as well as by Nguyen *et al.* in photocatalytic gas stream reactors.[85,86] It was further shown by Ohno *et al.* that the TiO_2 mediated photoepoxidation of alkenes could be carried out both stereoselectively and stereospecifically.[87] During the present study, the photoepoxidation of 1-hexene in gas streams and the direct reaction of its most reactive partial photoepoxidation products are investigated in Chapter 8.

Although TiO_2 can be seen as a highly promising photocatalyst for both decomposition and synthetic reactions, its commercialisation has remained unusually scarce due to the generally low efficiency of TiO_2 based devices.[46] As the process crucial to the TiO_2 mediated decomposition of contaminants hinges on the production of high energy molecules on the TiO_2 surface, the available semiconductor surface area is particularly important to the efficiency of photocatalytic purification devices. The currently used TiO_2 photocatalysts; monoliths and macrostructured powders, have a relatively limited surface area,[88] effectively restricting the production of $OH^{\cdot}$ and $O_2^{-\cdot}$ radicals. As such, an increase in photocatalytic efficiency can be achieved by increasing the surface area available for the adsorption of reactants. In addition to addressing the low efficiency, morphological modifications of the catalysts further allow to reduce the volume of photocatalytic reactors (another setback to the practical application of TiO_2 as a photocatalyst).

During this study, in order to establish a commercially viable TiO_2 photocatalytic gas phase purification reactor, the efficiency of the system was improved through two main techniques. Firstly, a specific photoreactor design (as described in Chapters 6 and 7) was established in order to maximise the contact between the TiO_2 and the gas phase contaminants. The second avenue investigated in order to enhance the photocatalytic activity of TiO_2 was to convert the morphology of the semiconductor to high surface area nanostructures (as described in Chapter 3).

1.2.2 Nanostructured Semiconductors as Photocatalysts

Nanostructures are materials for which at least one dimension resides within the nanoscale ($< 1\ \mu$m). In recent years nanostructures have received particular interest due to their physicochemical properties which often render them ideal for a variety of different applications. Amongst these unique properties, one of the most useful remains the large increases in surface areas inherent to nanomaterials. The large surface area of nanomaterials was successfully used by Jong-Heun Lee to enhance the gas-sensing properties of semiconductors by using nanostructured systems instead of thin films.[89] For gas phase photocatalytic applications, this increase in surface area leads to an increase in contact sites between the gas molecules and the photocatalysts, effectively increasing a system's photocatalytic efficiency.

It thus becomes clear that the use of nanostructures in the present series of studies would greatly increase the efficiency of the designed photocatalytic purification technologies. Although many different nanostructured materials have been created, three structures in particular are known to possess extensive surface areas: nanotubes, aerogels, and nanofibres.[90–92]

Nanotubes

Semiconductor nanotubes were first developed in the late 1990s.[93] In 2001 Gong *et al.* demonstrated the successful synthesis of TiO_2 nanotube arrays with lengths of up to 50 nm through anodisation.[93] Due to their high surface areas, these structures have been successfully used in a variety of applications ranging from drug delivery to photostimulated hydrolysis.[90,94] The inherent advantages of the nanotubular morphology were further demonstrated by Lee *et al.* in their studies on ZnO nanotube arrays wherein ZnO nanotubes displayed a three fold increase in photoelectrochemical

water splitting efficiency with respect to ZnO nanorods.[95]

Although nanotubes possess many promising characteristics, the synthesis of TiO_2 nanotubes at a large scale remains significantly challenging. The standard procedure for TiO_2 nanotube synthesis hinges on the electrochemical formation of nanotube arrays on the surface of Ti plates, effectively complicating the large-scale synthesis of TiO_2 nanotubes.[93] Furthermore, once the TiO_2 nanotube arrays have been formed, a further complex procedure is required to separate these arrays from their original substrate.[96] As a consequence of these limitations, the industrial application of TiO_2 nanotubes remains limited.

Aerogels

More promise for the application of nanostructures in the elimination of gas contaminants can be seen in the use of aerogels. Aerogels are highly mesoporous solids with exceedingly large surface areas first developed in 1932.[97] These large internal surface areas arise from the successful removal of solvents from wet gel monoliths whilst maintaining the structural integrity of a polymer network. Figure 1.12 shows the two main synthetic phases which lead to the formation of low density and high porosity aerogels: polymerisation and solvent extraction. Initially, a polymer monolith with a high internal surface area is created by the cross linked polymerisation of a series of monomers in a solvent. The formation of an aerogel from the monolith is then performed by removing the solvent from the polymer gel without causing a collapse of the network. This procedure creates materials with high porosities (>90% by volume) and internal surface areas ($\sim$ 1200 m^2g^{-1}).

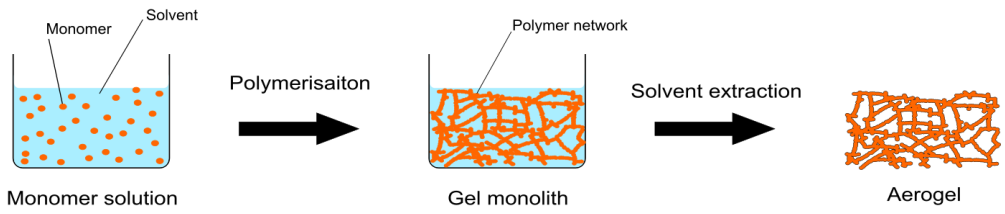

Fig. 1.12 Scheme showing the main phases leading to the formation of an aerogel monolith; polymer network formation through polymerisation and aerogel monolith synthesis through solvent extraction.

Due to their high surface areas, the use of TiO_2 aerogels in the purification of gas streams can allow the development of highly efficient photocatalytic purification reactors. The advantages

of TiO_2 based aerogels were shown clearly by Cao *et al.* during their studies wherein SiO_2/TiO_2 aerogel monoliths were used to decompose trichloroethylene an order of magnitude above the commercially available TiO_2 nanopowder, Degussa P25.[98] However, the monoliths created by Cao *et al.* displayed significant mechanical fragility and required supercritical CO_2 drying in order to create a stable aerogel.[98] Supercritical drying is a complicated and expensive procedure which limits the commercial applications of TiO_2 based aerogels. This limitation was overcome by Sarawade *et al.* with an ambient condition synthesis of SiO_2 aerogels in 2010.[99] Unfortunately, SiO_2 is a non-photoactive material, which means that the created aerogels could not be used as successful photocatalysts.

Even though the photocatalytic application of aerogels cannot be taken advantage of efficiently, their large surface area means that aerogels can still be used for the removal of contaminants from gaseous environments through adsorption.[97] A similar adsorption removal technique is already commercially applied by PpTek ltd. for the removal of siloxanes from biogas with the use of simple polymeric media.[9,100]In order to investigate this potential application for SiO_2 aerogels, as well as to establish an effective comparison between photodegradative and absorptive methods of gas purification, the adsorptive properties of SiO_2 aerogels were studied as discussed in Chapter 4.

Nanofibres

In light of the complicated synthetic requirements of TiO_2 nanotubes and aerogels, it becomes clear that these two nanostructures remain unsuitable as TiO_2 based photocatalytic agents for the removal of contaminants from gas streams. An alternative nanostructure which maintains high surface areas whilst displaying a high mechanical stability can be found in electrospun nanofibres. This mechanical stability of nanofibres is of particular importance in photocatalytic reactors as this means that, unlike nanoparticulates, nanofibres do not require immobilisation on a substrate before they can be commercially used.

First developed by Taylor in the late 1960s,[101–103] the electrospinning procedure uses the high voltage extrusion of a polymer solution through a capillary in order to create nanoscale fibrils which can then be collected on a grounded substrate.

The detailed formation mechanism for electrospun nanofibres can be summarised in four steps.

Firstly, (Figure 1.13 A), a high electric field potential is applied to the polymer solution, under the electrostatic forces of the current, the meniscus of the solution forms a conical structure called the Taylor cone. As the strength of the electrostatic forces in the solution is increased, drops of solution are then ejected from the tip of the Taylor cone. In polymer solutions with high viscosity the ejected droplets are then extruded into fibres (Figure 1.13 B). The solvent in the charged fibres subsequently evaporates, leading to the formation of solid structures (Figure 1.13 C). Finally, the charged fibres are collected by a grounded electrode under random orientation (Figure 1.13 D). The collected fibres can then be retrieved from the electrode in the form of a mechanically resistant non woven mat.

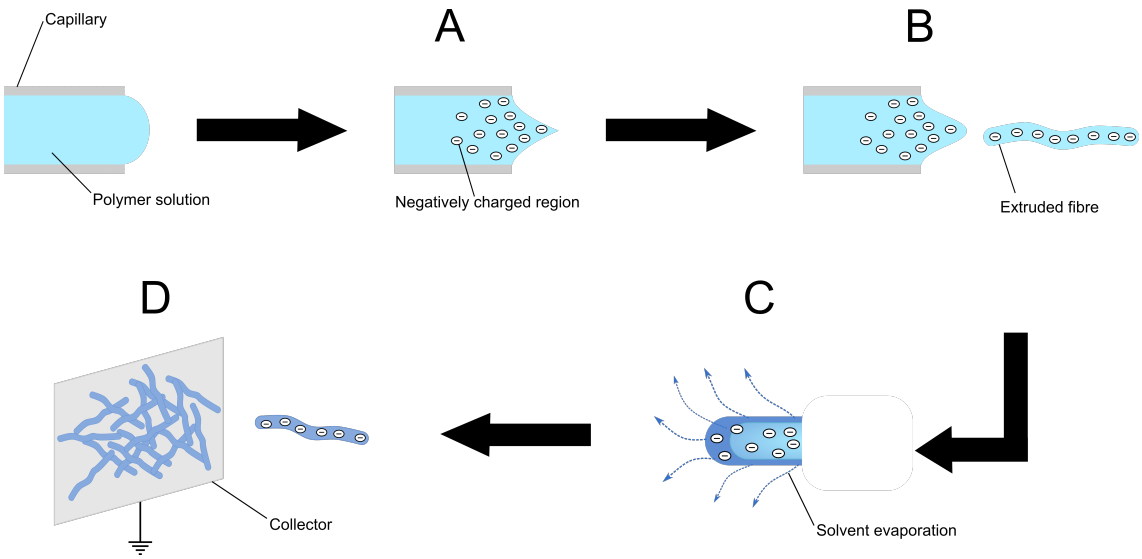

Fig. 1.13 Schematic representation of the key processes in the formation of electrospun nanofibres. These processes are: the formation of the Taylor cone (A), the extrusion of polymer fibres from the Taylor cone (B), the evaporation of the solvent and hardening of the fibres (C), and the collection of the charged fibres onto a grounded material (D).

The morphology of electrospun nanofibres can be controlled by a wide variety of factors. The most important amongst these factors are the initial polymer solution viscosity, the strength of the applied electric field and the distance between the capillary tip and the collector. These parameters have been extensively studied in literature [104] and the effect of their modification upon the created structures has been thoroughly investigated. [105] As such, a high degree of control on the specific morphology of nanofibres can be achieved. The versatility of the electrospinning technique is further enhanced by the simplicity through which it can be adapted for the formation of a wide variety of metal oxide nanofibres.

By adding a metal oxide precursor to the electrospinning solution, it is possible to create precursor laden nanofibres. The precursor can then be converted into its corresponding metal oxide through high temperature calcination which also allows to eliminate the polymer from the nanofibres. This method was demonstrated by Shao *et al.* in 2002 with the synthesis of SiO_2 nanofibres.[106] The technique was further adapted by Lee and Xia in 2006 as well as by Fang *et al.* in 2015, for the synthesis and application of TiO_2 [107] and WO_3 [108] nanofibres, respectively.

TiO_2 nanofibres have a surface area of $\sim 15\ m^2g^{-1}$,[109] this is significantly lower than the $\sim 1200\ m^2g^{-1}$ surface area displayed by aerogels.[98] Nonetheless, this remains a significant increase over macroscale TiO_2 films ($< 0.2\ m^2g^{-1}$).[88] As such it was possible for Rezaee *et al.* to demonstrate the efficacy of TiO_2 nanofibres in water purification through the decomposition of the Reactive Blue 19 dye in aqueous solutions.[110]

The versatility of the electrospinning technique in combination with the photoactivity of TiO_2 nanofibres renders them a promising nanostructure for the enhanced photodecomposition of contaminants in gas streams. During the present study, the synthesis, doping, and effectiveness of TiO_2 nanofibres as gas purification photocatalysts were investigated. Chapter 3 presents the synthesis of TiO_2 nanofibres with enhanced morphologies for the photodecomposition of gas phase contaminants. The photodecomposition properties of the created nanofibrous structures and their relative efficiencies were then studied and are presented in Chapter 5.

It is important to note that due to a perceived synthetic complexity as well as an inherently time consuming synthetic procedure, TiO_2 nanofibres have received limited industrial and academic interest. Indeed, the TiO_2 nanostructure most used for photocatalytic applications remains a simple nanopowder.

Aeroxide P25

The most common commercially available TiO_2 nanopowder is Aeroxide P25 (P25). P25 is synthesised through the gas-phase flame pyrolysis of $TiCl_4$ which allows to create nanoparticles with an average diameter of 21 nm.[111] It is known to be a particularly effective photocatalyst due to two main properties: a high surface area and a hybrid crystal structure composition. The surface area of P25 lies in the range of 35 - 65 m^2g^{-1}, this is significantly higher than that of TiO_2

films (< 0.2 m^2g^{-1}).[88,112] This surface area enhances the contact area between the catalyst and the reagents, leading to P25 displaying a higher photocatalytic activity with respect to dense TiO_2 films.

The second main factor in the high photocatalytic performance of P25 lies in its crystal composition. P25 nanoparticles are composed of a combination of anatase and rutile at a ratio of approximately 3:1. The combination of the anatase and rutile crystal structures was shown by Su *et al.* to display higher photoactivity than either the rutile or anatase structures alone.[113] Furthermore, they demonstrated that the photoactivity of rutile/anatase composites peaked at a composition of 60% anatase, which is consistent with the composition of P25.[113] This higher photocatalytic activity of rutile/anatase composites with respect to the individual crystal structures is a subject of significant academic interest.[112,114] It is commonly accepted that the increase in photoefficiency arises from the misalignment of the conduction and valence bands of rutile and anatase.[113–115]

Although the relative band alignments of rutile and anatase (and consequently the movements of the photogenerated charges between the two species) have been a matter of contention, this was conclusively settled in 2013 by Scanlon *et al.*[114] By combining mathematical modelling with experimental data, Scanlon *et al.* demonstrated that anatase had a higher electron affinity than rutile, meaning that photogenerated e^- will flow from rutile to anatase.[114] As such, the band alignment between the two crystal phases can be depicted as shown in Figure 1.14.

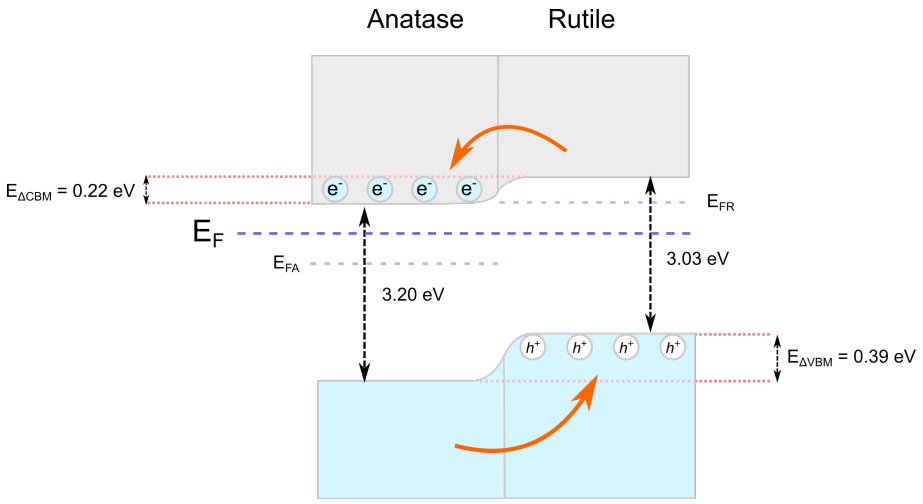

Fig. 1.14 Conduction and valence band alignment for rutile/anatase TiO_2 composite materials as proposed by the experimental and theoretical studies of Scanlon *et al.*[114] The orange arrows indicate the flow of charged species whilst the blue and white circles represent the photogenerated electrons and holes, respectively. E_F shows the Fermi level of the combined system whilst E_{FA} and E_{FR} show the Fermi levels of anatase and rutile, respectively. $E_{\Delta CBM}$ shows the energy difference between the conduction band minima of the two crystal structures whilst $E_{\Delta VBM}$ shows the energy differences between the valence band maxima of rutile and anatase.

From Figure 1.14 it becomes readily apparent that photogenerated e^- will tend to transition to (or remain in) the anatase crystal structure whilst photogenerated h^+ will tent to transition to (or remain in) the rutile structure. This is further illustrated by the band bending shown at the interface of the anatase and rutile structures in Figure 1.14. The preferential movement of charges in the complex material results in a shift of the Fermi level to an energy in-between the Fermi levels of the anatase and rutile structures, as shown in Figure 1.14. The charge separation thus achieved leads to longer lifetimes for the excitons in composite structures with respect to those observed in individual crystals. As such, composite materials such as P25 will tendentially demonstrate higher efficiency with respect to materials composed solely of a single crystal phase.

During the present study, the photocatalytic effectiveness of P25 as a purification agent for gas streams was compared to that of a variety of TiO_2 nanofibres. Chapter 5 studies the photodegradation properties of P25 in static gas environments whilst comparing its gas purification effectiveness with that of TiO_2 nanofibres and SiO_2 aerogels. The nanopowder was further used in Chapters 6 and 7 in order to study the photocatalytic purification of gas streams.

1.3 Biogas

In order to demonstrate the applicability of TiO_2 nanostructures as gas purification technologies, their effectiveness in the purification of industrially relevant gas streams needs to be demonstrated. The present study arises as an industrial project jointly funded by PpTek ltd. and Innovate UK with the aim of developing commercially viable photocatalytic purification technologies for the purification of biogas (and, to a lesser extent, gas streams in general). As such, the performed experiments focus on the use of TiO_2 nanostructures as purification agents for biogas as described in Chapters 5 and 6 whilst also discussing the ambient air purification potential of the developed technologies in Chapter 7.

1.3.1 Biogas as an Energy Source

The term "Biogas" is usually used to describe the gas generated by the anaerobic decomposition of organic matter in natural waste, sewage, and landfill sites.[116] Although the composition of biogas changes depending on the nature of the materials and waste digested, it contains four primary components in varying quantities: methane (CH_4, 40-70 %), carbon dioxide (CO_2, 25-5 %), hydrogen (H_2, 1-5 %) and nitrogen (N_2, 0.3-3 %).[117,118] The higher enthalpy of combustion of methane (55.5 MJ/kg)[24] with respect to commonly used fossil fuels (44.8 MJ/kg for Diesel)[24] in addition to the large methane content of biogas, has led to its widespread use in spark engines as an alternative fuel source.[116,119,120] Furthermore, the combustion of biogas is ecologically favourable as CH_4 has a global warming potential 28 times larger than that of CO_2 over a period of 100 years.[4] However, due to the variable nature of the waste precursors of biogas, the presence of a large quantity of contaminant species is observed within the gas.[8]

1.3.2 Sources of Biogas Contamination

Of the many contaminants present in biogas there are two species of chemicals which, even at very low concentrations, can result in severe damage to spark engines: sulfides (in particular hydrogen sulfide, H_2S), and siloxanes. Hydrogen sulfide is a particularly important contaminant in biogas due to both its toxicity and chemical reactivity in concentrations as low as a few parts per million. When H_2S is burned in the presence of water and oxygen it will readily undergo oxidation to form

sulphur dioxide (SO_2) and sulphuric acid (H_2SO_4) as described in Equations (1.15) and (1.16).[121] These two chemicals can lead to high corrosion and critical engine failure.[122] As such, a large number of studies have been carried out in order to remove H_2S from biogas and improve the lifetime of industrial combustion engines.[121–123]

$$2\,H_2S + 3\,O_2 \xrightarrow[\Delta]{} 2\,SO_2 + 2\,H_2O \tag{1.15}$$

$$H_2S + 2\,O_2 \xrightarrow[\Delta]{} H_2SO_4 \tag{1.16}$$

Similarly, the combustion of siloxanes can form SiO_2 microcrystallites which will ultimately lead to combustion engine failure.[124] As such, their removal from biogas has become a key element in industrial biogas purification and is one of the main topics of study during this thesis.

Siloxanes in Biogas

Siloxanes are a family of chemical compounds which have achieved widespread use in cosmetics and detergents due to their low toxicity and high chemical stability.[13] As a result of their widespread use, siloxanes have become a non-negligible element in human waste. Furthermore, due to their high chemical stability, the decomposition of siloxanes often requires energetic conditions exceeding those supplied through anaerobic digesters. This has led to siloxanes becoming a persistent contaminant in biogas.[124]

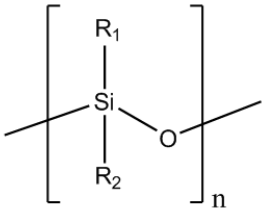

Fig. 1.15 General molecular structure of siloxanes.

Chemically, siloxanes are defined as a subgroup of silicon containing molecules with a Si−O backbone, as shown in Figure 1.15. As this definition encompasses many different molecules with

increasingly complex names, a simplified nomenclature is used to distinguish individual siloxanes. This nomenclature divides siloxanes in two groups linear, and cyclic. These groups are assigned the the letters L and D, appended by a number corresponding to the number of silicon atoms within a molecule. In this manner, the linear, two-silicon molecule, hexamethyldisiloxane is named L2. The chemical structure, IUPAC and simplified nomenclatures for two common siloxanes found in biogas are shown in Figure 1.16 .[16,125]

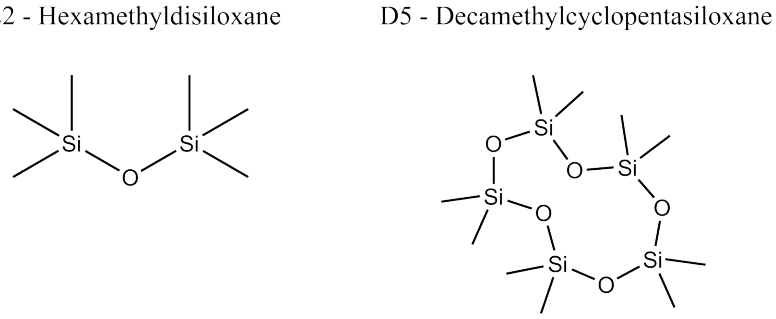

Fig. 1.16 The specific molecular structures of L2 and D5, two common siloxanes in biogas. The names of the siloxanes are reported in the form; simplified nomenclature – IUPAC nomenclature.

Upon complete oxidation, siloxanes will usually decompose to form SiO_2 microcrystallites which are known to lead to two major issues in industrial combustion engines. Firstly, the hardness of SiO_2 leads to internal abrasion and eventual engine failure.[12] Secondly, the microcrystallites can lead to the formation of a thermally insulating layer which causes overheating and destruction of sensitive engine elements.[13] A further issue with siloxanes resides in their particular chemical stability which leads to long term bioaccumulation.[18]

1.3.3 Elimination of Siloxanes in Biogas

Many different studies have been conducted towards the removal of siloxanes from biogas. A large number of the developed techniques purify biogas through the capture of siloxanes. The most common siloxane capture methods function through the use of adsorbents (such as activated carbon) or cryogenic condensation at low temperatures (-20 to -70°C).[9–11,16] As absorption techniques are those most used industrially,[9,17] the effectiveness of both aerogels and nanofibres as absorptive agents for the removal of siloxanes was investigated during the present study, as discussed in Chapter 4.

Although both adsorption and cryogenic distillation can purify biogas, the problem of siloxane disposal remains. In order to overcome this drawback it becomes necessary to purify biogas through the chemical conversion of siloxanes. Two different methods have been proposed for the chemical removal of gas phase siloxanes: reactive liquid extraction and photocatalytic decomposition. The former method, pioneered by Schweigkofler and Niessner in 2001, focuses on the cleavage of the $Si-O$ bond through acid/base catalysis.[7] Photocatalytic decomposition, the second process used to chemically decompose siloxanes, uses photocatalysts for the heterogeneous degradation of siloxanes. A number of studies have been carried out demonstrating the decomposition of siloxanes through TiO_2.[14,15] This technique presents a large number of advantages for the purification of biogas with respect to both standard adsorption and reactive purification methods.

TiO_2 Photocatalysis of Siloxanes

As discussed in Section 1.2.1 and shown in Equation (1.10), photoexcited TiO_2 generates high energy electrons and holes. These charges can then react with chemical species absorbed onto the semiconductor surface, giving rise to the $OH^{\cdot}$ and $O_2^{-\cdot}$ radicals, as shown in Equations (1.11) and (1.12). The photogenerated $O_2^{-\cdot}$ can also further react with protons on the TiO_2 surface in order to create the $HO_2^{\cdot}$ radical, as shown in Equation (1.17). The high reactivity of these radicals has made them ideal candidates for the photodecomposition of siloxanes in both the liquid and gas phases.[14,126–129]

$$O_2^{-\cdot} + H^+ \longrightarrow HO_2^{\cdot} \tag{1.17}$$

A mechanism for the decomposition of siloxanes was reported by Ren-De Sun *et al.* as shown in Equations (1.18) to (1.23).[126] The photogenerated radicals on the TiO_2 surface react with the methyl groups of the siloxanes in a series of abstraction reactions (Equations (1.18) to (1.20)), leading to the formation of the neutral $-Si-CHO$ species and the regeneration of a hydroxide ion as shown in Equation (1.20).

$$-Si-CH_3 + OH^{\cdot} \longrightarrow -Si-CH_2^{\cdot} + H_2O \tag{1.18}$$

$$-\mathrm{Si}-\mathrm{CH}_2^{\cdot} + \mathrm{O}_2 \longrightarrow -\mathrm{Si}-\mathrm{CH}_2\mathrm{OO}^{\cdot} \tag{1.19}$$

$$-\mathrm{Si}-\mathrm{CH}_2\mathrm{OO}^{\cdot} + \mathrm{e}^{-} \longrightarrow -\mathrm{Si}-\mathrm{CHO} + \mathrm{OH}^{-} \tag{1.20}$$

Although, the created $-\mathrm{Si}-\mathrm{CHO}$ species is stable, it will further react with photogenerated $\mathrm{OH}^{\cdot}$ radicals in a series of reactions in order to create a neutral tetraoxide molecule as shown in Equations (1.21) to (1.23).[126]

$$-\mathrm{Si}-\mathrm{CHO} + \mathrm{OH}^{\cdot} \longrightarrow -\mathrm{Si}-\mathrm{CO}^{\cdot} + \mathrm{H}_2\mathrm{O} \tag{1.21}$$

$$-\mathrm{Si}-\mathrm{CO}^{\cdot} + \mathrm{O}_2 \longrightarrow -\mathrm{Si}-(\mathrm{CO})\mathrm{OO}^{\cdot} \tag{1.22}$$

$$-\mathrm{Si}-(\mathrm{CO})\mathrm{OO}^{\cdot} + \mathrm{HO}_2^{\cdot} \longrightarrow -\mathrm{Si}-(\mathrm{CO})\mathrm{OOOOH} \tag{1.23}$$

The tetraoxide formed in Equation (1.23) is unstable and degrades through homolytic fission, leading to the formation of O_2 as well as a $-\mathrm{Si}-(\mathrm{CO})\mathrm{O}^{\cdot}$ radical and a $\mathrm{OH}^{\cdot}$ radical, as shown in Equation (1.24). The $-\mathrm{Si}-(\mathrm{CO})\mathrm{O}^{\cdot}$ radical will further decompose to form an $\mathrm{Si}^{\cdot}$ radical species as well as CO_2 (Equation (1.25)). Finally, the siloxane decomposition is completed through the quenching of the generated $\mathrm{Si}^{\cdot}$ and the photogenerated $\mathrm{OH}^{\cdot}$ in order to create SiOH moieties (Equation (1.26)).[126]

$$-\mathrm{Si}-(\mathrm{CO})\mathrm{OOOOH} \longrightarrow -\mathrm{Si}-(\mathrm{CO})\mathrm{O}^{\cdot} + \mathrm{OH}^{\cdot} + \mathrm{O}_2 \tag{1.24}$$

$$-\mathrm{Si}-(\mathrm{CO})\mathrm{O}^{\cdot} \longrightarrow -\mathrm{Si}^{\cdot} + \mathrm{CO}_2 \tag{1.25}$$

$$-\mathrm{Si}^{\cdot} + \mathrm{OH}^{\cdot} \longrightarrow -\mathrm{SiOH} \tag{1.26}$$

This transformation of siloxanes into SiOH is a major drawback for their photocatalytic degradation in biogas. Indeed, the photocatalytic activity of TiO_2 based siloxane photodegradation

reactors is known to decrease with extended reaction times (up to 18 months of continual use)[14] due to the accumulation of SiO_x species on the TiO_2 surface.[14] Hay *et al.* demonstrated that even at low SiO_x deposits, the photodegradation efficiency of TiO_2 was drastically inhibited and that at higher SiO_x concentrations, the photoactivity of the semiconductor was negated.[14] This effect was attributed to the insulating nature of the SiO_x species which prevented electron mobility from the semiconductor to adsorbed molecules.[14]

In addition to the limited lifetime of the TiO_2 a further limitation to the commercialisation of these technologies arises from the relatively low efficiency of current photocatalytic reactors. Indeed, although the use of a photocatalysts for the decomposition of siloxanes is a preferable technique compared to those already in use, current systems cannot withstand the intensive demands of large-scale industrial processes.

1.4 Kinetic Factors in TiO_2 Purification Reactors

One of the most important aspects of TiO_2 photocatalytic reactors is their speed and efficiency. Chemically, these requirements are investigated by studying the kinetic properties of the performed reactions. Heterogeneous photocatalytic systems (such as TiO_2 air purification photoreactors) are governed by a many complex variables. However, three main factors can be discerned in the kinetics of these reactions: the interaction between the surface of the catalyst and the studied reagents, the effect of light irradiation on the photocatalyst, and the concentration of the photocatalyst.

1.4.1 The Effects of Surface Area on Reaction Kinetics

The rate of a chemical reaction can be described as the loss (or production) of a chemical species over a given period of time. Mathematically this is represented according to the rate law shown in Equation (1.27), where ν is the rate of the studied chemical reaction, C is the concentration of a reagent chemical species, k is the rate constant of the reaction and n is the order of the reaction.

$$\nu = \frac{dC}{dt} = -kC^{\,n} \tag{1.27}$$

Heterogeneous photocatalytic reactions proceed through a wide variety of chemical species in many reaction steps. This means that the development of a universal rate law for heterogeneous photocatalytic reactions has yet to be achieved. In addition to this, the standard rate law shown in Equation (1.27) does not take into account the interaction of the reagents with the catalyst species. In heterogeneous catalysis, the interaction between the reagents and the catalysts is of crucial importance.[46,130,131] As such, the study of the adsorption of chemical species on substrates is a matter of significant academic interest.

The adsorption of chemicals on substrates

The adsorption of a gaseous chemical species (G) on a substrate (S) can be described as shown in Equation (1.28) where the gaseous species joins with the substrate in a reversible reaction to form a single complex (GS). The rate constants of the adsorption and desorption events are shown in Equation (1.28) as k_a and k_d, respectively.

$$\mathrm{G} + \mathrm{S} \underset{k_d}{\overset{k_a}{\rightleftharpoons}} \mathrm{GS} \tag{1.28}$$

As the adsorption is reversible, the rates of adsorption and desorption will reach equilibrium at a fixed temperature. From this equilibrium, it was possible for Irving Langmuir to establish the Langmuir isotherm, as shown in Equation (1.29).[132] The isotherm allows to correlate the surface coverage of a chemical (θ, defined as the occupied fraction of total available adsorption sites on the substrate) with the partial pressure of the studied chemical (p), and the ratio between the adsorption and desorption rate constants ($K = \frac{k_a}{k_d}$).

$$\theta = \frac{Kp}{1 + Kp} \tag{1.29}$$

The Langmuir isotherm is based on three crucial assumptions. Firstly, the adsorption of a gas on a solid surface cannot proceed beyond the formation of a monolayer. Secondly, all adsorption sites on the substrate are equivalent and the surface is uniform. Finally, it is assumed that the ability of species to adsorb on a given site is unaffected by the occupation of neighbouring adsorption sites such that there are no interactions between neighbouring molecules.

Although the assumptions of the Langmuir isotherm remain valid for low pressure systems, the model only supplies information of a system at equilibrium. No information is given on the rates of adsorption and desorption. As the adsorption of species on a catalyst surface is necessary prior to photocatalytic reactions, the time taken to reach equilibrium is an important factor for identifying the rate determining step of the studied systems. A number of mathematical models have been developed in order to supply a more in-depth analysis of the adsorption of gaseous chemicals on substrates.[133] During this thesis, the models studying the adsorption kinetics of chemicals on substrates are applied and discussed in Chapter 4.

Nonetheless, in most cases the rates of adsorption are far larger than those of reaction on heterogeneous catalysis.[24,131] This signifies that during heterogeneous catalytic reactions, the adsorption and desorption rates can often be assumed to lie at equilibrium, thus enabling the use of the Langmuir isotherm for the determination of reaction rates.

Langmuir-Hinshelwood kinetic model

By applying the Langmuir isotherm to the general rate law described in Equation (1.27), it is possible to extrapolate the rates of heterogeneous reactions. This is known as the Langmuir-Hinshelwood (L-H) model, allowing to take into account the role of surface coverage in heterogeneous catalyst reactions.[134] The L-H model for the reaction of a single species is shown in Equation (1.30).

$$\nu = k\theta = \frac{Kkp}{1 + Kp} \tag{1.30}$$

However, heterogeneous photocatalysis often forms reactive intermediates which compete with the initial reagents for a catalyst's active sites. As such, the L-H model described in Equation (1.30) must be adapted to take into account the competitive adsorption between the partial decomposition products and the decomposed reagent. The adapted L-H model, can be seen in Equation (1.31) where K_R is the ratio between the adsorption and desorption constants for the initial reagent, P_R is the partial pressure of the initial reagent and K_n and P_n are the adsorption/desorption constant ratio and the partial pressure of the n$^{\text{th}}$ species competing for adsorption, respectively.

$$\nu = \frac{K_R P_R}{1 + K_R P_R + \Sigma_n K_n P_n} \tag{1.31}$$

Due to its simplicity and versatility, the L-H model has become one of the most used kinetic models for the study of heterogeneous catalytic reactions.[24] However, theis model can become complex when involving multiple reagent species and different active sites.[131]

Additionally, it is important to note that in the case of photoactivated reactions, the L-H model does not take into account the light intensity and adsorption coefficients of the substrate. In other words, the model does not consider the activation of the photocatalyst.

1.4.2 The Influence of Light Intensity on Reaction Kinetics

As the photocatalytic reactions of TiO_2 arise from the photoexcitation of electrons, the intensity of the incident light and, more importantly, the absorbed light, will control the population of excited electrons and thus determine the rate of photocatalytic reactions. Commonly, it is assumed that the light is supplied to the TiO_2 in excess, rendering this factor a constant in photocatalytic reaction kinetics. Consequently, only few academic studies have addressed the importance of light intensity on the photocatalysis.[130,131,135]

However, under experimental conditions an increase in reaction rate is often observed with an increase in intensity. It therefore important to establish kinetic models which take into account the effects of photon flux. The general form of these models is reported in Equation (1.32) where ν is the rate of the photocatalytic reaction, k' is the reaction constant (independent of the light intensity), C_R is the concentration of the studied reagents, I is the intensity of incident light, and n is the kinetic order of the reaction.[131] The value of n has been reported in literature to vary from 0.5 to 1.[131,135] At low photon fluxes the concentration of excitons can be lower than that of adsorbed reagents, leading to a rapid depletion of the excitons through chemical reactions. This leads to a first order regime, wherein n is equivalent to 1. At higher intensities, the rate of exciton formation outpaces that of exciton depletion, resulting in a half order regime.[135]

$$\nu = k' C_R I^n \tag{1.32}$$

Equation (1.32) can be further expanded by taking into account the effects of the absorption of chemicals as well as the role of the photogenerated $OH^{\cdot}$ and $O_2^{-\cdot}$ in the chemical reactions. Many different models have thus been developed incorporating the L-H model as well as the presence of the radical species.[131] Equation (1.33) shows one such model developed by Brosillon *et al.* wherein β, γ, and χ are independent parameters related to the formation of radicals on the TiO_2 surface.[135]

$$\nu = \frac{\beta I C_R}{1 + \gamma I + \chi C_R} \tag{1.33}$$

Although it can be seen from Equation (1.33) that the incorporation of the photon flux results in the use of more complicated mathematical models, the importance of light intensity remains evident. However, in order to achieve a complete understanding of the photodecomposition kinetics on TiO_2, the concentration of the catalysts, or their active surface area, also needs to be considered.

1.4.3 Catalyst Concentration Effects on Reaction Kinetics

An increase in catalyst loading increases the surface area and number of active sites available for photoreactions, causing an increase in the rate of photocatalysis. However, it has been shown that the rate of reaction will only increase up to a certain concentration of catalysts after which the rate of reaction will decrease.[136,137] In a photocatalytic slurry reactor used for the purification of liquid solutions, this effect was seen to arise from a light scattering effect and poor penetration caused by the excessive presence of catalysts.[138,139]

A similar effect occurred in thin film photocatalyst gas-phase reactors. At small film thicknesses (< 1 μm) the incident photon flux will only be partially absorbed, leading to a decrease in photoreactor efficiency. Conversely, at high film thicknesses, the incident light is completely absorbed before reaching the lower layers of the film, leading to the presence of a permanently inactive fraction of the photocatalysts.[140]

As such, an optimal film thickenss at which photocatalytic efficiency is maximised, exists. However, this ideal film thickness varies depending on the nature and morphology the photocatalysts, as well as the technique used for the deposition of the catalytic film.[131] Consequently, the ideal film thickness often needs to be determined experimentally.

In order to evaluate the kinetics of TiO_2 based reactions; the adsorption properties of the catalyst, the intensity of light irradiation, and the concentration of the catalyst exposed to both the light and reagents, must all be considered. Only by achieving a balance between these factors it becomes possible to optimise the efficiency of photocatalytic reactors. This balance remains the bottleneck to the commercialisation of TiO_2 photocatalytic reactors as it is difficult to maximise the contact between the catalysts and reagents. During this thesis two techniques are applied to overcome this limitation: the modification of the morphology of the catalysts and the development of novel techniques for the deposition of thin films on optically transparent substrates. The improvement of photocatalytic rates through high surface area nanostructures is presented in Chapter 5 while the development of novel catalyst deposition techniques is shown in Chapter 6.

1.5 Thesis Overview

This thesis aims to provide a comprehensive study of the gas purification properties of TiO_2 based nanomaterials. Chapter 1 provides the theoretical groundwork for the performed experiments. The analytical techniques used in this thesis are discussed in Chapter 2. These include Scanning Electron Microscopy (SEM), X-Ray Diffraction (XRD), Fourier Transform Infrared Spectroscopy (FTIR) and reflectance spectroscopy as well as Gas Chromatography combined with Mass Spectrometry (GC-MS) and Flame Ionisation Detection (GC-FID). Chapter 2 provides an understanding of the functioning and background of each technique used to analyse the experimental results.

Chapter 3 provides the experimental details for the synthesis of the diverse nanostructures used during this study. The synthesis of pure metal oxide nanofibres (TiO_2, SiO_2 and WO_3) is reported as well as that of more complex, novel, fibrous nanostructures (SiO_2/TiO_2 core/shell nanofibres, hollow TiO_2 nanofibres and porous TiO_2 nanofibres). A thorough characterisation of the different nanofibres as well as their relative advantages and disadvantages as gas purification

agents is presented in Chapter 3.

The removal of contaminants from the gas phase is presented in Chapters 4 to 7. Chapters 4 and 5 study the removal of siloxanes from the gas phase in static environments through absorption and photocatalytic decomposition, respectively. In Chapter 4 the absorptive properties of pure nanofibres are investigated and compared to those of industrial siloxane absorption agents as well as to the siloxane removal properties of SiO_2 aerogels synthesised under ambient pressures. Chapter 5 studies the siloxane photodecomposition properties of the different catalysts in static gas environments. During the experiments presented in Chapter 5 the photodecomposition properties of the different nanostructures are compared to those of P25 and WO_3 doped TiO_2 nanofibres.

Chapter 6 investigates the photodecomposition properties of TiO_2 in gas streams. Two different gas flow reactors are studied for the decomposition of a variety of siloxanes. Specifically, the applicability of the technique for biogas purification was analysed in terms of turnover number (TON) and lifetime of the TiO_2 photocatalysts. The regeneration of the photocatalysts was further investigated to demonstrate the long term applicability of the developed technologies.

The photocatalytic flow reactors developed for the purification of biogas were extended to the photodecomposition of Volatile Organic Contaminants (VOCs) in Chapter 7. The targeted VOCs were IsoproPyl Alcohol (IPA), acetone, and styrene. The photocatalytic properties as well as the selectivity for the decomposition of each of the contaminants, are extensively studied. The versatility of the photodecomposition reactors is emphasised in Chapter 7 with a study on the partial decomposition products of styrene, showing the potential of the created reactors to act as synthetic pipelines for complex chemical species. This potential for the developed photocatalytic reactors is further explored in Chapter 8 wherein the epoxidation of 1-hexene is studied in addition to the reaction of the partial photodecomposition products of 1-hexene with diisopropylamine in order to establish new synthetic reaction pathways.

The thesis ends with Chapter 9 where the results of the project are summarised and the future prospects of this research are presented. Section 9.1 summarises the results of this study and highlights the strengths of the developed technologies. The potential of the performed experiments is further discussed in Section 9.2 where the application of the created technologies at an industrial scale is addressed whilst also highlighting the future academic studies which can be carried out from the knowledge gained in this thesis.

2. Instrumentation

During the present study, a number of different analytical techniques have been employed in order to analyse the created catalysts and quantify their photocatalytic properties. The structures and electronic properties of the studied catalysts were investigated through Scanning Electron Microscopy (SEM), X-Ray Diffraction (XRD) and diffuse reflectance spectroscopy. SEM and XRD allowed to characterise the morphology and crystal structures of the studied catalysts, respectively. Diffuse reflectance spectroscopy was performed in order to determine the band gap of the created materials.

In addition to these techniques, Gas Chromatography-Mass Spectrometry (GC-MS) and Gas Chromatography-Flame Ionisation Detection (GC-FID) were used to study the photocatalytic properties of the created catalysts. Further studies on the photodecomposition of contaminants in gas streams were carried out using Fourier Transform InfraRed spectroscopy (FTIR). The present chapter establishes the theoretical background as well as the mechanisms of analysis for all of the different analytical techniques used.

2.1 Scanning Electron Microscopy

The scanning electron microscope is arguably the most important tool of the modern nanotechnologist, allowing to visualise the morphologies of created structures with a resolution of up to a couple of nanometres.[141] During the present study, SEM imaging was used extensively to characterise the nanostructures synthesised in Chapter 3 as well as the catalysts used for the purification of gas streams in Chapters 4 to 7.

First developed in 1935 and successively refined until reaching its final form in 1961,[141–143] the modern scanning electron microscope is designed to overcome the limitations in resolution

inherent to light microscopes. In wave based detection systems the maximum resolution achievable is limited by the wavelength of the wave used for detection. This means that optical microscopes are limited by wavelengths of visible light. In SEM machines, the wavelength limitation is overcome by the use of electrons. This is possible as, following from the de Broglie relationship, the wavelength of a particle is determined by its momentum. As such, by changing the speed of the electrons used for imaging, it is possible to change the wavelength of the electrons and thus overcome the diffraction limits of optical microscopy. However, SEM machines need to be operated at high vacuum conditions ($10^{-4} - 10^{-8}$ Pa) in order to avoid electron interaction with the gaseous particles present at ambient pressure. Figure 2.1 shows the simplified scheme of a scanning electron microscope.

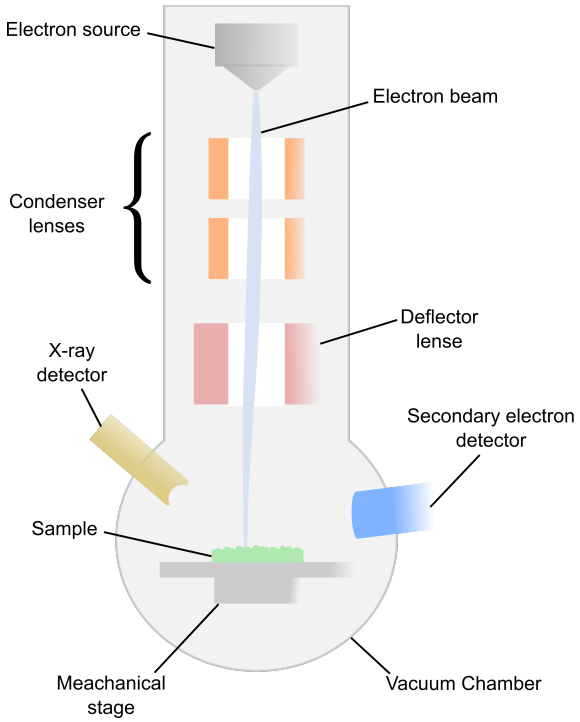

Fig. 2.1 Schematic representation of the main components of the scanning electron microscope.

During the operation of a SEM, electrons are emitted from a source and accelerated to a desired energy (usually 10-30 kV) by using an electron gun. The electron source may vary between different machines but the most common remains a tungsten filament which releases electrons through thermionic emission.[141] The accelerated electrons are focused into a narrow beam by a series of condenser lenses and probe lenses, and brought to impact on the surface of the studied sample. The location of the beam on the sample surface can be controlled through either a series of deflector coils which allow small shifts in the beam location, or through the use of a mechanical

stage under the sample which allows for larger shifts in the studied area. When colliding with the studied surface the electrons can undergo two main types of interaction: elastic, and inelastic scattering. These interactions can be monitored with the appropriate detectors and allow to generate an image of the studied surfaces.

Electrons which interact with the sample through elastic scattering are called backscattered electrons. Backscattered electrons are usually emitted from the studied samples from the same direction in which they collided with the sample. As such, back scattered electron detectors are placed nearly vertically above the samples. Furthermore, due to the high energy of the back scattered electrons, the acquired images can only be achieved with relatively low resolutions. This low resolution of backscattered electrons in combination with the complexity of detecting these electrons usually signifies that most SEM machines will not possess backscattered electron detectors.

As such, most scanning electron microscopes will detect the electrons arising from the inelastic scattering of the incident beam, the secondary electrons. Secondary electrons are the electrons generated when the incident electron beam causes the emission of core electrons from the surface atoms of the studied material. As they originate from the molecular core, secondary electrons have comparatively little energy (1-300 eV). This low energy means that it becomes easier to deflect the electrons through the use of potential difference, thus allowing for a much more flexible positioning of their detector. In addition to this, secondary electrons often allow to achieve high resolution images of the studied surfaces as, unlike backscattered electrons which travel relatively deep into a sample's surface, secondary electrons will only originate from the top of the studied surface ($\sim$10 nm deep) due to their low energy. This shallow depth penetration in addition to an inherent high depth of focus signifies that secondary electron detection is the preferred method for the study of sample topography though SEM.

Although the primary use of SEM instruments resides in observing the morphology of created samples through secondary electron detection, it is also possible to study their elemental composition by analysing the energy emissions which follow the release of secondary electrons .

2.1.1 Energy Dispersive X-Ray Spectroscopy

SEM machines can be equipped with an energy dispersive x-ray (EDX) detector. Through EDX, it is possible to study the elemental composition of observed materials through the use of x-ray fluorescence.

The generation of secondary electrons from the core shell of studied atoms leads to the formation of holes within these atoms. The created holes allow for the relaxation of outer shell electrons towards the core shell of the atoms. As the outer shell electrons undergo relaxation, they release energy in the form of x-ray fluorescence. The energy of the x-rays is specific for each different element. This allows to differentiate between the different sources of detected x-rays. Furthermore, as each individual atom undergoing the release of secondary electrons will undergo relaxation through x-ray florescence, the intensity of the detected x-rays will be determined by the amount of each individual atom irradiated. As such, through EDX it is possible to gain both qualitative and quantitative elemental analyses of the surfaces observed through SEM.

During the present study SEM analysis was used primarily in order to ascertain the morphology and composition of the nanostructures created in Chapter 3 as well as the SiO_2 aerogel beads created in Chapter 4. A JEOL-JSM 820 Scanning Microscope equipped with a cryogenically cooled EDX detector was used for all of the performed SEM analyses.

2.2 X-Ray Diffraction

Through SEM it is possible to observe the morphology and composition of created structures. However, this does not supply any information about the arrangement of the different atoms composing the nanostructures (their crystalline arrangement). This information can be gathered through XRD by studying the diffraction of x-rays from studied materials. Crystalline materials such as TiO_2 and WO_3 are composed of atoms arranged periodically in crystal structures. When x-rays interact with these periodic structures, they undergo diffraction. The diffracted waves can then undergo constructive or destructive interferences, which are detected in order to determine the nature of the studied crystals.[144] The interaction of x-rays with the atomic planes of a crystal is depicted in Figure 2.2.

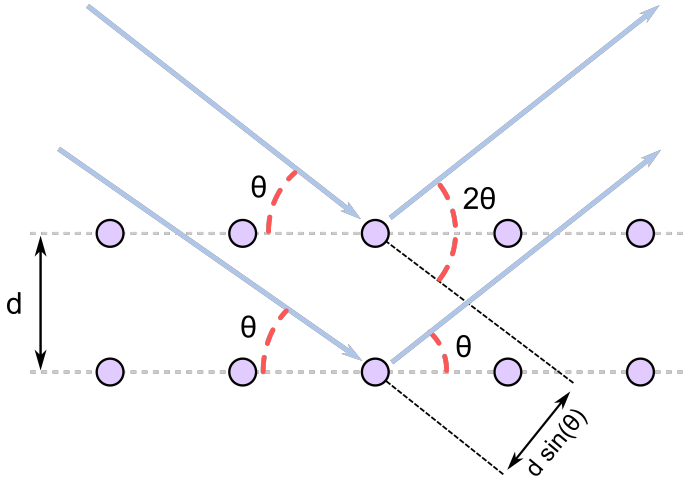

Fig. 2.2 Schematic representation of the interaction of x-rays with the atomic planes of a crystal which allows to derive Bragg's law.

As x-rays collide with crystal surfaces, they are diffracted by the crystal planes of the material. The diffracted x-rays will undergo constructive and destructive interferences with each other, leading to the formation of interference patterns. The angle at which the n^{th} (where n is an integer number) constructive interference patterns can be observed is determined by the wavelength, λ, and incidence angle of the x-rays, θ, as well as the spacing between the atomic lattices in the crystalline sample, d, as described by Bragg's law in Equation (2.1), and shown in Figure 2.2.[145] It can be seen in Figure 2.2 that the diffracted x-rays will be emitted at the same angle θ with which the incident beam collided with the sample. This means that, relative to the incident beam, the x-rays will be diffracted by an angle of 2θ (as shown in Figure 2.2). As such, during powder XRD, the relative angles of the incident beam and the x-ray detector are commonly fixed at θ and 2θ, respectively.

$$n\lambda = 2dsin(\theta) \tag{2.1}$$

By irradiating a crystal through all of its faces, it is possible to build a pattern of constructive interferences for any given crystalline sample. As each different species will yield a different XRD pattern, it is possible to determine the nature and crystallinity of unknown samples by correlating the gathered patterns with a database. Experimentally, two different types of XRD are commonly used to study sample crystallinity: single crystal XRD and powder XRD.

Single crystal XRD is usually employed for samples with unknown crystalline configurations

and does not necessarily require the use of a database. In this technique a single crystal of a given sample is studied through XRD in all possible orientations. This allows to construct a 3D pattern of constructive interference spots from which it is possible to establish the nature and configuration of the base unit cell composing the crystal. Unfortunately, single crystal XRD is often a time intensive technique which requires relatively large crystals ($\sim$100-200 μm^3) in order to function correctly. As such, its use within nanotechnology remains limited.

Powder XRD is a much faster technique with respect to single crystal XRD. During powder XRD, the diffraction of the incident x-ray beam is only studied along one axis of the sample. This means that powder XRD spectra are significantly less time intensive when compared to their single crystal counterparts. Inevitably, the choice of limiting the x-ray diffraction to a single axis of the sample, leads to the generation of less informative spectra. This loss of information makes it impossible to determine the exact unit cell of any species studied through powder XRD. Nonetheless, it remains possible to identify the Miller Indices corresponding to the constructive interferences observed in a powder XRD spectrum. Furthermore, as each different material will yield a different powder diffraction XRD (due to inherently different lattice spacing) it is possible to identify unknown samples through correlation with a known database. As nanotechnology often focuses on the construction of novel architectures from materials with known crystal structures, powder XRD is often preferred over single crystal XRD. This can be attributed to the fact that powder XRD provides a sufficient depth of analysis whilst minimising the time required to study any created samples.

In addition to this, the information supplied by powder XRD is not limited to the nature of the different species composing the studied samples. From powder XRD spectra it is also possible to determine the relative composition of each species in a given sample as well as the crystallinity and crystallite size of the particles in the studied sample.

The relative composition of the studied samples can be determined by monitoring the intensity of the diffraction peaks in the XRD spectra. The diffraction peaks in a powder XRD spectrum arise from the x-ray diffraction of different crystal planes. As a sample contains more of a specific plane, this will increase the intensity of the observed diffraction. This allows the determination of the relative composition of a studied sample by comparing the intensities of the diffraction peaks of each different species in relation to each other. This study of peak intensities can also be

taken further during the analysis of thin films through powder XRD wherein it becomes possible to establish the relative crystallinity of the thin films.

The crystallinity of a studied sample can be judged qualitatively by observing the broadness of a sample's diffraction peaks. Equation (2.1) shows clearly that the constructive interference patterns in an ideal crystal will occur at specific values of θ. However, as a crystal diverges from ideal crystallinity as a consequence of imperfections in the crystalline structure, distortions in the lattice separation distance will be present. These distortions can lead to the occurrence of constructive x-ray interferences at slightly different θ values with respect to a perfect crystal, causing a broadening of the diffraction peaks in the XRD spectra. Consequently, poorly crystalline samples will yield broad XRD peaks whilst highly crystalline materials will generate very narrow peaks.

By further studying the peak broadness it is possible to determine the crystallite (grain) size for each crystal plane observed through powder XRD. The relationship between the peak broadness and the crystallite size is described by the Debye-Scherrer equation as shown in Equation (2.2).[146] In Equation (2.2), D_{avg} is the mean crystallite dimension of a given plane, K is the shape factor of the studied crystal lattice (ranging from 0.62 to 2.08, according to the shape of the crystal lattice), λ is the wavelength of the incident x-rays, θ is the angle of the diffraction peak, and β is the full width half maximum, in radians, of the studied peak taking into account instrument broadening.

$$D_{avg} = \frac{K\lambda}{\beta cos(\theta)} \tag{2.2}$$

During the present study powder XRD was used in order to analyse the nanostructures created in Chapter 3 as well as to study the effects of the WO_3 doping in TiO_2 nanofibres performed in Chapter 5. All powder XRD spectra recorded during this study were performed using a Siemens Powder X-500 diffractometer equipped with a Cu plate with a peak x-ray wavelength of $1.54\,\text{Å}$. All spectra were collected at an angle of 2θ with respect to the incident x-rays which were projected onto the sample at an angle θ (this is known as the $\theta/2\theta$ detection mode).

2.3 Diffuse Reflectance Spectroscopy

The importance of the electric properties of photoactivated materials in photocatalysis was discussed in Chapter 1. A large variety of the electronic properties of materials such as charge mobility, conductivity and band gap can be quantified through different analytical techniques. Of these properties, the size of a material's band gap is of essential importance during photochemical reactions. As such, during the present work, the band gaps of the synthesised photocatalysts were investigated.

A material's band gap can be traditionally determined by studying its spectral absorption patterns through ultraviolet-visible (UV-Vis) spectroscopy. By monitoring the wavelengths of light absorbed by a given sample it is possible to determine the minimal energy required for the photonic excitation of that sample through UV-Vis spectroscopy. This technique for the determination of a system's band gap was first developed by Jan Tauc in 1968.[147] Tauc successfully established a mathematical model correlating the absorption coefficient of a studied system, α, with its band gap, E_g. Tauc's correlation can be expressed as shown in Equation (2.3) where $h\nu$ is the energy of incident light, A is a proportionality constant of the studied material and n is a constant whose value depends on the studied electronic transition. For direct and indirect electronic transitions n has a value of $\frac{1}{2}$ and 2, respectively.[148]

$$\alpha h\nu = A(h\nu - E_g)^n \tag{2.3}$$

Equation (2.3) can be used determine a material's direct band gap from a UV-VIS spectrum by plotting $(\alpha h\nu)^2$ as a function of $h\nu$. The created graph, known as a Tauc plot, displays a linear section which corresponds to the absorption of the sample. By extrapolating this linear region to the abscissa it is possible to determine the optical band gap of the studied material. Figure 2.3 shows the extrapolation of the linear region in the Tauc plot of the P25 used during the present study, showing a band gap of 3.09 $\pm$ 0.06 eV .

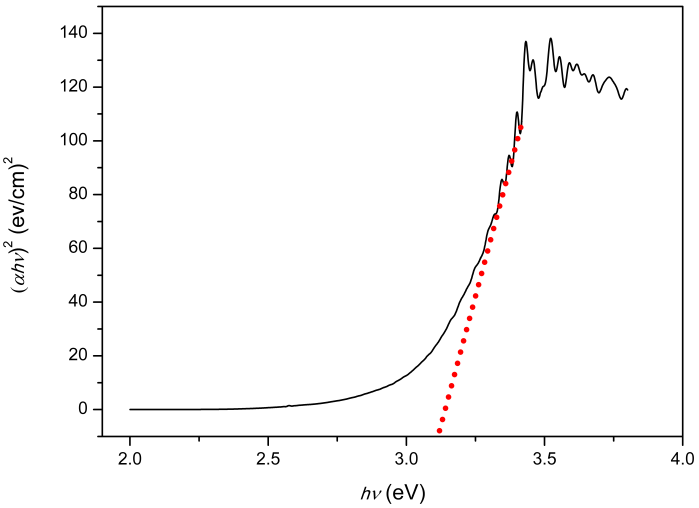

Fig. 2.3 Tauc plot of P25. The extrapolation of the linear portion to the abscissa which allows to determine the band gap of the material is shown as the red dotted line.

In traditional UV-Vis spectroscopy, the absorption spectrum of a sample (and thus its absorption coefficient) is determined by monitoring the wavelengths of light which are transmitted directly through the sample. This limits the application of traditional UV-Vis spectroscopy to gaseous, liquid, and thin film solid samples. As such, an alternative method is necessary for the study of the band gaps of powders, bulk materials and thick films. This method was presented in 1999 by Kumar *et al.* who successfully determined the band gap of thick films through reflectance UV-VIS spectroscopy.[149]

Reflectance UV-VIS spectroscopy determines the wavelengths of light absorbed by a studied material by analysing the diffuse reflection of a beam of light from the surface of the sample. When light is shone onto a material, it undergoes two types of reflection: specular reflection and diffuse reflection. Specular reflection is the direct reflection of light from smooth surfaces in a single direction. This type of reflection will occur primarily on uniformly polished surfaces. In the case of materials with non-uniform surfaces, specular reflection only occurs in very small quantities.

The incident light that does not undergo specular reflection in contact with a material's surface will enter the material through refraction and internal reflection. Once inside the material's surface, the light will continue to undergo scattering, gradually losing intensity or being emitted back into the air. The light emitted from the surface in this manner will be emitted in a wide variety of directions,

it is thus called diffuse reflection. The diffusely reflected light will have lost intensity relative to the light absorption properties of the material. From this, it becomes possible to determine the UV-VIS absorption of a studied sample from its diffuse reflectance spectrum.

The model of Kumar *et al.* allowed to determine the absorption coefficient of a species from its diffuse reflectance spectra as shown in Equation (2.4). In this mathematical model α_λ is the absorption coefficient of the material at a given wavelength, t is the thickness of the material, R_{max} is the maximum observed reflectance intensity in the spectrum, R_{min} is the minimum observed reflectance in the spectrum, and R_λ is the reflectance intensity at the given wavelength.[149]

$$2\alpha_\lambda t = \ln(\frac{R_{max} - R_{min}}{R_\lambda - R_{min}}) \tag{2.4}$$

By combining Equations (2.3) and (2.4) it becomes possible to generate a Tauc plot and determine a sample's band gap from its diffuse reflectance.

However, because of its widely scattered nature, the diffuse reflectance of a sample is often too weak to detect from a single point. An integrating sphere is thus used to concentrate the diffuse reflections from all directions into a signal strong enough for spectroscopic detection. Figure 2.4 shows the basic principle behind the operation of an integrating sphere to measure the diffuse reflectance of a given sample. A light source is shone onto the studied sample through an aperture in the integrating sphere. Upon colliding with the studied sample, the beam undergoes diffuse reflection in all directions onto the walls of the integrating sphere. As the walls of the integrating sphere are lined with a white diffuse reflecting coating, the beams are further scattered within the sphere without undergoing energetic losses due to absorption. Effectively, increasing the concentration of diffusely reflected light within the sphere. Finally, the concentrated light is recorded by a detector, allowing to produce a spectrum of the diffuse reflectance of the sample in relation to incident light wavelength. In order to avoid blinding the detector through the light source, a baffle is introduced between these two elements.

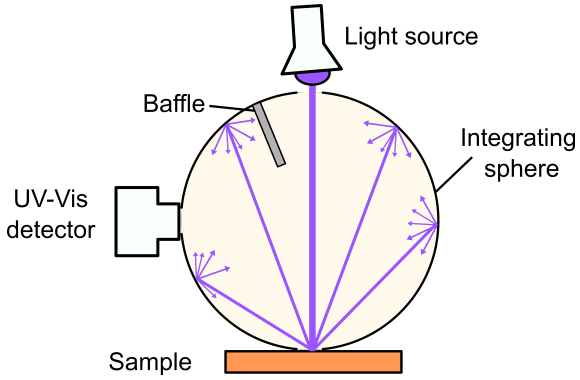

Fig. 2.4 Diagram showing the operation of an integrating sphere for the measurement of a sample's diffuse reflectance.

Diffuse reflectance spectroscopy is an essential asset in heterogeneous photocatalysis as it allows to determine the band gap of the studied photocatalysts and thus gain an enhanced understanding of the observed processes. During the present study, diffuse reflectance spectroscopy was used to determine the band gap of the nanostructures created in Chapter 3 as well as that of the WO_3 doped TiO_2 nanofibres used for enhanced siloxane decomposition in Chapter 5. Experimentally, the band gaps of the materials were determined using an Ocean Optics ISP-REF integrating sphere equipped with an inbuilt tungsten-halogen illumination source (300 nm $\leq \lambda \leq$ 1000 nm) and an ASEQ LR1 UV-Vis detector.

2.4 Gas Chromatography

Having established the techniques used for the characterisation of the synthesised catalysts, it now becomes essential to discuss the analytical methods employed to study the photodecomposition properties of the catalysts. The simplest way to study photodecomposition reactions is by monitoring the different chemical species present during the reactions as well as their relative concentrations. Unfortunately, due to the complicated nature of photodecomposition reactions, this often means carrying out an analysis of a mixture containing a variety of different chemical species. Gas chromatography, GC, (also known as gas-liquid chromatography) is the most commonly used method for the qualitative and quantitative chemical analysis of complex mixtures.

Initially developed in 1952 by A.T. James and A.J.P. Martin, GC has become one of the most useful analytical tools in modern chemistry.[150,151] GC functions on a basic principal similar to that

of liquid chromatography. That is to say, that a mobile phase containing the studied chemicals is passed over a stationary phase. As the chemicals in the mobile phase interact with the stationary phase, they proceed at different speeds through the system, thus allowing for an effective separation of the different chemicals in a studied mixture. The principal components of a gas chromatograph are shown in Figure 2.5

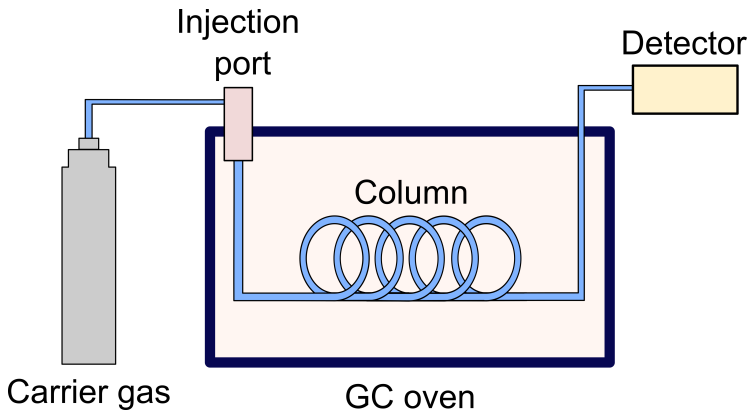

Fig. 2.5 Simplified representation of the principal components of a gas chromatograph.

During GC the mobile phase is composed of a carrier gas (usually He or H_2) which is passed through the system at a controlled pressure. As the carrier gas flows through the GC, a small quantity ($\sim$ 0.01 - 100 μL for liquids and $\sim$ 100 μL for gasses) of the sample to be analysed is introduced into the system through an injection port. The injection port is maintained at high temperatures in order to vaporise the different chemical components within the sample. Once the sample is vaporised it is carried into the column by the carrier gas though a splitless injection. In cases in which the concentration of chemicals in the sample exceeds the capacity of the system, the vaporised sample may be introduced into a column through a split injection. This means that only a controlled fraction of the gaseous samples is introduced into the system whilst the remainder of the sample is purged by the carrier gas through a separate port.

Once the gaseous sample reaches the column, it will start interacting with the stationary phase of the GC. The stationary phase is in the form of a liquid coating on the inside of a very fine tube (usually made of fused silica), known as the column. As the gas sample passes through the column, the different chemicals in the sample will adsorb and desorb from the stationary phase at different rates. These different adsorption and desorption rates will lead to the chemicals proceeding through the column at different speeds, effectively causing a separation of the sample mixture in its component species. The time taken for each eluent to reach the end of a GC column is known

as its retention time. The the retention times for the chemicals eluted from the column as well as their degree of separation from each other are determined by a wide variety of factors in addition to the flow rate of the carrier gas. Amongst these factors the nature of the stationary phase and the temperature of the column are the most important.

As the speed of elution of the different chemicals is dependent on the time each chemical spends adsorbed onto the stationary phase, raising the temperature will decrease the retention times by lowering the rate of adsorption of chemicals onto the stationary phase whilst decreasing temperatures will lead to an increase in retention times. However, as differences in temperature will affect the elution of different chemicals proportionally to their level of interaction with the stationary phase, an increase in temperature can disproportionately increase the elution time of some species with respect to others, leading to the elution of multiple species at similar if not identical times, effectively causing imperfect mixture separations. As such, GC systems are equipped with highly precise ovens in order to allow a complete control over the temperature of the columns and elution times of the studied species, as shown in Figure 2.5.

The nature of the stationary phase within the column is the second crucial factor affecting the elution times of different chemical species. As different chemicals display different properties arising from their functional groups, they will interact differently with the stationary phase. Polar molecules will adsorb preferentially on a polar stationary phase whilst nonpolar species will be adsorbed preferentially on a nonpolar stationary phase. As such, polar columns will be more appropriate for the separation of polar molecules as they will retain these species longer and thus improve their relative separations whilst nonpolar columns will be preferred for nonpolar molecules. Although the nature of the stationary phase can be varied up to the point where the separation of molecules of different chiralities can be performed, most GC systems are equipped with either polar or non-polar columns.

Finally, as the different chemicals are eluted from the column, they are recorded and analysed by a detector. Many different types of detectors exist, catering to different chemical species with different sensitivities and detection limits. During this study, two different GC detection methods were used, flame ionisation detection (FID) and mass spectrometry (MS).

2.4.1 Flame Ionisation Detection

The FID is probably the sturdiest detector used for GC. This sturdiness can be attributed to the relatively simple design of the detector. Figure 2.6 shows a schematic diagram of the cross section of a FID. As the eluates exit the GC column in the gas phase, they are initially mixed with a fuel gas (commonly hydrogen). The fuel/eluate mix is then carried through the FID where it is further joined to an oxidant gas (commonly air). As this eluent/fuel/oxidant mix is further transported along the nozzle head of the FID, it reaches a flame which combusts the eluate, converting it into ions. The generated ions are then collected by a series of negatively charged collector plates connected to an ammeter. As the ions collide with the collector plates they induce a current which is detected by the ammeter, amplified and monitored. Finally, the combustion products of the eluate are vented out of the system through an exhaust port.

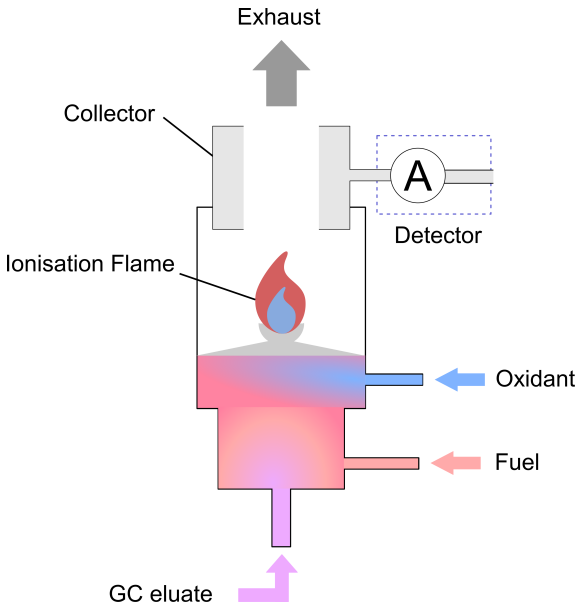

Fig. 2.6 Schematic representation of the principal components of FID detector used during GC-FID.

Unfortunately, FID cannot distinguish between different species. This limitation makes it essential to use standard samples in order to identify the different species in an analysed mixture. As each species will be eluted from the GC column at different times, one can identify a given species through FID by comparing a standard's elution times with those of the unknown mixtures. Although the requirement for known standards limits its versatility, FID remains an important tool for the analysis of chemical mixtures.

As the intensity of the current detected during FID is relative to the amount of ions colliding the detector at a given time, the detected FID signal is proportional to the concentration of the eluates in a studied sample. It thus becomes possible to calibrate the observed FID signals for different eluates in order to quantitatively determine their concentration within a mixture.

During the present study GC-FID was used to study the adsorption and photodecomposition of siloxanes in static gaseous environments over different photocatalysts. The studies on the siloxane adsorption properties of different materials are presented in Chapter 4 whilst Chapter 5 presents the photodecomposition studies. During these experiments, the concentration of hexamethyldisiloxane (L2) was quantified by calibrating and monitoring the area under the L2 peak in the spectra generated by a Perkin Elmer autosystem GC-FID. The GC-FID used during the experiments was equipped with a 50 m wax capillary column. During the duration of the experiments the gas flow rate was kept at 1.5 ml min^{-1}, the oven and injection temperatures were maintained at 60°C. H_2 was used as the carrier gas and supplied using a hydrogen generator, SP300HC. Under these conditions, the L2 retention time was observed to be 150 s.

2.4.2 Mass Spectrometry

MS is probably the most commonly used detector in combination with GC. This preference for MS can be attributed to the greater wealth of information gathered about the eluates with respect to that gathered with alternative detection techniques such as FID. In its simplest terms MS detection functions through the ionisation of the eluates as they exit the GC column and the separation of the ions according to their mass-to-charge ratio.

Although in recent years many different variations of mass spectrometers have been designed, MS instruments are all composed of three main parts: the ion source, the mass selector and the detector. Figure 2.7 shows a schematic diagram of the most common type of mass spectrometer used in GC-MS, a quadrupole mass spectrometer using Electron Ionisation (EI) as an ion source.

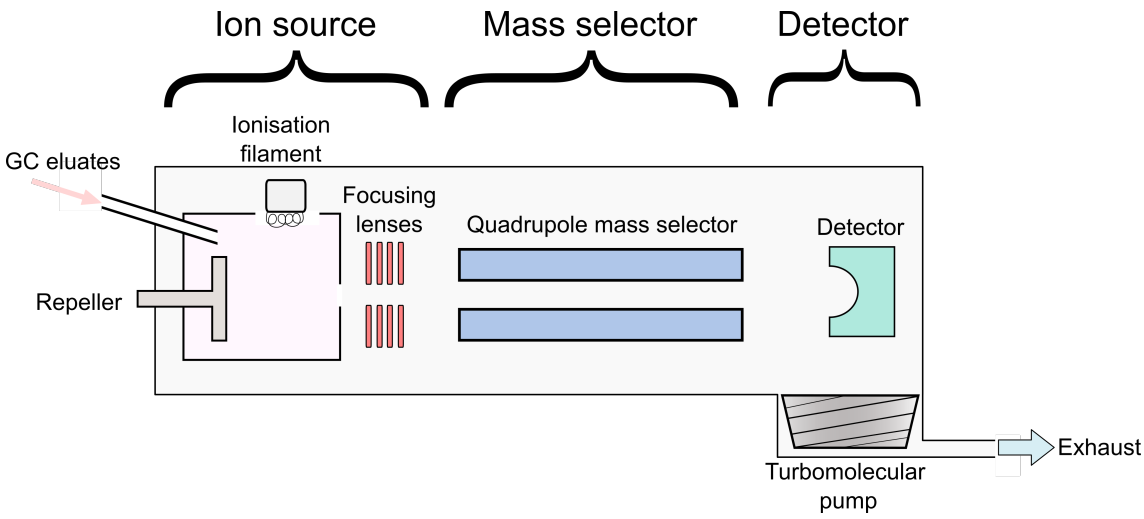

Fig. 2.7 Schematic representation of the principal components of the most common MS detectors used during GC-MS. The three main components present in all MS detectors can be clearly seen; the ion source, the mass selector, and the detector.

As can be seen in in Figure 2.7, eluates exit the GC column directly into the ion source. During EI, the most common ion source in GC-MS, the eluates from the GC column are introduced into a chamber where, through electron bombardment (provided by the thermionic emission of electrons from a heated filament), the eluates are ionised. Due to the high energy of the electron beam, the studied species may undergo fragmentation into smaller samples. This fragmentation process is a well-known one and proceeds with regularity such that it is often possible to predict and identify the nature of the specific fragments of a given molecule. Once ionised, the studied species is emitted from the ion source by electrical repulsion and focused through a series of electric lenses before reaching the mass selector. The ion source in GC-MS is commonly maintained at high temperatures (up to 300°C) in order to avoid the condensation of the GC eluates within the system.

The mass selector will separate the created ions according to their mass-to-charge ratio by using electric or magnetic fields. The motion of ions in electric and magnetic fields in a vacuum is governed by Newton's second law of motion (Equation (2.5)) as well as the Lorentz force law (Equation (2.6)) . These two laws can be combined as shown in Equation (2.7). In Equations (2.5) to (2.7), F is the force applied a given ion, q is the charge of the ion, E is the strength of the electric field affecting the ion, a is the acceleration of the ion and $v \times B$ is the vector cross product of the ion velocity and magnetic field.

$$\mathbf{F} = m\mathbf{a} \tag{2.5}$$

$$\mathbf{F} = q(\mathbf{E} + \mathbf{v} \times \mathbf{B}) \tag{2.6}$$

$$\mathbf{a}(\frac{m}{q}) = \mathbf{E} + \mathbf{v} \times \mathbf{B} \tag{2.7}$$

From Equation (2.7) it becomes readily apparent that the path taken by an ion in a magnetic field will be dependent on its mass-to-charge ratio. The quadrupole mass selector (the most commonly used mass selector in GC-MS), uses this relation in order to selectively filter ions. A quadrupole mass selector is comprised of four cylindrical rods which are placed parallel to each other. Through the use of a DC voltage, an electric field is induced between the rods. As the ions created in the ion source enter this electric field, they will be deflected according to their mass-to-charge ratio. By varying the strength of the magnetic field it is possible to control the path of the ions, inducing them to either reach the MS detector or to collide with the rods. Commonly, a quadrupole detector can be used in two modes: a single ion detection mode which will only allows a specific mass-to-charge ratio to reach the MS detector, and a scanning mode wherein the quadrupole selector is used to scan a range of mass to charge ratios in order to identify the different ions created from the fragmentation of the studied species.

Finally, after being filtered through a quadrupole, the ions collide with a detector which monitors their concentration and correlates it to the mass-to-charge ratio allowed at a given time by the quadrupole. It is thus possible to plot the mass-to-charge ratio in relation to signal intensity for a given species, this plot is called a mass spectrum. As each individual species will fragment in slightly different ways, each species will generate a unique mass spectrum. As such, by correlating the mass spectrum of an unknown species to a database, it becomes possible to identify specific unknown molecules. Furthermore, by monitoring the intensity of the peaks in relation to elution time it also becomes possible to quantitatively measure the concentration of the unknown species within a mixture.

It is nonetheless important to note that due to the small the mean free path of ionic species in

air, MS often has to operate at low pressures in order to ensure the detection of the created ions. This means that GC-MS devices are often more expensive than GC-FID systems as they need to include high vacuum pumps (such as turbomolecular pumps) in order to operate successfully. This requirement of a high vacuum in addition to the use of a filament for the generation of ions also renders GC-MS systems comparatively more fragile.

During the present study GC-MS was used extensively to monitor the secondary decomposition products achieved from the photodecompositions of styrene and 1-hexene on TiO_2 in gas flow reactors, as discussed in Chapters 7 and 8. A PerkinElmer Autosystem XL gas chromatograph equipped with a PerkinElmer TurboMass mass spectrometer was used. The GC was equipped with a Restek RXI-5ms column 30 m in length with an internal diameter of 0.25 mm and a film thickness of 0.25 μm. Helium was used as a carrier gas with a flow rate of 40 ml/min. The analysed liquids were injected into the GC column by using an automated split injection with a split ratio of 29.8, an injection volume of 0.2 μl and an injector temperature of 220°C. MS was performed by using EI in combination with a quadrupole mass selector. The MS scanned the mass region between 45 and 300 m/z (amu/e) for a total of 22 minutes with a 4 minute solvent delay.

2.5 Fourier Transform Infrared Spectroscopy

Although GC techniques, and in particular GC-MS, are powerful tools in the study of the photodecomposition properties of photocatalysts, they present a number of drawbacks which make them unsuitable for the direct monitoring of gas phase photodecomposition reactions. Amongst these drawbacks, the most salient remain the inability of direct in-line exhaust monitoring as well as the destructive nature of the analytical technique. Fourier transform infrared spectroscopy (FTIR) represents a facile solution to these issues.[152]

IR spectroscopy, similarly to UV-Vis spectroscopy, studies the energies absorbed by samples over a specific range. Where UV-Vis spectroscopy monitors the absorption of radiation ranging from 200 to 800 nm, FTIR spectroscopy monitors the absorptions of molecules in the IR region of the electromagnetic spectrum (between 2 and 25 μm). As the energy used during FTIR spectroscopy is significantly smaller than that used during UV-VIS spectroscopy, the nature of the absorptions observed is significantly different. Instead of exciting electrons in a system to different energy

states, the low energy absorbed from the IR radiation leads to a change in vibrational energy levels within the same electronic state. As the vibrational states of a studied species will be dependent on molecular configuration factors such as; size, functional groups, and even bond order, FTIR can often be used as a preliminary source of structural information for the species.

In addition to the advantages gained by the preliminary structural analysis of studied species, FTIR presents a number of practical advantages such as the availability of analysis at room temperature and pressure as well as a high versatility which allows for the analysis of gas, solid, and liquid samples. Amongst the many practical advantages of FTIR, the most important must be the limited presence of mobile parts within its instrumentation which renders FTIR spectrometers particularly sturdy. This can be seen in the schematic representation of a FTIR spectrometer shown in Figure 2.8, where the Michelson interferometer composes the sole moving part of the instrument.

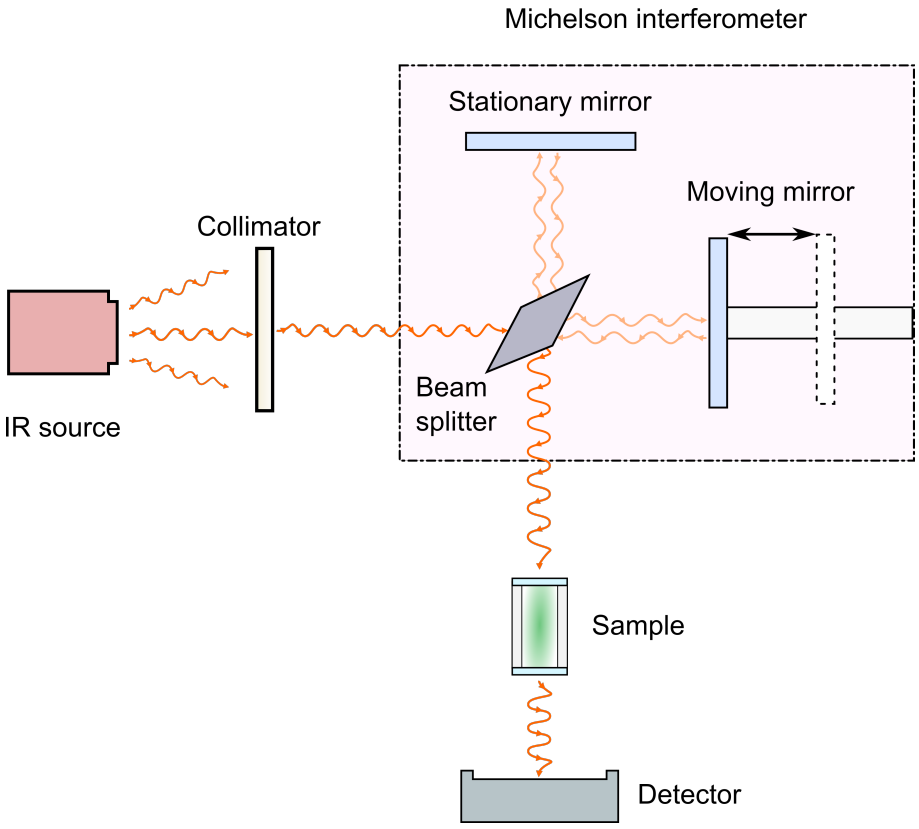

Fig. 2.8 Schematic representation of the principal components of a FTIR spectrometer. The path of a single IR wavelength can be seen in the system.

As seen in Figure 2.8, FTIR spectrometers function through a mechanically simple process. Initially, an IR source (usually a silicon carbide filament heated at 1200 K) emits a full spectrum of IR radiation (similar to a black body emission) which is then collimated in order to ensure a minimal

spread as it propagates through the spectrometer. Following collimation, the IR radiation enters the Michelson interferometer, the device which will allow to scan across the different wavelengths composing the IR radiation. In the Michelson interferometer, the radiation is initially split into equal parts by a beam splitter. One of the two generated beams is directed to a stationary mirror from which it is reflected once more to the beam splitter. The second IR beam generated from the beam splitter is directed to a moving mirror. This moving mirror reflects the IR beam back to the beam splitter where it is combined with the beam reflected from the stationary mirror. The combined beam is then brought to exit the Michelson interferometer.

The mobile mirror allows to change the path length traversed by the IR radiation, this difference in path length is known as the optical path difference (OPD). The OPD can lead to the beam from the moving mirror to undergo destructive or constructive interference with the beam originating from the static mirror. As the two beams are not composed of a single IR wavelength but rather a spectrum of wavelengths, the combined beam exiting the interferometer will display different maxima (beyond the point of full constructive interference) at different OPDs, corresponding to the constructive interference of specific wavelengths. As such, through this technique, the Michelson interferometer allows to effectively isolate each wavelength whilst maintaining a source which emits a full spectral radiation.

The combined beam exiting from the interferometer is passed through the studied sample. In the case of gas phase samples, the studied species are kept in a cylindrical cell of known path length capped with IR transparent windows (usually NaCl or KBr). In a continuous gas flow system, the cell is equipped with an inlet and an outlet port in order to allow for the gas stream to fill and pass through the IR cell during its flow.

Once the IR beam has interacted with the studied sample, it collides with a detector. Commonly, in FTIR spectrometers the detector is composed by a pyroelectric species which generates a current relative to the intensity of incident IR radiation. From the current of the detector it is possible to generate a plot known as in interferogram which shows the evolution IR intensity in relation to the OPD. Figure 2.9 shows the interferogram of L2.

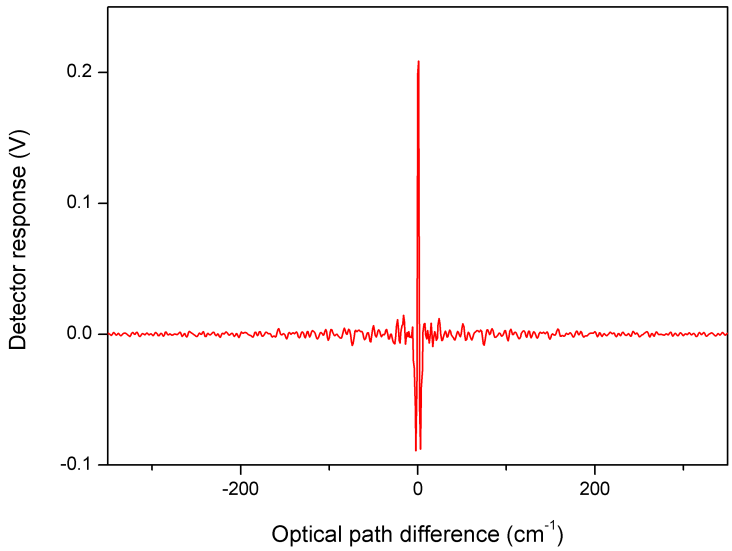

Fig. 2.9 FTIR interferogram of L2. The IR pulse containing all of the scanned wavelengths is detected and plotted as a function of optical path difference.

As can be seen from Figure 2.9, the interferogram of a system can be difficult to interpret as it does not give a clear separation of the recorded wavelengths. As such, an interferogram needs to be clarified in order to deconvolute the IR intensity in relation to wavelength. This is carried out by applying an algorithm known as the fast Fourier transform which allows to apply the Discrete Fourier Transform integral approximation to convert the signal from a spatial to a frequency domain, yielding a plot of IR spectral absorbance (or transmittance) in relation to beam frequency. As frequency is inversely related to wavelength, traditionally IR spectra plot the observed absorbance as a function of the number of waves within a cm, this is known as the wavenumber and is presented in units of cm^{-1}. Thus, by comparing the FTIR spectrum of a sample with that of the spectrometer without a sample, it becomes possible to determine the sample's IR absorbance energies. As each different molecule possesses different vibrations, the IR spectrum of a given species will be a fingerprint of that molecule. The FTIR spectrum of L2 as well as the assignment of the vibrational modes relating to the main peaks in the spectrum are shown in Figure 2.10.[153,154]

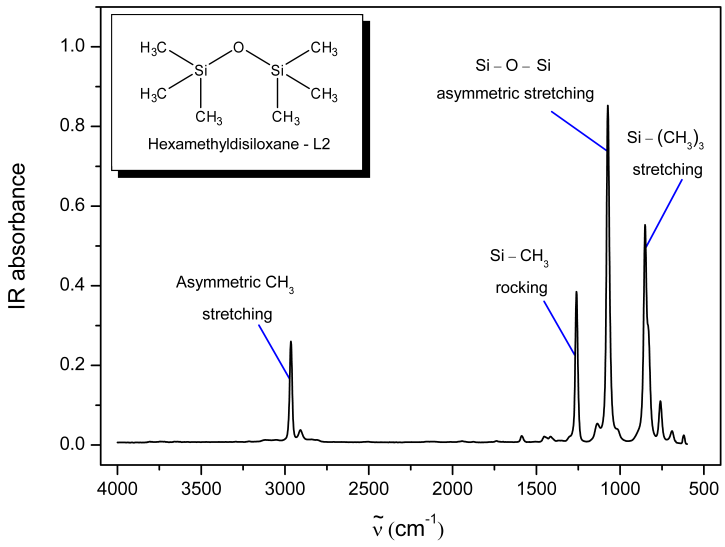

Fig. 2.10 FTIR absorption spectrum of L2. The vibrational modes leading the main observed IR absorptions are assigned to each peak.

FTIR is not limited to qualitative identification of samples. By applying the Beer-Lambert law, it is possible to correlate the absorbance of the FTIR spectral peaks to the concentration of the studied species.[152] The Beer-Lambert law is shown in Equation (2.8), where A is the absorbance of a given peak in the IR spectrum, ϵ is the molar absorptivity of the studied molecule, l is the path length of the IR beam through the sample and c is the sample's concentration.

$$A = \epsilon c l \tag{2.8}$$

By calibrating the FTIR peak areas in relation to known concentrations of a given species, it is possible to quantify the concentration of the species in unknown mixtures. However, in order to get an accurate quantification from an unknown mixture, the monitored FTIR peaks must not overlap with those of other species present in the mixture.

During this thesis, the photodecomposition of both siloxanes and common VOCs in gas streams were studied using FTIR spectroscopy, as discussed in Chapters 6 and 7, respectively. The IR spectra were collected using a Perkin Elmer SpectrumOne FTIR spectrometer with a gas phase IR cell (130 mm long) equipped with NaCl windows (25 mm in diameter).

3. Nanoarchitecture Synthesis

In order to remove siloxanes from biogas two main techniques have been commonly used, adsorption and photodecomposition. These techniques and their application in the removal of siloxanes from biogas have been discussed in Chapter 1. During the following series of experiments, we present the creation of different nanostructures with enhanced surface areas for the photocatalytic decomposition of siloxanes in gas streams.

Initially, the electrospinning technique was used to successfully synthesise WO_3, SiO_2, and TiO_2 nanofibres. These materials were chosen for their known photoactivites both in the industrial[48,155,156] and academic[14,157,158] sectors. Their morphology, composition and electronic properties were characterised through Scanning Electron Microscopy (SEM), X-Ray Diffraction (XRD), and diffuse reflectance measurements, in order to ascertain their suitability for the photodecomposition of siloxanes in gas streams.

Templating techniques were subsequently used to develop nanofibres with enhanced surface areas. It was thus possible to develop SiO_2/TiO_2 core/shell nanofibres, hollow TiO_2 nanofibres, and porous TiO_2 nanofibres. These synthesised nanoarchitectures were characterised through SEM and XRD to determine their suitability as photocatalysts.

From the characterisation of the created structures, it was possible to establish two suitable candidates for the industrial photodecomposition of contaminants in gas streams.

3.1 Introduction

Semiconductors, in particular TiO_2, are known to display promising photodegradative properties for the removal of siloxanes from biogas.[14,126–129] However, even though a number of patents have

been developed using semiconductors for the purification of gas and liquid systems,[48,155,156] their efficiency remains very low due to a focus on thin film catalysts. The semiconductor efficiency can be increased by increasing the contact surface area between the pollutant molecules and the chosen catalysts. It was previously shown by Jong-Heun Lee that due to the large surface area displayed, gas sensing devices based on nanostructured species were by far more efficient than their thin film counterparts.[89]

Although many different nanostructured materials have been created in recent years, two in particular are known to possess extensive surface areas: nanotubes and nanofibres.[90,91] Of these two nanostructures, TiO_2 nanofibres were chosen as the more suitable candidate for the purification and removal of siloxanes from biogas. This choice was made in the light of the more versatile synthesis procedure underlying the formation of nanofibres with respect to nanotubes, as described in Chapter 1. Indeed, the standard procedure for TiO_2 nanotube synthesis impedes the large scale production of TiO_2 nanotubes due to its complex and inefficient experimental limitations.[93,96]

Nanofibrous structures, on the other hand, do not possess such problems. Their synthesis procedure allows not only for the formation of nanofibres of many different metal oxides (such as TiO_2[107] and ZnO[159]) but also for the creation of composite material structures.[160,161] Furthermore, the synthesised nanofibres are easily removed from their original substrate without the use of complicated procedures. This advantage signifies that nanofibres used for gas purification systems will be able to completely use their large surface area as filter meshes for gas purification, thus becoming highly efficient photocatalytic biogas purification systems.

The heterogeneous photocatalytic process for the decomposition of siloxanes by TiO_2 nanofibres can be enhanced through two different techniques: doping and surface modification. Doping focuses on the introduction of secondary species in the catalyst structure at concentrations below 1 mol%. However, the introduction of dopants often requires expensive materials and complex techniques.[162–164] As such, the use of doping agents to further increase the efficiency of TiO_2 nanofibrous catalysts at an industrial level can be difficult.

The second means of enhancing TiO_2 nanofibres is through surface modification. An increase in the surface area of a catalyst is known to lead to an increase in photodegradative properties arising from an increased accessibility of reaction sites.[65] A number of techniques exist allow to create nanofibres with significant surface porosity, leading to nanostructures with enhanced surface

areas.[165–167] However, these procedures often involve a variety of solvent mixtures and allow for very little control over the created nanostructure morphology. These technical limitations severely limit the industrial application of enhanced surface area nanofibres.

In this series of experiments, the synthesis of nanofibres from three different materials (TiO_2, WO_3, and SiO_2) and three novel architectures (core/shell, hollow, and porous TiO_2 nanofibres) was performed. The created architectures were then studied and compared in order to ascertain their viability as enhanced photocatalytic agents for the decomposition of siloxanes in biogas.

3.2 Experimental

3.2.1 Chemicals and Characterisation Techniques

All chemicals used during the following experiments were sourced from Sigma-Aldrich UK and used as received unless otherwise stated.

The characterisation of the synthesised nanostructure morphology during this study was performed through SEM using a JEOL-JSM 820 Scanning Microscope. Prior to SEM imaging, the SiO_2 nanofibre samples were gold coated for 5 minutes using an Edwards S150 sputter coater to eliminate charging effects from the electron beam used during SEM imaging. The width, length and diameters of the created nanostructures were measured by using the Image J analytical software (National Institutes of Health, USA) in conjunction with the gathered SEM images.

The crystal structures of the semiconductor nanofibres were analysed using powder XRD with a Siemens Powder X-500 diffractometer using a Cu plate at a wavelength of $1.54\,\text{Å}$. Elemental analysis was performed on the studied samples using Energy Dispersive X-ray spectroscopy (EDX).

The band gap of the semiconductor nanofibres was determined by using an integrating sphere (Ocean Optics ISP-REF) equipped with an inbuilt tungsten-halogen illumination source (300 nm $\leq$ λ $\leq$ 1000 nm) and an ASEQ LR1 UV-Vis detector. Through the use of the Tauc relation it was then possible to determine the band gap of the studied materials from their UV-Vis diffuse reflectance spectra.

3.2.2 Semiconductor Nanofibre Synthesis

Semiconductor nanofibres of three different metal oxides were synthesised during this study: TiO_2, SiO_2, and WO_3. The general procedure for nanofibre synthesis consists in two principal steps: the preparation of a semiconductor precursor solution and the subsequent conversion of the precursor solution into semiconductor nanofibres through an electrospinning procedure. Due to the high versatility of the electrospinning procedure, it was possible to change the component semiconductors of the nanofibres by simply modifying the nature of the precursor. As such, the electrospinning procedure used for the three different semiconductor nanofibres was maintained constant.

TiO_2 Nanofibre Precursor

The precursor for the formation of TiO_2 nanofibres was created by making a polymer solution of polymethylmethacrylate (PMMA, 7 wt%, $\overline{M_W}$: 996 000) in dimethylformamide (DMF). The solution was stirred magnetically until the complete dissolution of the PMMA was observed. Acetylacetone (1 wt%) and titanium tetraisopropoxide (TT^iP, 7 wt%) were then added, successively, to the polymer solution. The created transparent yellow solution was magnetically stirred for 1 minute before being used for the synthesis of TiO_2 nanofibres through electrospinning.

WO_3 Nanofibre Precursor

The precursor for the synthesis of WO_3 nanofibres was prepared by creating a polymer solution containing a precursor to WO_3. Initially, a polymer solution of PMMA (7.6 wt%, $\overline{M_W}$: 996 000) in DMF was prepared. The solution was magnetically stirred until all of the PMMA had dissolved. Following the dissolution, tungsten (VI) chloride (3 wt%) and acetylacetone (1 wt%) were added to the polymer solution. The resulting transparent brown solution was magnetically stirred for 1 minute prior to its use in the synthesis of WO_3 nanofibres through electrospinning.

SiO_2 Nanofibre Precursor

The precursor for the formation of SiO_2 nanofibres required a slightly different process due to the immiscibility of tetraethylorthosilicate (TEOS) in DMF. Initially, phosphoric acid (85 %, $50\,\mu L$)

was added dropwise to a solution of TEOS (50 wt%) in deionised water and stirred for 5 hours in order to create an initial SiO_2 sol-gel precursor. The created gel was then added to a solution of polyvinylalcohol (PVA, hydrolysed, 11 wt%, $\overline{M_W}$: 85 000 - 124 000) in deionised water and was stirred for a further 2 hours. Finally, the clear precursor solution was used for the formation of SiO_2 nanofibres through electrospinning.

Nanofibre Synthesis Through Electrospinning

In order to convert the precursor solutions into semiconductor nanofibres, the electrospinning procedure was applied. The chosen precursor solution was placed into a syringe and extruded from a stainless steel needle (23 gauge) by applying an electric current with a high potential difference (18 kV) to the needle. The high voltage charges caused the electrostatic extrusion of the precursor solutions and the formation of nanofibres. The feed rate of the precursor solution into the charged needle was controlled by using a syringe pump (protégé 3010 syringe pump, set at a feed rate of 2.5 ml/h). The created fibres were collected on a grounded rotating aluminium drum placed at a set distance (15 cm) from the needle tip. Figure 3.1 shows a schematic representation of the experimental set up used for the synthesis of nanofibres from selected precursors.

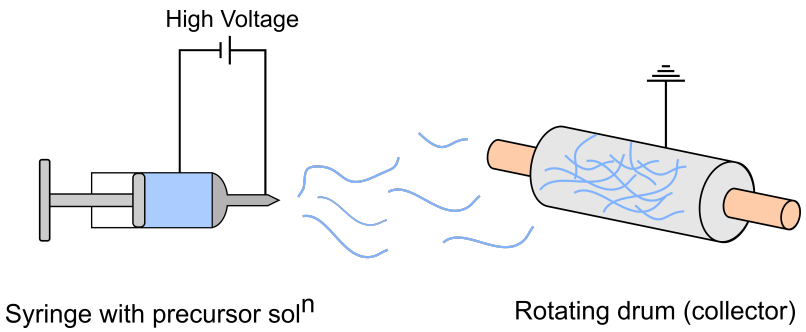

Fig. 3.1 Schematic diagram showing the experimental set up for the synthesis of nanofibres through electrospinning.

The created nanofibres were collected as a non-woven mat and placed in a steam bath (80°C, for 3 hours) in order to enhance the conversion of the semiconductor precursors into their respective hydroxide forms. This step was unnecessary during the formation of SiO_2 nanofibres as the Si in the as-spun nanofibres was already present as SiO_2. Following steam treatment, the fibres were finally calcined in a furnace in order to remove the polymer framework, leaving only the semiconductor nanofibres. The WO_3 and TiO_2 nanofibres were calcined at 500°Cfor 3 hours. However, the more

complex thermal decomposition kinetics of PVA signified that the complete mineralisation of the polymer in the SiO_2 nanofibres was only achieved after calcination at 900°C for 14 hours as, at lower temperatures the PVA was only decomposed into non volatile polyene species.[168,169]

Following calcination, the morphology, crystallinity and electronic properties of the created nanofibres were characterised as described in Section 3.2.1.

3.2.3 Core/Shell Nanofibre Synthesis Through Dip-Coating

The formation of core-shell nanofibres was carried out through a dip-coating procedure. Initially, SiO_2 nanofibres were synthesised through the electrospinning procedure described in Section 3.2.2. These nanofibres were then dip-coated into a titanium precursor solution which was subsequently converted into TiO_2 allowing for the final synthesis of a TiO_2 shell on the SiO_2 nanofibres.

Following the synthesis of the SiO_2 nanofibre mats as described in Section 3.2.2, the SiO_2 nanofibres were covered in TiO_2 layers of controlled thickness through a simple four step procedure. Firstly, the nanofibres were immersed into a solution of TT^iP (5 wt%) in IPA for 30 minutes. This allowed for the adsorption of the titanium precursor onto the surface of the silica. Secondly, in order to clean any non-adsorbed excess precursor from the surface of the sample, the fibres were immersed into a clean IPA solution. Thirdly, the adsorbed precursor remaining on the fibres was hydrolysed into $Ti(OH)_2$ by immersing the fibres into deionised water. Finally, the excess water in the fibre mat was removed by immersing the sample into clean IPA. Figure 3.2 shows the four step process involved in creation of the TiO_2 shell on SiO_2 nanofibre mats.

This four step procedure was repeated up to 10 times in order to allow for the formation of multiple shells on the TiO_2 nanofibres. Once the dip coating cycle was completed, the samples were allowed to dry under ambient conditions. The dry fibre mat was then calcined in a furnace (550°C, for 3 hours) in order to convert the $Ti(OH)_2$ into TiO_2 and create SiO_2/TiO_2 core/shell nanofibres.

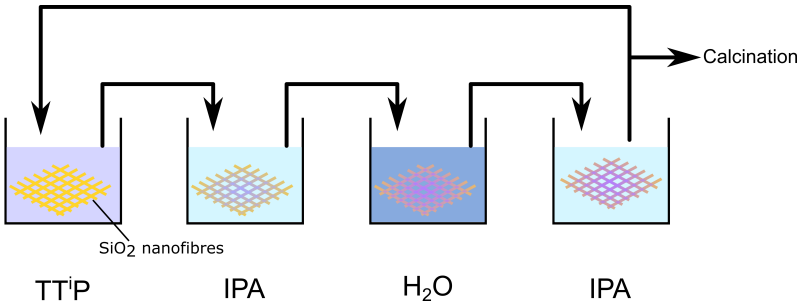

Fig. 3.2 Schematic representation of the experimental procedure for the creation of SiO_2/TiO_2 core/shell nanofibres.

Following calcination, the morphology and crystallinity of the created nanofibres were characterised as described in Section 3.2.1.

3.2.4 Hollow TiO_2 Nanofibre Synthesis Through Templating

Hollow nanofibres were created through a templating procedure similar to the "TUbes by Fibre Templates" (TUFT) process established by Bognitzki *et al.*[170] Initially, a nanofibre template was synthesised and coated with a semiconductor shell. After the coating, the template was removed, allowing the successful synthesis of hollow semiconductor nanofibres. Figure 3.3 shows the main steps leading to the synthesis of hollow TiO_2 nanofibres.

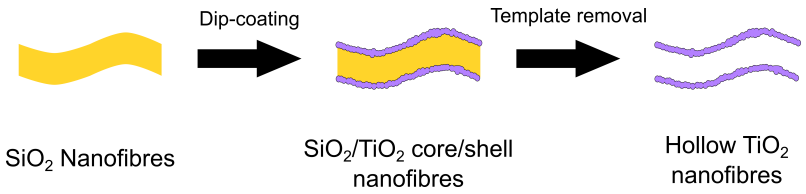

Fig. 3.3 Schematic representation of the principal steps for the template-assisted synthesis of hollow TiO_2 nanofibres.

SiO_2 nanofibres were used as the template for the creation of hollow TiO_2 nanofibres. SiO_2 nanofibres were synthesised using the precursor and electrospinning procedures described in Section 3.2.2. The as-calcined SiO_2 fibres were then converted into SiO_2/TiO_2 core/shell nanofibres by using the dip-coating procedure described in Section 3.2.3 in order to create an external TiO_2 layer on the SiO_2 template. The four step dip-coating cycle was repeated 8 times before calcination of the core/shell template. The procedure was repeated 8 times as the results from the formation of the SiO_2/TiO_2 core/shell nanofibres indicated that this lead to the formation of a TiO_2 shell of

approximately 80 nm, a thickness which would allow to visualise the hollow fibres through SEM whilst minimising their production and synthesis times.

Finally, the SiO_2 template was removed by base treatment. The core/shell fibres were immersed into a basic solution (KOH_{aq}, 6 M) and placed in an oven at 80°C. The immersed fibres were heated for 8 hours, this allowed for the complete dissolution of the SiO_2 master template. After base treatment, the hollow nanofibres were separated from the basic solution through Büchner filtration.

The morphology of the hollow nanofibres was analysed as described in Section 3.2.1.

3.2.5 Template-Assisted Nanofibres With Controlled Porosity

The synthesis of TiO_2 nanofibres with controlled porosity was carried out through a templating procedure similar to that described in Section 3.2.4. Initially a series of SiO_2 nanosphere (NS) templates were synthesised. The created templates were then embedded into TiO_2 nanofibres through electrospinning. Finally, the templates were removed from the synthesised fibres through a base treatment, resulting in the synthesis of nanofibres with controlled porosity.

The initial SiO_2 NS pore templates were created by using an adapted method of the Stöber technique[171] as presented by Bogush *et al.*[172] In order to create the NS, concentrated ammonia (15 ml, 35 %) was diluted in absolute ethanol (85 ml). A fraction (2 ml) of the diluted ammonia solution was then added to a solution of deionised water (2 ml), ethanol (15.2 ml), and TEOS (0.73 ml). The created solution was then heated in an oil bath (35°C) for 36 hours under magnetic stirring. The resulting milky solution was centrifuged at 5000 rpm for 2 hours. Following centrifugation, the solution was decanted and the remaining solid was allowed to dry at ambient conditions. After drying, the created NS cake was mechanically crushed and used to create a precursor for the electrospinning of templated nanofibres.

The precursor for NS templated TiO_2 nanofibres was formed by combining the NS with the standard precursor for the formation of TiO_2 nanofibres. The created NS (1.34 wt%) were added to a solution of PMMA (7 wt%, $\overline{M_W}$: 996 000) in DMF. The solution was then allowed to stir for 2 hours, after which the complete dispersion of the NS was observed as the solution had changed visually from opaque white to translucent. Acetyl acetone (1 wt %) and TT^iP (9 wt%) were sequentially added to the NS suspension and were allowed to mix for 1 minute. The precursor

solution was then immediately used for the synthesis of nanofibres through electrospinning as described in Section 3.2.2.

The as-spun templated nanofibres were base treated in order to remove the SiO_2 NS. The nanofibres were immersed in a basic solution (KOH_{aq}, 6 M) and placed in an oven (80°C) in order to ensure the complete removal of the SiO_2 NS. After 8 hours the solution was removed from the oven and the solid was separated from the basic liquid through Büchner filtration. The porous nanofibres, collected as a white powder, were then allowed to dry in ambient conditions. A schematic representation of the template removal procedure is shown in Figure 3.4.

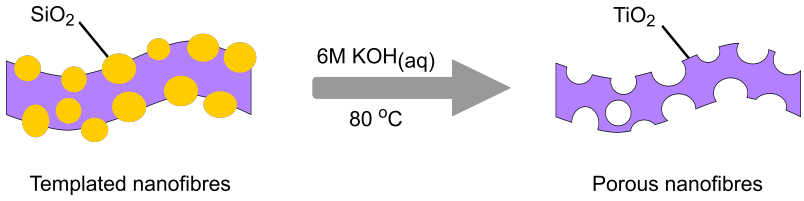

Fig. 3.4 Schematic representation showing the SiO_2 nanosphere removal process from the templated TiO_2 nanofibres.

The structures of the created NS as well as the templated and porous nanofibres were analysed as described in Section 3.2.1.

3.3 Results and Discussion

By studying and comparing the elemental, structural, electronic, and crystalline properties of the created nanoarchitectures it was possible to establish their relative suitability in the photodecomposition of siloxanes in biogas.

3.3.1 Electrospun Semiconductor Nanofibre Characterisation

TiO_2 Nanofibres

Elemental and crystallographic data was initially used to analyse the created TiO_2 nanofibres. The EDX spectrum of these structures is shown in Figure 3.5. The large peak observed in the EDX spectrum at 1 keV originates from the Al substrate used for the collection of the TiO_2 nanofibres.

The other observable peaks in the spectrum arise from Ti, indicating the creation of high purity nanofibres. The purity of the sample can be further seen by the XRD spectrum presented in Figure 3.6 which only shows the characteristic diffraction patterns of the TiO_2 anatase and rutile crystal structures. The assignment of the diffraction pattern was possible by correlating the spectral peaks with the ICDD database (ICDD # 21-1276 and # 1272 for the rutile and anatase peaks, respectively).

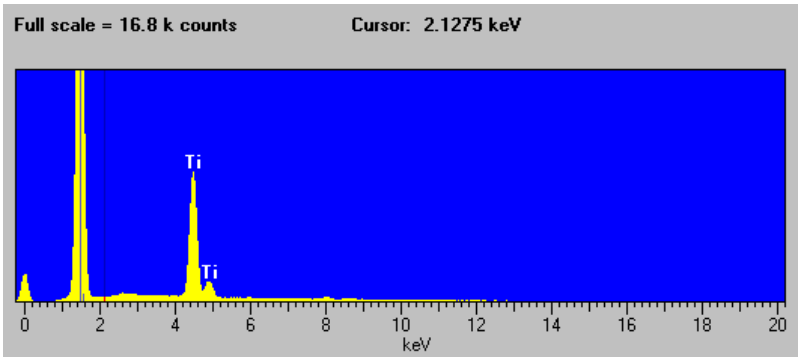

Fig. 3.5 EDX scan of the electrospun TiO_2 nanostructures. The large peak at 1 keV arises from the Al substrate onto which the fibres were collected.

By analysing the crystal structure of the TiO_2 nanofibres as shown in Figure 3.6, it was possible to determine that 60 % of the structures was anatase whilst the remaining 40% was rutile. The prevalence of the less thermodynamically stable anatase crystal structure can be explained by the TiO_2 particle size and nanofibre growth mechanism.[66] Due to the liquid nature of the TiO_2 precursor, the formation of TiO_2 crystals occurs through many different nucleation sites, leading to the formation of small TiO_2 crystals. As anatase is the thermodynamically stable crystal structure at particle sizes below 11 nm, the nanofibres will initially be composed of anatase crystals.[60] However, during calcination the TiO_2 crystals will undergo annealing and growth. As these crystals grow, the rutile crystal phase will become increasingly thermodynamically stable and the concentration of rutile TiO_2 crystals in the sample will tend to increase with increasing time at high temperatures. Due to the relatively limited nanofibre calcination times, not all of the TiO_2 crystals will have enough time to undergo the phase transition, causing the observed mixture of anatase and rutile crystal phases.

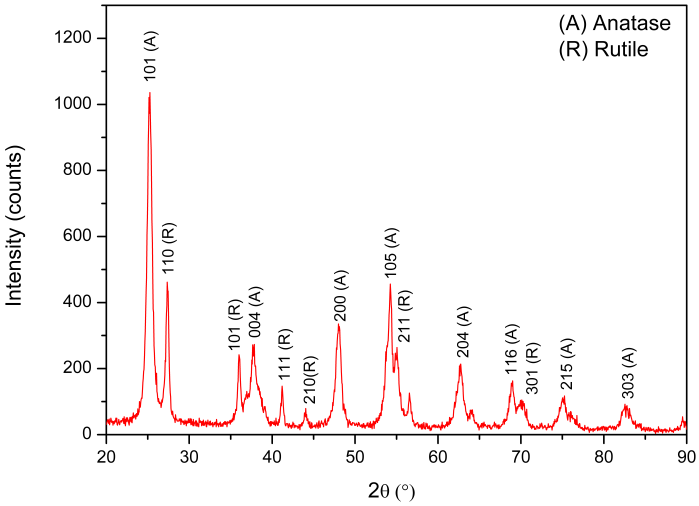

Fig. 3.6 X-ray diffraction pattern showing the crystal composition for the electrospun TiO_2 nanofibres. The peak assignments show the crystal face and structure corresponding to each peak, the assignment was carried out by using the ICDD database files # 21-1276 and # 21-1272 for rutile (R) and anatase (A) respectively.

The superior thermodynamic stability of the rutile phase can be further seen by comparing the crystallite size of the 110 and the 101 crystal faces for rutile and anatase, respectively. These crystal faces were chosen as they are known to be the most stable faces of their respective crystal structures.[66] The crystallite size of the two crystal faces was calculated by applying the Scherrer equation as described in Section 2.2. From this it was possible to determine that the crystallite size for the anatase 101 face was 20 nm whilst the 110 rutile face displayed a crystallite size of 28 nm. The higher crystallite size of the rutile arises from the greater thermal stability of the crystal structure.

Although a good understanding of the crystal composition of the TiO_2 nanofibre systems was achieved through XRD, it is only through SEM that it was possible to analyse the physical architecture of the created structures.

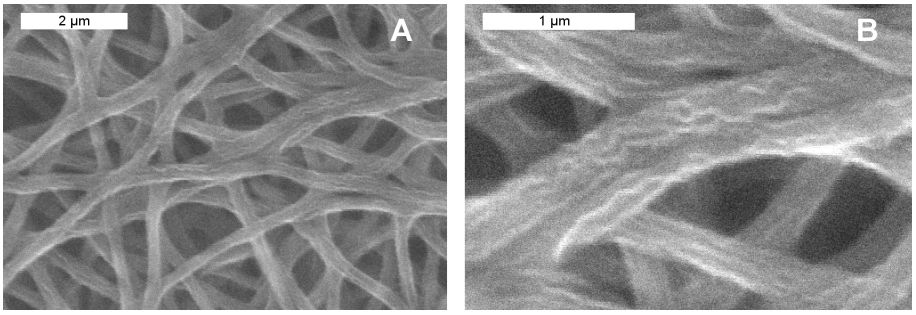

Fig. 3.7 SEM images showing the structure of the synthesised TiO_2 nanofibre mat (A) and the surface morphology of the individual fibres (B).

Figure 3.7 shows the SEM images of the structure of the synthesised TiO_2 nanofibre mat (A) and the surface morphology of the individual fibres (B), it is clear that the created structures were indeed fibrous in nature. The ridged surface of the nanofibres seen in Figure 3.7 (B) can be attributed to their growth mechanism. The TT^iP precursor concentration is distributed inhomogeneously in the electrospun nanofibres, thus leading to the formation of fibres wherein the TiO_2 is inter-dispersed with the polymer prior to calcination. As the fibres are calcined and the polymer is removed, it leaves pores on the surface of the fibres in the form of the observed ridges.[173] From Figure 3.7 it was further possible to determine that the fibres were created with a relatively homogeneous thickness of 310 ± 20 nm (based on 100 measurements over different areas of the same sample). As such, it is possible to determine that the electrospinning procedure allowed for the successful formation of homogeneous TiO_2 nanofibres. However, in order to achieve good photodecomposition abilities it is not only essential to create large surface area nanostructures but also to achieve photoactivity within these structures.

Figure 3.8 shows the Tauc plot achieved from the UV-Vis reflectance spectrum of the synthesised TiO_2 nanofibres as described in Section 2.3. The linear correlation within the Tauc plot confirms that the nanofibres are semiconductors with a direct band gap. From the plot it was possible to determine the TiO_2 nanofibre band gap to be 3.06 ± 0.02 eV. This is consistent with the experimentally determined band gap for P25 of $3.09 \pm .06$ eV and the literature band gap for TiO_2 crystals (3.11 eV).[174] Due to this band gap, the nanofibres will successfully create hydroxide radicals under UV_a illumination, thus allowing for their use in the photodecomposition of siloxanes in biogas.

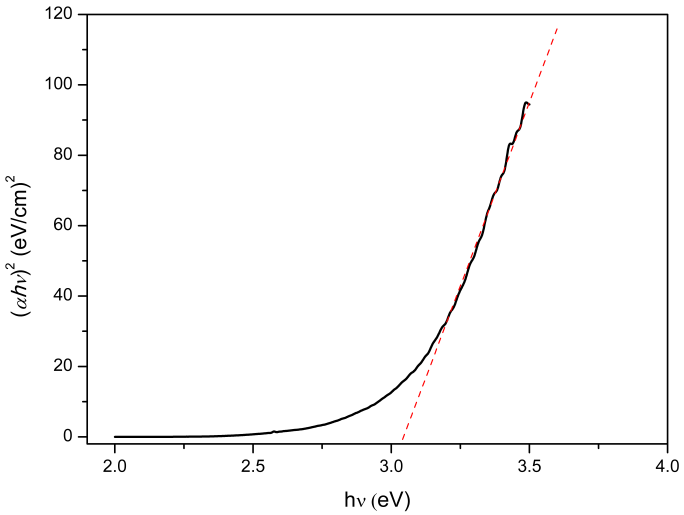

Fig. 3.8 Tauc plot derived from the reflectance spectrum of TiO_2 nanofibres, the linear portion shown as the segmented line shows the extrapolation of the nanostructure's band gap.

However, it is important to note the band gap of the TiO_2 nanofibres remains relatively high, meaning that their photoactivity will only achieve high levels of efficiency under artificial rather than solar illumination. WO_3 is known to possess a smaller band gap whilst maintaining photodegradative properties,[175,176] making it an appealing alternative to TiO_2 for the decomposition of siloxanes in biogas.

WO_3 Nanofibres

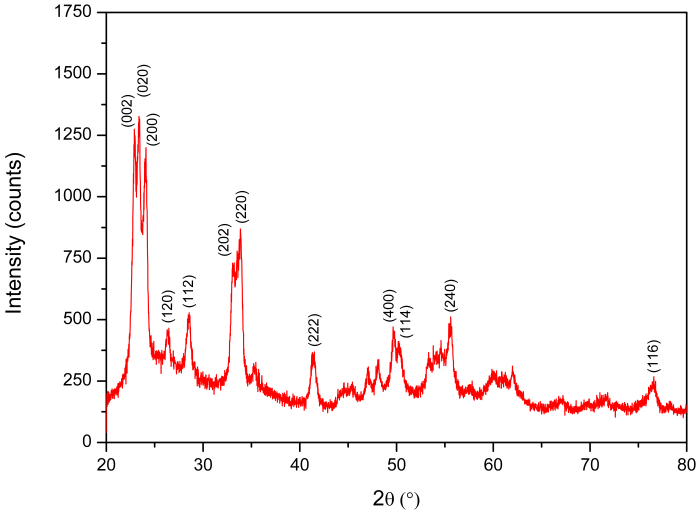

Fig. 3.9 X-ray diffraction pattern showing the crystal composition of the electrospun WO_3 nanofibres. The peak assignment showing the crystal face of each peak was carried out using the ICDD database file # 01-089-4478.

The XRD spectrum of the nanostructures created by electrospinning the WO_3 precursor can be seen in Figure 3.9. From this spectrum it becomes readily apparent that the created nanostructures were composed solely of WO_3. The assignment of the diffraction pattern as shown in Figure 3.9 was possible by correlating the spectral peaks with the ICDD database (ICDD # 01-089-4478). From the peak assignment it was further possible to establish that the crystal structures composing the nanostructures are all orthorombic, β-WO_3. This is consistent with the expectations as it is known that the orthorombic β-WO_3 crystal structure is the most stable of the WO_3 crystal structures at temperatures between 330°C and 740°C.[177] As the calcination process which removes the polymer framework from the nanofibres proceeds at 500°C, the formation of orthorombic WO_3 crystals will be favoured. The morphology of the created structures was studied through SEM imaging as shown in Figure 3.10.

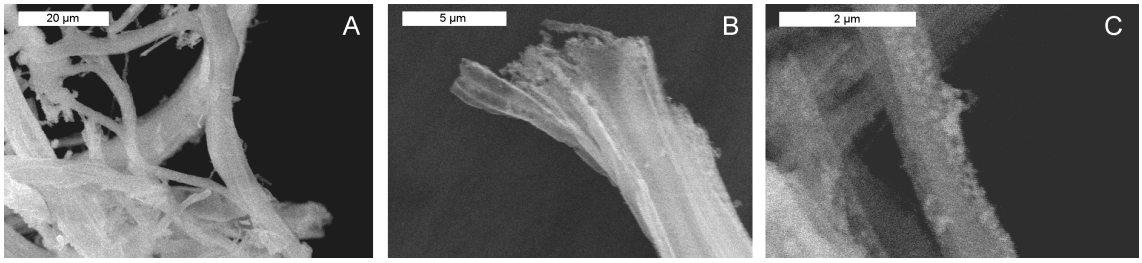

Fig. 3.10 SEM images showing the synthesised WO_3 fibre mat (A), the bundled WO_3 nanofibres (B) and the individual WO_3 nanofibre structures (C).

Figure 3.10 shows the synthesised WO_3 fibre mat (A), the bundled WO_3 nanofibres (B) and the individual WO_3 nanofibre structures (C). It becomes readily apparent that the created structures possessed a fibrous morphology, establishing the successful creation of WO_3 nanofibres through the electrospinning procedure. It is possible to notice that the nanofibres are significantly larger ($\sim 10\ \mu$m in width) than the previously synthesised TiO_2 nanostructures (nanofibre width of 310 $\pm$ 20 nm). Further examination of the nanostructures established that the large fibre size in the general sample morphology arises from the aggregation and bundling of smaller fibres, this effect is particularly pronounced in Figure 3.10 (B). The specific nanofibre structure seen in Figure 3.10 (C) clearly shows a rough surface, this roughness can be attributed to an inhomogeneous distribution of the precursor chemical similar to that which leads to the formation of the corrugated surfaces of TiO_2 nanofibres (as seen in Figure 3.7 (B)). By analysing the individual electrospun nanofibres, it was possible to observe a thickness of 650 $\pm$ 100 nm (based on 100 measurements over different areas of the same sample), the large uncertainty in this measurement arises from the bundled structures which render the distinction between individual fibres particularly complex. The observed fibre diameter is twice that of the synthesised TiO_2 nanofibres. This means that the WO_3 nanofibres will display a significantly smaller surface area when compared to their TiO_2 counterparts. However, it is important to remember that although the loss of surface area is a significant drawback, the use of WO_3 may display advantageous electronic properties.

The Tauc plot generated from the UV-Vis reflectance spectrum of the WO_3 nanofibres, as described in Section 2.3, is shown in Figure 3.11. From the linear nature of the Tauc plot, it is possible to establish the semiconductive nature of these nanofibres. Furthermore, it was possible to determine that the WO_3 nanofibres possessed a band gap of 2.89 $\pm$ 0.05 eV. This band gap is consistent with that determined experimentally for WO_3 powder (2.95 $\pm$ 0.02 eV) and that reported in literature (2.75 $\pm$ 0.06 eV).[178]

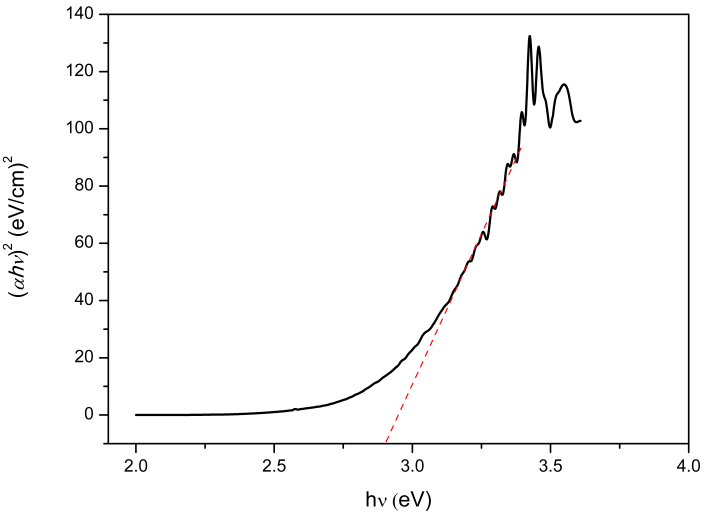

Fig. 3.11 Tauc plot derived from the reflectance spectrum of WO_3 nanofibres, the linear portion shown as the segmented line shows the extrapolation of the nanostructure's band gap.

The WO_3 nanofibres created through electrospinning can be considered a suitable alternative to TiO_2 nanofibres. As the WO_3 nanofibres possess a smaller band gap (2.89 eV) compared to the TiO_2 nanofibres (3.06 eV) , the WO_3 nanofibres will be able to use a larger portion of the solar spectrum in order to create photogenerated radicals for photodecomposition, effectively rendering the WO_3 nanofibres more energetically efficient than their TiO_2 counterparts. However, it is important to note that the tungsten chloride precursor used for the synthesis of WO_3 nanofibres is significantly more expensive than the TT^iP precursor used for the TiO_2 nanofibre synthesis. As such, even with a slightly lower efficiency, the TiO_2 nanofibres might be the more viable industrial photodecomposition catalysts. It is nonetheless important to note that both the TiO_2 and WO_3 nanofibres displayed a significant mechanical weakness. After the fibre calcination procedure, the created fibre mats became very brittle and poorly resistant to mechanical stress which led to the rapid conversion of the samples from large scale mats to powders (which still maintained the nanoscale fibre morphology).

This mechanical fragility can be attributed to the formation mechanism of the nanofibres. Indeed, for both the TiO_2 and WO_3 nanofibres the metal oxide crystals forming the nanofibres are created from many different nucleation sites after the formation of the fibre structures. This means that the metal oxide nanofibres will be composed of polycrystalline network with many defects as the different crystals will join in different orientations. These defects will lead to preferential

fracture points within the fibres, effectively making them mechanically fragile. This fragility can only be observed after calcination as the polymer networks act as mechanical supports for the fibres prior to calcination.

This mechanical fragility can be addressed by the use of a precursor wherein the final nanofibre material is formed during the electrospinning process rather than in the subsequent water treatment and calcination. Indeed, if the nanofibre material is already created during the formation of the fibres, then the loss of polymer framework will be less significant to the fibre integrity. The electrospinning process for the formation of SiO_2 nanofibres allows the generation of the final fibre material prior to calcination by polymerising the TEOS during the electrospinning procedure.

SiO_2 Nanofibres

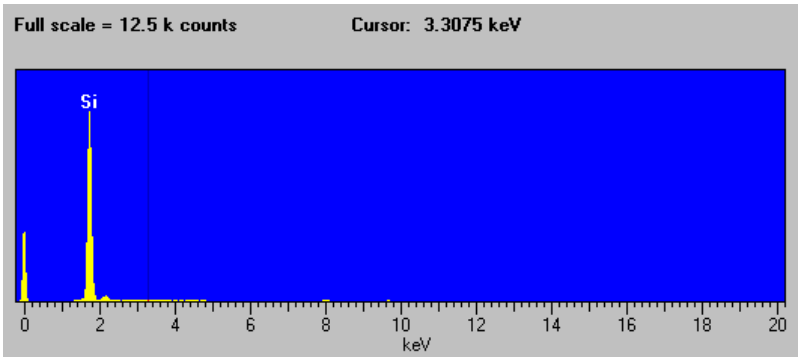

Fig. 3.12 EDX scan of the electrospun SiO_2 nanostructures.

The EDX spectrum of the created nanostructures seen in Figure 3.12 shows the high purity of the Si structures. A further understanding of the purity and nature of the Si structures was gained through their XRD pattern as shown in Figure 3.13. It is clearly visible from the low intensity of the XRD diffraction spectrum that the created nanostructures are only semi-crystalline. It was nonetheless possible, using the ICDD database (ICDD # 00-029-0085), to associate the observed diffraction peak to a crystal face and establish the sole presence of SiO_2 in the sample. Due to the large width of the XRD signal as well as its truncated nature, it becomes important to note that the reliability of the peak assignment carried out with the ICDD database should be considered with caution as it is based on the comparaison of previous literature spectra which were not truncated and present a sharper peak profile. The amorphous nature of the synthesised structures can be attributed to the synthetic procedure for the nanofibrous structures which leads to the direct polymerisation of the

TEOS precursor into a SiO_2 framework. This means that during the formation of the SiO_2, the $Si-O$ network will form in a disordered, amorphous, manner rather than in a controlled, crystalline, fashion. In order to further characterise the created structures, the SiO_2 nanofibres were analysed through SEM imaging.

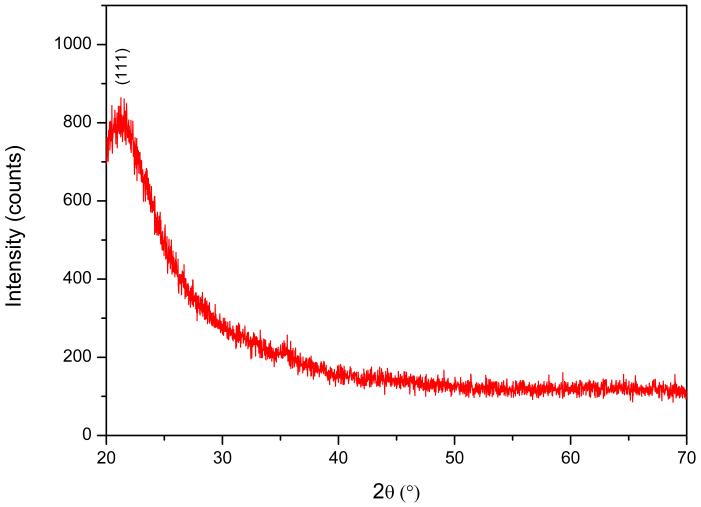

Fig. 3.13 X-ray diffraction pattern showing the crystal composition of the SiO_2 nanofibres. The peak assignment was carried out using the ICDD database file # 00-029-0085.

Figure 3.14 shows the structure of the synthesised SiO_2 nanofibre mat (A) and the surface morphology of the individual fibres (B), highlighting their fibrous nature. From Figure 3.14 (B) it is possible to observe that the surface of the SiO_2 nanofibres is smooth, unlike that observed for the TiO_2 (Figure 3.7 (B)) and WO_3 (Figure 3.10 (C)) structures. This difference in nanofibre surface morphology can be attributed to a more homogeneous distribution of the TEOS precursor within the supporting polymer framework. As the TEOS polymerised during electrospinning, it formed a more homogeneous structure. This meant that upon calcination, the local concentrations of PVA were uniform throughout the sample, thus inhibiting the formation of significant surface defects in the created systems. Further analysis of the nanofibres determined a fibre thickness of 263 ± 65 nm (based on 100 measurements over different areas of the same sample). The SiO_2 fibre thickness is significantly smaller than those observed for the TiO_2 (310 ± 20 nm) and WO_3 (650 ± 100 nm) nanofibres. This difference can be further attributed to the homogeneity of the polymer/precursor mixture during electrospinning. As the SiO_2 nanofibres were homogeneously mixed with their PVA framework, the removal of the PVA resulted in a global decrease in fibre thickness rather than the

localised decreases which lead to the corrugations and defects observed in the less homogeneously mixed TiO_2 and WO_3 nanofibres.

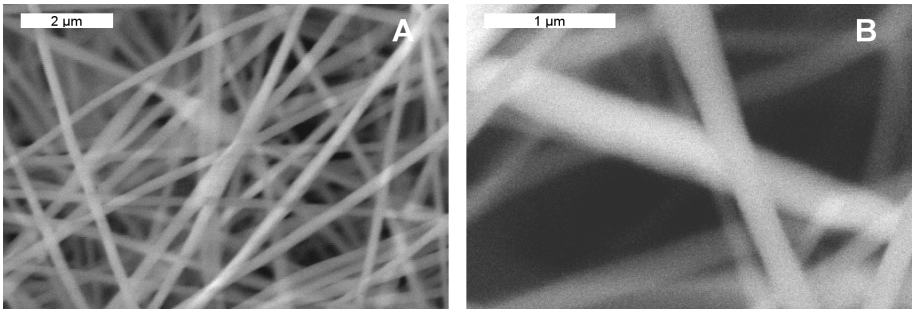

Fig. 3.14 SEM images showing the structure of the synthesised SiO_2 nanofibre mat (A) and the surface morphology of the individual fibres (B).

Although the SiO_2 nanofibres display promising structures, it is important to note that the electrical properties of SiO_2 can severely limit their use as photocatalysts. It is known that the band gap of SiO_2 ranges from 5 - 17 eV, depending on its crystallinity.[179,180] This signifies that even in the cases where the SiO_2 has its lowest known band gap, photons with a wavelength of 248 nm would be required in order to achieve meaningful electronic excitations. As the use of such high energy photons is unachievable from the solar spectrum, dedicated light sources would be required in the use of SiO_2 nanofibres for the photocatalytic purification of biogas. In addition to this, it is known that UV light below 290 nanometres is highly hazardous to humans,[181,182] meaning that the industrial requirements for the photonic activation of SiO_2 nanofibres remain prohibitive.

Nonetheless, the SiO_2 nanofibres were seen to display an excellent mechanical stability, maintaining the woven fibrous mat structure even under stress. As such, even if the fibres themselves cannot be used as photocatalytic biogas purification agents, the combination of the mechanical strength of the SiO_2 nanofibres with the inexpensive nature of the TiO_2 precursors could yield industrially promising photodecomposition catalysts.

3.3.2 Characterisation of SiO_2/TiO_2 Core/Shell Nanofibres

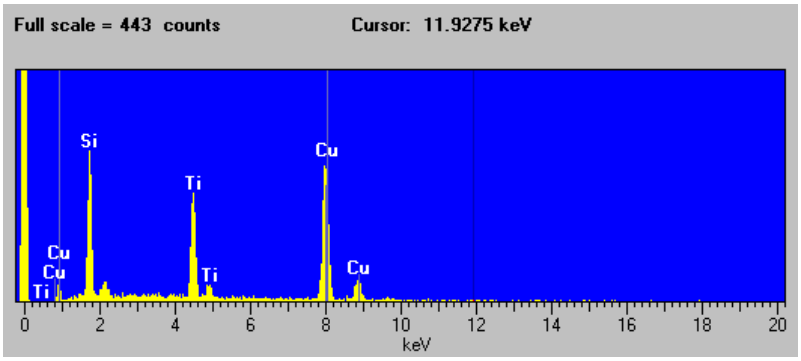

Fig. 3.15 EDX scan of the created SiO_2/TiO_2 core/shell nanostructures after 9 dip coating cycles. The Cu peaks originate from the Cu substrate onto which the fibres were placed for analysis.

Figure 3.15 shows the EDX spectrum of the core/shell nanofibres synthesised in Section 3.2.3 after nine dip coating cycles. It can be seen that the structures were composed solely of Si and Ti; the Cu peaks present in the spectrum arise from the substrate on which the fibres were placed during analysis. The purity and composition of the core/shell structures was further analysed by XRD, as shown in Figure 3.16.

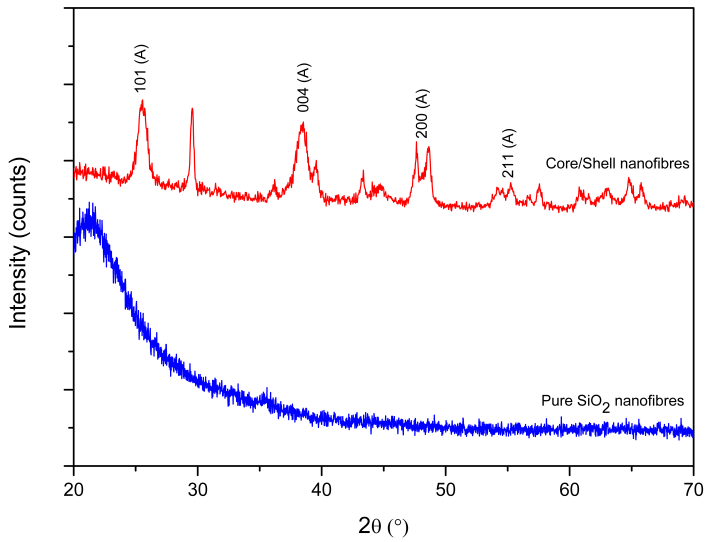

Fig. 3.16 X-ray diffraction patterns showing the amorphous nature of the created SiO_2 nanofibres (below) with respect to the same fibres after the dip-coating procedure. The peak observed at a 2θ value of $21.4°$ arises from the crystal structure of the calcite substrate onto which the fibres were placed during analysis.

Figure 3.16 shows the spectra of the SiO_2 nanofibre template before and after the dip coating procedure. From these spectra, in addition to the EDX analysis, it becomes clear that TiO_2 was successfully added to the SiO_2 mats through the dip coating procedure. Furthermore, it is possible to note that the TiO_2 crystals formed on the surface of the amorphous SiO_2 nanofibre structure were purely anatase. The identification of the anatase diffraction peaks was performed through correlation with the ICDD database (ICDD # 21-1272). The prevalence of the TiO_2 anatase crystal structure over the rutile crystal structure can be attributed to the relatively higher thermodynamic stability of anatase at small TiO_2 particle sizes.[60] As each dip coating cycle only supplied a monolayer coating (with the excess being washed off) of TT^iP before converting the precursor into $Ti(OH)_2$ crystals, the formation of small TiO_2 particles from the small $Ti(OH)_2$ crystals led to the formation anatase crystal structures.

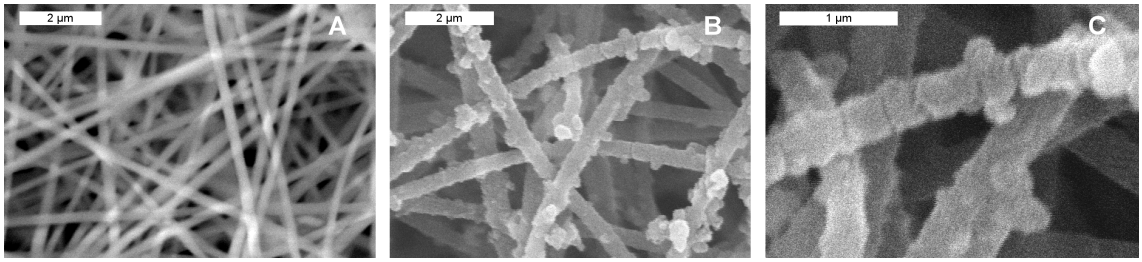

Fig. 3.17 SEM images showing the fibre mats of the uncoated (A) and dip coated (B) nanofibres. Figure C shows the individual fibre structure of the dip coated fibres. The core/shell structures shown in figures B and C were achieved after 10 dip coating cycles

The morphology of the dip coated nanofibres was further characterised through SEM imaging. Figure 3.17 shows the fibre mat morphology of the fibres before (A) and after (B) the dip coating procedure as well as the individual nanofibre morphology of the dip coated structures (C). From Figure 3.17 (A) and (B) it was possible to see that the TiO_2 coating on the SiO_2 nanofibres was successfully carried out without significant alterations to the nanostructure morphology, allowing to maintain the advantages inherent to the use of nanostructures for the purification of biogas. However, it is possible to see in Figure 3.17 (C) that the dip coating procedure led to the formation of a rough fibre surface. In a similar study on the growth of TiO_2 layers on ZnO rods Fan *et al.* proposed that the origin of the roughness could be attributed to the mismatch between the lattice of the TiO_2 crystals and the ZnO substrate which impeded the epitaxial growth of the TiO_2 on the substrate surface.[183] As a consequence of this the TiO_2 shell growth is believed to occur preferentially from a number of nucleation points on the surface rather than grow homogeneously. In this study, the

lattice mismatch leads not only to the formation of the surface roughness observed in Figure 3.17 (C), but also to the prevalence of the anatase crystal phase (due to its superior thermodynamic stability at small TiO_2 particle size) in the TiO_2 shells, as observed in Figure 3.16.

A better understanding of the TiO_2 shell growth can be gained by observing Figure 3.18. Figure 3.18 shows the evolution of the nanofibre mat morphology during increasing dip coating procedures: image (A) shows the uncoated nanofibre mat whilst images (B), (C), (D), (E), (F), and (G) show the nanofibre mat after 1, 2, 3, 4, 5, and 6 dip coating cycles. It can be seen that the surface of the SiO_2 fibres gradually becomes rougher after the fibres have undergone three or more dip coating cycles (Figure 3.18 (E) to (G)). The apparent smoothness of the fibre surface during the first two dip-coating cycles (Figure 3.18 (B) and (C)) can be attributed to the combination of a very thin surface coating which would have been visible with difficulty through SEM imaging and a more homogeneous coating achieved by the TiO_2 onto the SiO_2 fibres. Indeed, when the fibres are uncoated, there is no preferential deposition site for the TiO_2 precursor on the fibres. However, as the TiO_2 shell is grown on the fibres through many nucleation sites (caused by the lattice mismatch between the SiO_2 and the TiO_2) this will lead to the formation of preferable deposition sites as the TT^iP will preferentially bind with the TiO_2 shell than the SiO_2 nanofibre surface. As these preferential deposition sites become larger through increased dip coating cycles (seen as the large crystals on the fibre surfaces in images (E) to (G) which become more prominent as the number of dip coating cycles increases), the surface of the coated nanofibres becomes gradually less homogeneous, accentuating the fact that the original TiO_2 shell growth proceeded through many different nucleation sites.

The effect of the initial dip coating cycles providing preferential decomposition sites can also be seen by observing the nonfibrous crystalline residues present in the fibre mats in Figure 3.18. These residues, arising from TT^iP trapped in the fibre mat but unbound to the fibre surface, can be seen to appear in Figure 3.18 (C) as small particles near the fibres. As the number of dip coating cycles increases, the size of these residues increases, causing the formation of the large particulate clusters which can be seen in Figure 3.18 (E), (F), and (G). This size increase, like that of the TiO_2 shell on the SiO_2 nanofibres, can be attributed to the presence of initial TiO_2 residues which form preferential binding sites for the precursor and consequently grow gradually with each coating cycle.

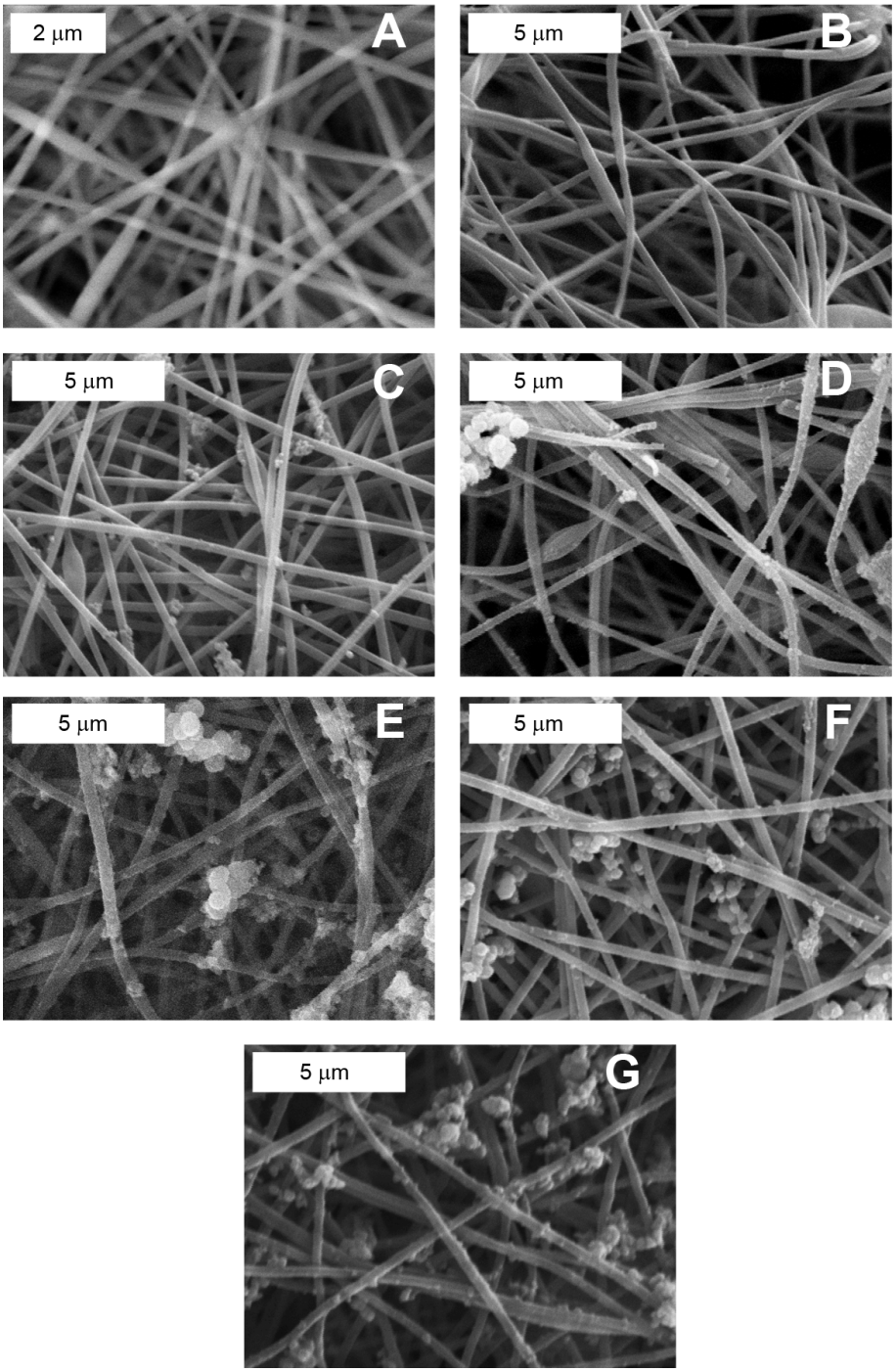

Fig. 3.18 SEM images showing the evolution of the SiO_2 nanofibre mat morphology before (A) and after one (B), two (C), three (D), four (E), five (F), and six (G) dip coating cycles.

By further analysing the created core/shell structures through SEM imaging, it was possible to establish a growth profile for the thickness of the TiO_2 shell in relation to the number of dip coating cycles performed. The growth profile for the TiO_2 shell thickness is shown in Figure 3.19. It was determined that each individual cycle contributed to a 10.1 ± 0.4 nm increase in TiO_2 shell thickness. This growth profile inevitably leads to the formation of small TiO_2 precursor crystals in

the nanofibre shell, consistently with the observed prevalence of the anatase crystal structure in the TiO_2 phase as shown in the XRD spectrum in Figure 3.16.

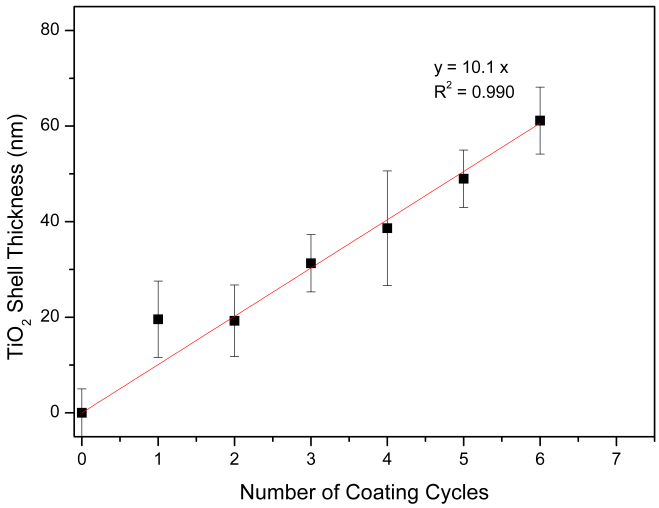

Fig. 3.19 Thickness of the TiO_2 shell coating on the synthesised core/shell nanostructures in relation to the number of dip coating cycles. The linear relationship establishing a 10 nm shell growth in each cycle can clearly be seen.

Finally, it is also important to note the presence of nanocrystallites disconnected from the templates in the core/shell nanostructured mats, as can be seen in Figure 3.17 (B) and (C). These nanocrystallites are believed to be TiO_2 impurities arising from the dip-coating procedure. The natural high surface area of a nanofibre mat renders it ideal for the trapping of solutions such as water or TT^iP mixtures. As a consequence of this high trapping ability, the cleaning procedure during the formation of the TiO_2 shells may be insufficient for the complete removal of excess precursor solution. Upon contact with water the trapped excess solution is then converted into the observed nanocrystallite structures which become less mobile throughout solutions and remain stuck within the nanofibre mat. It is believed that the occurrence of these crystals would not significantly impact the photocatalytic activity of the created nanostructures due to their relatively low surface area and adsorption sites. These limited adsorption sites signify that the photodegradation of siloxane species will still occur primarily on the nanofibre surface, thus rendering the overall contribution of the observed nanocrystallites towards siloxane photodegradation negligible.

3.3.3 Characterisation of Hollow TiO_2 Nanofibres

By removing the SiO_2 core of SiO_2/TiO_2 core/shell nanofibres as discussed in Section 3.2.4, the creation of hollow TiO_2 nanofibres was investigated. The created nanostructures were solely characterised through SEM imaging as both the crystal phase of the TiO_2 shell and the electronic properties of the TiO_2 nanofibres were previously characterised in Section 3.3.2 and Section 3.3.1, respectively. The known stability of TiO_2 to highly basic conditions signifies that any changes occurring in the shell's crystal structures and the TiO_2's electronic properties during the removal of the SiO_2 template can be considered as negligible.[59]

The SEM images of the fibre mat (A) and individual fibre (B) morphology of the created structures after the removal of the TiO_2 template can be seen in Figure 3.20. The presence of a large number of supra-micrometre length fibres can be observed clearly in Figure 3.20 (A), showing that the SiO_2 template was successfully removed whilst maintaining a nanofibrous TiO_2 structure. The hollow nature of the synthesised fibres can be seen Figure 3.20 (B). Through further SEM analysis it was possible to establish the nanofibre wall thickness to be 90 ± 17 nm (based on 50 measurements recorded for a variety of hollow fibres over different areas of a given sample). The calculated thickness is consistent with the shell growth profile depicted in Figure 3.19, further indicating that the TiO_2 shell remained unaffected by the template removal procedure. This demonstrates that the successful synthesis of hollow TiO_2 nanofibres was achieved through the procedure outlined in Section 3.2.4.

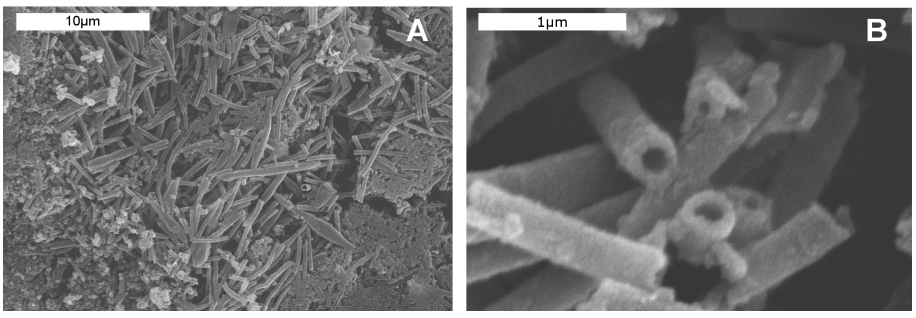

Fig. 3.20 SEM images showing the fibr emat (A) and individual fibre (B) morphology of the hollow TiO_2 nanofibres.

The hollow nanofibres can be of particular interest as enhanced catalysts for the photodegradation of siloxanes in biogas due to their increased surface area. The hollow morphology of the

nanofibres effectively doubles the active sites available for the photodecomposition of gaseous reagents. As such, it becomes apparent that these architectures are an ideal enhancement from the simple TiO_2 nanofibres synthesised in Section 3.2.2. However, it was important to note that these nanostructures displayed significant technical limitations.

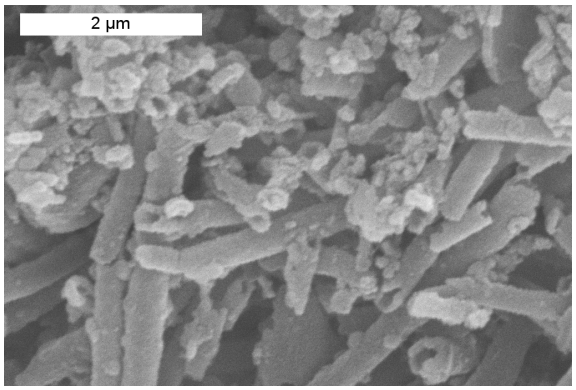

Fig. 3.21 SEM image showing the damage on the general hollow nanofibre structure following mechanical stress.

It can be clearly seen from Figure 3.21 that the created nanofibres are highly prone to mechanical damage through fracturing. This weakness can be attributed to the TiO_2 shell formation process on the SiO_2 template. As discussed in Section 3.3.2, the SiO_2/TiO_2 lattice mismatch impeded the epitaxial growth of TiO_2. As such, the shell formation occurred through a number of nucleation sites on the SiO_2 template. Through this mechanism, a number of defects are generated in the TiO_2 shells which will significantly weaken the hollow nanofibres.

This mechanical weakness could be a key shortcoming of the hollow nanofibres. Once the structures are broken down, the increase in surface area achieved by using TiO_2 hollow nanofibres rather than TiO_2 nanofibres (or even simple TiO_2 nanoparticulates) is lost. Furthermore, although the proposed synthetic procedure is appreciably facile, it remains more complex than the standard electrospinning procedure. As such, it becomes clear that a templating method allowing the generation of mechanically more resistant TiO_2 nanofibres whist still displaying an appreciable increase in surface area would allow to achieve industrially viable photocatalysts which maintain the advantages of increased surface areas.

3.3.4 Characterisation of Nanofibres with Controlled Porosity

By using a silica NS template for the production of porous TiO_2 nanofibres, it would be possible to achieve an enhanced surface area whilst maintaining the mechanical strength of the TiO_2 nanofibres. The electronic and crystallographic properties of TiO_2 nanofibres were previously characterised in Section 3.3.1. As TiO_2 is stable under highly basic conditions[59] it can be assumed that the base treatment for the removal of the SiO_2 templates only had negligible effects on the crystalline and electronic properties of the electrospun TiO_2 nanofibres. As such, the nanostructures created as described in Section 3.2.5 were characterised solely through SEM imaging.

Initially, the SiO_2 NS were characterised in order to ensure suitability for the templating procedure. Figure 3.22 shows low (A) and high (B) magnification SEM images of the created NS. It is possible to observe the large scale synthesis of SiO_2 nanospheres without surface defects. Further analysis of the NS sample established that the spheres possessed a diameter of 253 $\pm$ 20 nm (based on 100 measurements recorded from a variety of different images taken at different locations on a single sample). In order to understand the high degree of homogeneity of the NS, it is important to understand their synthetic mechanism.

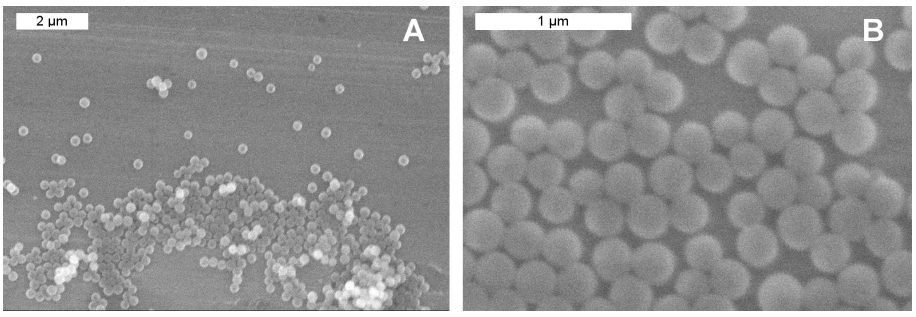

Fig. 3.22 SEM images showing low (A) and high (B) magnifications of the synthesised SiO_2 nanosphere templates.

The main mechanism for the creation of the silica NS templates is the hydrolysis of the TEOS silicon alkoxide. This hydrolysis is governed by a number of factors including the reaction temperature and reagent concentrations which are known to affect the ultimate NS size.[172] However, it was postulated by Bogush *et al.*[172] that the narrow size distribution of the created particles was independent of these factors. The main NS growth mechanism was established to occur through a series of aggregation events which proceed at different rates with decreasing speed as the NS

size increases. These decreasing rates arise from a decreasing probability of particle aggregation with increasing particle size caused by the increased charges on the particle surfaces which lead to inter-particle repulsive forces, as described by the DLVO theory of colloidal stability.[184] As such, irrespective of the final particle size, any synthesis procedure for SiO_2 NS hinging on the condensation of TEOS will lead to a small particle size distributions (as observed during this study).

From the morphology of the NS as seen in Figure 3.22 as well as their calculated size, the spheres were deemed suitable templates for the formation of porous TiO_2 nanofibres. This was established as the NS diameter was significantly smaller than that of the TiO_2 nanofibres (310 ± 20 nm). The difference in diameter signifies that the removal of NS template would not cause fracturing of the nanofibres (as would be observed if the NS diameter were close to or larger than the TiO_2 nanofibre diameter).

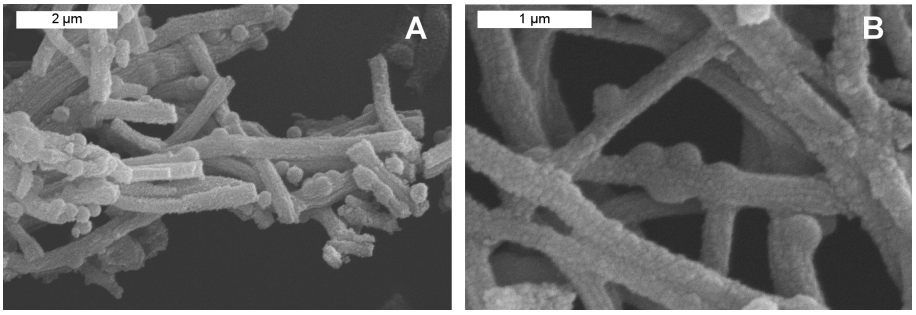

Fig. 3.23 SEM images showing the structure of the templated TiO_2 nanofibres at low (A) and high (B) magnifications.

The structure of the embedded SiO_2 templates in the electrospun TiO_2 nanofibres can be seen in Figure 3.23 at low (A) and high (B) magnifications. It becomes apparent that the SiO_2 NS were successfully embedded in the TiO_2 nanofibres. The average nanofibre width was calculated to be 333 ± 60 nm, over 100 measurements of a variety of different embedded fibres in different locations of the same sample whilst the average NS diameter was calculated to be 325 ± 41 nm over 100 measurements of different embedded spheres in various locations of the same sample. It is clearly visible that the embedded sphere diameter is larger than that of non-embedded SiO_2 spheres. This increase in diameter arises due to a TiO_2 coating on the NS surface which can be seen clearly in Figure 3.24 where the sphere surface is no longer smooth as observed in Figure 3.22 (B) but displays the typical rough surface observed in TiO_2 nanofibres.

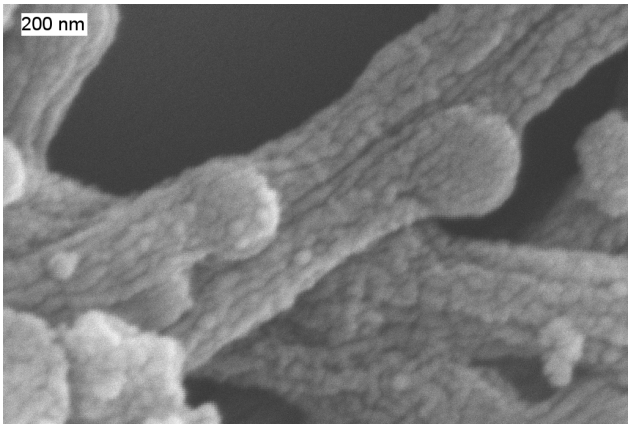

Fig. 3.24 SEM image showing the TiO_2 covering on the embedded silica spheres in templated TiO_2 nanofibres.

Although the NS templates presented a TiO_2 coating, this did not significantly affect the removal of the SiO_2 templates through base treatment. This can be seen clearly in Figure 3.25; Figure (A) shows the structure of the porous nanofibre mat whilst Figure (B) shows the individual structure of the porous fibres. Figure 3.25 (A) shows that the fibre morphology was maintained throughout the system even following the mechanically demanding base treatment and Büchner filtration. Furthermore, from a series of 100 measurements of different nanofibres in various locations of the same sample, it was possible to calculate the average fibre width to 362 ± 65 nm. This value is higher than the fibre thickness recorded previous to the treatment however the two values lie within each other's confidence intervals which allows the attribution of this discrepancy to experimental error. The maintenance of fibre thickness during the base treatment further demonstrates the chemical stability of the TiO_2 fibres.

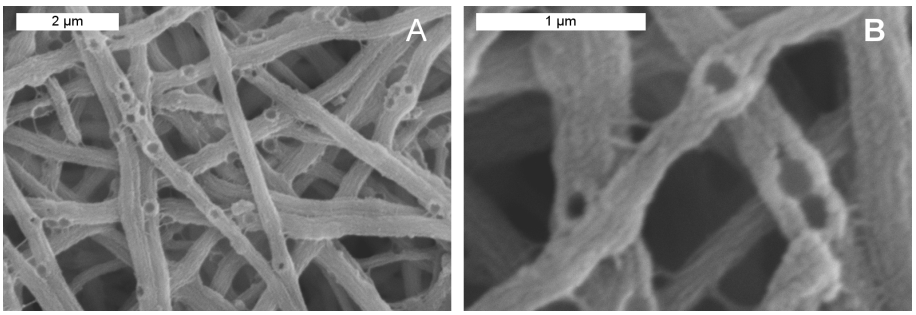

Fig. 3.25 SEM images showing the fibre mat (A) and individual fibre (B) morphologies of the porous TiO_2 nanofibres following template removal.

Through SEM analysis it was possible to establish the diameter of the created pores as

215 ± 38 nm (average value over 80 measurements of different pores on a variety of fibres in the same sample). The calculated pore size is significantly smaller than the actual SiO_2 NS diameter. This is believed to arise as a consequence of the embedding of the NS in the nanofibre surface. Indeed, in order for NS to embed themselves successfully in the fibres, more than 50% of the sphere volume has to reside in the fibre. If this is not the case, the spheres will detach themselves with facility from the fibre surface leaving damaged, non-porous, systems. On the other hand, spheres that are embedded above 50 % by volume into the nanofibres will be maintained and result in successful pores, meaning that the externally measured pore diameter is in fact only the chord of a segment of the spherical hole. The relationship between the observed pore diameter and the diameter of the NS templates is represented schematically in Figure 3.26.

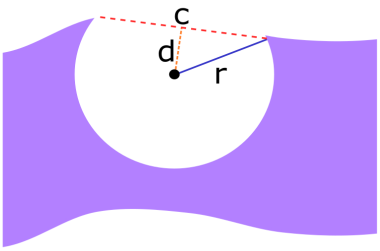

Fig. 3.26 Diagram showing the relationship between the observed pore diameter, c, and its true radius, r, in the porous TiO_2 nanofibres

Figure 3.26 shows the relationship between the chord of a circular segment, c, the radius of the circle, r, and the distance between the centre of the circle and the chord, d. This relationship can further be expressed mathematically as shown in Equation (3.1). By combining the distance from the sphere centre with the circular radius it is possible to determine the size of the NS segment embedded in a TiO_2 fibre, E, as represented by Equation (3.2). As such, it becomes possible to determine the embedding percentage $\%_E$ of the templates into the TiO_2 nanofibres using Equation (3.3). For the created samples it was possible to calculate that, on average, 76.3% of the individual NS surface was embedded during the electrospinning procedure.

$$d = \sqrt{r^2 - \frac{c^2}{4}} \tag{3.1}$$

$$E = r + d \tag{3.2}$$

$$\%_E = \frac{E}{2r} \times 100 \tag{3.3}$$

With a controllable NS size it becomes possible to estimate both the final nanofibre porosity and increases in surface area achieved from the templating procedure. This controllable porosity in combination with the previously discussed mechanical and chemical resistance of the TiO_2 nanofibres, render the created nanostructures very appealing. These properties signify that these structures would remain effective photocatalysts even when exposed to the harsh industrial conditions required for biogas purification. It is thus apparent that as well as being a viable enhancement to normal TiO_2 nanofibres, the created porous nanofibres are also a more appealing alternative to hollow TiO_2 nanofibres for the photocatalytic degradation of siloxanes.

3.4 Conclusions

In conclusion, during this study it was possible to successfully create a number of different nanostructures for the removal of siloxanes from biogas.

Initial synthetic studies were performed to create nanofibres of three different materials: SiO_2, TiO_2, and WO_3. The synthesised fibres were characterised through SEM, EDX, and UV-Vis reflectance techniques. It was determined that although the WO_3 nanofibres possessed the smallest band gap (2.89 eV) of the three materials, the cost of the precursor required for nanofibre synthesis limited their industrial application. The precursor cost for the formation of both SiO_2 and TiO_2 nanofibres made these two species more attractive at an industrial level. However, the SiO_2 nanofibres can not be photoexcited due to the large band gap of SiO_2. This means that the removal of siloxanes in biogas by SiO_2 nanofibres would only be through adsorption rather than photodegradation. As such, TiO_2 nanofibres were considered the best candidates for the removal of siloxanes from biogas through photodegradation. Nonetheless, of the three different nanofibrous structures, the WO_3 and TiO_2 nanofibrous mats showed poor mechanical stability. Indeed, upon mechanical stress the TiO_2 and WO_3 nanofibre mats were rapidly converted into powders. Although the WO_3 and TiO_2 powders still maintained their nanostructured morphology, the macrostructured powder form could complicate their use as photocatalysts at an industrial scale. The synthesised SiO_2 nanofibres, on the other hand, showed excellent mechanical stability, maintaining their

macrostructure even under significant mechanical stress.

The mechanical strength of the SiO_2 nanofibres was further combined with the photoactivity of the TiO_2 nanofibres in core/shell nanostructures. SiO_2/TiO_2 core/shell nanostructures were synthesised by using a facile dip-coating procedure. From XRD and SEM analysis it was possible to establish the successful creation of the core/shell nanostructures as well as to gain an insight into the factors determining the structure morphology and composition. The presented technique achieved a fine control on the TiO_2 shell thickness, allowing the formation of shells with a minimum thickness of 10 nm. However, although the procedure for the formation of the TiO_2 shells is relatively facile, this procedure combined with the more complex synthesis of SiO_2 nanofibres might still result too difficult for large scale industrial applications.

Two additional nanoarchitectures were synthesised during this study in order to enhance the surface area of TiO_2 nanofibres; hollow and porous TiO_2 nanofibres were synthesised through templating techniques. The hollow nanofibres were established as possessing the highest possible surface area for TiO_2 nanofibres. However, due to the synthesis process underlying the formation of the hollow nanofibres, the structures resulted particularly brittle, rapidly deteriorating and losing their unique architecture. This mechanical fragility was not observed in the porous nanofibres. In depth analysis of the created structures established the versatility of the templating method for the creation of TiO_2 nanofibres with controlled porosity. It was determined that 76 % of the volume of the NS templates had been embedded in the fibres. By controlling the NS size it would thus be possible to control the nanofibre porosity and create nanofibres with an adjustable surface area. This adjustable surface area could become particularly useful in the photodecomposition of gas phase pollutants.

During this study, a number of different techniques were employed to create nanoarchitectures appropriate for the photodecomposition of siloxanes in biogas. It was thus possible to successfully synthesise not only nanofibres of different materials but also nanofibres with enhanced structures. Due to the inherent mechanical fragility, costs, and synthetic complexity of a number of the created structures; two structures were identified as promising candidates for the photodecomposition of siloxanes in biogas: TiO_2 nanofibres and porous TiO_2 nanofibres. However, it is only through extensive experimentation that it will be possible to truly establish the effectiveness of the photocatalytic properties of the created structures and their viability in gas phase purification devices.

4. Siloxane Adsorption Studies

As discussed in Chapter 1, the removal of siloxanes from biogas can be performed through a variety of techniques, the most promising of which are adsorption purification and photocatalytic purification. When combined with nanostructured architectures, photodecomposition becomes a particularly promising technique. However, it remains essential to achieve a good understanding of the adsorptive properties of different nanostructured architectures before their photocatalytic properties may be investigated.

The following chapter presents a synthetic pathway for the formation of high surface area SiO_2 aerogels under ambient conditions. The hexamethyldisiloxane (L2) adsorption properties of the synthesised aerogels were studied by monitoring of the material's adsorption kinetics. These adsorption properties were then compared to the adsorption properties of electrospun SiO_2 and TiO_2 nanofibres in order to gain an in depth understanding of the factors governing the adsorption of siloxanes on high surface area structures.

In order to ascertain the viability of the created materials to act as efficient adsorbents, their L2 adsorption properties were compared to those of two standard commercial adsorbents: the PpTek ion-exchange resin, and commercially synthesised silica gel. The silica gel studied was further used in a series of surface treatment procedures to gain a more complete understanding of the interactions between siloxanes and material surfaces.

It was finally demonstrated that although the nanostructured materials possessed high surface areas, more work needs to be performed before their application as biogas purification adsorbents becomes commercially competitive. Nonetheless, it was shown that TiO_2 nanofibres will successfully adsorb siloxanes to an appreciable degree, thus demonstrating their applicability in the photocatalytic purification of gas streams.

4.1 Introduction

With an estimated 40 million biogas energy plants constructed in China alone by the end of 2010,[74] the combustion of biogas for electricity generation is poised to become one of the major sources of renewable energy in the 21st century. However, because of the complex process of biogas generation, biomethane contains a number of noxious contaminants such as benzene and hydrogen sulfide.[185] Amongst the contaminants present in biogas, the most dangerous during combustion are the chemical family of siloxanes.[186] As biogas undergoes combustion in a spark engine, siloxanes are converted into SiO_2 microcrystals which have been known to cause catastrophic engine failure.[12,13]

A number of techniques have been used in literature in order to remove siloxanes from biogas.[187–189] Although a wide variety of systems were developed, ranging from siloxane removal by deep chilling[7] to biological degradation,[189] the prevalent technique for biogas purification is that of solid phase adsorption.[11] This procedure focuses on the use of high surface area filters to adsorb siloxanes, in order to remove them from the biogas prior to combustion.

Industrially, although a large amount of patents have been published concerning the removal of siloxanes from biogas,[10,16,17,190] three main adsorption technologies have gained industrial interest: activated carbon,[191] alumina/Silica beds,[17] and ion-exchange resins.[9] Of these three technologies, the ion-exchange resins have become the industrial standard thanks to their potential for the regeneration of saturated adsorption media. In the cases of activated carbon and alumina/silica adsorbents, the most efficient way of saturated media disposal is to return the saturated media to a landfill site as the removal of siloxanes from the adsorbents remains too energetically expensive. On the other hand, the ion-exchange resins, once saturated, can be regenerated through a facile thermal treatment which converts the siloxanes to silicon dioxide in a waste gas stream.[9] Nonetheless, even with this thermal treatment, the resins do not achieve full regeneration and eventually require disposal. In the light of this shortcoming, the development for alternative biogas purification methods becomes essential. The use of nanostructured materials as adsorbents can be an appealing evolution on the standard adsorption media.

Nanostructured compounds are known to display outstanding properties such as large surface area to volume ratios,[89] low densities,[192]and large internal volumes.[193] These properties render the nanostructures ideal candidates for the enhanced removal siloxanes through adsorption. During this

series of experiments, two different nanostructures were synthesised and used for the adsorption of L2: silica aerogels and nanofibres.

Silica aerogels are structures with extremely high porosities and large internal surface areas, making them ideal candidates for the adsorption of siloxanes.[92] However, the standard synthetic procedure for the generation of silica aerogels requires high temperatures and pressures,[194] thus rendering the industrial use of silica aerogels prohibitive. As such, an ambient pressure procedure for the synthesis of silica aerogels was developed during this series of experiments.

The second nanostructure used was that of electrospun nanofibres as they are known to have high surface areas whilst maintaining relatively facile synthesis techniques.[195] Furthermore, the electrospinning technique is highly versatile, allowing for the synthesis of chemically active nanostructured adsorbents. Indeed, the use of photoactivated TiO_2 has shown promising potential in the removal of siloxanes.[196] As such, the use of chemically active nanofibres could allow for a direct, *in situ*, treatment of the adsorbates, thus supplying an elegant solution to the adsorbent regeneration problem.

In this series of experiments, the L2 adsorption properties of silica aerogel, TiO_2, and SiO_2 nanofibres were studied and compared to those of industrial standard adsorbents. This comparison allowed to ascertain the viability of the synthesised materials as adsorption agents for the removal of L2 from biogas.

4.2 Experimental

4.2.1 Chemicals and Characterisation Techniques

All chemicals used during the following experiments were sourced form Sigma-Aldrich UK and used as received unless otherwise stated.

The morphology of the SiO_2 aerogel spheres synthesised in Section 4.2.2 was studied through Scanning Electron Microscopy (SEM), using a JEOL-JSM 820 Scanning Microscope. Prior to SEM imaging, the aerogel beads were gold coated for 5 minutes using an Edwards S150 sputter coater to eliminate charging effects from the electron beam used during SEM imaging. The diameter of the

aerogel beads was measured using a Workzone digital Vernier calliper.

The SiO_2 aerogel bead rough packing density was calculated by placing aerogel beads in a 10 ml measuring cylinder until the 5 ml mark was reached. As this left a number of interstitial gaps between the beads, some lightly crushed aerogel (obtained by mechanically crushing the beads using weak force and a spatula) was used to fill the inter-bead gaps. Once the whole $5\,cm^3$ volume in the measuring cylinder (the 5 ml mark) was considered occupied, the measuring cylinder was weighed in order to gather the mass of $5\,cm^3$ of aerogel, allowing to achieve a rough packing density.

The concentration of octadecylphosphonic acid (ODPA) on commercial silica gel beads applied during the coating procedures presented in Section 4.2.3 was monitored using Fourier Transform InfraRed vibrational spectra (FTIR). The spectra were recorded using a Perking Elmer Spectrum One in Attenuated Total Reflectance mode (ATR). By monitoring the intensity of the peak corresponding to the symmetric PO_2 stretch (1043 cm^{-1}) in the ODPA vibrational spectra, it was possible to monitor the presence of ODPA in the system.

The characterisation and analysis of the synthesised SiO_2 and TiO_2 nanofibres is described in Chapter 3.

During the adsorption experiments in Section 4.2.4 the L2 concentration was quantified by calibrating and monitoring the area under the L2 peak in the spectra generated by a gas chromatograph (GC) equipped with a flame ionisation detector (FID). The GC-FID used during the experiments was a Perkin Elmer autosystem equipped with a 50 m wax capillary column. During the duration of the adsorption experiments the gas flow rate was kept at 1.5 ml min^{-1}, the oven and injection temperatures were maintained at 60°C. H_2 was used as the carrier gas and supplied from a SP300HC hydrogen generator. Under these conditions, the retention time for L2 was 150 s.

4.2.2 Silica Aerogel Synthesis at Ambient Conditions

Low density SiO_2 beads were formed through a modified technique based on the work carried out by Sarawade *et al.*[99] A precursor solution was created by diluting sodium silicate solution (70 wt%, 1.2 ml) in de-ionised water (8.8 ml). The created solution was then acidified through the dropwise addition of HCl (6 M) under vigorous stirring, until a pH of 3.5 was observed (recorded

using a Hanna instruments pH 209 pH Meter). A significant increase in solution viscosity was observed upon the acidification of the sodium silicate precursor. Upon reaching the desired pH, the generated silica sol was added dropwise into a boiling tube containing a biphasic system of kerosene (5 ml) and aqueous ammonia (6 M, 3 ml). The biphasic system was chosen in order to convert the silica sol droplets into spherical hydrogels. Upon reaching the upper kerosene layer, the sol droplets are induced into a spherical morphology by the repulsive electrostatic interaction between the hydrophilic silica sol and the hydrophobic kerosene. The spheres thus created drop further into the aqueous ammonia solution where they undergo a rapid polymerisation, leading to the synthesis of spherical SiO_2 hydrogels. Figure 4.1 depicts the formation of SiO_2 hydrogel beads.

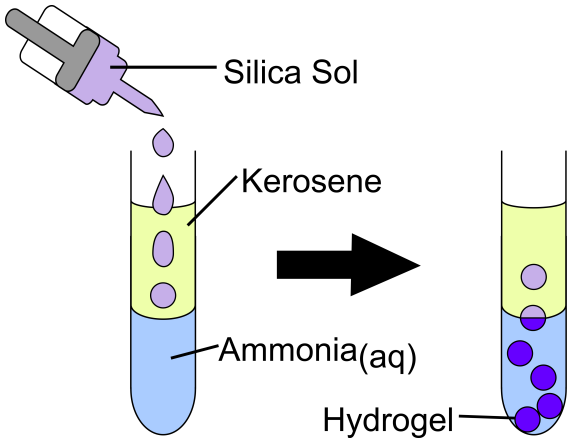

Fig. 4.1 Diagram showing the drop-wise formation of spherical SiO_2 hydrogel beads.

In order to minimise the collapse of the polymeric network upon drying, the as-created silica hydrogels were taken through an ageing process. Initially, the beads were immersed in excess ethanol for 48 hours under heating (55°C). Following the initial ageing, the beads were transferred to a solution of ethanol, trichloromethylsilane (TMCS) and n-hexane (1:1:8 molar ratio, respectively) and kept at ambient temperature for a further 12 hours. This ageing mixture was chosen based on the similar work performed by Zong *et al.* where it allowed to achieve a successful solvent exchange and surface modification of the aerogel beads in order to minimise the collapse of the polymer networks during drying.[197] Once aged, the created gel spheres were washed in n-hexane before drying under ambient conditions.

The synthesised aerogel morphology, bead diameter, and packing density were characterised as described in Section 4.2.1. Finally, the adsorption properties of the created aerogel beads were investigated as described in Section 4.2.5.

4.2.3 Surface Modification of Commercial SiO_2 Gels

Commercial silica gel beads (non-indicating, 2.0-5.0 mm in diameter, sourced from Geejay Chemicals Ltd.) were used to determine the effect of different surface chemical modifications on the L2 adsorption properties of SiO_2. Three different surface coatings were investigated: hexane, TMCS, and ODPA.

The hexane coating was achieved through an immersion technique. 0.5 g of the as-received silica gel beads were immersed in n-hexane (10 ml) at room temperature and pressure for 10 hours. After the immersion, the beads were removed from the hexane and allowed to dry under ambient conditions.

The TMCS surface modification of the SiO_2 beads was also performed through an immersion method. 0.5 g of the silica gel beads were immersed into a solution of ethanol, TMCS and n-hexane (1:1:8 molar ratio). The beads were then maintained at room temperature for 12 hours, decanted from the solution and dried under ambient conditions.

The surface modification of the silica gels with ODPA was achieved through a thermal coating procedure. 0.5 g of silica gel beads were placed in a round bottomed flask containing a solution of ODPA in toluene (10 mM, 25 ml) equipped with a reflux condenser. The mixture was heated until a steady reflux was observed, and kept under reflux for 10 hours. After this period, the beads were removed from the solution and allowed to dry under ambient conditions. In order to ensure that no ODPA was blocking the SiO_2 gel pores, two cleaning procedures were carried out. Firstly, the beads were annealed at high temperatures (200°C) for 2 hours. The second method investigated for the cleaning of beads was ultrasonic cleaning; the ODPA coated beads were placed in n-hexane (10 ml) and sonicated for 4 hours. The effectiveness of the cleaning techniques was investigated by y monitoring the intensity of the peak corresponding to the symmetric PO_2 stretch (1043 cm^{-1}) in the ODPA FTIR-ATR vibrational spectra of the prepared silica gel beads.

The L2 adsorption properties of the surface-modified silica beads were studied as reported in Section 4.2.5.

4.2.4 Nanofibre Synthesis Through Electrospinning

The specific synthetic procedures for the synthesis and morphological characterisation of TiO_2 and SiO_2 nanofibres through electrospinning are presented in in Chapter 3.

For this study, TiO_2 nanofibres were prepared by electrospinning a precursor solution of polymethylmethacrylate (PMMA, $\overline{M_W}$ 996 000, 8 wt%), titanium tetraisopropoxide (TT^iP, 9 wt%), acetyl acetone (1 wt%) and dimethylformamide (DMF, 82 wt%). The solution was fed through a stainless steel needle at a rate of 2.0 mlh^{-1} (controlled using a protégé 3010 syringe pump). A voltage (18 kV) was applied to the stainless steel needle allowing for the creation of charged nanofibres. The nanofibres were collected on a grounded drum at a distance of 15 cm from the needle tip. The as-collected nanofibre mats were steam treated (80°C, 3 h) and calcined (550°C, 3 h) in order to yield TiO_2 nanofibres.

SiO_2 nanofibre synthesis was carried out through a number of steps. Initially, a sol-gel precursor was made by mixing phosphoric acid (85%, 50 μL, added drop wise) and a tetraethyl orthosilicate solution (TEOS, 50 wt%). The created sol-gel was then added to a solution of polyvinylalcohol (PVA, hydrolised, $\overline{M_W}$ 85 000-124 000, 11 wt%) in de-ionised water and allowed to stir. Finally, the created precursor solution was electrospun using an applied voltage of 18kV and a feed rate of 2.0 mlh^{-1}. The fibres were collected on a grounded drum at a distance of 15 cm from the needle tip. Once the electrospinning process was completed, the nanofibre mat was calcined (900°C, 14 h) in order to yield SiO_2 nanofibres.

The siloxane adsorption properties of the SiO_2 and TiO_2 nanofibres were characterised as outlined in Section 4.2.5.

4.2.5 Siloxane Adsorption Onto High Surface Area Structures

The L2 adsorption capacities of the materials synthesised in Section 4.2.2, Section 4.2.3 and Section 4.2.4 were investigated using a method adapted from Nam *et al.*[198]

A round bottomed flask with known volume (115 cm^3) was stoppered with a suba seal and purged with dry nitrogen gas (10 minutes). L2 (0.2 ml) was then injected into the round bottomed flask and vaporised by placing the round bottomed flask in a heated graphite bath (130°C). Sep-

arately, a known sample of studied adsorbent material (<1 g) was placed in a conical flask of known volume (130 cm^3). The conical flask was then sealed using a suba seal and purged using dry nitrogen for 10 minutes. 10 ml of the previously prepared L2/N_2 gaseous mixture were then removed from the round bottomed flask and injected into the conical flask containing the adsorbent studied. The concentration of gaseous L2 in the conical flask was monitored through GC-FID. Figure 4.2 shows the main steps of the L2 adsorption experiments.

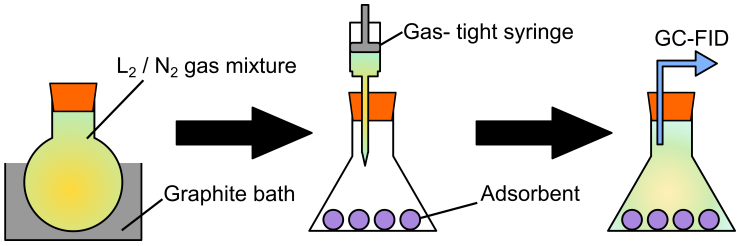

Fig. 4.2 Schematic diagram showing the three main steps in the siloxane adsorption studies: preparation of an L2/N_2 gaseous mix in a heated graphite bath, injection of the gaseous siloxane in an airtight flask containing the studied adsorbent, and L2 concentration sampling from the air tight conical flask.

The L2 concentration in the flask was observed to decline as the siloxane was adsorbed onto the studied materials. Once the siloxane adsorption was observed to have stopped, the system was assumed to have reached equilibrium. At equilibrium, a further injection of gaseous L2/N_2 (10 ml) was performed into the conical flask. The siloxane concentration was further monitored until its decline was observed to cease and the system had reached a novel equilibrium state wherein the rates of L2 adsorption and desorption from the adsorbent proceeded at equal speeds. Due to the increased concentration of L2, this second equilibrium state was observed to occur at a different level of L2 concentration in the gaseous phase as compared to the equilibrium concentration observed prior to the injection.

4.3 Results and Discussion

4.3.1 Silica Aerogel Characterisation

Through a number of characterisation techniques it was possible to achieve a thorough understanding of the synthetic processes underlying the creation of SiO_2 aerogel beads. Initial observations allowed to optimise the synthetic procedure. Further analysis on the perfected aerogels was then

conducted, allowing to achieve a good understanding of the physicochemical processes guiding the gel formation.

Silicic Acid Polymerisation

In order to achieve a successful silica aerogel, the properties and structure of the sol-gel network created prior to drying were finely controlled. The general scheme for the polymerisation reaction leading to the formation of a gel network from sodium silicate is shown in Figure 4.3. The polymerisation of silicic acid is known to proceed differently under basic[199,200] and acidic[201,202] conditions, yielding different gel network structures in each case. Gorrepati *et al.*[201] demonstrated that when sodium silicate is polymerised under acidic conditions, a large particle size is achieved in relatively short times. As the polymerisation progresses through condensation reactions, the large particles come together to form a highly porous network ideal for aerogel synthesis.[203]

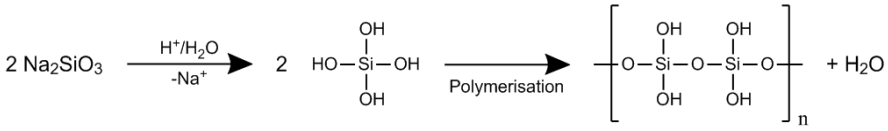

Fig. 4.3 Scheme showing the polymerisation of silicic acid from sodium silicate.

As such, during these experiments it was important to achieve a silicic acid sol-gel using acidic conditions. The original procedure outlined by Sarawade *et al.*[99] used acetic acid in order to acidify the sodium silicate. However, this procedure proved difficult to execute as the sol-gel was observed to reach gelation point before acidification of the sodium silicate occurred. The gelation point was defined as the point in which the solution was observed to lose fluidity, namely the solution could no longer be agitated through magnetically assisted stirring. This setback was overcome by substituting acetic acid with hydrochloric acid. In order to understand the efficacy of hydrochloric acid, an in-depth look at the nature of the sol-to-gel transition becomes necessary.

Silicic acid polymerisation occurs through a condensation reaction as shown in Figure 4.4 wherein the reaction will proceed at maximum rate when the concentrations of silicic acid and its conjugate base are equal. When silicic acid is in highly basic conditions, the anionic form will be prevalent in the mixture and polymerisation will be exceedingly slow due to ionic repulsion effects. Similarly, in highly acidic conditions the lack of silicic acid anions signifies that there are few, if

any, initiators in the solution, effectively slowing the rate of polymerisation. This effect has been observed in a number of literature studies where the fastest polymerisation rates were observed in the pH range of 6-8.[199,200,204]

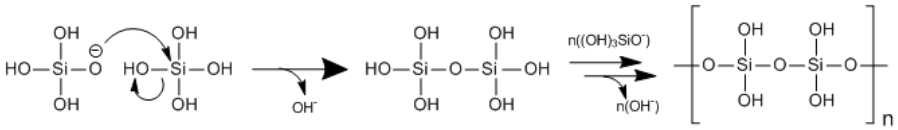

Fig. 4.4 Scheme showing the specific steps in the condensation reaction of silicic acid, leading to the formation of polysilicic acid.

The rapid polymerisation rate near neutral pHs becomes particularly problematic during the acidification of sodium silicate. As the sodium silicate is acidified and reaches neutral pH, the solution will undergo extremely fast gelation. If the solution is maintained at this pH for any significant amount of time, a hydrogel monolith will be formed by the complete gelation of the solution.

Weak acids, such as acetic acid, do not undergo complete dissociation in solution. This means that weak acids will take a relatively large amount of acid and a relatively long time to acidify the silica sol. As such, the sol itself will spend more time at neutral pH values, leading to a high level of polymerisation and resulting in the gelation of the system before sol acidification. On the other hand, strong acids, such as hydrochloric acid, dissociate fully allowing to use comparatively less acid to acidify the sol. This means that less time is spent at neutral pH values, allowing to maintain a low viscosity solution whilst achieving acidification. As such, the use of hydrochloric acid during the present experiment allowed a finer control over both the silicic acid polymerisation and the ensuing aerogels.

In light of the strong pH dependence of the silica sol, the effect of different ratios of hydrochloric acid to sodium silicate in relation to the time taken to reach the gelation point was monitored. The gelation times of solutions containing varying ratios of sodium silicate to hydrochloric acid can be observed in Figure 4.5. It is possible to identify three clear gelation regimes which correlate with the molecular polymerisation of silicic acid; these occur at low, medium, and high hydrochloric acid concentrations.

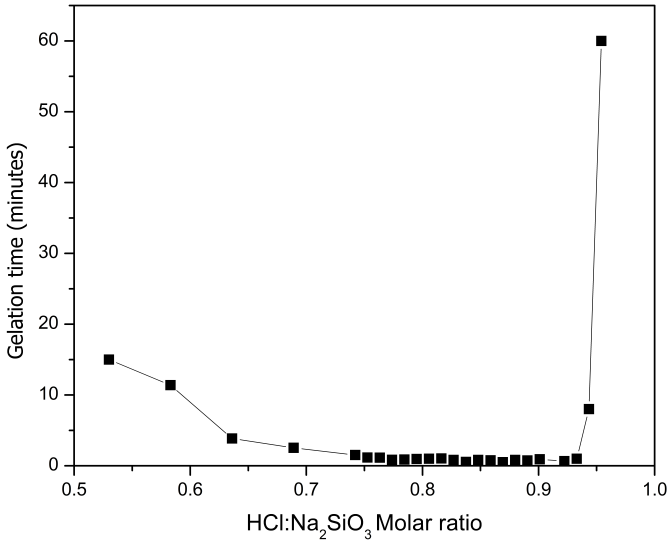

Fig. 4.5 Graph showing effect of changing HCL:Na_2SiO_3molar ratios on the gelation time of silicic acid solutions.

At low hydrochloric acid concentrations (HCl:Na_2SiO_3 = 0.53 - 0.69) the polymerisation proceeds relatively slowly, taking up to 15 minutes to reach the gel point. This slow gelation time can be explained by the overwhelming presence of the anionic silicic acid conjugate base in solution. The anionic molecules in solution will to repel one another leading to a hindering in the growth and formation of colloidal networks. This leads to the observed overall slow gelation times.

As more hydrochloric acid is added, a portion of the anionic conjugate bases of silicic acid become capped by protons. This capping eventually leads to near-equimolar concentrations of silicic acid and its conjugate base. Under these concentrations of hydrochloric acid (HCl:Na_2SiO_3 = 0.74 - 0.92) the polymerisation of silicic acid is at near ideal conditions as ionic repulsions are limited whilst maintaining the presence of the anionic initiator/propagator molecules. This means that polymerisation within the solution will proceed extremely rapidly (with gelation times as low as 30s when using a molar ratio of 0.87).

The proton capping of the studied species continues with further increases in the concentration of hydrochloric acid. Eventually, the capped species largely outnumber the anionic silicic acid molecules. This leads to a decreasing number of initiator molecules in the silica sol which causes an effective quenching of the polymerisation reaction as the initiator species are rapidly consumed by the formation of silicic acid oligomers. The effect of proton capping on silicic acid polymerisation

can clearly be seen in Figure 4.5 when the HCl:Na_2SiO_3 ratio lies in the range of 0.93-0.95.

This strong effect of acidic solutions on the gelation time of silicic acid is particularly important during the synthesis of spherical silica aerogels. Indeed, if the creation of millimetre-sized spherical aerogels is to be achieved, the processes involved in the formation of large scale polymer networks and their macroscopic aggregation need to be understood.

Aerogel Formation and Syneresis

After the initial steps of silicic acid polymerisation from monomers into oligomers, the cross linking of polymer chains and the formation of macroscopic structures occurs. The formation of the gel network has been extensively studied through molecular simulations by Garofalini and Martin.[203] As the polymerisation process proceeds, the formed oligomers undergo cross-linking and form nanometre sized colloidal particles. The formed colloids further undergo aggregation with increasing levels of polymer cross linking, eventually joining into a complete gel network. In order to achieve the synthesis of spherical aerogel granules it is essential to drop the silicic acid sol-gel into the kerosene:ammonia biphasic system prior to complete network formation but only after the generation of the colloids.

Indeed, if the silica sol is dropped too early, then spherical integrity will not be maintained. This will result in the formation of white micro- and nano- sized powders. However, if the sol is allowed to reach complete gelation, a solid hydrogel monolith is created, rendering impossible the liquid dropping process which allows the formation of spherical beads. In this series of experiments, an ideal gelation point was determined to occur at a ratio 0.95 HCl:Na_2SiO_3, 8 minutes after the addition of the acid to the sodium silicate solution. Figure 4.6 shows the surface morphology of aerogel beads synthesised at this gelation point.

In Figure 4.6, the external (A) and internal (B) surface structures of the created aerogel beads can be observed. It is possible to see that the aerogel beads are in fact a 3-dimensional network of interlinked colloidal particles. This particular morphology originates from the polymerisation pathway undertaken by silicic acid, wherein the formation of oligomers is followed by the formation of colloids and finally by colloidal aggregation into a macrostructured network. Inherently, this polymerisation route leads to the formation of highly porous gel networks as the polysilicic acid

networks tend to grow and develop around water clusters[203] which, upon the removal of water, remain accessible for gas adsorption.

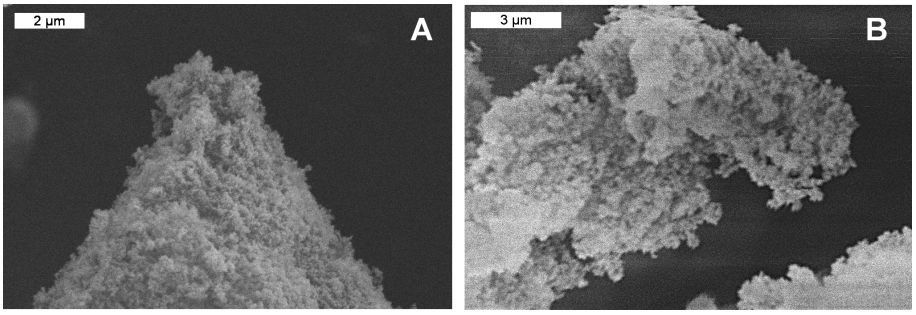

Fig. 4.6 SEM images showing the external (A) and internal (B) surface morphology of the created Silica aerogel granules.

However, by observing Figure 4.6 (B) it is possible to see a number of areas where the colloidal structure of the gel network is highly damaged. This damage arises during the evaporation of the liquid from the pores in the hydrogel during the drying process. Following initial bead formation, the hydrogels are brought to room temperature and allowed to dry under ambient conditions. As the interstitial liquid molecules trapped inside the hydrogel pores are replaced by air, a strong capillary force is exerted by the liquid meniscus onto the gel network. This capillary force, p_c, exerted on the pore walls, can be calculated as shown in Equation (4.1), where γ is the surface tension of the liquid, θ is the contact angle, and r is the pore radius, the negative sign indicates the tension in the liquid.[205] Due to the small radius of the gel pores, the capillary pressure exerted by the meniscus can be very large (>60 MPa)[206] and lead to the collapse of the gel network.

$$p_c = -\frac{2\,\gamma\,cos(\theta)}{r} \tag{4.1}$$

This network collapse caused by the extraction of liquids, also known as syneresis, often leads to the destruction of the highly porous nature of the gel networks, thus negating the most important property of silica aerogels when envisaged for adsorption applications. Initial attempts to dry the created spherical aerogel granules without prior treatment were unsuccessful as they resulted in the complete network collapse. However, by ageing the granules in a solution of TMCS, ethanol, and hexane (1:1:8 molar ratio), it was possible to limit the effects of syneresis. Indeed, it can be seen in Figure 4.7 that the aged silica gels underwent a contraction of only 40% with respect to their

original hydrogel size.

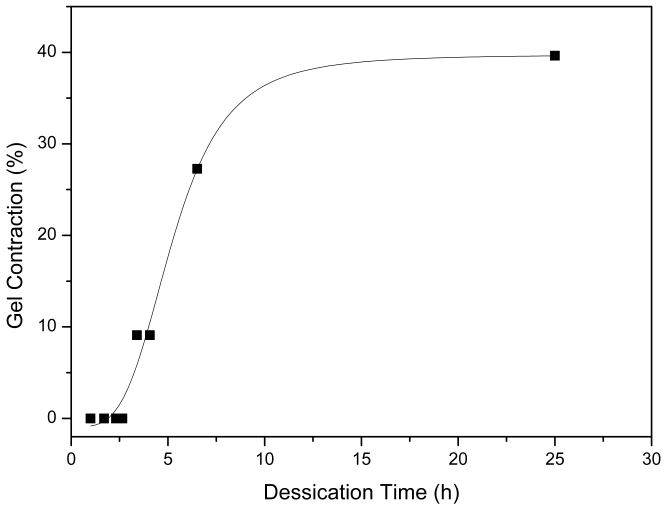

Fig. 4.7 Contraction of aerogel granules aged in a solution of TMCS, ethanol, and hexane, during drying in relation to the as-synthesised hydrogel beads. An indicative line has been plotted through the data points in order to highlight the changes in gel contraction in relation to time.

The solvent mixture limits the effects of syneresis by working on a number of different principles during drying. Firstly, the TMCS acts as a surface modification agent. It is known that the concentration of bridging bonds and the condensation reactions of terminal silanol (Si-OH) moieties in the polymer chain will allow the polymerisation and cross-linking processes to continue for long periods after the initial gel point.[207] As such, when the pore walls are brought together by syneresis, the condensation reactions between terminal groups in the walls will link and effectively close the pore, leading to the contraction of the silica gel. TMCS, when added to the gel will proceed to react with surface silanol moieties as shown in Figure 4.8, leading to a capping of the reactive surface molecules and inhibiting the condensation processes causing gel shrinkage.

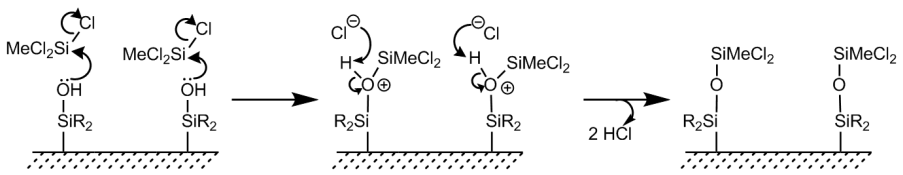

Fig. 4.8 Scheme showing the capping of surface silanol groups by TMCS during the aerogel ageing procedure.

The second process key to the success of the utilised ageing mixture is the hydrophobicity of

the TMCS-capped surfaces. As it is possible to see from Equation (4.1), the collapse of the gel during syneresis is highly dependent on the surface tension of the liquid phase in the pores. As such, it becomes clear that substituting water (γ = 71.99 mN/m at 25°C)[208] with a lower surface tension liquid, such as ethanol (γ = 21.97 mN/m at 25°C),[208] will reduce the Capillary pressure and subsequent pore collapse. However, it was seen that replacing the water with ethanol in an initial ageing phase was insufficient to minimise aerogel collapse. This collapse can be explained by two factors: firstly, it is likely that the internal pores of the material still contained water as they are difficult to access (causing solvent exchange to be slow and inefficient), and secondly, the surface tension of ethanol is likely to be too high for the pores to support.

The introduction of hydrophobic surface groups (TMCS) in the material leads to the ejection of water and ethanol from the internal capillaries of the gel. The presence of hexane supplies a replacement solvent with low surface tension (γ = 17.90 mN/m at 25°C)[208] to fill the capillaries and facilitate the removal of the polar solvents in an enhanced solvent exchange process. As such, by using the TMCS:ethanol:hexane solvent mixture, an efficient and powerful solvent exchange is achieved.

Nonetheless, the created aerogel granules still undergo contraction upon syneresis, as can be seen in Figure 4.7 and Figure 4.9. This contraction can be attributed to the presence of unreachable pores that, non withstanding the ageing treatment, maintain water within them; leading to high capillary pressures and eventual pore collapse. It should also be noted that the TMCS cannot be assumed to be completely efficient in quenching the silanol condensation reactions, leading to an inevitable gel contraction as the polymerisation processes terminate.

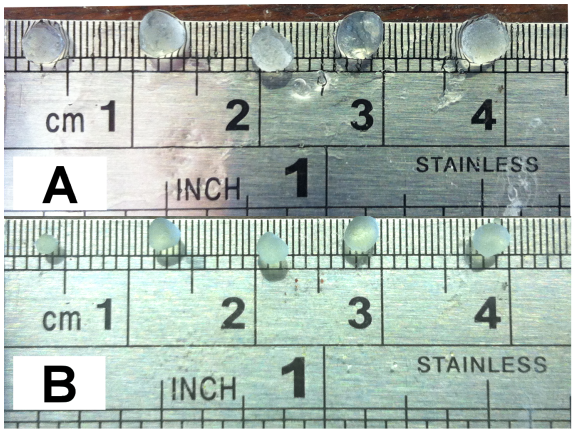

Fig. 4.9 Contraction of the synthesised aerogel granules as-synthesised (A) and after 25 hours of drying (B).

Despite the remaining contraction of the silica gel granules during drying, the beads displayed a density of 0.143 g cm^{-3}, comparable to that prevoiusly reported by Bhagat *et al.* for their synthesised aerogels (0.12–0.16 gcm^{-3}).[209] Furthermore, the opaque appearance of the synthesised granules (as seen in Figure 4.9), although uncommon for standard silica aerogels, coincides with the images reported by Bhagat *et al.*[209] This opacity can be attributed to the inherent light scattering caused by the colloidal microstructure of the synthesised beads (as shown in Figure 4.6).

In 2007, IUPAC defined an aerogel as *"A gel comprised of a microporous solid in which the dispersed phase is a gas"*.[210] As such, by observing the low density of the created surfaces as well as the microporous network observable in Figure 4.6, it is possible to establish the successful creation of an aerogel through the presented procedure. Due to their low density and macroscopic porosity, the created aerogels were deemed suitable candidates for biogas purification through siloxane adsorption procedures.

4.3.2 L2 Adsorption Studies on Enhanced Adsorbents

By monitoring the evolution of L2 concentration over time during the performed adsorption experiments it was possible to compare and contrast the different adsorbents. Further kinetic modelling of the adsorptions allowed to achieve an in-depth understanding of the different materials studied and their interactions with siloxanes.

$$\mathrm{L2}_{\,(g)} + \mathrm{A}_{\mathrm{Surface}} \rightleftharpoons \mathrm{L2\,A}_{\mathrm{surface}} \tag{4.2}$$

The dynamic equilibrium for the adsorption systems can be described as shown in Equation (4.2) where L2 represents the studied siloxane species, A is the studied adsorbent and L2A represents the adsorbed siloxanes. As there are no chemical reactions occurring in the studied systems, the siloxane concentration loss can be described using first order kinetics as shown in Equation (4.3) where $[L_2]_0$ is the initial concentration of L2, $[L_2]_t$ is the concentration at time t and k' is the adsorption rate constant which mathematically describes the overall rate of absorption.

$$[\mathrm{L_2}]_\mathrm{t} = [\mathrm{L_2}]_0\, \mathrm{e}^{-\mathrm{k't}} \tag{4.3}$$

This first order kinetic model was further developed by Ortega and Subrenat when studying the adsorption of siloxanes on porous materials as shown in Equation (4.4) where q_t is the adsorption capacity at time t, q_e is the adsorption capacity at equilibrium and τ is the global adsorption time of the system.[211] This model improves on the basic kinetic one presented in Equation (4.3) by observing the adsorption event directly from the adsorbent's point of view rather than by just monitoring the evolution of adsorbate concentration in the gas phase. This key difference allows to quantify the effects of the equilibrium capacity of the adsorbent on the rate of adsorption by incorporating this value in both the constant and the pre-exponential factors of the first order kinetic model. Thus, a comparison of the k' and τ values of different adsorbent materials allows for a good indication of their relative siloxane adsorption affinities.

$$q_t = (1 - e^{-\frac{t}{\tau}})q_e \tag{4.4}$$

A better insight into the initial adsorption events can be gained by using the mathematical model proposed by Baudau in 1990 based on the Bohart-Adams-Thomas adsorption model.[133] Baudu's kinetic model was successfully adapted in 2009 by Ortega and Subrenat for the adsorption of siloxanes onto industrial materials.[211] This adapted model can be expressed as shown in Equation (4.5) where m is the mass of the adsorbent, V is the volume of the adsorption vessel, C_0 is the initial siloxane concentration, C_t is the concentration at time t, and γ is the initial adsorption velocity.

$$\gamma = -\left(\frac{V}{m}\right)\frac{1}{C_0}\left(\frac{dC_t}{dt}\right)_{t=0} \tag{4.5}$$

By comparing the k', q_e, τ, and γ values for the different materials studied during the adsorption of L2, it is possible to achieve a better understanding of the interaction between L2 and the individual adsorbents.

Siloxane Adsorption on Silica Aerogel

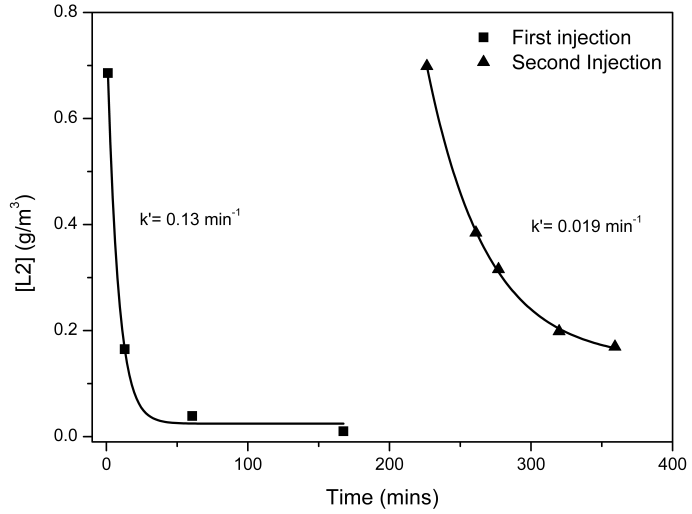

Fig. 4.10 Evolution of L2 concentration and adsorption constants over two subsequent siloxane injections in relation to time. The synthesised aerogel granules were used as adsorbent species.

Figure 4.10 shows the evolution of L2 concentration for two subsequent injections in the studied systems whilst using the synthesised aerogel granules as adsorbents. It can be seen from the k' values reported that the adsorption rate for the system was significantly decreased after the first injection of L2. The kinetic data for the two injections are shown in Table 4.1.

Table 4.1 Kinetic data for the adsorption of L2 onto silica aerogel granules over two consecutive injections.

Injection	k' (min^{-1})	γ 10^3 ($m^3 g^{-1} min^{-1}$)	τ (min)	q_e (mg_{L2} $g^{-1}_{aerogel}$)
1 st	0.131 ± 0.014	29.6 ± 0.25	7.89 ± 0.79	0.320
2 nd	0.0190 ± 0.009	6.00 ± 0.05	42.1 ± 1.60	0.248

The reported 85 % decrease in adsorption rate between the two injections can be attributed to a filling of the absorption sites in the aerogel. Initially, all of the adsorption sites on the gel are available for the L2. As these become occupied during the first adsorption, only the less accessible sites remain, meaning that it takes longer for the gaseous L2 to reach and adsorb onto these sites. This effect can be seen not only by the decrease in k' but also by the γ values which show a 79 % drop in initial adsorption velocity between subsequent injections. This indicates that the easily accessible adsorption sites are those preferentially occupied by L2. However, the adsorption

capacity at equilibrium after the second injection is only 23 % smaller than that of the first injection. The discrepancy in the large drops in γ and k' values with respect to the moderate drop in q_e can be explained by adsorption site accessibility.

As discussed in Section 4.3.1, the synthesis process leading to aerogel formation creates a large number of internal pores in the material. In order for a gas such as L2 to adsorb onto the internal pores of the aerogel, the gas needs to diffuse into the material. This means that the process of reaching and occupying these less accessible adsorption sites will be dominated by the slow diffusion of the gas through the material. As such, even though the adsorption process after the second siloxane injection is much slower (displaying decreased k' and γ values whilst having an increased τ value), the large presence of internal pores in the aerogel still allows for a significant siloxane intake beyond the occupation of the most accessible outer surface adsorption sites.

Through extended repeated injections it was possible to establish the total siloxane adsorption capacity of the material, q_max. This was determined by calculating the siloxane loading on the material after reaching a point where no further L2 concentration drop was observed in the system even after extended periods of time and further siloxane injections. The q_max of the synthesised aerogel was calculated to be 7.50 mg_{L2} $g^{-1}_{aerogel}$. This total capacity is lower than that previously reported in literature for activated carbon adsorbents which are known to possess L2 adsorption capacities of up to 100 mg g^{-1}.[16]

The large difference in siloxane adsorptive abilities between the two species can be attributed to their differing physical properties. Indeed, it is believed that the surface modification of the aerogel as performed in Section 4.2.2 could adversely affect its adsorption properties. However, as the surface modification is a crucial element in the synthesis of silica aerogel granules, it was impossible to examine the direct effects of the surface modification by using the aerogel granules. As such, commercial silica gel was used as an alternative model system to study the effects of surface modification on siloxane adsorption.

Siloxane Adsorption on Commercial Silica Gel

The adsorption of L2 by surface treated silica gel beads in relation to that of untreated silica gel can be seen in Figure 4.11. From this graph it is readily apparent that the application of a surface

treatment onto commercial silica gel has an important effect on the adsorption properties of the materials.

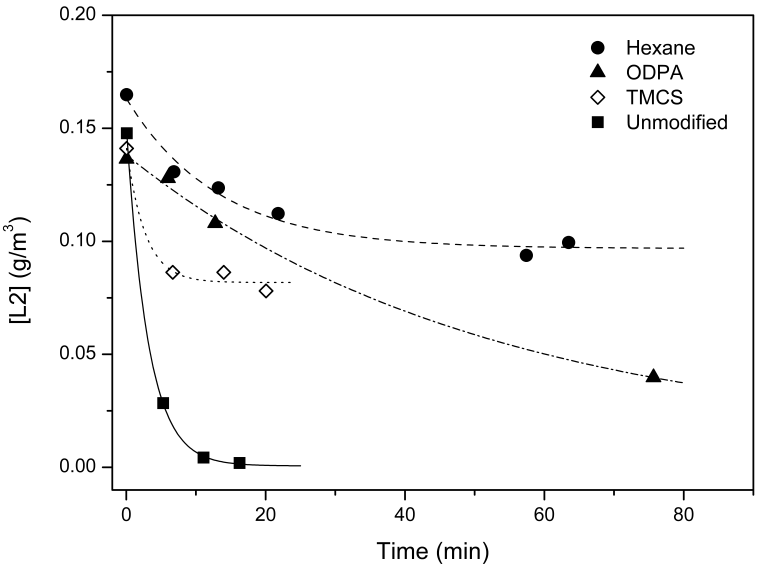

Fig. 4.11 Evolution of L2 concentration over time in silica gel samples with varying surface treatments.

A more in-depth understanding of the effects of silica gel surface treatment techniques can be gained from Table 4.2. By comparing the q_max of the studied species it is readily apparent that surface treatments, irrespective of their nature, will lead to a loss in adsorption properties. Indeed, untreated silica gel displays a q_{max} of 140 mg g^{-1} whereas the q_{max} of the modified gels are around one third of this value. This drop in q_{max} can be explained by the occupation of adsorption sites by the surface modifying agents which limits the L2 adsorption onto the material.

The effect of site blockage is readily apparent from the hexane wash which causes a 58 % reduction in q_{max}. During a hexane wash the surface of the silica gel remains chemically unmodified, meaning that the observed decrease in adsorption capacity and k' values arise from the blockage of adsorption sites by the hexane. However, it is important to note that washing the silica gel with hexane resulted in a large increase in initial adsorption velocity ($\gamma = 226 \times 10^3$ m^{3}g^{-1}min^{-1} for hexane washed samples, and $\gamma = 95.9 \times 10^3$ m^{3}g^{-1}min^{-1} for unmodified samples). This increase can be attributed to a cleaning effect exhibited on the adsorption sites by the solvent wash. The unmodified silica gel was used as received, it is thus possible that a number of dry contaminants are present on the surface of the gel. As the gel is washed in hexane, the contaminants

are removed, allowing the adsorption sites to become larger and more accessible, leading to a large increase in initial adsorption rate. As such, it is possible to establish that the hexane wash had the dual effect of clogging of a large number of the material's adsorption sites whilst also removing surface contaminants, as seen by the reduced q_{max} and increased γ values.

Table 4.2 Kinetic data for the adsorption of L2 onto silica gel with varying surface modifications.

Surface treatment	k' (min^{-1})	$\gamma \ 10^3$ ($m^3g^{-1}min^{-1}$)	τ (min)	q_{max} ($mg_{L2} \ g^{-1}_{sample}$)
Untreated	0.321 ± 0.008	95.9 ± 0.7	3.12 ± 0.08	140
Hexane wash	0.132 ± 0.026	226 ± 2	13.1 ± 2.6	58.6
ODPA	0.0158 ± 0.005	30.8 ± 0.2	48.9 ± 15.0	43.8
TMCS	0.024 ± 0.009	168 ± 1	2.68 ± 1.00	45.6

The minimal effect on the nature of the surface coating on the q_{max} of the materials can be seen as the drop in q_{max} with respect to the untreated beads is similar for both the ODPA and the TMCS surface treatments. The slightly higher capacity shown by the the hexane washed samples can be explained by the fact that the hexane, on the contrary to the two other surface treating agents, was not chemically bound to the silica gel. This means that during the drying procedure, less hexane was retained by the silica gel. The similar q_{max} for the TMCS and ODPA surface modified samples indicate that the two procedures have an equal effect in adsorption site occupation, meaning that the observed differences in kinetic adsorption properties are solely due to the chemical interaction between the L2 and the silica surface coatings.

Indeed, by comparing their different adsorption kinetics the effects of the different surface modification agents can be studied. The TMCS modified silica gel beads displayed significantly higher adsorption constant (k'=0.024 min^{-1}) and initial adsorption rate ($\gamma = 168 \times 10^3$ $m^3g^{-1}min^{-1}$) values with respect to the ODPA modified structures (k'=0.016 min^{-1}, $\gamma = 30.8 \times 10^3 m^3g^{-1}min^{-1}$). This can be attributed to a greater van der Waals bonding affinity between TMCS and L2 as compared to that between ODPA and L2.

Figure 4.12 shows the functional groups on the surface of the silica gel after TMCS and ODPA modification. It becomes readily apparent that the $Si-Me_3$ functional groups resulting from the TMCS modification are significantly more polar than the large C chains applied by the ODPA modification. As such, the relatively polar L2 molecule will preferentially form van der Waals bonds with the TMCS modified surface, leading to faster adsorptions. This is clearly represented

not only by the higher k' and γ values of the TMCS modified systems with respect to the ODPA modified ones but also by the lower global adsorption times ($\tau = 2.68$ min and $\tau = 48.9$ min for the TMCS and ODPA samples, respectively).

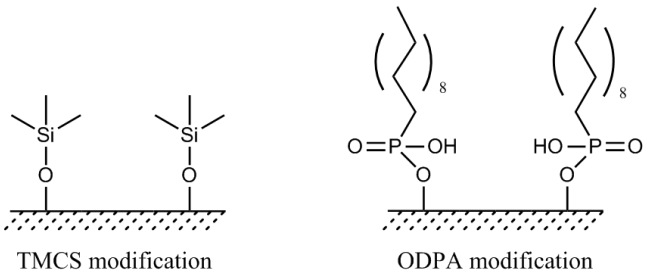

Fig. 4.12 Silica gel surface functional groups after TMCS and ODPA modification.

The surface modification of silica gel can thus be seen as having an important effect on both the kinetics and adsorption capacities of silica gels. As surface modification is a necessary process in the formation of silica aerogels at ambient pressure (as discussed in Section 4.3.1), this casts doubts on the applications of silica aerogels as adsorption agents for biogas purification.

However, the silica aerogel limitations arise from the loss of adsorption sites caused by surface treatment procedures. As such, the use of alternative high surface area nanoarchitectures would allow to maintain the advantages of nanostructures whist acting as viable adsorbents for biogas purification. Nanofibres are an ideal candidate as they are high surface are architectures whose synthesis does not require the application of a surface treatment.

Siloxane Adsorption on Semiconductor Nanofibres

Figure 4.13 shows the adsorption of L2 onto both SiO_2 and TiO_2 nanofibres. A strong distinction between the different nanofibres is readily apparent, with TiO_2 nanofibres displaying faster L2 adsorption rates.

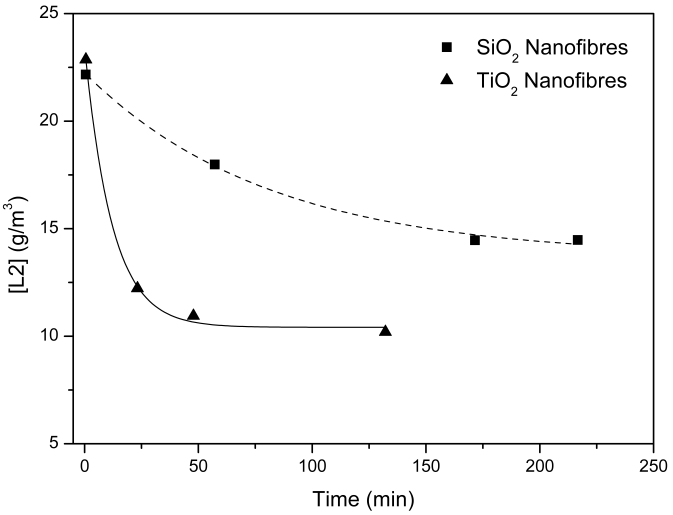

Fig. 4.13 Evolution of L2 concentration over time in SiO_2 and TiO_2 nanofibres.

The kinetic data for the adsorption of L2 onto the semiconductor nanofibres are shown in Table 4.3. The TiO_2 nanofibres can be seen to display both a higher adsorption kinetic constant (k'= 0.083 min^{-1}) and initial rate of adsorption ($\gamma = 15.4 \times 10^3$ $m^3g^{-1}min^{-1}$) with respect to the SiO_2 nanofibres (k'= 0.0124 min^{-1} and $\gamma = 8.91 \times 10^3$ $m^3g^{-1}min^{-1}$). These improved adsorption kinetics can be further seen by comparing the global adsorption times. The τ value for the TiO_2 nanofibres (12.0 min) is less than half that of the SiO_2 nanofibres (25.6 min), showing the overall difference in adsorption speed between the two semiconductor nanofibres.

Table 4.3 Kinetic data for the adsorption of L2 onto TiO_2 and SiO_2 nanofibres.

Adsorbent	k' (min^{-1})	γ 10^3 ($m^3g^{-1}min^{-1}$)	τ (min)	q_{max} (mg_{L2} g^{-1}_{sample})
SiO_2 Nanofibres	0.0124 ± 0.0002	8.91 ± 0.07	25.6 ± 2.3	17.0
TiO_2 Nanofibres	0.0830 ± 0.011	15.4 ± 0.1	12.0 ± 0.8	16.3

The superior adsorption properties of the TiO_2 nanofibres can be attributed to the difference in surface structure between the different fibres. The SEM images presented in Figure 4.14 allow to see clearly that the TiO_2 nanofibres possess a much rougher surface when compared to SiO_2 nanofibres. This difference in surface morphology arises from the chemical processes underlying the nanofibre synthesis which are discussed extensively in Chapter 3 and cause the TiO_2 nanofibres

to display a larger quantity of adsorption sites when compared to SiO_2 nanofibres. These adsorption sites will then lead to the faster adsorption of L2, as can be seen by the higher k' and γ values as well as the lower τ value.

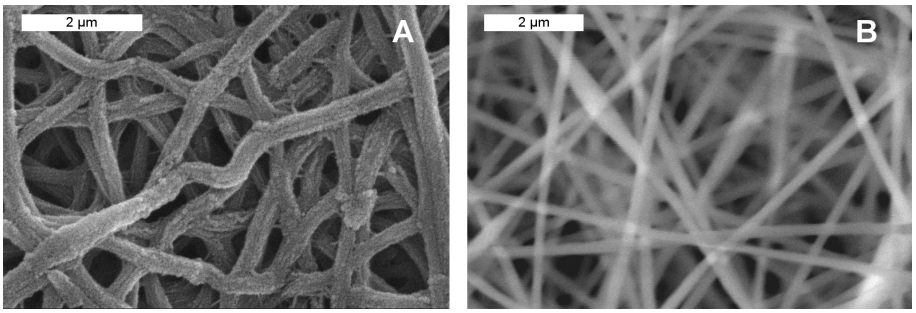

Fig. 4.14 SEM images showing the surface morphology of TiO_2 (A) and SiO_2 (B) nanofibres. The difference in surface roughness between the two semiconductors can be clearly seen.

It is important to note that even though the TiO_2 nanofibres display superior adsorption kinetics, the SiO_2 nanofibres display a marginally enhanced q_{max}. This enhanced q_{max} arises from the preferential formation of van der Waals forces between the L2 molecules and the SiO_2 nanofibres due to the presence of the surface $Si-O-Si$ groups on the nanofibres. As the TiO_2 nanofibres form weaker bonds, they will be able to retain slightly less L2 adsorbate molecules and consequently have a lower q_{max}.

Overall, both of the studied nanofibre samples display better q_{max} than the synthesised silica aerogel granules. However, the nanofibre q_{max} still fall largely short of those displayed by industrial adsorbents (with activated carbon displaying L2 adsorption capacities of up to 100 mg g^{-1}).[16] Nonetheless, only with a precise comparison between the adsorption of industrial standard adsorbents and that of the synthesised samples, is it possible to fully understand the differences between the systems and gauge the industrial viability of the created nanostructures.

Comparison of Industrial, Commercial, and Synthesised Adsorbents

In 2008 John Hayward and Pptek Ltd patented a siloxane removal system based on the use of ion-exchange polyamide resins.[9] Although the resins used by Pptek Ltd have a poor temperature stability (decomposition of the resins is observed above 160°C)[100] they have nonetheless become the industrial standard for siloxane purification with PpTek Ltd becoming the market leader in biogas filtration systems. As such, the adsorption media used by PpTek Ltd was the industrial

adsorbent used to evaluate the effectiveness of the synthesised adsorbents.

Table 4.4 shows the adsorption kinetics for the PpTek polyamide media in comparison to the other adsorbent media synthesised. A clear difference can be seen between the commercially designed adsorption media (PpTek resin and unmodified silica gel) and the synthesised nanostructures.

Table 4.4 Comparison of the L2 kinetic adsorption data of the synthesised adsorbents and PpTek's ion exchange resin.

Adsorbent	k' (min^{-1})	$\gamma\ 10^3$ ($m^3g^{-1}min^{-1}$)	τ (min)	q_{max} ($mg_{L2}\ g^{-1}_{sample}$)
PpTek media	0.245 ± 0.032	1441 ± 0.7	4.08 ± 0.24	108
Silica gel	0.321 ± 0.008	95.9 ± 0.7	3.12 ± 0.08	140
SiO_2 Nanofibres	0.0124 ± 0.0002	8.91 ± 0.07	25.6 ± 2.3	17.0
TiO_2 Nanofibres	0.0830 ± 0.011	15.4 ± 0.1	12.0 ± 0.8	16.3
Silica Aerogel	0.131 ± 0.014	29.6 ± 0.25	7.89 ± 0.79	7.50

The synthesised nanostructures display vastly slower adsorption kinetics compared to the two commercial adsorbents, showing differences in k' ranging from 91% for the SiO_2 nanofibres to 37% for the SiO_2 aerogels, with respect to the PpTek commercial standard. This arises from a larger total surface area as well as an improved vacancy of surface pores in the commercial adsorbents with respect to their synthesised counterparts. The difference between the suitability of the two sets of samples is further emphasised by the lower global times of adsorption, higher adsorption capacities and higher initial reaction rates of the commercial samples. From the kinetic data it becomes readily apparent that the nanostructured samples, as synthesised, require further development before becoming commercially viable L2 adsorbents. However, the supplied kinetic data pertains to the adsorption of L2 and might not be representative of the general siloxane adsorption capacity of the materials. This was shown by Nam *et al.* who established the inadequacy of L2 adsorption by non-carbonaceous materials with well-defined meso- and macro- pores but determined that such compounds could display greater adsorption affinity with larger and heavier siloxanes.[198]

Important information can nonetheless be gathered by comparing the kinetic data of the nanofibrous samples with the aerogel granules. Although the different synthesised samples possess similar k' values, the differences in γ, τ, and q_{max} are informative on the effects of different morphologies. The aerogel granules display faster initial adsoprtion and lower global adsorption times with respect to the nanofibrous structures due to the highly porous nature of the aerogels. Even if the corrugated surface of the TiO_2 nanofibres increases the surface area of the material, this

is still smaller than the highly porous system generated by the colloidal polymerisation process underlying the formation of the aerogels (as discussed in Section 4.3.1). As such, the aerogel granules display better initial L2 adsorption properties. However, the aerogel granules display a very low q_{max} when compared to the nanofibrous structures caused the surface treatment of the aerogel which occupies the pores in the material, inhibiting its maximum L2 loading.

The comparison of the adsorption kinetic data also allows a further understanding of the commercial adsorbents. The initial adsorption speed displayed by the PpTek media ($\gamma = 1441 \times 10^3$ $m^3 g^{-1}$ min^{-1}) is significantly larger than that of the studied samples, indicating a large initial availability of L2 adsorption sites on the material. This property is of particular importance for the treatment of biogas as it signifies that the material can be used as a filtration agent even with the large gas flows required by industrial conditions. As such, even though the silica gel has a higher q_{max}, the Pptek media remains the more interesting adsorbent for the removal of L2 from biogas.

Furthermore, it is crucial to remember that in an industrial environment it is not simply sufficient for a material to have good adsorption properties. Indeed, it is possible to see that the silica gel displays better k', τ and q_{max} values with respect to the Pptek media. However, the increased L2 intake of the silica gel comes at the price of a stronger bonding between the L2 and the adsorbent, meaning that a much higher energy input will be required to regenerate the silica gel with respect to the Pptek media. As such, it becomes readily apparent that an ideal adsorbent for the industrial removal of siloxanes will achieve a balance between good adsorption properties and energetically inexpensive desorption techniques.

4.4 Conclusions

During this study it was possible to establish a facile, ambient pressure procedure for the formation of SiO_2 aerogel granules. The effects of gel syneresis were countered by the surface modification of the gels which reinforced the polymer networks. This surface modification technique, however, was insufficient in the complete prevention of syneresis as the created SiO_2 aerogel granules still exhibited a 40% reduction in volume. Nonetheless, SEM characterisation and density measurements allowed to establish the formation of a highly porous material with a density of 0.143 gcm^{-3}.

Through L2 adsorption experiments it was established that the synthesised aerogel granules

displayed an adsorption capacity of 7.5 $mg_{L2}\ g^{-1}_{aerogel}$. The low adsorption capacity of the aerogel was attributed to the effects of surface treatment agents which blocked the material's pores. This was demonstrated by investigating the adsorption properties of surface modified silica gels.

Irrespective of the nature of the surface treatment, the modified silica gel samples displayed a drop in adsorption capacity of about 65% arising from the occupation of the gel's adsorption sites by the surface modification agents. The adsorption studies further highlighted the importance of the nature of surface modification agents with respect to the adsorbate species. Indeed, the silica gel samples modified with the polar TMCS displayed an initial adsorption rate 81% higher than that displayed by the gels modified with the nonpolar ODPA.

Further adsorption studies on synthesised TiO_2 and SiO_2 nanofibres showed that the nanofibrous samples displayed better adsorption capacities than the synthesised aerogel. Nonetheless, the aerogel samples demonstrated a better affinity with the adsorbate, displaying initial adsorption capacities two-fold larger than those of the nanofibres. These differences between the two types of nanostructures revealed that siloxane adsorbents need to display not only a high adsorption capacity but also a high affinity to the siloxanes in order to remove siloxanes from gases phase in a time-efficient manner.

This importance of adsorbents with fast adsorption kinetics and good adsorption capacities was highlighted with the adsorption studies on performed the PpTek ion exchange resin. The Pptek media displayed a high adsorption capacity (108 $mg_{L2}\ g^{-1}_{media}$) and an initial adsorption rate 50 times larger than that of the synthesised silica aerogel. As such, the PpTek media not only allows for the removal of a large quantity of siloxanes, but also allows this removal to occur very rapidly.

In conclusion, although a number of nanostructures were synthesised and studied as adsorbents, a lot of work remains to be carried out before these structures can be used as novel adsorption agents for the industrial removal of siloxanes from biogas. This is clear as the synthesised structures not only displayed vastly inferior adsorption kinetics with respect to the industrial standard, but also had significantly smaller adsorption capacities.

Nonetheless, although the synthesised materials might not be competitive in the removal of siloxanes from biogas through adsorption, the photochemical properties of the TiO_2 nanofibres render these materials significantly more important for industrial applications.

5. Static Photodegradation of Siloxanes

The use of semiconductor nanomaterials for the photocatalytic removal of siloxanes from biogas displays high potential for the creation of a novel family of biogas purification devices. The prospects and advantages for the photocatalytic purification of biogas have been presented extensively in Chapter 1. However, only very academic few studies have been performed in order to characterise the siloxane photodecomposition abilities of TiO_2 nanostructures.[14,126,212] During the following series of experiments the photocatalytic activity of TiO_2 nanofibres was thoroughly studied and kinetically modelled. Particular importance was given to the effects of siloxane photodecomposition on the photocatalyst and the lifetime of the catalysts.

Further studies were carried out in order to improve the photocatalytic activity of TiO_2 nanofibres through the synthesis of WO_3 doped TiO_2 nanofibres. These doped nanofibres were successfully characterised and their photocatalytic abilities for the decomposition of hexamethyldisiloxane (L2) were investigated in static reaction conditions.

From the photodecomposition properties of the pure and WO_3 doped TiO_2 nanofibres it was possible to gain an understanding of the effects of doping on siloxane photodecomposition. Furthermore, the efficiency of the porous TiO_2 nanofibres synthesised in Chapter 4 as well as that of P25, an economical alternative to nanofibres, were also investigated by studying their L2 photodecomposition properties. By comparing the decomposition properties of these materials it was possible to establish an ideal photocatalyst for the decomposition of siloxanes in biogas as well as gain a stronger understanding of the principles underlying the studied reactions.

5.1 Introduction

Although the use of TiO_2 as a photocatalyst for gas purification has been known for many years in both academic[69,123,213] and industrial[47,214,215] environments, only a few studies[14,126,212] have been performed investigating the gas phase photodecomposition of siloxanes by TiO_2. In previous siloxane photodecomposition studies, research has focused on understanding the siloxane photodecomposition pathway and products[126] as well as the catalyst lifetimes[14] and limitations.[212] As a consequence of this focus, the study of the effects of photocatalyst morphology on the photodecomposition abilities as well as the kinetics of siloxane photodecomposition remain to be investigated.

During this series of experiments, TiO_2 nanofibres were enhanced through the introduction of WO_3 impurities. It is known that semiconductor mediated photocatalysis hinges on the generation of highly reactive hydroxide species through the use of photoexcited electrons.[65,175] As such, it is possible to increase the photocatalytic efficiency of studied semiconductors electronically through two different means: an increase in excited electron population and an increase in electron lifetime. Both of these processes increase the photocatalytic activity of the doped semiconductors by causing an increase in the population of photoexcited electrons. The introduction of a large variety of low concentration ($\sim$ 1 mol%) impurities in the studied semiconductor species has been known to improve TiO_2 photocatalytic efficiency through both processes.[216–219] Of the different metal oxide dopants known to improve the photocatalytic degradation properties of TiO_2, WO_3 presents a significant number of advantages. Primarily, WO_3 is a low cost,[220] non-toxic,[221] semiconductor which has been used successfully as a TiO_2 doping agent in a large number of studies.[222–224] As such, WO_3 was chosen as a doping agent for TiO_2 nanofibres in this project due to both its chemical properties and low cost which make it appealing at both an industrial and academic level.

Nonetheless, it is important to note that in order to achieve an appropriate understanding of the effects of WO_3 doping on TiO_2 nanofibres, a precise understanding of the decomposition's kinetics must be achieved. During these experiments, it was possible to gain a more comprehensive understanding of the photocatalytic degradation of siloxanes by investigating the decomposition of L2 over TiO_2 nanofibres in a static environment. From this, it was possible to gain an appreciable understanding of the effects of electronic and morphological differences between nanostructures. This was achieved by comparing the kinetic decomposition data for the pure TiO_2 nanofibres, the

WO_3 doped TiO_2 nanofibres, and porous TiO_2 nanofibres to P25. Consequently, it was possible to establish the relative viability of each of the studied structures as photodecomposition agents for the purification of biogas.

5.2 Experimental

5.2.1 Chemicals and Characterisation Techniques

All chemicals used during the following experiments were sourced from Sigma-Aldrich UK and used as received unless otherwise stated.

The characterisation of the morphology and structure of the synthesised TiO_2 nanofibres is described in Chapter 3. The doped TiO_2 nanofibres were characterised through Scanning Electron Microscopy (SEM), using a JEOL-JSM 820 Scanning Microscope. The crystal structures of the semiconductor nanofibres were analysed using powder X-Ray Diffraction (XRD) with a Siemens Powder X-500 diffractometer using a Cu source at a wavelength of 1.54 Å.

The band gap of the WO_3 doped TiO_2 nanofibres was determined by using an integrating sphere (Ocean Optics ISP-REF) equipped with an inbuilt tungsten-halogen illumination source (300 nm $\leq \lambda \leq$ 1000 nm) and an ASEQ LR1 UV-Vis detector in order to gain the UV-Vis diffuse reflectance spectra of the studied samples. Through the use of the Tauc relation it was then possible to determine the band gap of the studied materials from their reflectance spectra.

The evolution of L2 concentration during the decomposition experiments in Section 5.2.3 was carried out by calibrating and monitoring the area under the L2 peak in the spectra generated by a Gas Chromatograph (GC) equipped with a Flame Ionisation Detector (FID). The GC-FID used during the experiments was a Perkin Elmer autosystem equipped with a 50 m wax capillary column. During the duration of the experiments the gas flow rate was kept at 1.5 ml min^{-1}, the oven and injection temperatures were maintained at 60°C. H_2 was used as the carrier gas and supplied using a SP300HC hydrogen generator. Under these conditions, the L2 retention time was observed to be 150 s.

5.2.2 Synthesis of Electrospun WO_3 Doped TiO_2 Nanofibres

The general procedures for the synthesis and morphological characterisation of nanofibres through electrospinning are presented in Chapter 3

WO_3 doped TiO_2 nanofibres were synthesised by preparing a TiO_2 nanofibre precursor solution of polymethylmethacrylate (PMMA, $\overline{M_W}$ 996 000, 8 wt%), titanium tetraisopropoxide (TT^iP, 9 wt%), acetylacetone (1 wt%) and dimethylformamide (DMF, 82 wt%). The solution was then doped by adding mechanically ground WO_3 powder (concentrations of 0 – 17.9 mol% of W with respect to Ti were investigated) and electrospun as discussed in Chapter 3. The solution was fed through a stainless steel needle at a rate of 2.0 mlh^{-1} (controlled using a protégé 3010 syringe pump). A voltage (18 kV) was applied to the stainless steel needle allowing for the creation of charged nanofibres. These nanofibres were collected on a grounded drum at a distance of 15 cm from the needle tip. The as-collected nanofibre mats were steam treated (80°C, 3 h) and calcined (550°C, 3 h) in order to yield WO_3 doped TiO_2 nanofibres.

The decomposition properties of the doped TiO_2 nanofibres were characterised as outlined in Section 5.2.3.

5.2.3 Siloxane Photodegradation in Static Systems

Four different photocatalysts were investigated for the removal of siloxanes during this experiment: P25, porous TiO_2 nanofibres, pure TiO_2 nanofibres, and WO_3 doped TiO_2 nanofibres with doping concentrations of 0.5, 1, 2, 3 and 17.9 mol%. The porous and pure TiO_2 nanofibres were prepared as detailed in Chapter 3.

In order to verify the photocatalytic properties of chosen nanomaterials, a simple static gas reactor was used. L2 (0.2 ml) was inserted into a round bottomed flask of known volume (115 cm^3) which was placed in a graphite bath at 130°C. The siloxane was then allowed to fully vaporise.

After this, the gaseous L2 in air (10 ml) was removed from the round bottomed flask using a syringe (BD Plasipack, 20 ml) and injected into a gas tight ampoule containing a known mass of a chosen photocatalyst. The glass ampoule was then placed in a UV chamber (Spectrolinker XL-1500 UV crosslinker) and the L2 concentration inside the ampoule was monitored through

GC-FID sampling. When the L2 concentration in the ampoule was seen to have stabilised, the UV lights (UV_a, with a spectral peak at 365 nm) were turned on. The change in L2 concentration in the system was monitored using GC-FID until it was observed to reach a new equilibrium. Figure 5.1 shows the standard experimental set up for the static photodecomposition of L2.

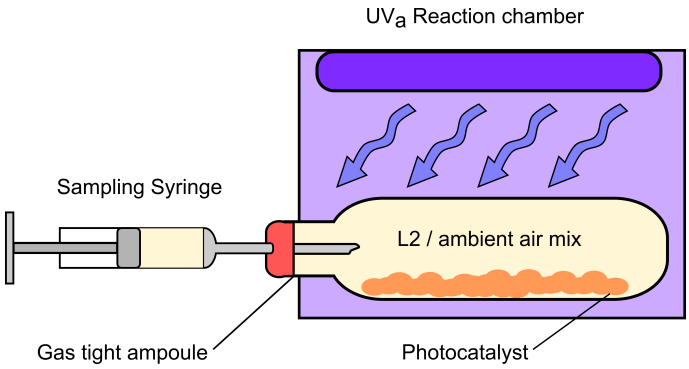

Fig. 5.1 Diagram showing the experimental set up for static gas phase L2 photodecomposition reactions. The samples taken were immediately analysed through GC-FID.

In order to study the lifetime, extended kinetics, and potential SiO_x loading on the TiO_2 catalyst, further experiments were performed. Following the observation of loss of reactivity in the system, a further injection of gaseous L2 in air (10 ml) was carried out in the airtight vial. The L2/air mixture was generated by using the procedure described above. A bleed needle was applied to the ampoule during injection in order to negate increased pressure effects on the studied photocatalysts and maintain a stable adsorption. Following the injection, the concentration of L2 within the system was monitored. Upon stabilisation, the UV lights in the photoreaction chamber were turned on and the L2 concentration was recorded until further stabilisation occurred. L2/air injections were repeated until no further L2 decomposition was observed upon illumination with UV light.

A further set of experiments focusing on the regeneration potential of the TiO_2 nanofibres were subsequently carried out. Following the photodecomposition experiments, when the L2 concentration was seen to remain stable even under UV illumination, the ampoule was removed from the UV chamber and placed in a graphite bath. The graphite bath was heated to 30°C and variations in L2 concentration were recorded though GC-FID. Once the L2 concentration was seen to be stable, the procedure was repeated for graphite baths at 60 and 80°C.

5.3 Results and Discussion

By studying the created nanostructures and investigating their photocatalytic abilities, it was possible to determine their suitability as industrial biogas purification agents.

5.3.1 WO_3 Doped TiO_2 Nanofibre Characterisation

Through SEM and XRD characterisation it was possible to determine that the introduction of doping agents had negligible effects on the standard TiO_2 nanofibre structures presented in Chapter 3. This can be seen by observing Figure 5.2 where the TiO_2 nanofibres doped with 17.9 mol% WO_3 display indistinguishable morphological structures when compared to pristine TiO_2 nanofibres. Indeed, it can be seen in Figure 5.2 that the surface of the doped nanofibres (A) displays the same ridged structure as that of the undoped nanofibres (B), indicating that in both systems the TiO_2 growth occurred inhomogeneously across the fibres such that the removal of the supporting polymer causes the formation of these ridges. Additionally, the WO_3 doping can also be seen to have had no effect on the fibre thickness as it is possible to see in Figure 5.2 (A) and (B) that the observed fibres display a similar thickness distribution.

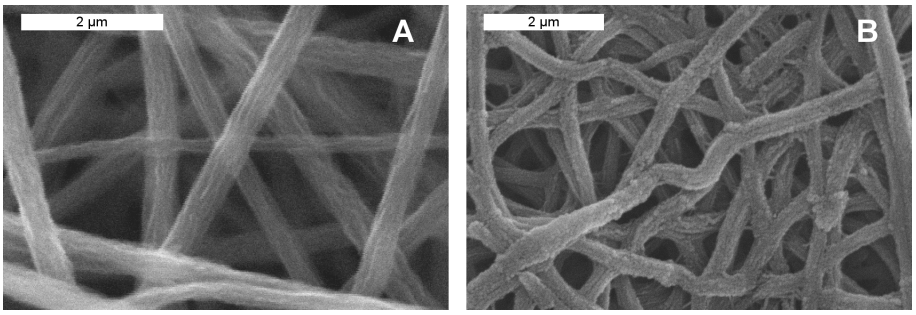

Fig. 5.2 SEM images of 17.9 mol% WO_3 doped TiO_2 nanofibres (A) and pure TiO_2 nanofibres (B). It can be seen that the doped nanofibres appear structurally indistinguishable from the pure TiO_2 samples.

By observing the XRD spectra in Figure 5.3 it can be seen that the WO_3 doped nanofibres do not present any WO_3 diffraction peaks as well as any rutile TiO_2 diffraction peaks (seen as the missing peaks when comparing the doped TiO_2 nanofibre spectrum to the pure TiO_2 nanofibre spectrum). It becomes clear that although the WO_3 doping did not display any diffraction peaks, it favoured the formation of the anatase TiO_2 crystal phase and hindered the formation of the rutile TiO_2 crystal

phase. This prevalence of the anatase phase arises from its relative stability low crystallite sizes, as discussed in Chapter 3. Indeed, the addition of WO_3 would supply further nucleation sites for the initial growth of TiO_2 and thus favour the formation of many small crystallites rather than fewer large crystals. This disruptive effect of the doping on the TiO_2 crystal structure can be further seen by the broader anatase peaks of the doped nanofibres indicating a loss in crystallinity caused by the WO_3 doping.

The 17.9 mol% WO_3 doped nanofibres were used to study the structural effects of doping as, having the highest dopant concentration, they were the most likely to show morphological and crystallographic alterations. As the doping was observed to have negligible effect on the structure of the nanofibres, any observed variations in siloxane photodecomposition properties between the doped nanofibres and standard TiO_2 nanofibres could be attributed to electronic doping effects.

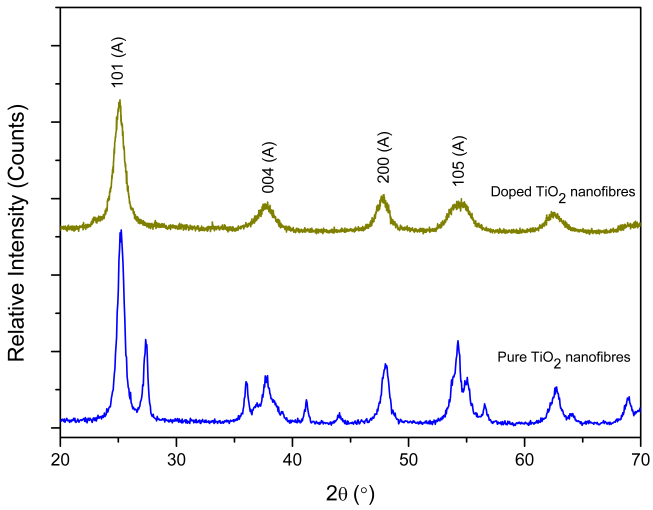

Fig. 5.3 XRD patterns of pure TiO_2 nanofibres (below) and 17.9 mol% WO_3 doped TiO_2 nanofibres (above). The peaks labelled show the strong presence of the TiO_2 anatase (A) crystal phase in both of the studied samples. The absence of the rutile TiO_2 crystal phase in the doped sample can be clearly observed from the missing TiO_2 peaks in the WO_3 doped TiO_2 nanofibre sample when compared to the pure TiO_2 sample. Peak assignment was carried out by correlation with the ICDD database (file # 21-1272).

The electronic effects of WO_3 doping were observed by studying the band gaps of the doped nanofibres in relation to dopant concentration. The band gap measurements for the studied nanofibre samples were determined by applying the Tauc relation to the UV-Vis diffuse reflectance spectra of the studied samples, as described in Section 2.3. The calculated band gaps for the doped samples

can be seen in Figure 5.4 where the 1 mol% WO_3 doped TiO_2 nanofibres display the smallest band gap (2.96 $\pm$ 0.02 eV). This observation is consistent with expectations as well as literature results[224–226] as the introduction of low level impurities in TiO_2 will generate interstitial energy states in the electronic band gap of the material.[46] As the electronic excitation to and from these interstitial WO_3 levels will require less energy a lowering of the band gap will be observed in the studied materials, effectively resulting in a bathochromic shift, as reported by Bellardita *et al.*[225]

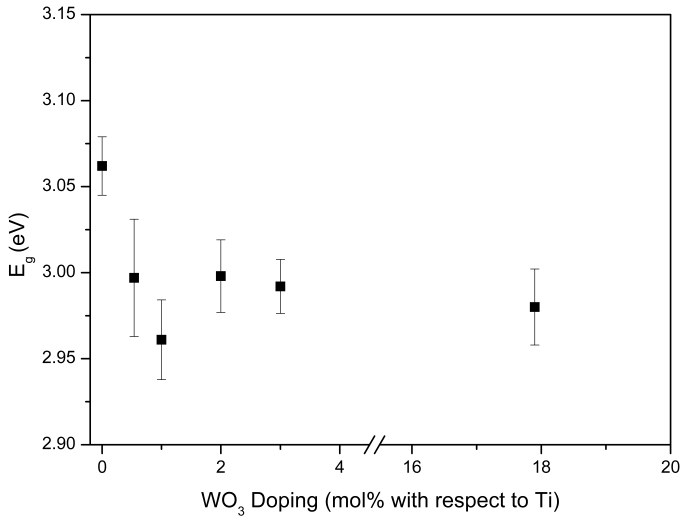

Fig. 5.4 Calculated band gaps of the WO_3 doped TiO_2 nanofibres in relation to WO_3 mol% content of the precursor solution. The band gaps were calculated by applying the Tauc relation to the diffuse reflectance spectra of each sample.

However, as the WO_3 concentration increases beyond 1 mol%, this leads the WO_3 band gap to become increasingly independent in the studied systems. As the WO_3 band gap becomes more independent, some of the energy supplied during photoexcitation will be preferentially used to excite electrons from the WO_3 conduction band to the WO_3 valence band, effectively reducing the number of interstitial band gaps available for TiO_2 electronic excitation and thus leading to the observed increase in band gap of 2 mol% WO_3 doped nanofibres (E_g = 3.00 $\pm$ 0.02 eV). Beyond 2 mol% the WO_3 band gap becomes increasingly dominant over the TiO_2. Due to its relatively lower energy requirements, the dominance of the WO_3 leads to a gradual decline in band gap energy in the observed systems (E_g = 2.99 $\pm$ 0.02 eV and E_g = 2.98 $\pm$ 0.02 eV for 3 and 17.9 mol% WO_3 doping, respectively). It is important to note the large size of the experimental error in the presented band gap measurements. Although this error does not impact the drop observed for the WO_3 doping concentration of 1 mol% or the subsequent rise at 2 mol% (as these trends lie outside

the error margins), the gradual drop observed for the higher WO_3 doping concentrations lies within experimental error. As such, although a trend can be observed by solely considering the numbers, this trend must be considered with caution as it may only be an artefact of experimental error.

From the electronic studies of the WO_3 doped TiO_2 nanofibres, all of the created structures were expected to display increased siloxane photodegradation properties with respect to TiO_2 nanofibres. The lower band gap of the doped structures signifies that more electronic excitation could occur in the studied systems, leading to a higher population of photogenerated hydroxide radicals. The 1 mol% WO_3 doped TiO_2 nanofibres were expected to display a particular effectiveness in siloxane removal due to their particularly low band gap. Nonetheless, the band gap of the photocatalysts is only one of many factors affecting the speed and efficiency of photodecomposition. As such, it was essential to investigate the effectiveness of all of the doped nanofibres for the decomposition of siloxanes.

5.3.2 Static Siloxane Photodecomposition

Pure TiO_2 Nanofibres for Siloxane Decomposition

The evolution of L2 in relation to time and UV illumination whilst using pure TiO_2 nanofibres is shown in Figure 5.5. Three distinct events can be seen occurring in the first stages of static photodecomposition: adsorption onto the photocatalysts, photoinduced desorption, and photodecomposition. Upon an initial injection the L2 is rapidly adsorbed onto the catalyst surface, leading to an exponential decrease in L2 concentration in the studied system. This adsorption process eventually reaches an equilibrium state and leads to a constant siloxane concentration prior to light illumination.

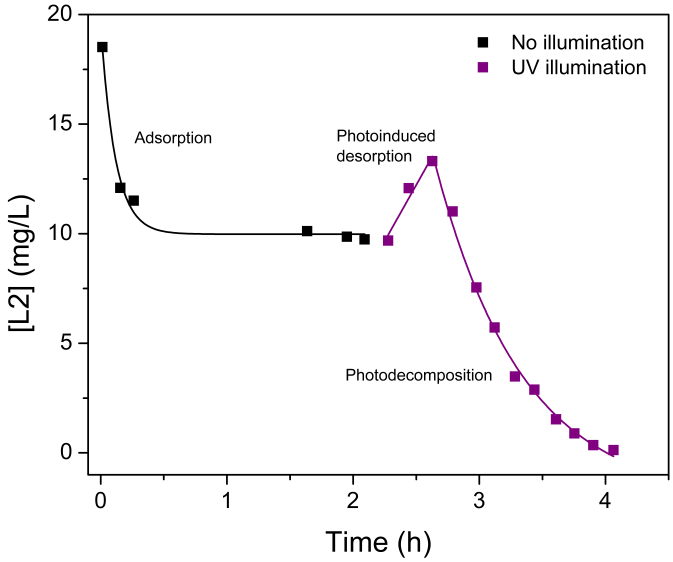

Fig. 5.5 Evolution of L2 concentration in a static reactor system equipped with pure TiO_2 nanofibres in relation to time and UV illumination. The three main events occurring during the initial stages of siloxane photodegradation can be clearly seen.

Upon UV illumination, a significant increase in L2 concentration can be observed. This increase arises from the photoinduced desorption of the siloxane from the photocatalyst surface. Photoinduced desorption is caused by the photonic excitation of the catalyst surface which, due to the occurring electronic transitions, becomes more repulsive. The increased surface negativity in combination with the natural molecular motion of the adsorbates at room temperature leads to partial desorption of the adsorbate species. This phenomenon is commonly known as the Menzel, Gomer, and Redhead model.[227]

Concurrently with the photoinduced desorption, photodecomposition occurs. Initially the rate of photodesorption remains higher than that of photodegradation, as seen in Figure 5.5 with an increase in L2 concentration in the system. However, the rate of photodegradation soon outweighs that of photodesorption and the concentration of L2 drops rapidly. As the time of photodegradation is extended, the fall of L2 concentration in the system can be seen to follow an exponential decay as shown in Figure 5.6. Over an extended period of time the rate of removal of L2 can be seen to plateau due to the consumption of L2 in the system. Indeed, after undergoing extensive photodegradation the concentration of L2 becomes low enough that only a minimal amount of siloxane will be adsorbed on the TiO_2 surface, causing an overall drop in photocatalytic activity. Thus, even though the studied reaction still proceeds at low L2 concentrations, the rate of decomposition drastically

decreases with decreasing siloxane concentrations.

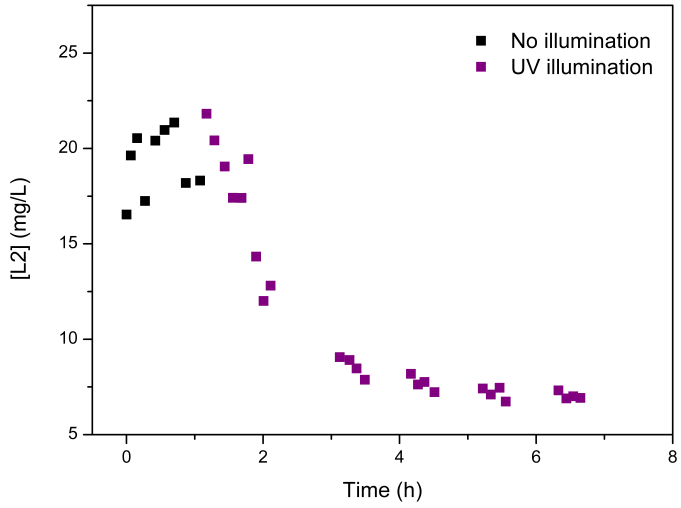

Fig. 5.6 Evolution of L2 concentration in a static reactor system equipped with pure TiO_2 nanofibres in relation to time and UV illumination. As the nanofibres are exposed to UV light the exponential decay in L2 concentration can be clearly seen.

By studying the kinetics of the photodegradation process it is possible to gain further understanding of the photocatalytic degradation of L2. The photocatalytic degradation of siloxanes is often complex and can involve a large number of steps, as previously proposed by Ren-De Sun *et al.*[126] This presence of multiple reaction pathways as well as the generation of intermediate photodecomposition species is not a unique feature of siloxane photodegradation, allowing to study the photodecomposition reactions through the mathematical models established for the general decomposition of gas-phase contaminants. A number of models describing the kinetic decomposition of airborne contaminants by TiO_2 were developed by de Lasa *et al.*[130] These models not only take into account the presence of different reaction pathways and intermediates but also consider the importance of adsorption on the catalyst surface.

Although the models presented by de Lasa and co-workers are thorough, allowing for the determination of quantum efficiency and yield of the studied photocatalysts, they are also significantly complex. Indeed, the gain in specificity within these models is often at the cost of simplicity as many different factors (such as incident photon rate, photocatalyst mass variations and contaminant adsorption isotherms on the photocatalyst) need to be precisely calculated to supply reliable data. During the present series of experiments, a simpler, pseudo-first order, kinetic model was adopted

for the study of the photocatalysed decomposition of gaseous L2. A similar model was presented by Zhang *et al.* during their studies on the photodecomposition of benzene on lanthanum doped TiO_2 films.[228]

Furthermore, it is important to note that in the studied systems photodecomposition occurs at a much slower rate than adsorption (as can be seen in Figure 5.5). This allows to assume that the system will always be at adsorption equilibrium during the photodecomposition reactions.

In order to establish a kinetic model, the general process for the photodegradation of L2 by TiO_2 for the studied reactions, as shown in Equation (5.1), was considered. For simplicity Equation (5.1) portrays the decomposition of L2 as an elementary reaction step although, as discussed in Chapter 1, the decomposition of siloxanes proceeds through a variety of intermediates. However, it is important to note that the nature and ultimate fate of the unknown intermediates did not affect the kinetic analysis on the decomposition of L2 as this was performed solely by studying the reaction's reagents.

$$\mathrm{OH^{\cdot}} + \mathrm{O_2} + \mathrm{O(SiMe_3)_2} \xrightarrow[TiO_2]{hv} \mathrm{H_2O} + \mathrm{CO_2} + \mathrm{SiOx} \tag{5.1}$$

From Equation (5.1) it can be seen that, chemically, the rate of siloxane photodegradation depends on the concentrations of oxygen, the hydroxide radical, and L2. As such, the rate of decomposition of L2, ν, can be described as a function of the concentrations of these three reagent species as well as the rate constant, k. This is shown in Equation (5.2).

$$-\frac{d[O(SiMe_3)_2]}{dt} = \nu = k[\mathrm{OH^{\cdot}}][\mathrm{O_2}][\mathrm{O(SiMe_3)_2}] \tag{5.2}$$

The concentration of oxygen in ambient air can be assumed to remain constant during the photodegradation reactions due to its high concentration relative to L2 (140 mg/L of O_2 in air[24] and $\sim$ 20 mg/L of L2 in air during experimentation). Similarly, the concentration of water (the source of hydroxide radicals) in air is also significantly higher (relative ambient humidity in the UK exceeds 10% by volume , equalling more than 123 mg/L, all year round)[229] than the studied concentrations of L2. As such, the concentration of hydroxide radicals on the TiO_2 surface remains roughly constant throughout a single photocatalysis reaction.

By allowing the concentrations of both the hydroxide radical and oxygen to remain constant

throughout the reaction, it is possible combine these two values in the reaction constant as shown in Equation (5.3), and create a modified rate constant, k'. By replacing the modified rate constant into Equation (5.2) it is possible to simplify the photodecomposition of L2 by TiO_2 into the pseudo-first order rate reaction shown in Equation (5.4).

$$k' = k[OH^{\cdot}][O_2] \tag{5.3}$$

$$\nu = k'[SiO(Me)_6] \tag{5.4}$$

$$ln[SiO(Me)_6] = -k't + ln[O(SiMe_3)_2]_0 \tag{5.5}$$

The integrated form of a first order reaction can be described as shown in Equation (5.5). Thus, by plotting the logarithm of the concentration of L2 against reaction time it is possible to demonstrate a linear relationship with a gradient of $-k'$ and an intercept corresponding to the initial L2 concentration in the system. It can be seen from the linearity of the logarithmic plot of siloxane concentration decay in relation to time in Figure 5.7 (A) that L2 photodecomposition in the studied systems proceeds according to pseudo-first order reaction kinetics. It was thus possible to establish that the k' for the photodegradation of L2 on clean TiO_2 nanofibres is 2.19 h^{-1}.

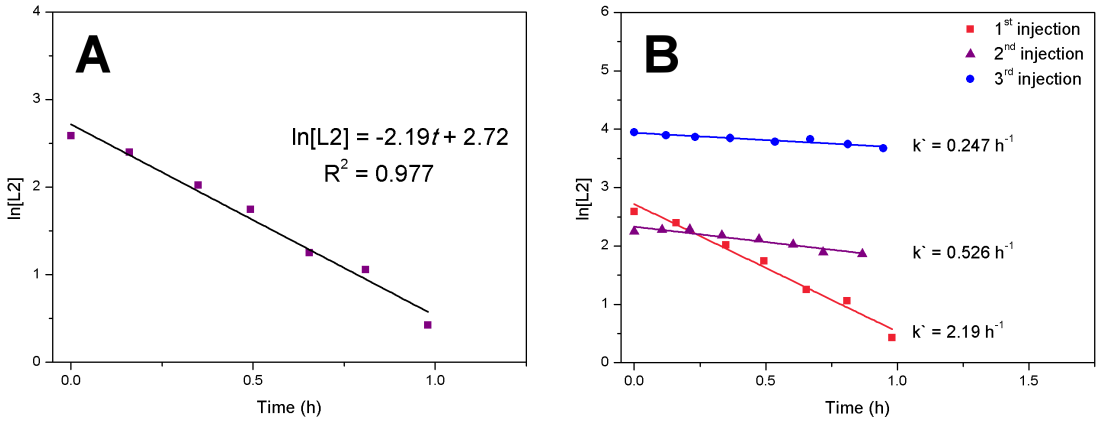

Fig. 5.7 First order reaction behaviour as observed during the photodegradation of L2 on a clean catalyst (A) and on the same catalyst upon multiple subsequent degradation events (B). The drop in rate constant can be clearly observed upon multiple injections

As L2 was further injected into the system, the observed decomposition reactions proceeded at a slower rate. This can be seen clearly in Figure 5.7 (B) where the kinetic constant decreased from 2.19 h^{-1} to 0.247 h^{-1} from the first to the third injection of L2 on the studied photocatalyst.

The decay of k' in relation to the total amount of L2 decomposed can be further seen in Figure 5.8 where the rate constants are observed to undergo a exponential decrease with increasing quantities of decomposed siloxane. This decrease indicates the presence of a second limiting factor. From a chemical point of view this could be either the $OH^{\cdot}$ or O_2 concentrations. However, since each injection on L2 into the system was performed from a renewed L2/air mixture it can be assumed that both the O_2 and H_2O concentrations in the gas phase vastly outweighed the concentration of L2 not only during any individual photodegradation experiment but also throughout the whole series of photodegradations. As such, it becomes clear that the loss in catalyst reactivity must be attributed not to a chemical but to a physical factor.

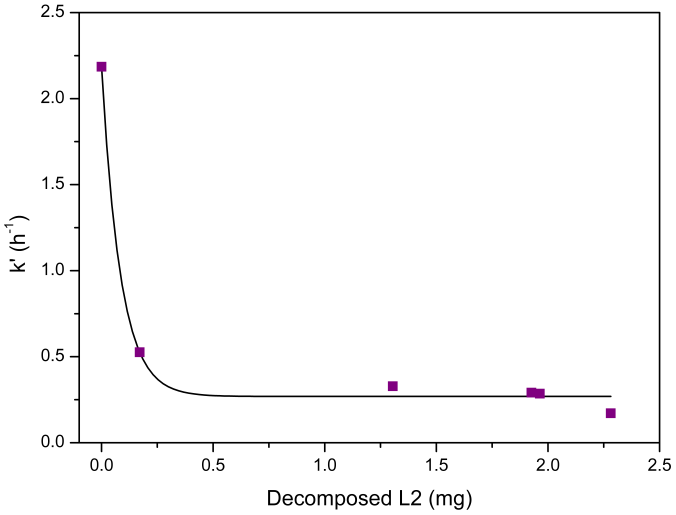

Fig. 5.8 Evolution of first order L2 photodecomposition rate constants of 0.202 g of TiO_2 nanofibres in relation to the total amount of L2 decomposed during a given experiment.

One of the most important physical factors in the photodegradation of L2 by TiO_2 is the availability of active sites. In order for the photodegradation of L2 to reach completion, the L2 must react with both electrons and holes from the photoactivated TiO_2. If the L2 cannot come into contact with the catalyst surface, the photodegradation will be inhibited and only a small number of L2 molecules will undergo degradation. As siloxanes degrade, they form a layer of SiO_x on the catalyst surface. This causes inhibition and eventual cessation of the photocatalytic process, as the insulating

SiO_x layer prevents electron transfer from the catalyst to the adsorbate molecules.[126] Thus, the exponential decay in the reaction rate in relation to increased L2 decomposition can be attributed to the inhibition of electron transport from the TiO_2 caused by the build-up of SiO_x species. These observations are consistent with the studies of Hiroki Tada wherein a similar exponential decrease of k' in relation to SiO_x build-up was caused by to the increasing inability of the TiO_2 photoexcited electrons to undergo electron tunnelling and reach the catalyst surface.[127]

Table 5.1 shows the evolution of k' in relation to total L2 decomposed for a 0.202 g catalyst sample. From this, it was possible to estimate that TiO_2 nanofibres decomposed a total of 13.8 mg of L2 per gram of TiO_2. It is important to note that at equivalent experimental conditions, a reduction of photocatalyst mass by a quarter resulted in an equal reduction in k', corresponding to the reduction in available photoactive sites with the loss of photocatalyst. As such, when comparing k' values between different photocatalysts, the mass of studied photocatalyst was kept constant (0.05 g) between experiments.

Table 5.1 Modified rate constant for a 0.202 g TiO_2 nanofibre sample in relation to the number of siloxane injections and the total amount of L2 decomposed before each injection.

Injection	Total L2 Decomposed(mg)	k'(h^{-1})
1	0	2.19
2	0.62	0.526
3	1.75	0.328
4	2.37	0.291
5	2.41	0.285
6	2.73	0.171

The nature of the photocatalyst poisoning can be further understood from the results of the thermal studies. Figure 5.9 shows the evolution of L2 in the ampoule upon heating at increasing temperatures after the photocatalytic decomposition of 2.93 mg of L2 on TiO_2. It can be seen that increases in temperature only resulted in a minimal increase in L2 concentration (0.204 mg L2 increase at 60°C) due to its desorption from the TiO_2 surface. As the temperature was increased, the L2 concentration remained roughly constant, demonstrating the complete desorption of L2 at 60°C. A maximum of 0.204 mg of L2 were desorbed during these studies compared with a previous total loss of 2.93 mg of L2. Additionally no peaks other than that of L2 were observed in the GC-FID measurements during the experiment, further corroborating the presented understanding of the nature of the final decomposition product of L2 as a non-volatile species.

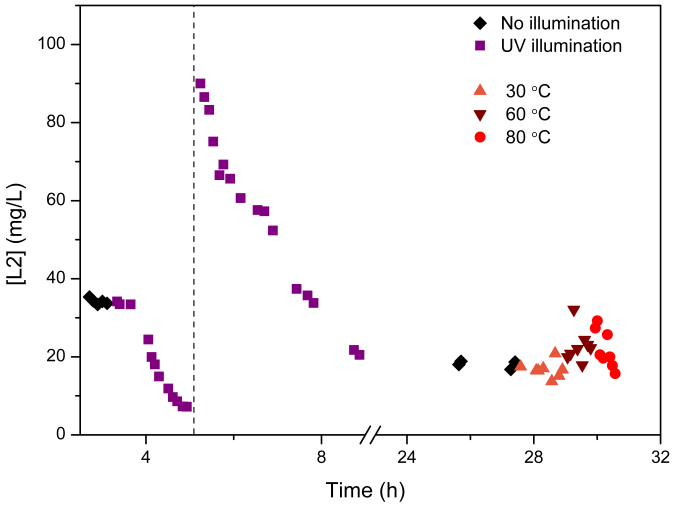

Fig. 5.9 L2 concentration in relation to temperature in the studied ampoule after photocatalysis. The dotted line shows the point at which L2 was supplied through a second injection, 6 injections were performed in total.

WO_3 Doped TiO_2 Nanofibres for the Photodecomposition of L2

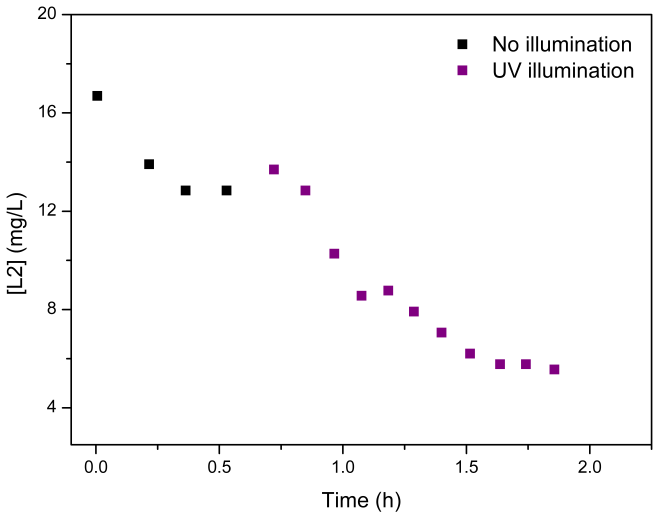

Fig. 5.10 Evolution of L2 concentration in a static photodegradation reactor using 0.051 g of 1 mol% WO_3 doped TiO_2 nanofibres.

In order to determine the effectiveness of the WO_3 doping on TiO_2 nanofibres, their photodegradative abilities were investigated. The evolution of L2 concentration in the static reaction vessel prior to, and during, illumination for 1 mol% WO_3 doped TiO_2 nanofibres can be seen in Figure 5.10.

The WO_3 doped nanofibres showed the same photodecomposition profile as that of TiO_2 nanofibres; displaying adsorption, photodesorption, and photodecomposition events prior to, and during, the initial stages of catalyst illumination. This similarity indicates that the photodecomposition of L2 on both TiO_2 and doped TiO_2 nanofibres proceeds along similar pathways. As such, it becomes possible to study the kinetics of L2 photodecomposition on doped TiO_2 nanofibres by using the pseudo-first order kinetic model outlined in Equation (5.5).

Figure 5.11 shows the kinetic constants of the studied concentrations of WO_3 nanofibres. It can be seen that the rate of decomposition of L2 increases sharply until peaking at a WO_3 concentration of 1 mol%. Following the peak, the kinetic rate constants decrease with increasing WO_3 concentration in the nanofibres. The kinetic rate constant profile can be seen to be the inverse of that of the band gap of the doped samples (presented in Figure 5.4). The datum for the kinetic constant of the 2 mol% WO_3 doped TiO_2 nanofibres appears spuriously low. However, a close observation of its band gap in Figure 5.4 also shows a relatively high E_g (although this lies within the range of experimental error). Further investigation on the properties of the 2 mol% WO_3 doped TiO_2 nanofibres would be required in order to determine the veracity of this unexpected data.

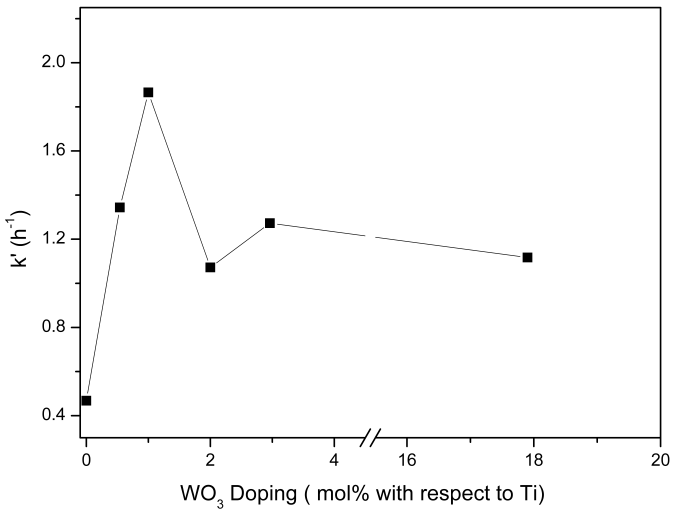

Fig. 5.11 L2 photodecomposition kinetics for 0.050 $\pm$ 0.005g samples of WO_3 doped TiO_2 nanofibres in relation to dopant concentration.

The correlation between the band gap of the doped nanofibres and the k' displayed by the same nanofibres shows the crucial importance of the population of excited state molecules in the L2 photodecomposition process. However, although the band gap of the system is an important

part in determining the population of excited species, the lifetime of the excited species also plays a significant role in L2 photodecomposition. Indeed, if the excitons generated during photonic excitation recombine too rapidly for the formation of hydroxide radicals to occur, the photodegradation reaction becomes effectively inhibited and fails to occur. Doping agents are known to not only lower the band gap of a material (through interstitial band gap states) but they can also act as electron/hole traps. In the case of WO_3 doping, the photoexcited electrons from the TiO_2 transition to the lower conduction band of the WO_3 impurities, effectively separating the exciton. As an equivalent transition for the photogenerated hole to the WO_3 valence band is energetically unfavourable, the lifetime of the exciton is thus increased, allowing for the formation of more hydroxide radicals for the photodecomposition of L2.

The region of transition between the band gap of the dopant and the doped species (TiO_2 and WO_3 respectively, during this study) is known as the space charge region. It was established by Pleskov[230] as well as Gautron *et al.*[231] that the drop in potential between the band gap of TiO_2 and a dopant species (the space charge drop) should not be inferior to 0.2 V, in order to allow for an efficient exciton fission. As the concentration of dopant species in the TiO_2 increases, a narrowing of the space charge region between the two species occurs, effectively increasing the efficiency of exciton separation. However, beyond a certain concentration of dopant, the space charge region becomes narrower than the light penetration depth of TiO_2. This signifies that at relatively high concentrations there is effectively no driving force to cause the fission of excitons, thus effectively increasing electron-hole recombination and decreasing exciton lifetime. As such, it becomes clear that the doping of WO_3 in TiO_2 nanofibres will have a concentration at which the exciton separation efficiency (and thus exciton lifetime) will be maximised. Nonetheless, it is important to note that the dopant concentration at which exciton separation is the most efficient, will not necessarily be that wherein the band gap of the doped materials will be at a minimum.

From the gathered results, it is possible to establish an ideal doping concentration of 1 mol% of WO_3 in TiO_2 nanofibres for the photodecomposition of L2. This observation is consistent with the photocatalytic studies of Bellardita *et al.*[225] as well as those of Song *et al.*[226] wherein a 1 mol% concentration of WO_3 dopant displayed the highest contaminant photodegradation efficiency. Bellardita *et al.* attributed the ideal concentration mainly to a lengthening of the exciton lifetime[225] whilst Song *et al.* strongly emphasised the importance of the bathochromic shift caused by the WO_3 doping. From this study, the importance of the bathochromic shift is readily apparent,

however it is most likely that the efficiency of 1 mol% WO_3 doping arises from a combination of band gap narrowing as well as the extension of the exciton lifetime which enhance the generated exciton population as well as the exciton lifetime. The efficiency of the 1 mol% WO_3 doped TiO_2 nanofibres is further emphasised when compared to the photodegradative activity of pure TiO_2 nanofibres. Indeed, at equal catalyst loadings (0.05 g of catalyst), the 1 mol% WO_3 doped TiO_2 nanofibres displayed a k' value of 1.94 h^{-1}, 122% greater than that of pure TiO_2 nanofibres (k' = 0.437 h^{-1}).

Morphological Effects on Siloxane Photodecomposition

Although the study of the L2 photodegradative abilities of WO_3 doped TiO_2 nanofibres allows to investigate the electronic enhancements to TiO_2 nanofibres, no indication is given as to the efficiency of the nanofibrous structure itself. The effects of morphology and surface area on the photodecomposition of L2 can be understood by investigating the photodegradative properties of both the porous nanofibres synthesised in Chapter 3 and P25. From these studies, it will be possible to understand the advantages of the nanofibrous architectures on the photodecomposition of L2 as well as illustrate the effects of enhancing the nanofibrous surface area through templating techniques.

The L2 decomposition kinetics of both P25 and porous TiO_2 nanofibres were studied and compared to those observed for the doped and undoped TiO_2 nanofibres. Table 5.2 shows the kinetic constants for the studied samples as well as the relative percentage difference of the values in relation to P25 in order to highlight the variations in rate constants.

Table 5.2 Modified rate constants for the studied photocatalysts. The mass of each sample was maintained constant at 0.050 $\pm$ 0.005 g.

Photocatalyst	k'(h^{-1})	Relative % difference
P25	0.437	0
TiO_2 nanofibres	0.468	6.9
Porous TiO_2 nanofibres	0.496	12.8
1 mol% WO_3 doped TiO_2 nanofibres	1.94	126.5

From Table 5.2 the effect of structural variation can clearly be seen as unmodified TiO_2 nanofibres display an L2 decomposition rate constant 6.9% higher than that of P25. The higher photocatalytic activity of the nanofibres over P25 can be explained through a combination of

surface porosity as well as interparticle charge transfer as described by Choi *et al.*[232] Although TiO_2 nanoparticulates display a higher surface area than the TiO_2 nanofibres, the latter structure displays a higher mesoporosity due to the electrospinning synthetic procedure. During nanofibre synthesis, the formation of TiO_2 nanofibres occurs through many different nucleation points, leading to the formation of polycrystalline, mesoporous structures. The high mesoporosity of these structures enhances the adsorption of gaseous substrates (in this case, siloxanes) on the structures, thus allowing for an increase in surface bound species available for photodecomposition. This mesoporosity combines synergistically with an enhanced exciton lifetime arising from the polycrystalline nature of the synthesised nanofibres which enhances charge carrier separation.

The effects of increasing surface area can be seen more clearly by observing the 6% increase in photocatalytic activity displayed by the porous TiO_2 nanofibres relative to the pure TiO_2 nanofibres. Aside for the templating procedure used in the formation of the porous TiO_2 nanofibres, the two samples were synthesised in nearly identical conditions. This signifies that the growth mechanism of the polycrystalline TiO_2 nanofibres in both cases can be assumed to have proceeded identically, such that any observed kinetic differences between the samples arise from the difference in surface areas of the materials.

Finally it is essential to note the exceptionally large increase in photocatalytic decomposition rate shown by the 1 mol% WO_3 doped TiO_2 nanofibres (126 % difference with respect to the photodecomposition rate of P25). This increase can be attributed to the beneficial electronic effects as a result of the doping of TiO_2 with impurities, as discussed extensively in Section 5.3.1 and Section 5.3.2.

From the collected results the 1 mol% WO_3 doped TiO_2 nanofibres can be considered a suitable candidate for the decomposition of siloxanes in biogas.

5.4 Conclusions

In conclusion, during this study it was possible to demonstrate the viability of a variety of TiO_2 nanostructures for the photodecomposition of siloxanes in in static gas environments.

Initially a series of WO_3 doped TiO_2 nanofibres were synthesised in order to enhance the

photoactivity of TiO_2 nanofibres. Through extensive characterisation it was determined that although the WO_3 had little effect on the general TiO_2 nanofibre structure, the formation of the anatase TiO_2 crystal phase was favoured. This preference for the TiO_2 crystal phase was attributed to the prevalence of small TiO_2 crystallites arising from an increase in nucleation sites supplied by the WO_3 doping. Further characterisation of the doped nanofibres allowed to investigate the electronic effects of doping. The 1 mol% WO_3 doped TiO_2 nanofibres displayed the smallest band gap (2.96 ± 0.02 eV) amongst the studied samples. This observed minima was attributed to the electronic interactions between the WO_3 and the TiO_2 band gap as well as the rising dominance of the WO_3 band gap with increasing dopant concentrations. The importance of the 1 mol% WO_3 doping of TiO_2 nanofibres was further observed during the L2 photodecomposition studies.

During the photodecomposition studies it was possible to establish a facile pseudo first-order kinetic model for the static photodecomposition of siloxanes on the studied photocatalysts. By modelling the decomposition of L2 on TiO_2 nanofibres it was thus possible to determine the initial photodecomposition rates for both 0.202 and 0.050 g samples of TiO_2 nanofibres to be 2.91 h^{-1} and 0.437 h^{-1}, respectively. However, with increasing amounts of siloxane decomposition, the decomposition rate was observed to decrease rapidly until becoming negligible. This drop in rate constant was attributed to a build-up of SiO_x on the active sites of the photocatalyst, impeding the decomposition of siloxanes. It was postulated that as the SiO_x accumulated on the TiO_2 surface, this provided an insulating layer and hindered electron transfer from the TiO_2 to the adsorbed species on the photocatalyst surface. This understanding of the decomposition mechanism was supported by a series of thermal regeneration studies which showed of the lack of volatile species in the studied systems after photodegradation. A total L2 decomposition ability of 13.8 $mg_{L2}g^{-1}_{TiO_2}$ was determined for the synthesised TiO_2 nanofibres before total catalyst inhibition.

The photodecomposition properties of WO_3 doped TiO_2 nanofibres were studied in relation to WO_3 concentration. It was found that the L2 decomposition kinetics inversely followed the profile of the band gap variations in relation to WO_3 concentration. 1 mol% WO_3 doped TiO_2 nanofibres were seen to display the highest L2 decomposition kinetics (k' = $1.94h^{-1}$ for 0.051 g of photocatalyst). Although this coincided with the lowest band gap measurement, the observed effect in decomposition kinetics was attributed to a synergistic effect between the bathochromic shift and an increase in exciton lifetime caused by the WO_3 doping.

Finally, the relative effectiveness for siloxane photodecomposition of a variety of different TiO_2 nanostructures was studied by comparing their photodecomposition constants. From these studies, it was possible to emphasise the importance not only of the nanofibrous structure over that of P25, but also of the effectiveness of templating techniques in enhancing photocatalytic activity through surface area modifications. Nonetheless, the crucial importance of impurity doping was exhibited by the 1 mol% WO_3 doped TiO_2 nanofibres which displayed a k' value 126% larger than that of pure P25.

Overall, it was possible to demonstrate the viability of TiO_2 as a siloxane photodecomposition agent in static reactors. These advances highlight the potential of the application of TiO_2 photocatalysts in the purification of biogas. In particular, the use of WO_3 doped TiO_2 nanofibres could allow for the creation of highly efficient biogas purification catalysts and pave the way for a novel generation of industrial gas purification devices.

6. Siloxane Decomposition in Gas Streams

In Chapter 5 the photodegradation of siloxanes over TiO_2 in a static environment was successfully demonstrated by using hexamethyldisiloxane (L2). However, in order to apply the studied techniques at an industrial scale, the photodecomposition of siloxanes by TiO_2 needs to be demonstrated in gas flow conditions. During the following series of experiments a gas flow photoreactor was created and used to study the decomposition of decamethyltetrasiloxane (L4), octamethylcyclotetrasiloxane (D4) and decamethylcyclopentasiloxane (D5) by TiO_2 photocatalysts in gas streams. The photodecomposition studies were performed by using L4, D4, and D5 rather than L2 in order to further approach the developed technologies towards a successful industrial application as L4, D4, and D5 are the highest concentration siloxane contaminants in biogas.[125,233] Although use of L2 in Chapter 5 allowed to demonstrate the effectiveness of the decomposition technique with respect to siloxanes, its relatively weak concentration in biogas signifies that the study of the photodecompositions of L4, D4, and D5 will provide a better approximation of how the designed reactors would perform under industrial conditions.

Initial studies focused on the demonstration of photocatalytic decomposition in gas streams and the determination of an appropriate method for the quantification of TiO_2 photocatalytic activity loss. After the establishment of a turnover number (TON) for the decomposition of siloxanes in the studied systems, chemical studies were carried out to develop effective and industrially suitable TiO_2 regeneration procedures. In parallel to the regeneration studies, a series of engineering studies were performed investigating a number of catalyst supports as well as the effects of gas/catalyst contact times on the lifetime of the established reactors.

By performing both the engineering and chemical studies it was possible to establish a global profile for the studied flow decomposition reactions. Only through the development of such a profile it is possible to establish the presented technologies as viable systems for the photocatalytic

elimination of siloxanes in biogas.

6.1 Introduction

The effectiveness and kinetics of the photodecomposition of siloxanes by TiO_2 were previously demonstrated in Chapter 5 and have been further studied in academic literature.[15,168,212] However, in order to achieve industrial applicability for the studied technologies, the decomposition of siloxanes in a static environment remains insufficient as current systems for the purification of biogas are based on the removal of siloxanes from gas streams.[7,10,234] As such, it becomes essential to investigate the photodecomposition of siloxanes by TiO_2 in gas flow conditions.

Amongst the current literature studies performed, the successful decomposition of gas-phase siloxanes over photoactivated TiO_2 monoliths was first shown Hay *et al.* in 2010.[14] However, all of the current literature studies have used TiO_2 for the removal of contaminants in domestic atmospheres.[14,126,235] This signifies that these technologies used relatively low gas flow rates with streams containing only minimal concentrations of siloxanes. Furthermore, although the studies identified the loss of photocatalytic activity and carried out initial determinations of the nature of the photocatalyst's poisoning, no extensive investigation was carried out in order to achieve the renewal of TiO_2 photocatalytic activity.

The present series of experiments aimed to demonstrate the potential for TiO_2 photodecomposition technologies in the industrial removal of siloxanes. Initial studies focused on the photodecomposition of siloxanes over P25 in gas streams and the quantification of the TiO_2 photocatalytic lifetime. P25 was chosen as the photocatalyst due to its well known activity.[42,115,236] Although it was shown in Chapter 5 that TiO_2 nanofibres and doped TiO_2 nanofibres displayed superior photodegradative properties, P25 possesses a lower cost and ease of production. Following the initial photodegradation studies, two main points of interest were pursued: the regeneration of the photocatalytic activity of the systems and the effects of engineering parameters on the photoreactor.

The deactivation of heterogeneous catalyst activity has been a subject of extensive academic study.[237–239] It is commonly accepted that this loss of catalytic properties can be attributed to five different phenomena: poisoning, fouling, thermal degradation, vapour formation, and crushing.[240] Due to the relatively mild photoreaction conditions as well as the chemically inert nature of TiO_2,

the main sources of photocatalytic deactivation during the current study would proceed through the poisoning and fouling mechanisms. As such, a number of regeneration techniques, aiming to remove the solid deposits causing the deactivation of the TiO_2 photocatalysts through thermal and chemical means, were investigated. Furthermore, two different techniques of catalyst recoating were also pursued in order to establish alternative approaches to photocatalytic regeneration. During these regeneration experiments, particular attention was given to the scalability of the studied techniques in order to gauge their relative industrial applicability.

The study of the system's engineering parameters was of particular importance for the applicability of the technology in the industrial purification of biogas. It is known that the siloxane content of biogas can vary significantly depending on the sources and pre-treatment of the biogas.[7,13,187] As such, the development of versatile systems which can be tailored to the individual siloxane content of different biogas production sites can be an essential advantage of these technologies. During the present study, a series of experiments were carried out in order to study the effects of gas/catalyst contact time as well as the importance of different catalyst supports. Furthermore, two different procedures for the coating of the P25 on glass supports were developed and investigated.

By combining the studies on the engineering parameters of the system to those carried out on the chemical nature of the photodecomposition and the regeneration of photocatalytic activity, it will be possible to establish the importance and versatility of the created photocatalytic reactors. It is only by achieving this combined knowledge that the developed systems can become competitive photocatalytic filters for the purification of biogas.

6.2 Experimental

6.2.1 Chemicals and Characterisation Techniques

All chemicals used during the following experiments were sourced form Sigma-Aldrich UK and used as received unless otherwise stated.

2D fluid dynamic simulations of the different catalyst supports were carried out using the Flowsquare fluid dynamic simulation software.[241]

The concentration of L4, D4, and D5 during the flow photodecomposition reactions was monitored via gas phase Fourier Transform InfraRed spectroscopy (FTIR). The IR spectra were collected using a Perkin Elmer SpectrumOne FTIR spectrometer with a gas phase IR cell (130 mm long) equipped with NaCl windows (25 mm in diameter). By monitoring the area under the peak corresponding to the siloxane Si−O−Si stretch (1204 - 938 cm^{-1} for D5 and 1200 - 950 cm^{-1} for D4 and L4), it was possible to quantify the photodegradation of siloxanes in the flow reactors.

6.2.2 General Flow Reactor Design

Figure 6.1 shows the general experimental set up used for the study of the photocatalytic decomposition of siloxanes in gas flow systems. In order to simulate an industrial continuous flow reactor incorporating siloxanes, a chosen carrier gas (either methane, sourced from the domestic supply, or compressed air, sourced from BOC UK) with a controlled flow rate (20 l/h) was loaded with a specified siloxane, as described in Section 6.2.3. The siloxane loaded gas was then channelled into a series of quartz tubes loaded with glass supported TiO_2 photocatalysts inside a UV chamber (Spectrolinker XL-1500 UV crosslinker equipped with six UV_a Fluorescent tubes displaying a spectral peak at 365 nm). Two different types of catalyst supports were used during the present study: TiO_2 coated glass rods, and TiO_2 coated glass spheres (labelled in Figure 6.1 as (A) and (B), respectively).

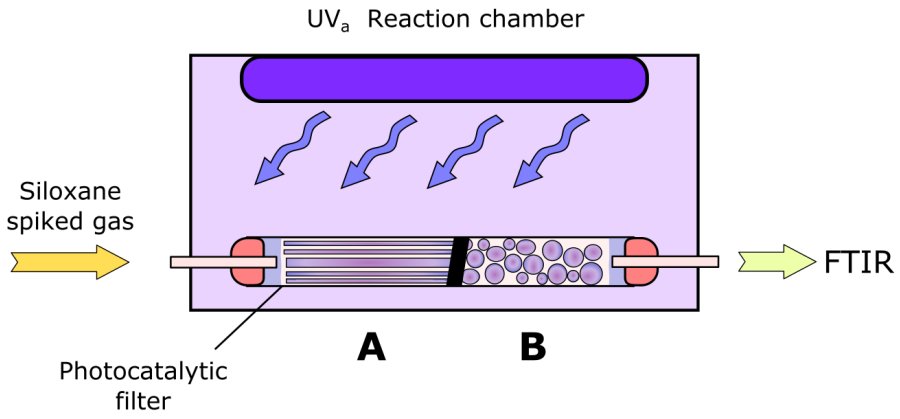

Fig. 6.1 Diagram showing the experimental set up used for the photodecomposition of siloxanes in gas streams. During these studies two different catalyst supports were used: glass rods (A), and glass beads (B).

Due to the modular nature of the system, it was possible to investigate the effects of gas/catalyst

contact time by modifying the length of the quartz tubes as well as the mass of supported catalyst during the study. The concentration of the outflow gas was monitored using an in-line IR spectroscopy cell. Once the concentration of siloxane was observed to stabilise in the gas stream, UV illumination was commenced and its effects on the siloxane concentration in the gas stream were monitored.

6.2.3 Siloxane Loading in the Gas Streams

The introduction of siloxanes in the carrier gas streams during this experiment was carried out with two different procedures as a result of the varying viscosity and volatility of the studied siloxanes. In order to introduce the more volatile siloxanes (L4 and D4) into the gas stream, the chosen gas was passed at a specific flow rate (20 l/h) over a known amount (5 ml) of pure siloxane liquid in a Dreschel bottle as shown in Figure 6.2 (A). The concentration of siloxanes in the gas stream was controlled by modifying the length (L) of the dip tube above the liquid.

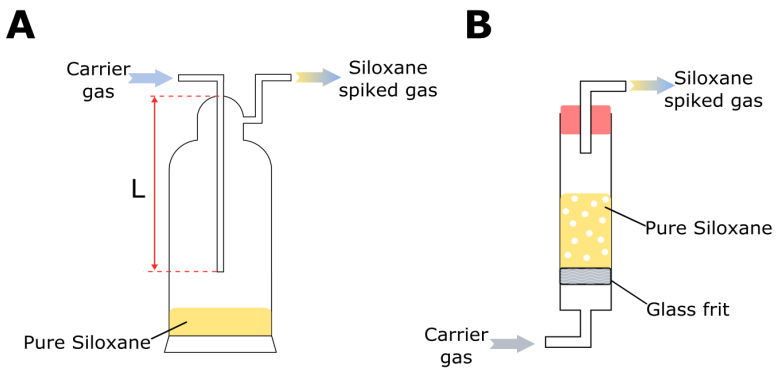

Fig. 6.2 Schematic diagram depicting the methods used for the controlled introduction of volatile (A) and non volatile (B) siloxanes in gas streams during the present series of experiments.

The method presented in Figure 6.2 (A) was determined to be ineffective for the transfer D5 to the carrier gas due to its low volatility.[242] As such, a more thorough method, shown in Figure 6.2 (B) was implemented. A known amount of D5 (5 ml) was placed in a gas dispersion tube above a glass frit, the chosen carrier gas was then passed with a controlled flow (20 l/h) through the frit and the D5, generating a siloxane saturated carrier gas. The glass frit allowed to disperse the flow into bubbles, thus maximising the gas/liquid contact area and ensuring an appropriate loading of the D5 into the gas stream.

6.2.4 TiO_2 Photocatalyst Immobilisation on Glass Substrates

Early investigations revealed the inadequacy of using P25 in its powder form as this often lead to the displacement of the powders and occlusion of the gas streams. As such, the immobilisation of P25 on specific substrates was considered. During this study, two different immobilisation methods; dip coating and Gyration Induced Adhesive Coating (GIAC), were developed in order to coat the studied photocatalysts in a controlled manner on two different substrates: borosilicate glass rods and borosilicate glass beads.

Dip-Coating of P25 on Glass Rods

In order to coat the P25 onto glass rods, a facile dip-coating procedure was developed. P25 (6 wt%) was dispersed into a solution of polymethymethacrylate (PMMA, 6 wt%, $\overline{M_W}$: 996 000) and acetone. The nanoparticles were subsequently immobilised on the chosen glass substrates (glass rods 250 mm long with varying diameters of 2 and 0.5 mm) by dip-coating the glass substrates in the created suspension.

Dip-coated rods were allowed to dry at ambient air and subsequently coated a further 3 times, allowing for complete desiccation of coated layers between each coat. Finally, the PMMA binder was removed by calcining the glass rods in a furnace at 500°C for 3 hours. The as-calcined glass rods were placed into a quartz tube (250 mm in length, 6 mm internal diameter) in the photoreactive UV chamber described in Section 6.2.2.

Gyration Induced Adhesive Coating

The GIAC procedure was developed during this study in order to allow for a more industrially facile catalyst immobilisation procedure and resolve the shortcomings inherent to the dip-coating procedure. The technique uses mechanical coating in addition to glass bead substrates to achieve enhanced photocatalyst support.

Borosilicate glass beads ($\bar{d}$: 2.5 $\pm$ 0.3 mm, sourced from Glass Sphere S.R.O) were washed with acetone and ethanol. Following the cleaning procedure, the beads were placed in a concentrated basic solution of NaOH in de-ionised water (6 M) and brought to boil. Upon boiling, the beads were

allowed to reflux for 2 hours. This allowed to hydroxylate the glass surface and encourage catalyst adherence. Following hydroxylation, the beads were removed from the basic solution and washed in de-ionised water until the washings resulted neutral. The neural beads were further washed with acetone and dried at ambient conditions under a constant flow of compressed air. The dried beads were accurately weighed ($\pm$ 0.5 mg) and placed in a rotating drum with an appropriate amount of P25 in order to achieve a 4.5 mg_{TiO_2}/g_{beads} loading of catalyst. The drum was allowed to rotate overnight, after which the coated beads were weighed once more in order to precisely establish the loading of the created samples.

The GIAC coated beads were loaded into quartz tubes (10 mm internal diameter, length varying from 85 to 245 mm) equipped with glass wool. Figure 6.3 shows the general set up of the catalyst coated glass beads into the quartz tubes. Once packed, the tubes were placed in the photoreactive UV chamber described in Section 6.2.2 and used for the photodecomposition of siloxanes in gas streams. Due to the modular nature of the system and variable tube length, it was possible to study the effects of contact time on the photodecomposition of siloxanes.

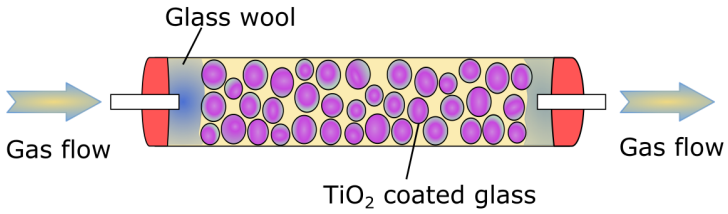

Fig. 6.3 Schematic diagram showing the placement of GIAC coated TiO_2 glass beads in the quartz photoreactor tubes.

6.2.5 TiO_2 Photocatalyst Regeneration Techniques

As the siloxanes in the gas stream were decomposed, the photocatalytic activity of the TiO_2 decreased due to the build-up of a SiO_x layer as discussed in Chapter 5. In order to render the use of TiO_2 photocatalysts industrially viable, the development of a method for catalyst regeneration became essential. During this study, five different catalyst regeneration methods were investigated: Thermal regeneration, non-polar solvent washing, base washing, chemical recoating, and mechanical recoating.

Thermal Regeneration of Poisoned Catalysts

In order to investigate the viability of thermal regeneration, poisoned TiO_2 catalysts were introduced into a furnace (with their glass support) and placed under a controlled gas flow (20 l/h) for 30 minutes. Compressed air and argon (Sourced from BOC UK) were used as the flow gases during the studied experiments. After 30 minutes the system was considered to be completely purged and the furnace was heated at 20, 80, 120 or 450 °C. The thermal treatment was allowed to continue with an active gas flow for 12 hours. After the thermal treatment, the catalysts were removed from the furnace, allowed to cool, and replaced in the photocatalytic reactor described in Section 6.2.2. The photodegradative abilities of the regenerated catalysts were investigated as described in Section 6.2.2.

Non-Polar Solvent Washing

It is known that photocatalytic mineralisation proceeds through a variety of reaction pathways, leading to the formation of many different species.[243–245] Similarly, the photodecomposition of siloxanes on TiO_2 proceeds through a number of complex pathways, leading to the formation of several silicon based species. As these species are formed directly in contact with the TiO_2 photocatalyst they will be preferentially mineralised and inhibit the photodecomposition abilities of the photocatalysts. In order to remove these species, the poisoned TiO_2 photocatalysts were washed with a non-polar solvent.

Poisoned TiO_2 photocatalysts were immersed in n-hexane for a period of 5 hours. After the immersion period, the catalysts were dried in an oven at 80°C under ambient conditions. The dried catalysts were then replaced in the photocatalytic reactor described in Section 6.2.2. The photodegradative abilities of the regenerated catalysts were investigated as described in Section 6.2.2.

Base Washing

In order to remove the created SiO_2 impurities from the surface of the photocatalysts a base washing procedure was investigated. Spent TiO_2 photocatalysts were immersed into a solution of NaOH (6 M, in de-ionised water). This solution was then placed in an oven 80°C and left for 2 hours.

After this, the basic solution was decanted from the spent catalysts and the catalysts were rinsed with de-ionised water prior to desiccation under ambient conditions. The dried catalysts were then replaced in the photocatalytic reactor and their photodegradative abilities were investigated as described in Section 6.2.2.

Chemical Recoating

A more thorough procedure for catalyst rejuvenation was studied with the chemical recoating procedure similar to that used for the formation of TiO_2 shells on SiO_2 nanofibres in Chapter 3. The spent catalysts were immersed in a solution of titanium tetraisopropoxide (TT^iP, 0.8 M) in isopropyl alcohol (IPA) for 1 hour. The beads were then immersed subsequently pure IPA, de-ionised water and IPA solutions, for one minute in each solution. The TT^iP–IPA–Water–IPA cycle was repeated 5 times after which the catalysts were calcined in an oven at 500°C for 12 hours.

After calcination, the fibres were allowed to cool at ambient conditions and placed into the photocatalytic reactor where their photodegradative abilities were investigated as described in Section 6.2.2.

Mechanical Recoating

Mechanical coating was investigated as a facile method for catalyst rejuvenation through the GIAC procedure. The spent catalyst beads were placed in a rotating drum with an appropriate amount of photocatalyst in order to achieve the desired loading. The breads were rotated for a period of 8 h before being removed from the system and replaced in the photoreactor. The photodegradative abilities of the regenerated catalysts were investigated as described in Section 6.2.2.

6.3 Results and Discussion

By studying the decomposition of gas-phase siloxanes in the gas streams it was possible to attain a greater understanding and control over the gas-phase purification of biogas through photocatalytic methods. Initial studies were performed using glass rod catalyst supports and methane streams spiked with D5. After the photodecomposition profiles were determined and a suitable catalyst

substrate was chosen, the decomposition of D4 and L4 were studied by using compressed air as a carrier gas.

6.3.1 Rod Supported TiO_2 Photocatalyst Efficiency

Decomposition Profile

Figure 6.4 shows the D5 concentration profile during a gas flow photocatalytic experiment over TiO_2 coated glass rods (TiO_2 loading of 22 mg, contact time of 0.4 s) as well as uncoated glass rods. Two events of particular importance can be observed in the studied system during irradiation: desorption, and photodecomposition.

As UV illumination is initiated on the system, the concentration of D5 increases, this arises from a combination of thermal and photonic effects similar to those observed in static photodecomposition reactors as discussed in Section 5.3.2. As the system is initially irradiated, the siloxane molecules adsorbed on the surface of the substrates become partially charged, leading to their ejection from the substrate as a consequence of the high intermolecular repulsion forces.[227] This photonic desorption effect combines with the thermal desorption of D5 from the substrates. Indeed, due to the nature of the UV illumination source, the temperature of the photoreactor increased to 60°C over a period of 30 minutes. This thermal increase in the system supplies energy to the siloxane molecules adsorbed onto the TiO_2 catalysts and substrates, causing them to break their weak bonds to the catalyst surface. As the bonds are broken, the siloxanes are ejected into the gas stream, effectively increasing the observed siloxane concentration. Unfortunately, due to the nature of the UV source, the relative importances of the photodesorption and thermal desorption cannot be deconvoluted and must be treated as a single effect.

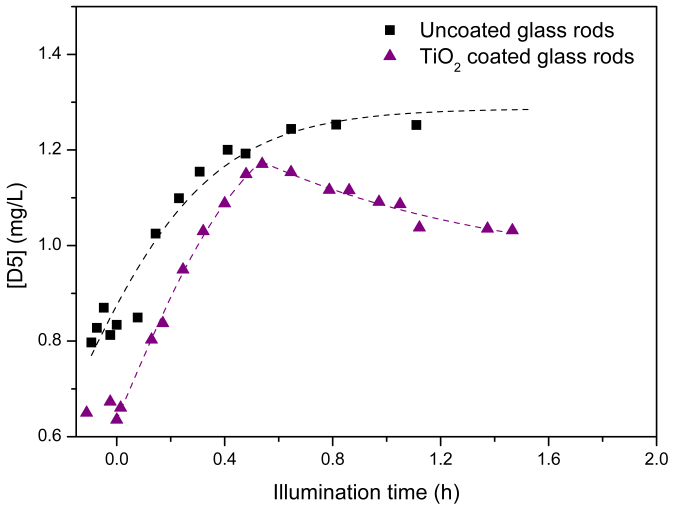

Fig. 6.4 Initial evolution of D5 concentration in a spiked methane stream in relation to UV illumination over uncoated and TiO_2 coated glass rods. The Desorption and photodecomposition effects can be readily observed following UV illumination.

The desorption effects can be clearly seen occurring in Figure 6.4 for the first 30 minutes following the initiation of UV illumination of the catalysts. It is possible to see that the desorption effects occur on both the uncoated glass substrate and the TiO_2 coated rods, demonstrating the independence of the observed phenomenon from the nature of the catalysts. However, as the UV illumination time proceeds beyond 30 minutes, the siloxane concentration is seen to reach a steady state as the system reaches a novel equilibrium under UV irradiation and the rise in temperature. The attainment of a steady state can be observed by the plateau observed in the D5 concentration for the uncoated glass substrates at illumination times beyond 30 minutes.

However, the plateau in siloxane concentration is only observable in the case of the uncoated substrate as the TiO_2 photocatalysts undertake the decomposition of D5 in the gas stream. By observing the concentration of D5 in the gas stream passing over the TiO_2 photocatalysts in Figure 6.4, a clear drop in concentration can be seen beyond 30 minutes of illumination. This observed drop in concentration arises from the photocatalytic degradation of siloxanes in the gas stream by TiO_2. Although the D5 photodegradation occurs from the onset of UV illumination in the system, it can only be observed after the first 30 minutes as it is in direct competition with the thermal and photonic desorption effects. Initially the desorption effects are significantly more important than the photodegradation, leading to the observed increase in D5 concentration in the

gas streams. Eventually, as the system attains a new state of equilibrium, photodecomposition can be observed. By comparing the clean rods with the TiO_2 coated substrates it it possible to determine an average drop in D5 concentration of 0.2 mg/L, this is significantly higher than the concentration of D5 commonly observed in biogas of $\sim$ 0.04 mg/L.[13] As such. it becomes clear that notwithstanding the initial increase in siloxane concentration, P25 coated glass rods display sufficient decomposition abilities to become viable agents for the removal of siloxanes from biogas.

Catalyst Turnover Number

Nonetheless, as the decomposition experiments were extended, the effects of catalyst poisoning could be clearly observed. Figure 6.5 (A) shows the effects of extended UV illumination on the concentration of D5 in the gas stream whilst using TiO_2 coated glass rods (TiO_2 loading of 20 mg, contact time of 0.4 s) as photocatalysts.

Following the establishment of an initial steady state arising from to the photodecomposition of D5 on TiO_2, the concentration of the siloxane is seen to increase gradually until a second steady state is achieved after 2 hours of illumination. This increase in siloxane concentration can be attributed to a gradual poisoning of the P25 by the non-volatile species produced during the decomposition of siloxanes.[126] The SiO_x species build up an insulating layer on the TiO_2 surface which causes the effective inhibition of the catalyst's photoactivity .[127] It is important to note that a similar gradual poisoning of the TiO_2 catalyst was observed by Lamaa *et al.* during a series of experiments on the decomposition of D4 in gas streams.[243]

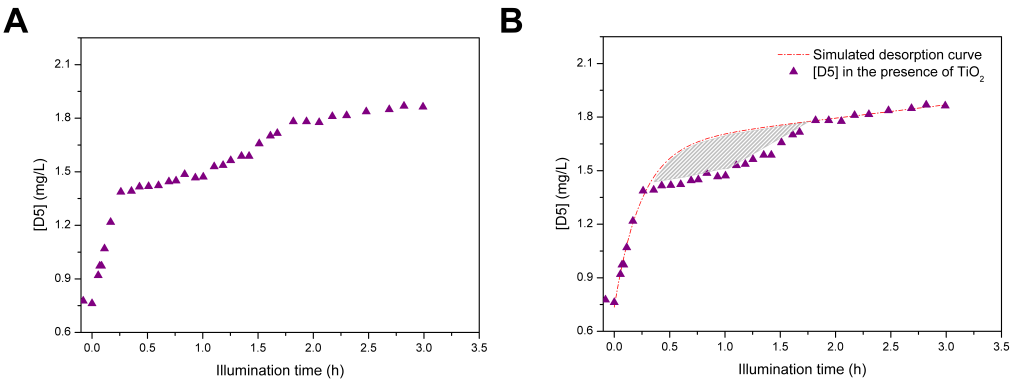

Fig. 6.5 Evolution of D5 concentration in a spiked methane stream in relation to UV illumination. The gradual poisoning of the photocatalyst system is seen in image (A). Figure (B) shows the non-photocatalytic desorption curve simulated in order to determine the TON of the studied systems, the shaded area shows the TOF from which the TON was determined.

From the gradual increase in siloxane concentration it is possible to estimate the turnover number (TON) of the P25 coated glass rods. The TON was calculated by plotting the simulated, non-photocatalytic, exponential increase in siloxane concentration arising from the standard desorption of the siloxane species from the substrate. The simulated plot was compared with the observable photodecomposition portion of the D5 concentration profile. The area difference between these two plots allowed to determine the total amount of D5 decomposed in relation to illumination time, this value is also known as the turnover frequency (TOF). By multiplying the turnover frequency with the flow rate of the system, Q, it was possible to determine the total amount of siloxanes decomposed during the experiment. The TON was then defined as the total amount of siloxanes decomposed (in mg) divided by the total amount of TiO_2 photocatalyst used (m_{cat}, in g) as shown in Equation (6.1). For the studied system the TON was calculated to be 250 $\pm$ 20 mg_{D5}/g_{TiO_2}. The simulated, non-photocatalytic, desorption curve as well as the TOF for the studied system are shown in Figure 6.5 (B).

$$TON = \frac{TOF\, Q}{m_{cat}} \tag{6.1}$$

Catalyst Regeneration

Although the photodecomposition results indicate a good applicability of the photocatalysts as purification agents for the removal of siloxanes in biogas, their limited lifetime can severely hinder the catalyst's industrial applications. As such, it becomes essential to develop methods which allow to achieve the partial or complete regeneration of the photocatalytic activity of poisoned TiO_2 catalysts.

Initially, thermal regeneration was investigated. Figure 6.6 shows the effects of a 450°C regeneration on poisoned TiO_2 photocatalysts. It can be seen in Figure 6.6 (A) that the poisoned catalyst shows a photodecomposition profile similar to that of the plain glass rod substrates (observed in Figure 6.4) demonstrating the complete loss of TiO_2 photocatalytic activity.

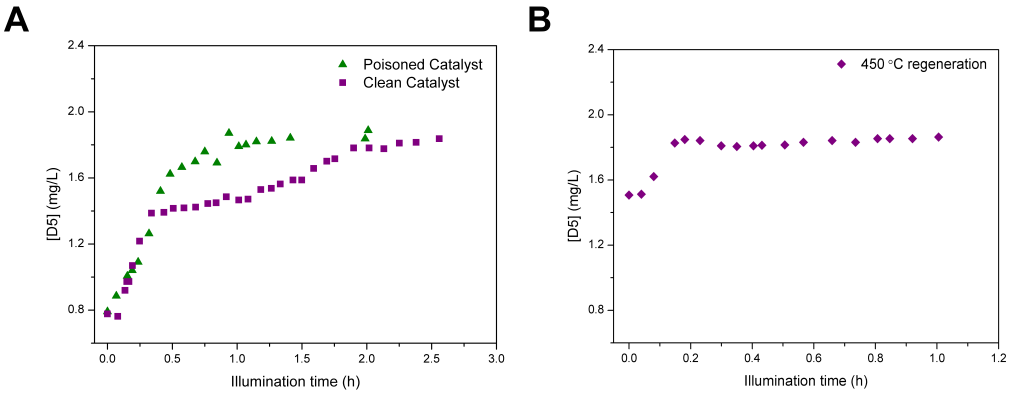

Fig. 6.6 Evolution of D5 concentration in a photoreactor over clean, poisoned, and thermally regenerated photocatalysts. Figure (A) shows the complete inhibition of photocatalytic properties upon poisoning whilst figure (B) shows the effective renewal of the photocatalytic activities after thermal regeneration at 450°C.

Following the thermal treatment at 450°C, the D5 concentration profile under illumination (as seen in Figure 6.6 (B)) can be seen to exhibit a drop in siloxane concentration arising from the photodecomposition of D5. By analysing the concentration profile of the system, it was possible to establish a TON of 23 ± 5 mg_{D5}/g_{TiO_2} for the photocatalyst rods regenerated at 450°C. This TON corresponds to an effective regeneration of catalytic ability of 9.2 %. Table 6.1 shows the extent of thermal regeneration at lower temperatures. The thermal regeneration at 450°C was determined to be the most effective thermal procedure although the extent of regeneration remains minimal.

Table 6.1 Regeneration of poisoned catalyst's photocatalytic abilities as achieved by thermal regenerations at different temperatures.

Regeneration Temperature (°C)	TON (mg_{D5}/g_{TiO_2})	% Regeneration
20	0	0
80	2.0 ± 0.5	1
450	23 ± 5	9.2

The renewed photocatalytic activity can be attributed to the removal of the less volatile partial siloxane decomposition products from the surface of the catalysts. Indeed, it was recently shown by Laama *et al.*[243] and by Chemweno *et al.*[235] in two independent studies that the decomposition of siloxanes in flow reactors generates a number of partial photodecomposition products. These products accumulate on the surface of the TiO_2, preferentially occupying the catalyst's active sites and inhibiting the photodecomposition of siloxanes. As such, the removal of these species from the catalyst surface will lead to the observed partial regeneration of the TiO_2 catalysts.

Although these thermal treatment techniques demonstrate a partial regeneration of the photocatalysts, the low efficacy of the regeneration as well as the high energetic requirements render this technique impractical for industrial applications. Furthermore, the thermal regeneration procedure can cause the mineralisation of the partial decomposition products, counterproductively leading to a further generation of the insulating SiO_x species on the catalyst surface.

Due to the known role of the SiO_x species in the poisoning of TiO_2 catalysts,[126,235,246] a targeted regeneration procedure was investigated. Base washing was used for this purpose due to the high solubility of SiO_2 in basic solutions. Unfortunately, the base regeneration technique resulted inadequate for the studied systems as, following the base treatment, the P25 was removed from the glass substrates (as seen in Figure 6.7). This poor adhesion of the P25 on the glass substrates severely limits its industrial applicability for the photodecomposition of siloxanes in biogas. Furthermore, it is important to note that the use of P25 coated on glass rods is not only limited by the difficulty of base regeneration but also by the mechanical complexity of the dip-coating procedure as well as the inherent fragility of the glass rod substrates.

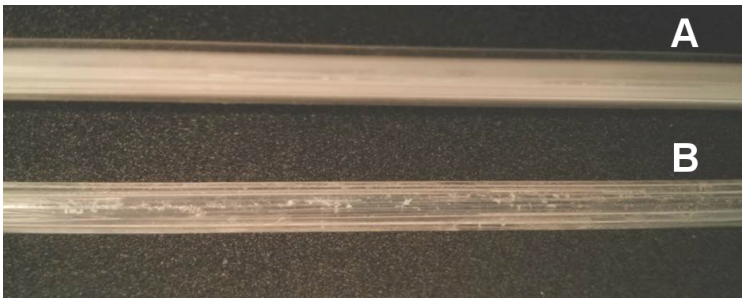

Fig. 6.7 TiO_2 coated glass rods prior to (A) and after (B) base treatment. The loss of photocatalyst after base treatment is clearly visible.

As such, the development of an alternative catalyst support becomes of paramount importance if the studied technologies are to be applied at an industrial scale.

6.3.2 Bead Supported TiO_2 Photocatalyst Efficiency

Glass beads coated with TiO_2 nanoparticles through the GIAC procedure were studied as alternatives to the dip coated glass rods. Initial studies on the stability of the catalyst coating on the beads supplied promising results. Indeed, the effect of immersion of the catalyst coated beads in both aqueous and non-aqueous liquids was seen to result in only a minimal loss of catalyst (an average

loss of 2 ± 0.5 mg of TiO_2 was observed from samples containing 28.6 mg of TiO_2). This improved adhesion can be attributed to the base treatment carried out on the glass beads during the GIAC procedure which formed OH functional groups on the glass surface, thus allowing the generation of a chemical bond between the TiO_2 and the glass, effectively ensuring an enhanced adhesion of the system.

An ulterior advantage of the use of the GIAC coated beads resides in the variation in flow dynamics caused by the different catalyst support structures. It can be seen from the 2D flow dynamics simulations in Figure 6.8 that spherical glass supports display major improvements over their cylindrical counterparts.

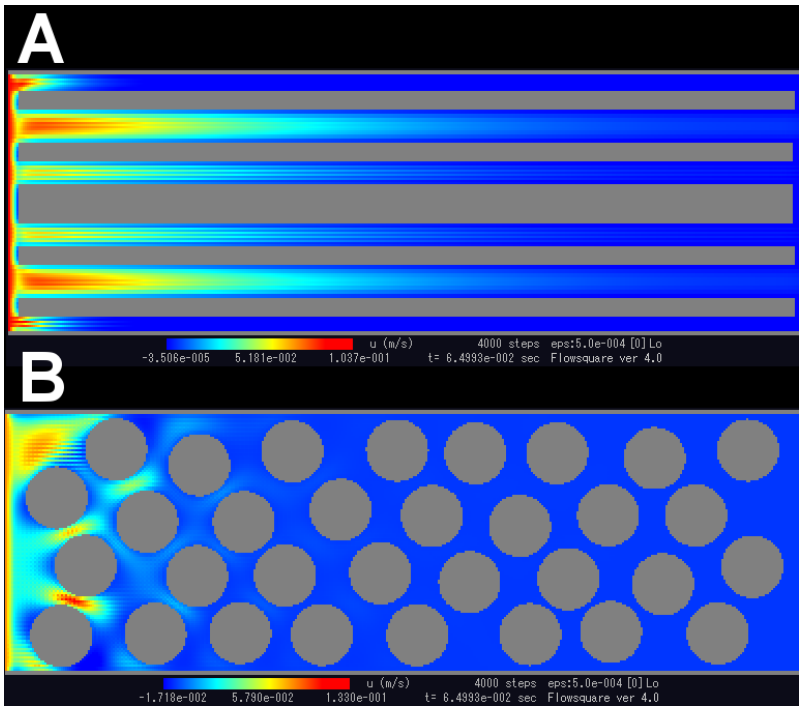

Fig. 6.8 Results of the flow dynamic simulations carried out showing the velocity of the gas flow in 2D cross-sections of the photoreactors over rod (A) and bead (B) supported TiO_2 catalysts. The presence of preferential flow channels when using glass rod supports can be clearly seen. 2D flow dynamic simulations were carried out using the Flowsquare flow dynamic simulation software[241] taking into account the experimental gas flow rate, density and temperatures.

The velocity of the fluid flowing through the photocatalytic reactors is shown in Figure 6.8 (A) and (B) for the glass rod and sphere substrates, respectively. It can be seen that the use of glass rods leads to the formation of preferential flow channels throughout the system. This signifies that the majority of the siloxane filled gas streams will only come into contact with a very limited portion of the TiO_2 catalyst. This minimal gas-catalyst contact is further exacerbated by the generation

of a laminar flow near the surface of the glass rods. This can be observed in Figure 6.8 (A), where the fluid velocity is greatly reduced at the glass rod interface, meaning that the amount of siloxanes coming into contact with the studied systems at any given moment is further limited. The mathematical complexities of the laminar behaviour of fluids along cylindrical rods were extensively presented by K. Chen in 1973.[247]

Spherical systems, however, do not induce laminar but rather turbulent flows when coming in contact with fluid streams. By observing Figure 6.8 (B), the lack of preferential flow channels is readily apparent as the fluid maintains a homogeneous velocity throughout the whole system. It is of further importance to note that the fluid velocity at the surface of the beads is close to that in the bulk fluid, meaning that a greater gas/catalyst contact can be achieved. The observation of turbulent, rather than laminar, fluid flows over glass spheres is consistent with the calculations and observations of Patil and Lidbury during their study of fluid flows in randomly packed porous bed reactors.[248] This turbulent flow is of particular importance during the photocatalytic elimination of siloxanes from gas streams as it indicates an equal distribution of the siloxane stream amongst all of the TiO_2 catalysts as well as a good contact between the siloxane molecules and the catalysts.

Effects of Contact Time on Siloxane Decomposition

In addition to the aforementioned advantages, the use of the spherical glass substrates allows for an increased modularity of the system. Through the use of glass beads it was possible to modify the contact time between the gas streams and the catalysts by simply adding or removing beads from the quartz tubes. However, this versatility was not possible with the glass rod supports due to the mechanical and experimental limitations of the dip-coating procedure which significantly restricted the dimensions of the glass supports employed.

By studying the photodecomposition of siloxanes over the TiO_2 catalysts at different contact times, it was possible to achieve an improved understanding of the scalability of the created reactors. Figure 6.9 shows the total amount of decomposed D4 before catalyst deactivation was observed. From the presented data it becomes possible to establish a linear relationship between the total mass of decomposed D4 and the contact time with the TiO_2 catalyst. As such, it was possible to determine that the total amount of decomposed D4 increased by 10 mg per second of increased contact time.

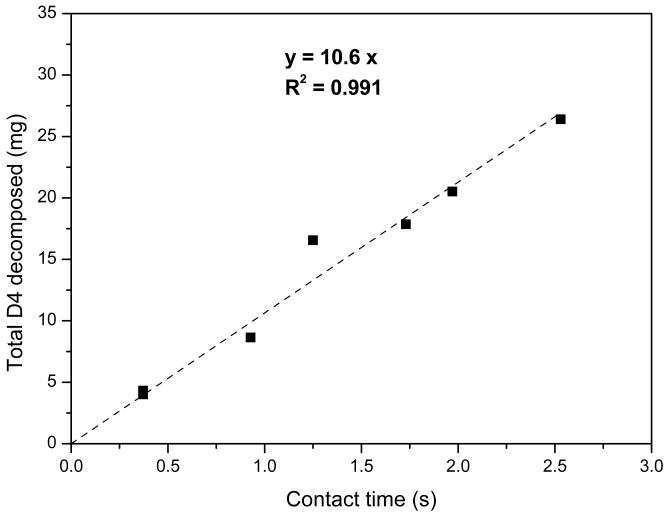

Fig. 6.9 Graph showing the correlation between gas-catalyst contact time and the total amount of D4 decomposed before the loss of photocatalytic activity is observed in the system. The linear correlation between the two effects can be clearly observed.

The determination of this correlation was an essential asset to the eventual industrial application of the developed technologies. Indeed, a good understanding of the correlation between gas-catalyst contact time and the maximum amount of siloxane decomposed can be used in order to engineer and tailor the eventual lifetime and size of the developed photoreactors.

Photodecomposition of L4 and D4

The photodecomposition of gas streams loaded with L4 and D4 is shown in Figure 6.10. The siloxane concentration profiles for L4 and D4 can be seen to display the three main events previously observed during the photodecomposition of D5: desorption, photodecomposition, and catalyst poisoning. From these photodecomposition profiles it was possible to establish the TON for the photodecomposition of D4 and L4 by the bead-supported TiO_2. The TON for the decomposition of D4 and L4 were determined to be 146 ± 6 mg_{D4}/g_{TiO_2} and 113 ± 6 mg_{L4}/g_{TiO_2}. The higher TON of the photodecomposition of D4 with respect to that of L4 indicates that the number of Si atoms (and thus, the number of generated SiO_x species) is not the only factor affecting the observed poisoning of the TiO_2.

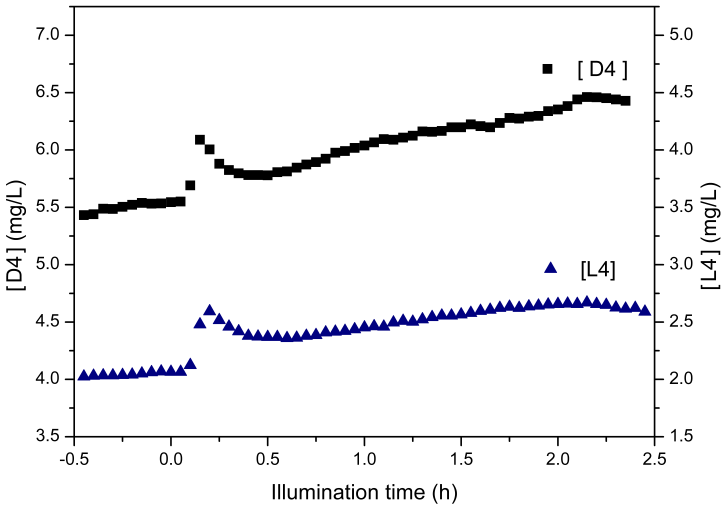

Fig. 6.10 Evolution of the concentrations of D4 and L4 in separate gas streams during photodecomposition experiments using TiO_2 coated glass beads as active photocatalysts.

The effects and sources of heterogeneous catalyst deactivation have been presented extensively by Bartholomew.[240] Amongst the different sources of catalyst deactivation, the effects of carbon fouling were observed in a number of different systems. It has been suggested that carbon fouling arises from the incomplete mineralisation of carbon containing species.[249–251] As the carbonaceous molecules are decomposed, they are known to form coke. Coke is a general term commonly used for the incomplete mineralisation products arising from the decomposition of hydrocarbons.[250] The generated coke is then believed to occupy and clog the reactive sites of heterogeneous catalysts, leading to the eventual loss of photocatalytic activity similar to that caused by the SiO_x species generated during the photodecomposition of siloxanes. As such, the difference in TON observed between the photodecomposition of D4 and L4 on TiO_2 can be attributed to differences in carbon fouling due to the higher carbon content of L4. Another indication of the presence of carbon fouling can be seen in Figure 6.11 where the deactivated catalysts (B) display a significantly darker yellow coloration with respect to the unused catalysts (A). This coloration of the catalysts is indicative of the deposition of carbonaceous species on the catalyst surface as has been previously described in literature.[252]

Fig. 6.11 Yellow coloration of the poisoned TiO_2 coated beads (B) with respect to unused TiO_2 coated beads (A).

This understanding of the origins of the photocatalytic deactivation of TiO_2 is an essential asset to determining suitable catalyst regeneration techniques. Although thermal regeneration has been determined partially effective and base treatment allows to target the main cause of photocatalytic deactivation (the SiO_x species), the development of alternative regeneration techniques specifically targeting the incomplete siloxane mineralisation products, remains of crucial importance. One such method is that of washing the catalyst with non-polar solvents which would allow to preferentially remove non-polar species unbound to the TiO_2 surface.

Photocatalyst Regeneration

During these experiments a number of different regeneration techniques were used in order to renew the photocatalytic activity of the poisoned catalysts.

The TON for the photocatalytic decomposition of D4 on TiO_2 catalysts regenerated through a variety of techniques are shown in Table 6.2. It can be seen that although all of the washing methods provided an effective regeneration, the recoating procedures (regenerations of 103.4 % and 105.6 % for the TT^iP and GIAC recoating techniques, respectively) were by far superior to the simple washing techniques (regenerations of 62.9 % and 83.5 % for the basic and non-polar solvent washes, respectively). This difference further emphasises the complexity of achieving photocatalyst regeneration through the targeted elimination of the poisoning species. Indeed, the partial regeneration achieved through the washing techniques indicates the persistence of a number of chemically bound poisoning elements on the TiO_2 surface.

This setback inherent to the chemical regeneration techniques, however, does not affect the

recoating regeneration procedures. During the recoating techniques the surface of the deactivated catalysts is used as a non-reactive support for a novel catalytic coating which negates any effects caused by partial (or complete) decomposition products on the catalyst surface. Nonetheless, by comparing the washing techniques with each other as well as the recoating techniques, it is possible to gain a further understanding of the nature of the poisoning caused by the photomineralisation of siloxanes.

Table 6.2 Regeneration of the photocatalytic abilities of the TiO_2 nanoparticulates after a variety of different techniques. The mass difference shows the variation in mass of the studied samples after the performed regenerations.

Regeneration method	Mass difference (mg)	TON (mg_{D4}/g_{TiO_2})	% Regeneration
Pristine TiO_2	n/a	150 ± 6	n/a
Base washing	$- 3.2 \pm 0.5$	94 ± 6	62.9
Hexane washing	0 ± 0.5	126 ± 6	83.5
TT^iP recoating	2.9 ± 0.4	156 ± 6	103.4
GIAC recoating	12.8 ± 0.6	159 ± 6	105.6

By observing the TON and % regeneration of the two samples regenerated through the washing procedures as shown in Table 6.2, it becomes clear that the non-polar solvent washing procedure (83.5 % regeneration) was significantly better than the base washing (62.9 % regeneration) procedure. The higher effectiveness of non-polar washing over the base washing regeneration procedure can be attributed to two main factors. Firstly, the non-polar solvent washing technique is believed to act solely on the removal of incomplete photodecomposition products from the active sites of the TiO_2; it was theorised by Laama *et al.*[243] that the more stable partial decomposition products of D4 were species with little or no polarity. These species would be preferentially extracted from the surface of the TiO_2 catalysts through the non-polar solvent washing procedure. On the other hand, due to the highly polar aqueous nature of the base washing regeneration procedure, extraction of the fouling agents from the active sites would prove significantly less favourable. The second factor leading to the advantageous regeneration of the non-polar solvent washing with respect to the polar solvent washing, can be attributed to the natural shortcomings of the base washing technique. Indeed, the base mediated regeneration technique focuses on the use of aqueous NaOH. As such, the washing of the catalysts subsequent to the immersion in the basic solution may not allow for the removal of all of the NaOH from the system. Any leftover base in the system would effectively act as a fouling agent by preferentially occupying the active sites of the TiO_2. It is further important to

note that during their studies, Ren-De Sun *et al.* also reported a limited renewal of photocatalytic activity after washing the solvent in a dilute basic solution.[126]

Comparatively to the washing regeneration techniques, the differences between the two recoating procedures can be explained by the total amount of novel catalyst added on top of the deactivated catalysts. Table 6.2 shows that the total amount of active catalyst (the mass of catalyst gained after the recoating procedure) is by far superior in the case of the GIAC recoated beads (2.8 mg of active catalyst for the TT^iP recoated beads as compared to 12.8 mg of active catalyst for the GIAC recoated beads). As such the increased mass of TiO_2 on the GIAC coated beads leads to more photocatalytically active surface area accessible for the photodecomposition of siloxanes as compared to the TT^iP recoated beads. However, it is also important to observe in Table 6.2 that the recoated catalysts display TON values higher than that of the clean counterparts. Whilst the TON for TT^iP recoated beads remains within the experimental error for the studied systems, this is not the case for the beads recoated with the GIAC procedure. This supra 100 % regeneration for the GIAC coated beads can be attributed to the increased loading of TiO_2 on the glass beads (the clean beads were observed to have a TiO_2 loading of 4.5 mg_{TiO_2}/g_{beads} whilst the GIAC recoated beads had a loading of 6.5 mg_{TiO_2}/g_{beads}). These increased TiO_2 loadings on the glass beads can lead to increased surface areas which would further increase the amount of active sites available for siloxane photodegradation, thus increasing the TON of the systems.

Overall, it becomes clear that a large variety of techniques can be developed for the regeneration of deactivated TiO_2 catalysts. However, it was important to note that due to industrial limitations, the GIAC recoating technique can be considered the most viable approach developed for the regeneration of deactivated TiO_2 photocatalysts. This is the case since the GIAC procedure is already required in order to achieve an initial coating of TiO_2 on the glass beads, signifying that the only additional costs faced by using this procedure for the regeneration of the catalyst lie only in the procurement of the additional P25.

6.4 Conclusions

During this series of experiments, initial studies allowed to demonstrate that the photocatalytic decomposition of siloxanes presented in Chapter 5 was maintained in gas flow conditions. An

effective reduction of siloxane at concentration levels 500 % higher than those commonly found in biogas was observed. However, as the photocatalytic decompositions were prolonged, a decline in photocatalytic activity occurred. This decline allowed to quantify the lifetime of the photocatalysts as a TON in terms of mass of decomposed siloxanes per mass of catalyst used. By examining and comparing the evolutions of TON in different systems it was possible to establish a linear correlation between the contact time and the total amount of siloxane decomposed before photocatalytic deactivation. Furthermore, by comparing the TON of different systems the strengths and qualities of a variety of different regeneration techniques were successfully studied.

Three main types of regeneration methods were investigated: thermal regeneration, liquid washing regenerations, and catalyst recoating regenerations. The thermal regenerations were seen to be mildly effective, achieving only a 9 % regeneration at high temperatures. More promising results were achieved with the washing techniques which achieved regenerations of up to 83.5 % by eliminating the partial siloxane decomposition products fouling the TiO_2 catalyst surface. However, the most successful regenerations were observed whist using recoating techniques which led to the complete renewal of TiO_2 photocatalytic activity. This complete photocatalytic renewal was possible as a consequence of the the deposition of a novel photoactive layer on top of the depleted TiO_2 layers. Of the different regeneration techniques, the recoating of deactivated TiO_2 through the GIAC procedure was established as the ideal method for industrial applications.

In conclusion, during these experiments, the photocatalytic decomposition of siloxanes on TiO_2 during in flow streams was successfully studied with an aim to adapt the technologies to industrial environments. The GIAC procedure allows for the facile creation of glass supported photocatalysts for siloxane decomposition. These photocatalysts can be used in a in order to achieve both a favourable decomposition rate and a desired photocatalyst lifetime. Finally, the deactivated photocatalysts could be recoated with the GIAC procedure. This versatile system signifies that the developed techniques could be used to pave the way for second generation biogas purification devices.

Furthermore, the developed photocatalytic reactors could be used for the decomposition of a wide variety of non-siloxane species in gas streams. Many volatile organic compounds (VOCs) are emitted in industrial, domestic, and urban environments such that the development of an economical and efficient method for their removal becomes an increasing necessity in the 21st century.

7. Volatile Organic Molecule Degradation

In Chapters 5 and 6 it was possible to demonstrate the successful photodecomposition of siloxanes in the gas phase by using immobilised TiO_2 photocatalysts. Due to the versatility of the designed systems, it was postulated that the created device could be used for the elimination of alternative chemical contaminants present in gas streams. During the present series of experiments, an improved photoreactor design was used to study the decomposition of three model Volatile Organic Compounds (VOCs) in gas streams: acetone, isopropyl alcohol (IPA), and styrene.

Initial studies allowed to determine the effects of TiO_2 loading on the glass bead substrates used during the photoreactions by monitoring, through Fourier Transform Infrared Spectroscopy (FTIR), the evolution of CO_2 production in gas streams loaded with acetone. From these, it was possible to establish an ideal catalyst loading for the designed systems in order to maximise the decomposition of VOCs in gas streams. By monitoring the VOC concentrations in the photoreactor exhausts it was further possible to determine the conversion percentage for each species as well as their photodecomposition rates.

Finally, by analysing the CO_2 production from the photodecomposition of styrene it was possible to demonstrate the production of secondary photodecomposition products. The identity of these products was elucidated through Gas Chromatography coupled with Mass Spectrometry (GC-MS). Through literature studies it was possible to propose schematic mechanisms for the TiO_2 mediated formation of secondary photodecomposition products.

The successful decomposition of the different VOC species as well as the identification of partial photodecomposition products, demonstrate the versatility and importance of the created technologies. As such, through the performed studies, it was possible to show the applicability of the designed photoreactor not only as an air purification device but also as the active element in a chemical synthesis pipeline.

7.1 Introduction

With the growth of the service industry and the industrialisation of rural environments, the 20th and 21st centuries have seen humans spend increasing amounts of time in enclosed environments. In the mid 1990's it was estimated that the American population spent on average 87% of their time in indoor environments and an additional 6% in transport vehicles.[253] As a consequence of this, the quality and nature of indoor environments has become of paramount importance. Many studies have been carried out on the nature of indoor air contaminants[254–256] and their effects on human health.[257,258] Amongst the different classes of harmful contaminants identified in indoor air, that of VOCs is of particular importance due to its diverse origins and prevalence in domestic as well as workplace environments.[259–261]

In recent years, a number of technologies have been developed for the elimination of VOCs in indoor environments. However, these techniques are often impractical or highly energetic. This can be seen clearly in the case of the device constructed by Kung-Ming Chu[262] which relies on the use of adsorbent species for the removal of VOCs (which generates the problem of adsorbent disposal) and in the case of the device constructed by Stephen T. Homeyer *et al.*[263] which requires operating temperatures exceeding 120°C. As such, the development of an alternative method for the effective removal of VOCs from ambient air has garnered significant academic[264–266] and commercial[267–269] interest. Of the different techniques studied for ambient air purification, that of photodecomposition is amongst the most promising as it offers a facile and energetically economical solution.

Photodecomposition is a technique that can be first attributed to Mashio *et al.* in 1956 with their study on the autooxidation of organic solvents by TiO_2.[270] However, this research failed to gain traction and it wasn't until 1977 when, after the popularisation of TiO_2 photolysis by Honda and Fujishima,[271] that Frank and Bard demonstrated the elimination of cyanide in aqueous suspensions of TiO_2[272] causing the use of photocatalysis for the removal of pollutants to be actively considered. Since then, a large number of studies have been carried out in order to determine the mechanisms, kinetics, and efficiency of the photodecomposition of organic contaminants by TiO_2.[273–275]

During the present series of studies, TiO_2 was used as a photocatalyst in a novel photoreactor design in order to achieve the photodecomposition of three VOCs: acetone, IPA, and styrene. Although many alternative photocatalyst materials have been investigated since the studies of Frank

and Bard in 1977, TiO_2 has remained the optimal catalyst for the photocatalytic elimination of organic pollutants due to its low cost and high chemical stability.[276–278]

The three VOCs studied were chosen not only for their well-known toxicity to human and animal life,[279–281] but also as illustrative species to demonstrate the effectiveness of the photoreactions on different chemical families. Indeed, the study of the photodecomposition of acetone, IPA, and styrene can be seen as qualitatively representative of the photodecomposition processes on carbonyl, hydroxyl and vinyl moieties, respectively, as these are the principal sites of reactivity on the VOCs. As such, through a successful study of the effectiveness of the designed photoreactor as a purification device for VOCs in gas streams, it is possible to determine the viability of the developed system for the purification of indoor environments.

Furthermore, it is known that in particular conditions photoreactors do not carry out the complete mineralisation of VOCs.[81] As such, during the present series of experiments a study on the partial photodecomposition products of styrene was carried out, allowing to ascertain the photosynthetic potential of TiO_2 photocatalysis.

7.2 Experimental

7.2.1 Chemicals and Characterisation Techniques

Acetone was sourced from VWR and used as received. IPA and styrene were sourced from Fisher Scientific and used as received. All remaining chemicals used during the following experiments were sourced form Sigma-Aldrich UK and used as received unless otherwise stated. During the photodecomposition experiments, UV_a light was supplied by a cold cathode lamp sourced from Xenta whilst the compressed air used as carrier gas was sourced from BOC.

The characterisation of the P25 coating on glass beads was carried out through the use of Scanning Electron Microscopy (SEM), using a JEOL-JSM 820 Scanning Microscope. Prior to SEM imaging, the TiO_2 coated beads were gold coated for 5 minutes using an Edwards S150 sputter coater to eliminate charging effects from the electron beam used during SEM imaging.

The concentration of VOCs during the flow decomposition studies was monitored using gas

phase FTIR. The IR spectra were collected using a Perkin Elmer SpectrumOne FTIR spectrometer with a gas phase IR cell (130 mm long) equipped with NaCl windows (25 mm in diameter). The degradation of VOCs was examined by monitoring the area under specific vibrational peaks. The peak studied for the photodecomposition of acetone was that corresponding to the carbonyl stretch (1850 - 1650 cm^{-1}). In order to study the photodecomposition of IPA, the peak corresponding to the OH stretch (3700 - 3600 cm^{-1}) was monitored. Styrene photodecomposition was investigated by monitoring the peaks corresponding to its sp^2 C-H stretching and out of plane C-H ring bending (3140 - 2940 cm^{-1} and 940 - 870 cm^{-1}, respectively). A further understanding of the reactions was achieved by monitoring the concentration of CO_2 generated during the systems. The CO_2 concentration was studied by observing the area under the peak arising from its asymmetric stretch (2390 - 2230 cm^{-1}).

In order to analyse the photodecomposition products of styrene, a PerkinElmer Autosystem XL Gas Chromatograph (GC) equipped with a PerkinElmer TurboMass Mass Spectrometer (MS) was used. The GC was mounted with a Restek RXI-5ms column 30 m in length with an internal diameter of 0.25 mm and a film thickness of 0.25 μm. In order to achieve a suitable separation of the different species in the studied liquids, an appropriate GC method was developed using helium as a carrier gas with a flow rate of 40 ml/min. The analysed liquids were injected into the GC column by using an automated split injection with a split ratio of 29.8, an injection volume of 0.2 μl and an injector temperature of 220°C. The GC oven was held at 50°C for 4 minutes then heated to 200°C using a ramp rate of 20°C/min. After holding at 200°C for 4 minutes, the the oven was further warmed to 300°C using a ramp rate of 40°C/min. Lastly, the oven was held at 300°C for 4 minutes. During this run MS was performed by Electron Ionisation (EI). The MS scanned the mass region between 45 and 300 m/z (amu/e) for a total of 22 minutes with a 4 minute solvent delay.

7.2.2 P25 Immobilisation on Glass Beads

In order to develop a successful photocatalytic VOC decomposition reactor, the photocatalyst immobilisation on specific supports was essential. Due to their particular effectiveness in Chapter 6, glass beads were chosen as the preferred catalyst support during this series of experiments.

The immobilisation of the photocatalysts was performed through the use of the Gyration Induced Adhesive Coating (GIAC) technique described in Section 6.2.4. A known amount of

glass beads ($\bar{d}$: 2.5 $\pm$ 0.3 mm, sourced from Glass Sphere S.R.O) were base treated by washing in acetone and ethanol prior to being boiled in basic solution ($NaOH_{(aq)}$, 6M) for 2 hours. These base treated glass beads were then washed with de-ionised water until the washings were observed to be neutral, and accurately weighed in order to account for any loss of mass resulting from the base treatment. The known mass of glass beads was then placed in a rotating drum in combination with an appropriate amount of P25 in order to achieve the desired loading (loadings of 1, 3, 5, and 7 mg_{TiO_2}/g_{beads} were investigated) and allowed to rotate overnight. After the rotation, the beads were reweighed and their loading was precisely determined.

7.2.3 VOC Photodegradation Reactor Design

The photoreactor design used during this series of experiments was adapted from that presented by Verbruggen *et al.*[282] Figure 7.1 shows the general experimental set up for the photodecomposition reactions studied during this series of experiments. It can be seen that the photoreactor design varies significantly from that presented in Chapter 6 by using a larger quantity of catalyst loaded beads as well as changing the illumination source from an external system to a more encompassing internal UV_a source.

Introduction of VOCs in the gas stream

In order to introduce the VOCs in the gas stream during this series of experiments, the technique used for the introduction of siloxanes in the gas streams in Chapter 6 was reprised. A known amount (5 ml) of the studied VOC in liquid form was placed in a Dreschel bottle under a continuous gas stream (compressed air with a flow rate of 4.31 $\pm$ 0.51 L/h was used as a carrier gas during this series of experiments). By altering the length of the dip tube in the Dreschel bottle it was possible to control and maintain constant concentrations of the VOC species. The length of the dip tube was kept at 2, 5, and 17 cm for the study of the decompositions of acetone, IPA, and styrene, respectively.

Photodecomposition of VOCs

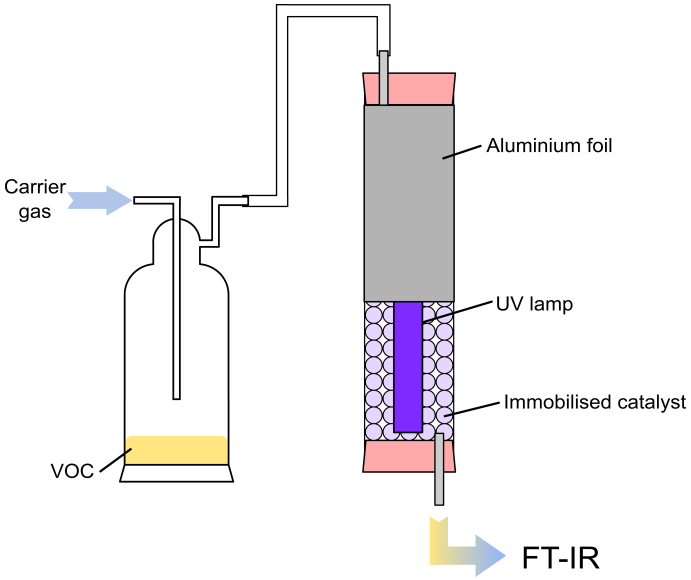

Fig. 7.1 Schematic diagram showing the experimental set up used for the photodecomposition of VOCs in gas streams. The lower half of the reactor tube is shown as exposed for illustrative purposes.

The VOC loaded gas stream was passed at a controlled flow (4.31 $\pm$ 0.51 L/h) through the photoreactor shown in Figure 7.1. The photoreactor was composed of a quartz tube (400 mm in length, 24 mm in internal diameter) containing a cold-cathode UVA fluorescent lamp (305 mm long, 4.0 mm in diameter with a spectral peak intensity of 365.44 nm and a power output of 22.6 mW) and a known mass (189.3 g) of catalyst-coated glass beads. By using rubber bungs equipped with stainless steel inlet/outlet tubes (plugged with glass wool) it was possible to render the system airtight whilst maintaining control on the UV_a lamp as well as on the gas stream. Finally, aluminium foil was wrapped around the quartz tube in order to reflect outgoing UV_a light and maximise the irradiation of the used photocatalysts.

After passing through the photoreactor, the gas stream was taken to a FTIR gas cell in order to monitor the VOC and CO_2 concentrations of the system. By monitoring these concentrations it was possible to gain invaluable insight on the photodegradation of VOCs by TiO_2 photocatalysts.

7.2.4 Exhaust trapping Technique

In order to achieve a further understanding of the mechanical processes governing the photodegradation of VOCs, chemical trapping followed by GC-MS analysis was performed on the exhaust of the photoreactor whilst using styrene loaded gas streams. The experimental set up for chemical trapping of the exhaust species is shown in Figure 7.2.

The exhaust stream was bubbled through a round bottomed flask containing a highly polar solvent (1,4-Dioxane) which acted as a trapping agent and allowed to concentrate the partial photodecomposition intermediates. The collection was carried out for a continuous period of 8 hours prior to analysis of the solution through GC-MS. In order to minimise the loss of trapping solvent as well as that of highly volatile species, the round bottomed flask was equipped with a condenser as shown in Figure 7.2.

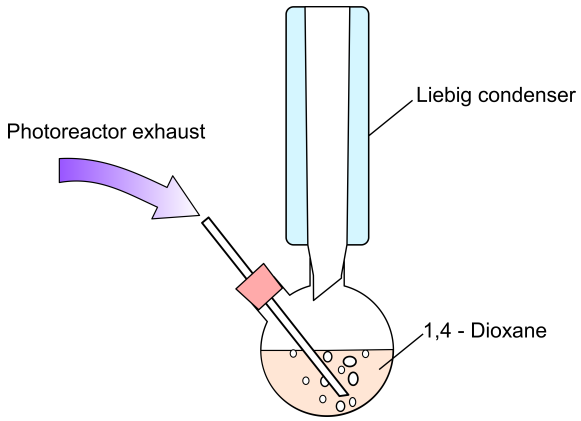

Fig. 7.2 Schematic diagram showing the experimental set up used for the chemical trapping of the photoreactor exhaust during the photodecomposition of styrene.

7.3 Results and Discussion

7.3.1 Effectiveness of Acetone Photodegradation

Figure 7.3 shows the effect of UV_a illumination on the CO_2 content of the gas streams loaded with acetone. The photocatalytic nature of the reaction is evidenced by the low and high CO_2 concentration steady states related to the illumination of the photoreactor. As the TiO_2 photocatalyst is illuminated with UV_a light, acetone is oxidised and eventually undergoes complete mineralisation,

leading to the observed CO_2 concentration increase in the gas streams. When the UV_a illumination in the system is ceased, the photocatalytic degradation of acetone is halted, leading to a drop in CO_2 concentration. A similar increase in CO_2 concentration arising from the complete mineralisation of acetone was observed by Verbruggen *et al.*[282]

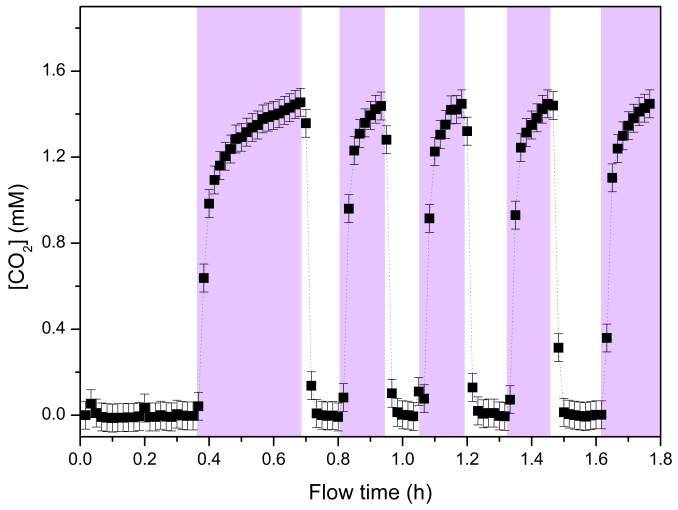

Fig. 7.3 [CO_2] in a gas stream containing acetone in relation to flow time and UV_a illumination. The white and violet (shaded) backgrounds correspond to periods of darkness and UV_a illumination, respectively.

As the concentration of CO_2 in the gas stream arises from the complete mineralisation of acetone, it was possible to evaluate the TiO_2 photocatalyst effectiveness by monitoring the increase in CO_2 concentration recorded at different catalyst loadings on the glass beads.

Effects of Catalyst Loading

From the steady state concentration of CO_2 achieved during the photodecomposition of the studied VOCs it was possible to establish an overall rate of CO_2 production, σ_{CO_2}, for each reaction. σ_{CO_2} was defined as the product of the difference between the steady state CO_2 concentrations in the presence and absence of UV_a illumination, $[CO_2]_{\Delta ss}$, and the gas flow rate, Q, through the system, as shown in Equation (7.1). The overall rate of CO_2 production was considered during this series of experiments rather than the absolute rise in CO_2 concentration as this allowed for a more appropriate representation of the studied systems by taking into account the effect of the gas flow

rate.

$$\sigma_{CO_2} = Q[CO_2]_{\Delta ss} \tag{7.1}$$

Figure 7.4 shows the rate of CO_2 production achieved during the photodecomposition of acetone by glass beads with different loadings. It can be seen that the production CO_2 increases proportionally with increasing TiO_2 loadings until reaching a maximum rate of 5.75 ± 0.07 $mmol_{CO_2}/h$ for a catalyst loading of 5 mg_{TiO_2}/g_{beads}.

The decrease in CO_2 production rate as the catalyst loading is increased to 7 mg_{TiO_2}/g_{beads} observed in Figure 7.4 can be attributed to an excessive TiO_2 loading on the catalyst beads. Indeed, although an increase in catalyst loadings leads to an increase in photocatalytic activity due to the introduction of more active sites for the photodecomposition of VOC species, the increased loadings also result in an increased UV_a adsorption of each individual bead. In the case of excessive catalyst loadings, only the beads closest to the UV_a lamp will become photoactive, effectively inhibiting and deactivating the beads furthest from the lamp. Due to the turbulent flow of the gas stream through the reactor, this inhibition of the external beads results in a significant loss in VOC decomposition. As a consequence of the dual effects caused by increases in catalyst loading, there exists an ideal TiO_2 loading on the glass beads for the photodecomposition of VOCs. It can be seen in Figure 7.4, that a loading of 5 mg_{TiO_2}/g_{beads} was optimal for the degradation of VOCs in the studied system.

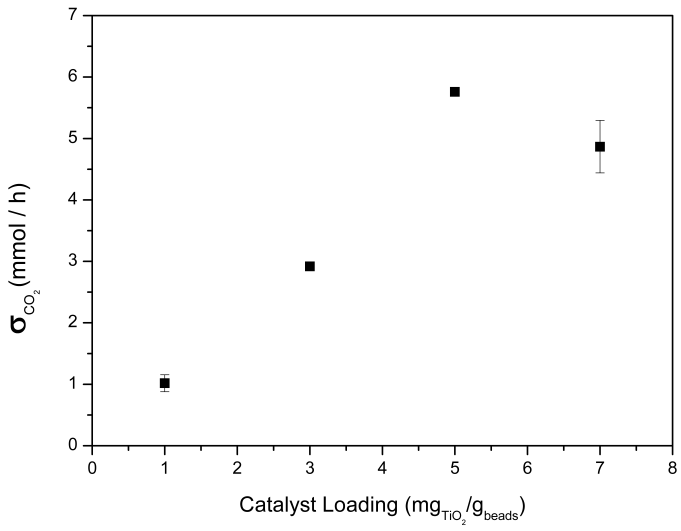

Fig. 7.4 Evolution of CO_2 production rates from the photodecomposition of acetone with respect to different catalyst loading.

Further analysis through mechanical abrasion and SEM imaging demonstrated ulterior advantages of the 5 mg_{TiO_2}/g_{beads} catalyst loading. It can be seen from the SEM images in Figure 7.5 that as the P25 loading on the beads is increased, the P25 on the surface of the beads has a tendency to form increasingly larger aggregates. These aggregates result from a weaker binding of the photocatalyst to the surface which leads to a significantly weaker adhesion of the catalyst coating on the surface of the glass beads.

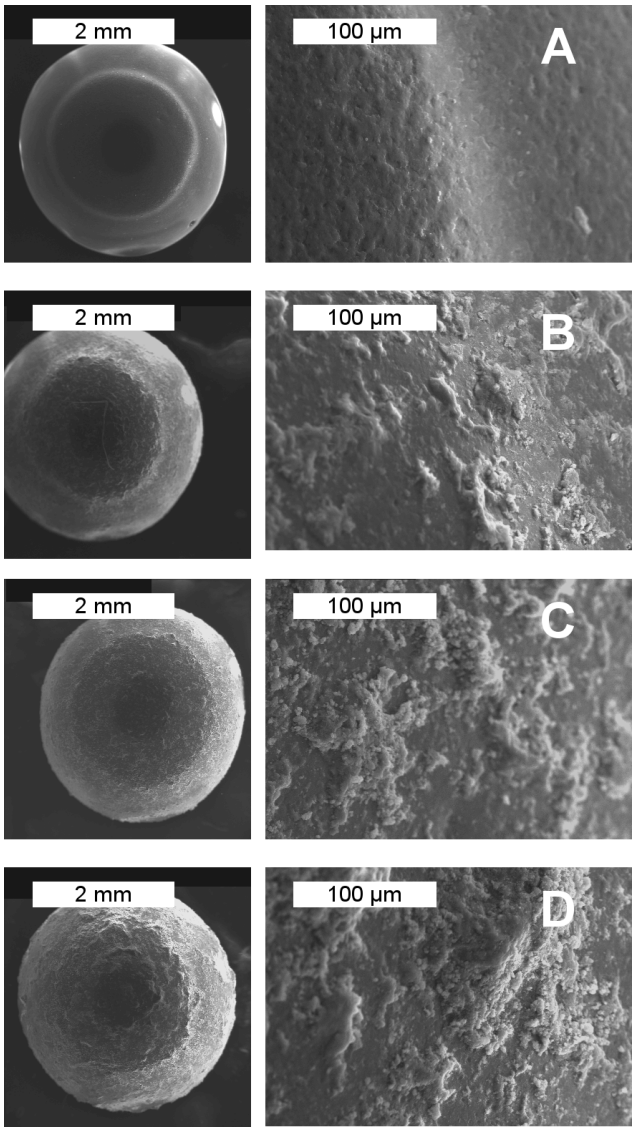

Fig. 7.5 SEM images of glass beads coated with TiO_2 using the GIAC method. The catalyst loadings are, 1 mg_{TiO_2}/g_{beads}, (A), 3 mg_{TiO_2}/g_{beads}, (B), 5 mg_{TiO_2}/g_{beads}, (C), and 7 mg_{TiO_2}/g_{beads}, (D).

The weaker adhesion of the larger aggregates can be seen in Figure 7.6 where the beads coated with a 1 mg_{TiO_2}/g_{beads} loading show a negligible loss in TiO_2 after mechanical abrasion (B) whilst

the beads with a 7 mg_{TiO_2}/g_{beads} loading show a nearly complete loss of surface catalyst after abrasion tests, becoming visually similar to the uncoated beads. From Figure 7.6 it can be seen that the beads coated with a 5 mg_{TiO_2}/g_{beads} loading displayed an intermediate level of catalyst loss, further emphasising the advantages of this catalyst loading.

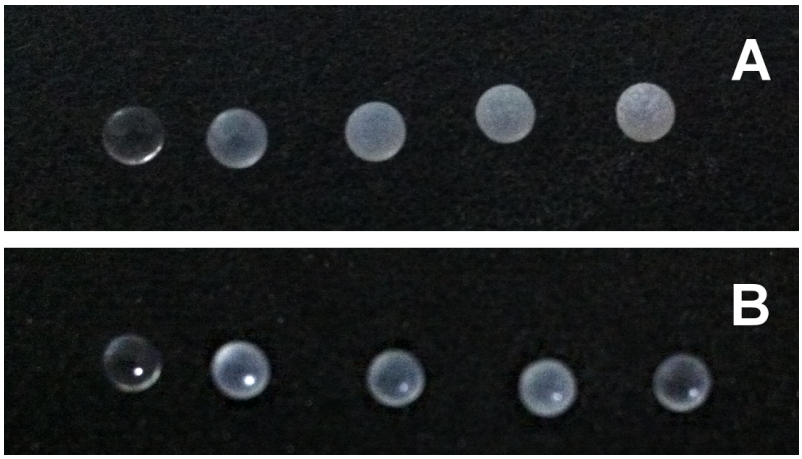

Fig. 7.6 Glass beads coated with TiO_2 using the GIAC method before (A) and after (B) mechanical abrasion. The catalyst loadings are, from left to right, 0, 1, 3, 5, and 7 mg_{TiO_2}/g_{beads}. The poor stability of the 7 mg_{TiO_2}/g_{beads} coating can be clearly seen.

Due to the heightened mechanical resistance of the 5 mg_{TiO_2}/g_{beads} coating with respect to the 7 mg_{TiO_2}/g_{beads} loading as well as their respective σ_{CO_2} (seen in Figure 7.6 and Figure 7.4, respectively), the 5 mg_{TiO_2}/g_{beads} loading was used for the study of the decomposition of all VOCs during this series of experiments.

Decomposition of Acetone

Although it was possible to determine the σ_{CO_2} for the reaction, this remains only a qualitative indication of the reactions occurring to the acetone molecules contained in the gas stream. It is indeed known that the photocatalytic mineralisation of acetone to CO_2 proceeds through a variety of stable chemical intermediates.[283] As such, it becomes essential to study the photodecomposition of acetone directly rather than from the concentration of the ultimate reaction product.

During these studies, the direct photodecomposition of acetone was observed by monitoring the difference in steady state concentration of acetone in the exhaust stream in the presence and absence of UV_a illumination. Figure 7.7 shows the evolution of acetone concentration in the exhaust stream.

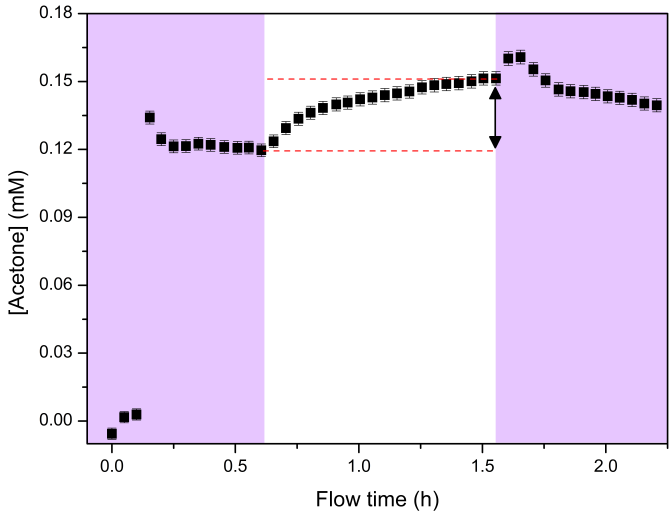

Fig. 7.7 Evolution of acetone concentration in the presence (violet/shaded area) and absence (white area) of UV_a illumination using a photoreactor loaded with 5 mg_{TiO_2}/g_{beads} catalysts. The dotted lines and arrow show the difference between the two steady state concentrations used to determine the decomposition rate of acetone.

A rapid initial increase in acetone concentration can be observed in Figure 7.7 as the acetone passes through the photoreactor, the acetone concentration then reaches a steady state as the catalyst surface is saturated. When the UV_a illumination is stopped, the photodecomposition process is halted and an increase in acetone concentration can be observed until a new steady state is reached. The difference between these two steady state concentrations is the concentration of photodecomposed acetone ($[\text{Acetone}]_{\Delta ss}$, shown by the arrow in Figure 7.7). By adapting Equation (7.1) it was possible to quantify the decomposition rate of acetone, $-\sigma_{Acetone}$, as a factor of gas flow rate, Q, as shown in Equation (7.2). For the studied experiment $-\sigma_{Acetone}$ was calculated to be 0.14 ± 0.02 mmol/h.

$$-\sigma_{Acetone} = Q[\text{Acetone}]_{\Delta ss} \tag{7.2}$$

From Figure 7.7 it also becomes possible to determine the conversion (the % of total reagent decomposed) of acetone in the studied system. The conversion for a given VOC, $C_{\%}$, in the studied photoreactor can be described as shown in Equation (7.3) where $[\text{VOC}]_{UV_a}$ and $[\text{VOC}]_{dark}$ are the steady state concentrations of the reagent with and without UV_a illumination, respectively. As such, it was possible to establish a conversion value of 21 % for the photodegradation of acetone.

$$C_{\%} = \frac{[\mathrm{VOC}]_{\mathrm{UV_a}}}{[\mathrm{VOC}]_{dark}} \tag{7.3}$$

During a similar study on the photodecomposition of acetone in a gas stream by Degussa P25, Žabová and Dvořák reported an acetone conversion of 35%.[284] The relatively higher conversion rate observed by Žabová and Dvořák can be attributed to their TiO_2 immobilisation substrate (polystyrene mesh) which allowed for a significant increase in gas-catalyst contact area with respect to the glass beads used in the present study.[284] Nonetheless, the advantages gained from the facile GIAC coating technique as well as the ease of catalyst handling render the presented catalyst supports significantly more viable for use at an industrial scale.

For the same experiment it was also possible to monitor the variations in CO_2 (as shown in Figure 7.8) and determine its σ_{CO_2} which was calculated to be 5.6 ± 0.6 mmol/h, 40 times higher than the rate of decomposition of acetone. Although a significant difference was expected in these concentrations due to the 1:3 stoichiometric ratio between reactant and products, the difference between the rates of acetone decomposition and CO_2 production far outweighs the expected factor of 3. Two different factors can be attributed as the cause of these incongruous results: the generation of partial decomposition intermediates, and the adsorption of organic residues on the catalyst surfaces.

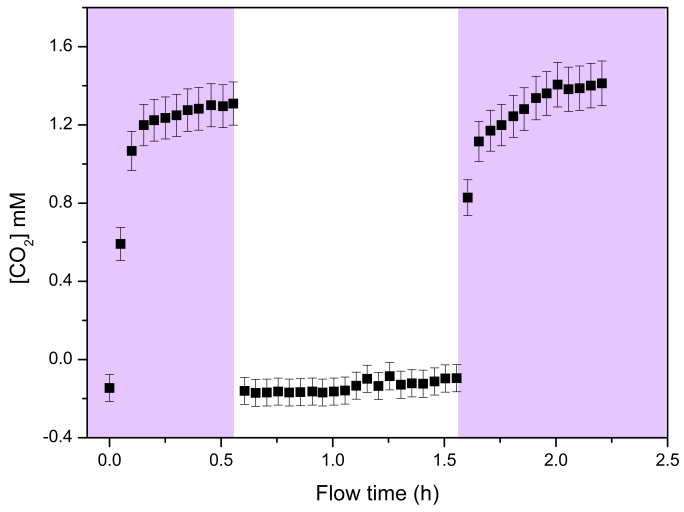

Fig. 7.8 Evolution of CO_2 concentration in a in the presence (violet/shaded area) and absence (white area) of UV_a illumination during the photodecomposition of acetone.

It is known that the mechanism for the oxidation of acetone proceeds through a large variety of pathways depending on reaction conditions.[283,285] Along these pathways acetone is converted into many different chemical species prior to complete mineralisation. Since the initial acetone oxidation steps are more kinetically favourable than complete mineralisation, it is likely that a number of partial decomposition products were formed on the surface of the catalysts.[285–287] These intermediate oxidation products contain carbonyl moieties (e.g. acetic acid,[283,285,288] formic acid,[285] and mesityl oxide[288,289]) which will interfere with the monitoring of the concentration of acetone. As the extinction coefficient of these species will differ from that of acetone, their overlap with the acetone carbonyl stretch can lead to the increase of the carbonyl peak area by unknown amounts. Effectively, this overlap of carbonyl peaks signifies that the observed drop in acetone concentration caused by UV_a irradiation, remains significantly smaller than that which is occurring in reality.

However, it is important to note that although the presence of partial photomineralisation products in the gas stream can, in part, explain the large discrepancy between σ_{CO_2} and $-\sigma_{Acetone}$, it does not fully clarify the observed results. The formation of partial decomposition products only occurs under UV_a illumination, signifying that the steady state concentration of acetone observed without illumination is authentic. Nonetheless, even if the complete mineralisation of acetone is to be assumed, the concentration of CO_2 produced far outweighs the absolute concentration of acetone present in the system without UV_a illumination. As such, the presence of an ulterior factor affecting the concentration CO_2 becomes readily apparent.

A similar production of CO_2 at concentrations exceeding the complete mineralisation of the photodecomposed species was reported by Verbruggen *et al.*[282] It was suggested that the origin of the excessive CO_2 concentration resided in the deposition of organic residue on the photocatalyst surface. During the present series of studies, the difference in CO_2 production observed whilst reusing the same catalyst (Figure 7.3 and Figure 7.8) was considered negligible and it was readily apparent that continued use of the same catalyst beads did not affect the reactor's photocatalytic activity. This led to same batch of beads being used continuously during all of the acetone photodegradation studies. However, the accumulation of partial decomposition products on the catalyst surface is a well-documented phenomenon.[285,288,290,291] As such, it is plausible that the observed excess in CO_2 concentration arises from the photodecomposition of carbonaceous deposits gathered on the catalyst surface during prior reactions.

In order to determine the extent of carbonaceous deposition on the catalyst surface, an experiment was carried out investigating the CO_2 output of a batch of previously used beads in an illuminated photoreactor whilst using a clean (VOC free) gas stream. The evolution of CO_2 concentration during this experiment is shown in Figure 7.9. It can be clearly seen that although no reagent is present in the gas stream, a significant quantity of CO_2 is generated from the decomposition of carbonaceous species on the catalyst surface. As these carbonaceous deposits are depleted, the production of CO_2 decreases and its concentration in the photoreactor exhaust is seen to decrease. However, when the gas stream is loaded with VOCs, a constant supply of partial decomposition products is maintained on the catalyst surface. This means that in a gas stream loaded with VOCs, the concentration of CO_2 generated from carbonaceous deposits on the catalyst surface will be equivalent to the maximum level observed in Figure 7.9. The maximum concentration of CO_2 produced by the carbonaceous deposits can thus be established as 1.03 ± 0.09 mM.

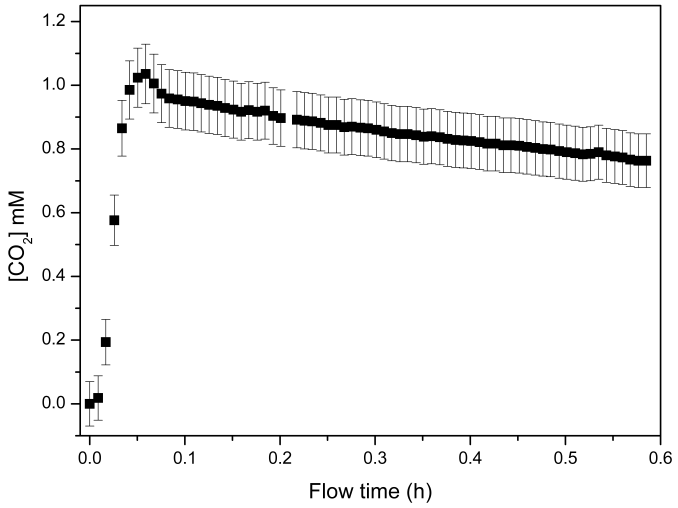

Fig. 7.9 Evolution of the concentration of CO_2 developed during the photocatalytic decomposition of carbonaceous residues on the photocatalysts in a flow reactor under UV_a illumination with a clean gas stream.

From Figure 7.8 it was observed that the photodecomposition reactions generated a steady CO_2 concentration of 1.31 ± 0.07 mM. By subtracting the total CO_2 generated from the carbonaceous residues from that observed during the photodecomposition of acetone, it is possible to determine that a concentration of 0.28 ± 0.11 mM of CO_2 originated from the photodecomposition procedure. By taking into account the factor of three originating from the stoichiometry of the system, it was

possible to determine that the CO_2 concentration produced by the reaction corresponded to a drop in acetone concentration of 0.09 ± 0.04 mM. The maximum concentration of acetone (as seen in Figure 7.7) in the photoreactor was 0.15 ± 0.002 mM, which coincides (within experimental error) with the calculated concentration drop. As such, the observed excess in CO_2 formation during the photodecomposition of acetone can be attributed to the decomposition of carbonaceous species on the surface of the TiO_2. Further evidence of these deposits was observed with catalyst beads exceeding 20 h of VOC photodecomposition wherein a yellow coloration, indicative of carbon deposition, was seen to appear on the TiO_2 coated beads.

Notwithstanding the complications in the quantification of the photocatalytic decomposition of acetone, it remains important to note its successful photodecomposition at a constant rate of 0.14 ± 0.02 mmol/h . This value remains several orders of magnitude larger than the acetone concentrations in residential and domestic environments of 2.2 - 9.9 nM .[292,293] As such, the presented technologies can be seen as an effective removal system for toxic levels of acetone in ambient air. However, as a consequence of mass-transport effects it is unlikely that the photoreactor would maintain the acetone removal rate observed during this series of studies at lower acetone concentrations. Furthermore, although the removal of acetone was successfully demonstrated with the designed photoreactor, the complications observed arising from the *in-situ* formation of partial decomposition intermediates highlight the importance of studying the successful photomineralisation of more complex organic VOCs.

7.3.2 Effectiveness of IPA Photodegradation

It is known in literature that the first process occurring during the photodecomposition of IPA is the formation of acetone.[286] This arises as the chemical oxidation from IPA to acetone is a facile and rapid step involving a single photon.[289,294] Figure 7.10 shows the evolution of the concentrations of IPA, acetone, and CO_2 in the exhaust stream of a photoreactor under the irradiation of UV_a light during IPA photodecomposition studies. It can be seen that as UV_a illumination is applied to the system, the IPA concentration drops and a rise in acetone and CO_2 concentrations occurs. These events are indicative of the photodecomposition of IPA occurring in the gas flow reactor as the IPA is converted into acetone on the surface of the TiO_2 and the created acetone is then further mineralised to eventually create CO_2.

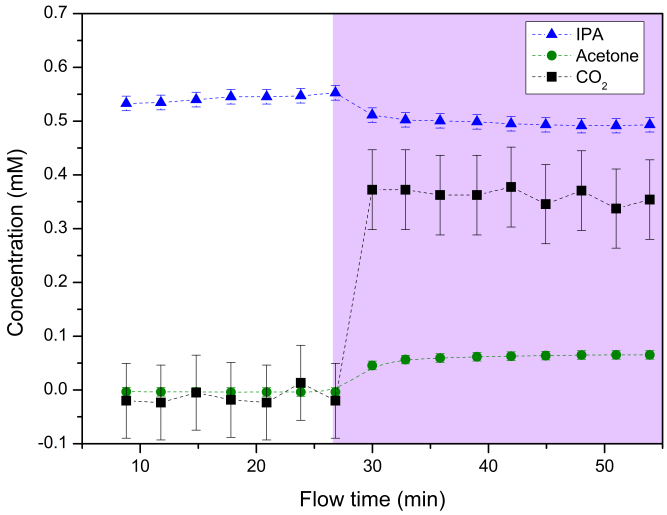

Fig. 7.10 Evolution of the concentrations of IPA, acetone, and CO_2 in a photoreactor in relation to UV_a illumination. The violet (shaded) section of the graph indicates the moment of UV_a irradiation during the experiment.

By analysing the steady state concentration changes in Figure 7.10 and applying Equations (7.1) and (7.2) it was possible to calculate the rate of decomposition of IPA as well as the rates of formation of acetone and CO_2. The rate of decomposition of IPA was determined to be 0.27 ± 0.08 mmol/h. Compared to the previously determined acetone photodegradation rate (0.14 ± 0.02 mmol/h), the rate of IPA photodecomposition is significantly higher. This difference is indicative of the initial photodecomposition kinetics for the two species.[286,289] The initial photodecomposition of IPA into acetone is vastly more energetically favourable than the decomposition and mineralisation of acetone, leading to the observed higher decomposition rate for IPA.[294] Furthermore, it is known that IPA displays a greater binding affinity to the surface of the TiO_2 catalyst than acetone leading to a greater decomposition of IPA.[289,294]

However, it is important to note that the conversion of IPA (calculated using Equation (7.3)) is of 11%, roughly half that previously calculated for the photodecomposition of acetone (21%). Although the photodecomposition of IPA is faster, the designed photoreactor is more effective at removing acetone due to the relative rates of decomposition of the two species. As the rate of elimination of acetone is approximately half that of IPA elimination, an accumulation of acetone on the catalyst surface will inevitably occur. As such, the acetone created from the decomposition of IPA occupies the active sites of the catalyst, effectively impeding the photodecomposition of

further IPA.

From Figure 7.10 the rate of production of acetone was calculated to be 0.30 ± 0.04 mmol/h. Although this rate is higher than that observed for the photodecomposition of IPA, both rates lie within the calculated error margins. In addition to this, the larger observed concentration of acetone is a value that must be considered with caution as it is based on the carbonyl IR stretch. As such, it is likely that the observed stretch is affected by the formation of carbonyl containing products from the photodecomposition of the acetone, as discussed previously. Nonetheless, the relatively high production rate of acetone with respect to the decomposition rate of IPA remains important as it further highlights the speed of the photoconversion process from IPA to acetone.

The rate of production of CO_2 was calculated to be 1.5 ± 0.4 mmol/h. This value results five times higher than the rate of photodecomposition of IPA, exceeding the expected stoichiometric ratio of 3 CO_2 molecules created for every IPA molecule decomposed. Furthermore, due to the high acetone production observed, the IPA photodecomposed did not all undergo complete mineralisation. It thus becomes apparent that the observed rate of CO_2 production arises not only from the mineralisation of IPA but also from other sources. Following the previous results for the photodecomposition of acetone, it is believed that the main factor causing an excessive generation of CO_2 is the photodecomposition of carbonaceous species deposited on the TiO_2 catalyst surface.

Although the photodecomposition of IPA was difficult to quantify, it was possible to demonstrate and study the effectiveness of the designed photoreactor for the decomposition of complex VOC species in the gas stream. By using the created photoreactor it was possible to extract partial photodecomposition intermediates before achieving complete mineralisation of the VOCs. It can thus become possible to use the designed reactors for the conversion of complex VOC molecules into useful synthetic precursors as well as to completely decompose the VOCs.

7.3.3 Effectiveness of Styrene Photodegradation

By studying the photodecomposition of styrene in gas streams it was possible to study the degradation of complex VOCs in the designed photoreactor. In the light of the excessive CO_2 production rates observed for the photodecompositions of acetone and IPA, each styrene photodecomposition experiment was carried out on pristine TiO_2 coated glass beads.

Styrene Mineralisation

Figure 7.11 shows the evolution of CO_2 and styrene in the photoreactor's exhaust in the presence and absence of light. In order to achieve a steady concentration of VOC, a much longer stabilisation period was required (2 hours) with respect to those observed for the photodegradation of IPA (5 min) and Acetone (10 min). This can be attributed to the lower volatility of styrene which lengthened the time taken before an adsorption/desorption equilibrium was reached within the system. Due to the time scale of the experiment presented in Figure 7.11 it may result difficult to observe the stabilisation of CO_2 concentration after UV_a illumination (flow time 4.15 to 4.5 hours). However it is important to note that at these flow times the CO_2 concentration was observed to fluctuate by $\pm$ 0.002 mM over a period of 20 minutes, allowing to establish the stabilisation of the CO_2 concentration in the gas flow.

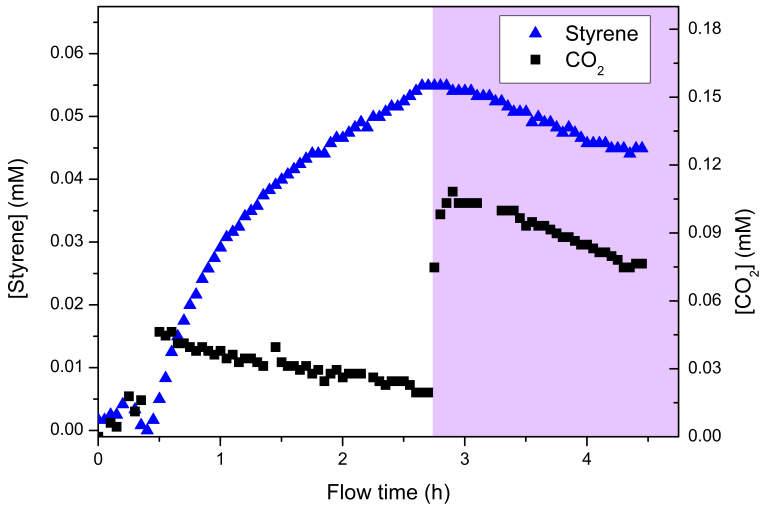

Fig. 7.11 Evolution of the concentrations of styrene and CO_2 in the photoreactor in relation to UV_a illumination. The violet (shaded) section of the graph indicates the moment of UV_a irradiation during the experiment.

It can be further seen in Figure 7.11 that upon illumination, the concentration of CO_2 decreases until reaching a steady state (flow time of 3 to 4 hours). This decrease in CO_2 production arises from the gradual depletion of the styrene adsorbed on the saturated catalyst surface. Prior to UV_a illumination, the styrene is observed to achieve a steady concentration as the surface of the TiO_2 catalyst is saturated by the adsorbate. As UV_a illumination is initiated, the styrene adsorbed onto

the TiO_2 is mineralised. However, due to the low concentration of styrene in the gas flow, the rate of photodecomposition of styrene exceeds that of adsorption, leading to the observed drop in CO_2 production as the stored styrene is depleted. After the drop in CO_2 concentration, a new steady state is reached when the adsorption of the styrene on the TiO_2 equilibrates with the rate of photodecomposition.

By studying the steady state concentrations of styrene in the presence and absence of UV_a illumination seen in Figure 7.11 it was possible to apply Equations (7.2) and (7.3) to determine the decomposition rate and conversion of styrene in the studied photoreactor. It was thus possible to determine that 18% of the styrene was successfully converted at a rate of 0.044 ± 0.002 mmol/h. This rate of decomposition is significantly lower than those observed for acetone (0.14 ± 0.02 mmol/h) and IPA (0.27 ± 0.08 mmol/h) due to the low concentration of VOC in the gas stream arising from the low volatility of the chemical species. Nonetheless, it is important to note that although a low decomposition rate was observed, the conversion of styrene (18%) was similar to that observed for acetone (20%) and IPA (11%), demonstrating the effectiveness of the designed photoreactor for the decomposition of complex VOCs as well as for the smaller, simpler, molecules.

A good understanding of the efficiency of the developed reactors for the decomposition of VOCs could also be achieved by commparing the rate constants of the three decomposition reactions. However, although the continuous flow nature of the designed reactors is ideal for the direct determination of the decomposition rate of the VOCs, the rate constants of the studied decomposition reactions cannot be determined. This inability to determine the studied reactions arises as a consequence of the lack of knowledge of the exact rate law and order of the decomposition reactions involved. Ideally, these parameters could be calculated experimentally in static decomposition reactors. In the present system it is nonetheless possible to estimate the decomposition constants of the studied reactions by making a number of assumptions. If the VOC decomposition reactors are taken to behave in a similar fashion to continuous stirred tank reactors, and the decomposition reactions are assumed to be irreversible first order reactions, then it becomes possible to to determine the decomposition rate constants for the studied reactions by applying Equation (7.4) as previously described by J.B. Rawlings and J.G. Ekerdt.[295] In Equation (7.4) $[VOC]_f$ is the original concentration of the VOC studied in the gas flow, $[VOC]_{dec}$ is the steady state of the VOC after it has undergone decomposition (during illumination in the present case), τ is the contact time of the VOCs with the TiO_2 catalyst, and k is the reaction rate constant.

$$\mathrm{k} \;=\; \frac{[\mathrm{VOC}]_{\mathrm{f}} - [\mathrm{VOC}]_{\mathrm{dec}}}{[\mathrm{VOC}]_{\mathrm{dec}}\ \tau} \tag{7.4}$$

By applying Equation (7.4) to the performed experiments it was possible to calculate the decomposition rate constants of acetone, IPA, and styrene to be 11.60 ± 0.02 h^{-1}, 5.25 ± 0.02 h^{-1}, and 9.71 ± 0.02 h^{-1}, respectively. These decomposition numbers are consistent with the observed conversion values wherein IPA displayed the lowest conversion of the three VOCs and acetone the highest. These values further highlight the lower decomposition of IPA with respect to acetone due to the more complex decomposition pathway of IPA, as previously discussed. Both though the conversion values and the kinetic constants, it can be seen that the photodecomposition of styrene proceeded at appreciable levels, similar to those of IPA and acetone, demonstrating that the increased complexity of the molecule did not cause a loss in photodecomposition potential. It is however important to note that the kinetic rate constants should only be considered qualitative as their calculation is based on a number of assumptions which do not fully apply to the studied system.

The efficiency of the studied reactor is further emphasised by the works of Sun *et al.* who, in a similar photodecomposition experiment, demonstrated a 20% conversion of styrene only at elevated temperatures (175°C),[296] whilst in the present study a similar styrene conversion was successfully achieved at room temperature.

As the styrene photodecomposition experiments were carried out on pristine catalyst beads, it was possible to investigate the production of CO_2 during the photodecomposition reaction. By applying Equation (7.1) to the CO_2 difference in steady state concentrations observed in Figure 7.11 it was possible to establish that the production rate of CO_2 was 0.248 ± 0.003 mmol/h, 5.6 times the photodegradation rate of styrene. This sub-stoichiometric production of CO_2 indicates that a portion of the styrene does not undergo complete mineralisation and is instead converted into stable decomposition products. The amount of CO_2 produced during the reaction (the selectivity of the reaction for CO_2) can be calculated as shown in Equation (7.5), where S_{CO_2} is the selectivity of the reaction for CO_2, $[\mathrm{Styrene}]_{\Delta \mathrm{ss}}$ is the amount of styrene photodecomposed, and $[CO_2]_{\Delta \mathrm{ss}}$ is the amount of CO_2 produced during the photoreaction.

$$\mathrm{S}_{\mathrm{CO}_2} \;=\; \frac{[\mathrm{Styrene}]_{\Delta ss}}{[\mathrm{CO}_2]_{\Delta ss}} \tag{7.5}$$

By applying Equation (7.5) it was possible to determine that only 70% of the decomposed styrene was fully mineralised into CO_2, demonstrating the formation of partial photooxidation products. In order to study these products, the exhaust of the photoreactor was bubbled through a chemical bath to trap which concentrated them and allowed their identification through GC-MS analysis.

Secondary Photodecomposition Products

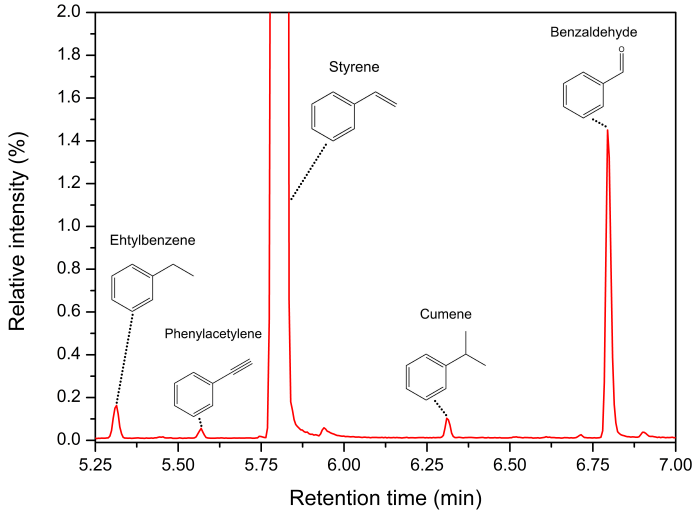

Fig. 7.12 Gas chromatogram of the chemical trap used to collect the exhaust products during the photodecomposition of styrene after 20h of reaction time. The nature of the different species was determined by correlating the mass spectrum of each peak with the NIST mass spectral library (NIST 98). The truncated peak observed at 5.8 minutes arises from trapped styrene and corresponds to 100% intensity.

Figure 7.12 shows the gas chromatogram achieved from by analysing the trapping solution after a 20 h styrene photodecomposition reaction, the assignment of the peaks was carried out by correlating the mass spectra of the peaks with the NIST database (NIST 98). The absence of the detected products in the GC-MS trace of the styrene dissolved in 1,4-dioxane demonstrated their origin from the partial photooxidation of styrene. It can be seen that the major secondary product formed during the photodecomposition of styrene was benzaldehyde. This observation coincides with those of Nie *et al.*,[81] Ren *et al.*[82] and Taffarel *et al.*[83] This preference for the formation of benzaldehyde could be explained by the relative stability of this species as well as the general

photodecomposition pathway for styrene.

Although there remains disagreement on the mechanistic details leading to the formation of benzaldehyde, Nie *et al.*[81] as well as Ren *et al.*[82] postulated that the photodecomposition of styrene proceeds through a concerted reaction between the superoxide anion ($O_2^{-\cdot}$) radical and the vinyl moiety of the styrene group. The general mechanism for the formation of benzaldehyde, as well as formaldehyde, is shown in Figure 7.13. It can be seen that the superoxide anion bonds with the vinyl group of styrene, leading to the eventual distribution of charge and homolytic cleavage of the vinyl bond. The cleaved species can then react with water adsorbed on the TiO_2 surface in order to create hydroxide radicals ($OH^{\cdot}$) as well as formaldehyde and benzaldehyde. Although both formaldehyde and benzaldehyde are formed in equal concentrations during this study, formaldehyde was absent from the trapping solution. This absence can be explained by the relatively high volatility of formaldehyde which caused it to elute during the solvent delay in the GC-MS studies.

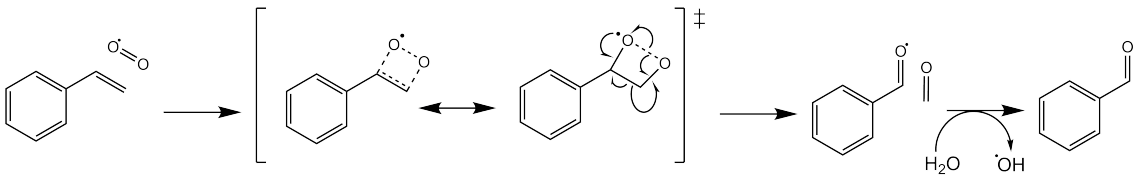

Fig. 7.13 Chemical scheme showing the $O_2^{-\cdot}$ mediated conversion of styrene into benzaldehyde and formaldehyde in the photocatalytic reactor.

The exact mechanism for the cleavage of the vinyl bond which forms benzaldehyde and formaldehyde remains uncertain. Ren *et al.*[82] postulated that this cleavage occurred through a polarisation interaction between water molecules and the bound superoxide-styrene system which altered the electron density of the styrene in order to facilitate the cleavage of adducts. However, although this hypothesis is plausible, it does not hold true for systems in gaseous environments due to the restricted presence of water. An alternative mechanism was proposed by Nie *et al.*[81] which established the adsorption and interaction of the styrene-superoxide species with the TiO_2 surface as the factor facilitating the cleavage of the vinyl bond. This proposed interaction of the system is more likely as it is known that the photodecomposition of styrene occurs primarily on the surface of the catalysts.

Furthermore, the interaction of styrene with the TiO_2 surface has been previously reported in literature and can explain the formation of ethylbenzene observed in Figure 7.12.[52] As shown in

Figure 7.14, water on the surface of the TiO_2 is photocatalytically cleaved, leading to the generation of protons (H^+). These protons can be reduced by photogenerated electrons on the TiO_2 surface in order to create active H species which insert into the vinyl bond of styrene molecules bound to the TiO_2 surface.

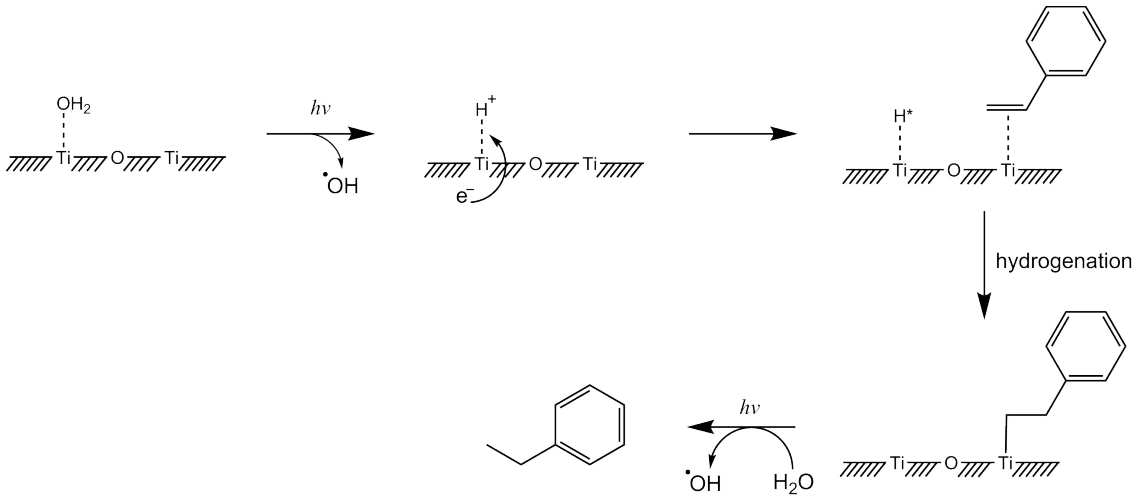

Fig. 7.14 Chemical scheme showing the H^+ mediated hydrogenation of styrene into ethylbenzene in the photocatalytic reactor.

The dehydrogenation of styrene into phenylacetylene as observed in Figure 7.12 can be similarly attributed to photogenerated radicals on the TiO_2 surface. As discussed in Chapter 1 the photonic excitation of TiO_2 leads to the formation of $OH^{\cdot}$ which can sequentially abstract protons from the vinyl moiety of the styrene as shown in Figure 7.15. This abstraction can occur due to the presence of the benzene ring which allows to disperse the created charge imbalance from the loss of the first proton, as shown in Figure 7.15.

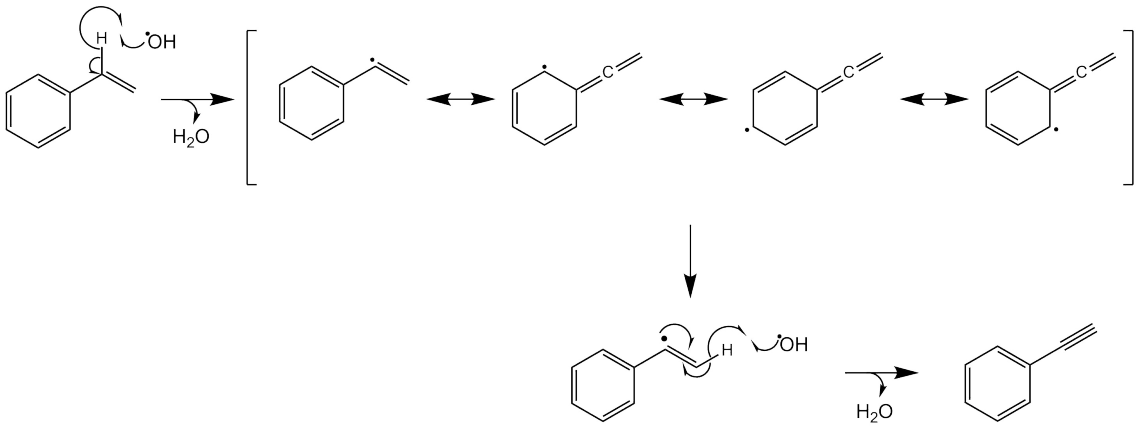

Fig. 7.15 Chemical scheme showing the OH˙ mediated dehydrogenation of styrene into phenylacetylene in the photocatalytic reactor. The resonance isomers of the created radical intermediate are shown, illustrating the charge stabilisation effect of the benzene ring.

Finally, the formation of cumene observed in Figure 7.12 is the most complex due to the addition of a methyl group to styrene. By studying the mechanisms for the formation of benzaldehyde and ethylbenzene, it is possible to postulate a viable pathway for the TiO_2 mediated conversion of styrene into cumene.

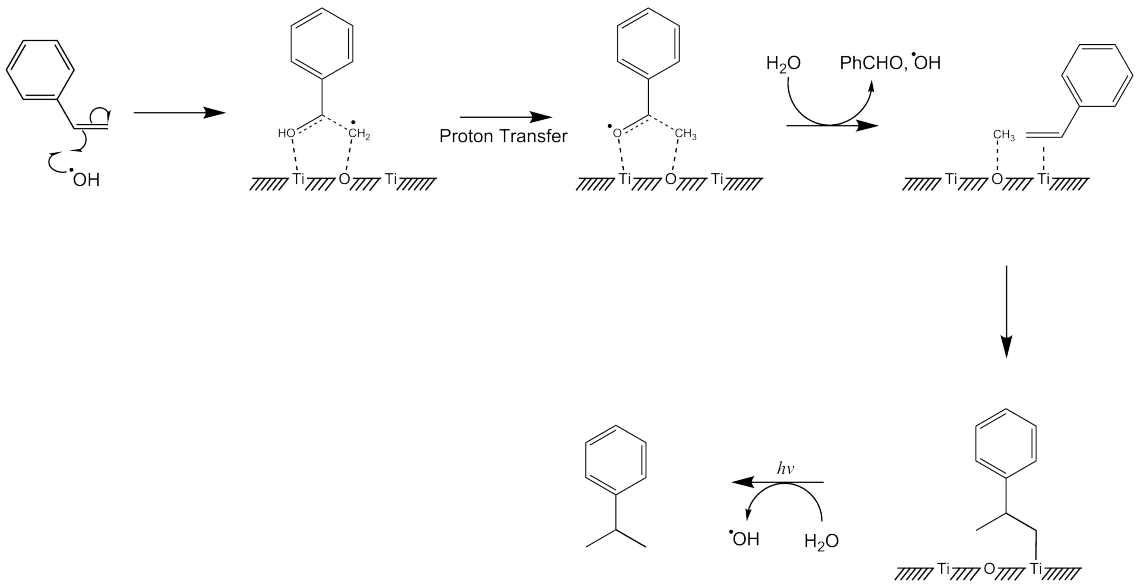

Fig. 7.16 Proposed chemical scheme showing the OH˙ mediated conversion of styrene into cumene.

As shown in Figure 7.16, a photogenerated OH˙ initially carries out a nucleophilic attack on the vinyl group of a styrene molecule. The generated radical intermediate is stabilised by the

TiO_2 surface, allowing to cleave the vinyl moiety and resulting in the formation of a benzaldehyde precursor and a methyl radical ($CH_3^{\cdot}$). The formed methyl radical can then create cumene by inserting itself into the vinyl bond of another styrene molecule bound to the TiO_2 surface, in a similar manner in which the hydrogen atoms are inserted in styrene to generate ethylbenzene.

Although these different photodecomposition products are collected as a mixture from the output of the photoreactor, their separation and isolation for eventual use remains relatively facile. This allows for the application of the designed photoreactors not only as purification devices but also as synthetic reactors for the creation of important and valuable chemical species.

7.4 Conclusions

Through the present series of experiments it was possible to demonstrate that the created photoreactor could be used for the photomineralisation of VOCs as well as for the generation of complex, synthetically useful, molecules.

Initially, a modified version of the photoreactor presented in Chapter 6 was used to successfully photomineralise acetone into CO_2. During these studies the production of CO_2 was monitored and the effects of different catalyst loadings on the glass bead supports were observed. From the variations in CO_2 concentration, an ideal TiO_2 loading on the glass beads of 5 mg_{TiO_2}/g_{beads} was established.

Further photodecomposition studies allowed to demonstrate the photoreactor effectiveness for the removal of two additional VOCs: IPA, and styrene. By studying the drops in VOC concentration during UV_a illumination, it was possible to determine the percentage conversion for each species. The highest photoconversion observed during this study was that of acetone (21%), followed by styrene (18%), with IPA showing the smallest drop in gas stream concentration (11%). The large difference between the acetone and the IPA was explained from the photodecomposition rates of the two species (0.14 ± 0.02 mmol/h and 0.27 ± 0.08 mmol/h for acetone and IPA, respectively) as well as the photodecomposition pathway of IPA which occurs through the formation of acetone as an intermediate, leading this species to occupy the TiO_2 active sites.

A more precise understanding of the photodecomposition processes was gained by studying

the production of CO_2 for each reaction. However, due to the deposition of carbonaceous residues on the surface of the catalysts, it was observed that the CO_2 production from used catalyst systems far outweighed the observed decompositions in the VOCs. As such, it was only possible to achieve a qualitative understanding of the CO_2 production during the photodecompositions of IPA and acetone.

As the styrene decomposition experiments were carried out on pristine catalysts, the production of CO_2 could be reliably quantified. It was possible to determine that the styrene decomposition reaction had a 70% selectivity for CO_2, demonstrating the formation of chemically stable side products in the reactor exhaust. Further GC-MS studies allowed to identify a number of side products from the photodecomposition of styrene. Although the major decomposition product was benzaldehyde, it was possible to propose mechanistic pathways for to the formation of each observed product, demonstrating the complexity of the chemical reactions occurring in the created photoreactor.

In conclusion, although the performed experiments exhibited some complications, the photodecomposition of three VOCs in gas streams was successfully demonstrated and analysed. From an industrial perspective, the created photoreactor can be seen as promising due to its compact volume which allows it to be used as a portable air purification device for domestic and commercial environments. Furthermore, from the styrene photodecomposition studies it could be seen that the photoreactor was also capable of producing complex molecules. As such, if combined with a suitable chemical isolation technique, the designed reactor could become a key element in a synthetic pipeline for the generation of complex and unusual chemicals from a fluid stream.

8. Hexene Photoepoxidation in Gas Flows

Chapter 7 showed the successful photodegradation of organic species over TiO_2 in gas streams. During these studies, the potential of the designed technologies was further highlighted with the creation of a variety of partial photooxidation products from the decomposition of styrene. Investigations in this potential for the creation of synthetically useful products were carried on in the following series of experiments.

Initially, the photoepoxidation potential of the TiO_2 photoreactor was studied by decomposing 1-hexene and trapping the produced exhaust chemicals. The epoxidation of hexene was chosen during these experiments as a suitable candidate to demonstrate the designed photoreactor's potential as a system for creating valuable chemical species.

Subsequent experiments focused on the *in situ* reaction of the partial photooxidation products issued from the decomposition of 1-hexene. For this purpose, the exhaust of the photoreactors was passed through diisopropylamine. The products of the reaction were detected and analysed, allowing to establish the nature of some of the more reactive species created during the partial photooxidation of 1-hexene. Through these experiments is was possible to demonstrate the high versatility of the TiO_2 based photoreactors developed.

8.1 Introduction

Photoactivated TiO_2 is well known for its photodecomposition properties.[46,66,128] As TiO_2 is irradiated by UV light, it generates high energy electrons which will react with H_2O and O_2 adsorbed on the surface of the semiconductor to create highly oxidising and reducing species ($O_2^{-\cdot}$ and $OH^{\cdot}$ are generated from O_2 and H_2O, respectively).[46,130] Due to their high oxidising and reducing potentials, these photogenerated radicals can lead to the complete photomineralisation

of organic molecules.[130] This particular property of TiO_2 in addition to its chemical stability, has led to a great amount of academic[46,130,297] and industrial[48,156] interest in the use of photoactivated TiO_2 as a photocatalyst for the decomposition of organic contaminants.

However, TiO_2 based photocatalytic decomposition techniques often carry out the complete mineralisation of the contaminants. This means that most of the time TiO_2 is used to transform contaminant molecules into CO_2. Whilst this is useful as a tool for the removal of organic contaminants, it is inconvenient from a chemical perspective as the produced CO_2 is so stable that it cannot be used for further reactions unless the system is supplied with significant amounts of energy.[76,77] This drawback of TiO_2 photocatalysis can be overcome by promoting the partial photooxidation of organic molecules.

Although the TiO_2 mediated photooxidation of organic molecules is non-selective in the presence of O_2,[298] a multitude of single decomposition steps, each proceeding at different rates, are required in order to achieve complete mineralisation of a molecule. It has been previously shown that initial oxidation steps proceed faster than any subsequent decomposition steps.[285–287] As such, in a system like that of a gas flow photodecomposition reactor where the products can be separated from the catalyst before complete mineralisation, a mixture of decomposition products can be created in addition to CO_2. This formation of partial photodecomposition products has previously been observed by Nie *et al.*,[81] Ren *et al.*[82] and Taffarel *et al.*[83] whilst analysing the photodecomposition of styrene.

The production of these partial photooxidation products can be improved by a precise tuning of the different factors governing the photocatalytic process. Of the many different different methods to improve the production of partial oxidation intermediates in flow reactors, the modification of the flow rate is certainly one of the simplest techniques. By modifying the flow rate of the organic species over a catalyst bed it is possible to modify the contact time between the catalyst and the reagents and thus minimise the occurrence of complete photomineralisation.[290] Further modifications to the system, such as modifying the reaction temperatures and the reagent concentrations can also be used to favour the production of the partial photooxidation intermediates.[85,86,299]

This optimisation of TiO_2 mediated photocatalytic flow reactions has received a significant amount of academic interest in recent years.[85,299] In particular, a number of studies have been performed on the production of propylene oxide directly from propylene.[85,86,299–302] Two main

approaches have been carried out in order to improve the photoepoxidation of propylene: physical modifications to the system, and modifications to the nature and structure of the catalyst. The former technique has focused on changing reaction conditions such as the reaction temperature, UV irradiation and reagent concentration.[85,86] By varying both the temperature and the ratio of propylene to oxygen in the gas stream, Murcia-López *et al.* were able to successfully increase the production of propylene oxide in their reactors by 10% .[302] They further enhanced this selectivity by modifying their photocatalyst and using nanostructured Bi_2WO_6 in combination with P25.[302] Similarly, Nguyen, Chan and Wu achieved an improvement of 54% on the selectivity of their photoepoxidation processes by shifting from pure TiO_2 to Au-doped titanium silicates.[86]

The epoxidation of alkenes is an industrially appealing technique due to the widespread use of epoxides in a variety of different processes. Amongst these processes, alkenes are known to be used commercially as the starting materials for both polymerisation reactions[84] and complex synthetic compounds.[32] Traditionally these epoxidations are produced through chemical means although the use of photoactivated TiO_2 in the presence of oxygen has also been demonstrated as an effective alternative.[301,303] Furthermore, it was shown by Ohno *et al.* that the epoxidation of 2-hexene could be carried out in both a stereoselective and stereospecific fashion.[87] This high selectivity enhances the importance of the technique as a means of generating synthetically useful organic precursors. During the present series of experiments, the photocatalytic reactor developed in Chapter 7 was used in order to study the photoepoxidation of 1-hexene over TiO_2 in gas streams.

Although photogenerated epoxides are known to be relatively stable species, the high reactivity of the different partial oxidation products signifies that many potentially useful compounds are often impossible to collect directly from TiO_2 gas flow photoreactors. As such, in addition to demonstrating the viability of the created reactor for the production of epoxides, this series of experiments aims to establish a tandem reaction system in order to take advantage of these highly reactive products. The tandem system consists of a one-pot reaction mixture connected to the gas stream, effectively allowing for the immediate use of the partial photooxidation products in synthetic reactions.

8.2 Experimental Procedure

8.2.1 Chemicals and Characterisation Techniques

P25 was sourced from Sigma-Aldrich UK and used as received. Toluene, 1-hexene, and diisopropylamine were all sourced from Fisher Scientific and used as received. During the photoepoxidation experiments, UV light was supplied by a cold cathode lamp sourced from Xenta whilst the compressed air used as the carrier gas was sourced from BOC.

In order to analyse the photodecomposition products of 1-hexene, Gas Chromatography coupled with Mass Spectrometry (GC-MS) was used. The GC-MS studies were performed through a PerkinElmer Autosystem XL Gas Chromatograph (GC) equipped with a PerkinElmer TurboMass Mass Spectrometer (MS). The GC was mounted with a Restek RXI-5ms coumn 30 m in length with an internal diameter of 0.25 mm and a film thickness of 0.25 μm. In order to achieve a suitable separation of the different species in the studied liquids, an appropriate GC method was developed using helium as a carrier gas with a flow rate of 40 ml/min. The analysed liquids were injected into the GC column by using an automated split injection with a split ratio of 29.8, an injection volume of 0.2 μl and an injector temperature of 220°C. The GC oven was held at 50°C for 4 minutes then heated to 200°C using a ramp rate of 20°C/min. After holding at 200°C for 4 minutes, the the oven was further warmed to 300°C using a ramp rate of 40°C/min. Lastly, the oven was held at 300°C for 4 minutes. During this run MS was performed by electron ionisation. The MS scanned the mass region between 45 and 300 m/z (amu/e) for a total of 22 minutes with a 4 minute solvent delay. The MS scan length was 0.2 s with an inter-scan delay of 0.1 s.

8.2.2 P25 Immobilisation on Glass Beads

The photocatalyst immobilisation on specific supports is an essential factor in order to develop a successful reactor for the photoepoxidation of hexene. Catalyst immobilisation was used to overcome the pressure build-up issues caused by the packing of loose photocatalyst powders whilst simplifying the handling and use of these catalysts. During the present series of experiments, glass beads were chosen as the preferred catalyst support due to the effectiveness demonstrated in Chapters 6 and 7.

The immobilisation of P25 on glass bead substrates was performed through the use of the Giration Induced Adhesive Coating (GIAC) technique described in Section 6.2.4. A known amount of glass beads ($\bar{d}$: 2.5 $\pm$ 0.3 mm, sourced from Glass Sphere S.R.O) were base treated by washing in acetone and ethanol prior to being boiled in basic solution ($NaOH_{(aq)}$, 6 M) for 2 hours. This base treatment allowed to increase the density of surface OH groups as well as the subsequent adherence of P25 on the glass beads.[304,305] Once base treated, the glass beads were then washed with de-ionised water until the washings were observed to achieve neutrality and accurately weighed in order to account for any loss of mass resulting from the base treatment. The known mass of glass beads was then placed in a rotating drum in combination with an appropriate amount of P25 in order to achieve a loading of 5 mg_{TiO_2}/g_{beads} and allowed to rotate overnight. After the overnight rotation, the beads were weighed once more and their loading was precisely determined.

8.2.3 Epoxidation Reactor Design

The photoreactor used during this series of experiments was adapted from that presented in Chapter 7. Figure 8.1 shows the experimental set up used for the photoepoxidation reactions performed during this series of experiments.

Introduction of Hexene in the Gas Streams

In order to introduce 1-hexene in the gas stream during the photoepoxidation experiments, the technique used in Chapters 6 and 7 for the introduction of siloxanes and VOCs in gas streams was used. A known amount (10 ml) of 1-hexene in liquid form was placed in a Dreschel bottle under a continuous gas stream (compressed air with a flow rate of 4.31 $\pm$ 0.51 L/h was used as a carrier gas during this series of experiments). The length of the dreschel bottle's dip tube was kept at 2 cm from the top of the dreschel bottle in order to ensure a constant concentration of 1-hexene in the gas stream.

Photodepoxidation of Hexene

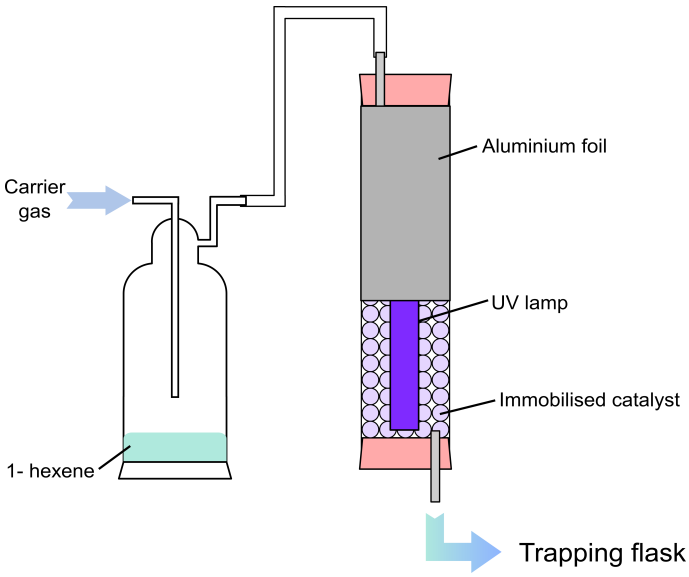

Fig. 8.1 Schematic diagram showing the experimental set up used for the photoepoxidation of hexene in gas streams. The lower half of the reactor tube is shown as exposed for illustrative purposes.

The gas stream containing hexene was passed at a controlled flow (4.31 $\pm$ 0.51 L/h) through the photoreactor shown in Figure 8.1. The photoreactor was composed of a quartz tube (400 mm in length, 24 mm in internal diameter) containing a cold-cathode UV_a fluorescent lamp (305 mm long, 4.0 mm in diameter with a spectral peak intensity of 365.44 nm and a power output of 22.6 mW) and a known mass (189.3 g) of catalyst-coated glass beads. By using rubber bungs equipped with stainless steel inlet/outlet tubes (plugged with glass wool) it was possible to render the system airtight whilst maintaining control on the UV lamp as well as on the gas stream. Finally, aluminium foil was wrapped around the quartz tube in order to reflect outgoing UV light and maximise the irradiation of P25.

After passing through the photoreactor, the gas stream was passed into a round bottomed flask. The flask allowed to successfully trap and collect the partial photooxidation products of the reaction.

Chemical Trapping

In order to study the epoxidation of hexene in the flow reactor, chemical trapping followed by GC-MS analysis was performed on the exhaust of the photoreactor. The experimental set up for

chemical trapping of the exhaust's partial photooxidation products is shown in Figure 8.2. The exhaust stream was bubbled through a round bottomed flask containing toluene which acted as a trapping agent and allowed to concentrate the produced chemical species. In order to ensure an increased retention of the reaction products, the trapping solution was kept in an ice bath. The collection was carried out for a continuous periods of time ranging up to 76 hours, prior to analysis of the solution through GC-MS. In order to minimise the loss of trapping solvent as well as that of highly volatile species, the round bottomed flask was equipped with a condenser as shown in Figure 8.2.

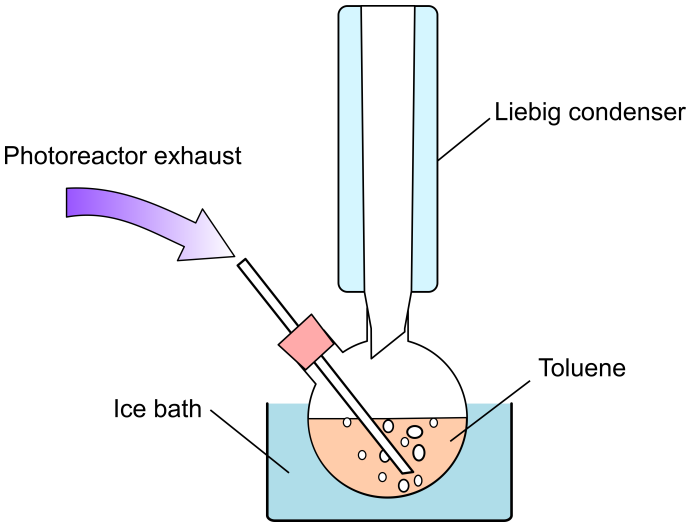

Fig. 8.2 Schematic diagram showing the experimental set up used for the chemical trapping of the exhaust during the photoepoxidation reactions of hexene in gas streams.

8.2.4 Synthetic Trapping

As a number of partial photodecomposition products are too reactive to be trapped through chemical trapping, their use in photosynthetic reactions has to occur directly in the exhaust of the photoreactor. In order to carry out such "pseudo *in-situ*" reactions, disopropylamine was added to the chemical trap depicted in Figure 8.2. Diisopropylamine was chosen for its well known reactivity towards epoxide groups.[306–308] As a result of this reactivity, by adding disopropylamine to the trapping solution any highly reactive epoxides produced during the photoepoxidation reaction were directly used to form more complex synthetic products.

Aliquots were taken from the synthetic reaction mixture over a flow period of 24-72 hours and analysed through GC-MS. Attempts were made to isolate the individual components of the mixture

through distillation techniques.

8.3 Results and Discussion

8.3.1 1-Hexene Photoepoxidation Product Analysis

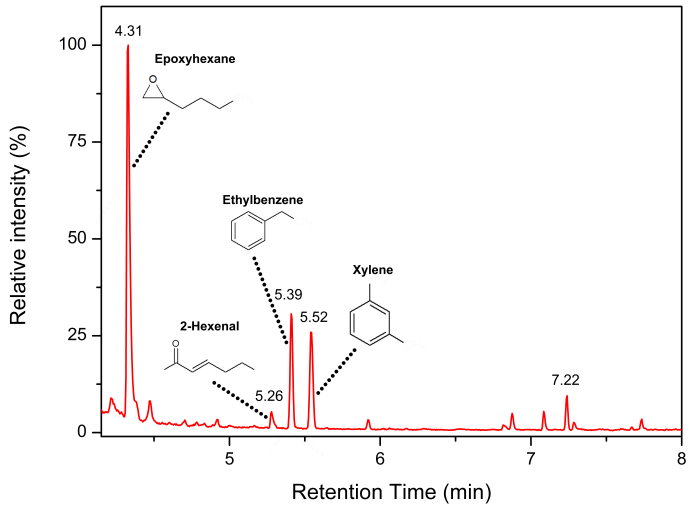

Fig. 8.3 Gas chromatogram of the toluene trap used for the collection of the partial photooxidation products of 1-hexene after 24 h of reaction time. The retention time of the main peaks in the spectrum has been marked above each peak. The nature of the peaks identifiable by correlating the MS of each peak with the NIST database (NIST 98) is also shown.

Figure 8.3 shows the gas chromatogram of the toluene trapping solution after 24 hours of continuous reaction time. Four main peaks with retention times of 4.31, 5.39, 5.52, and 7.22 minutes, are readily observable in the chromatogram. By correlating the mass spectra of the four main peaks with the GC-MS spectrum of toluene as well as the NIST mass spectrometry database it was possible to identify their corresponding molecules.

The peak observed in Figure 8.3 with a retention time of 4.31 minutes was attributed to the epoxide of 1-hexene, epoxyhexane. This attribution was done by correlating the mas spectrum achieved from the chemicals eluted at 4.31 minutes from the GC column (shown in Figure 8.4) with the mass spectral NIST database. This identification can be seen to correlate well with the peaks observed in the mass spectrum shown in Figure 8.4.Indeed, the highest mass recorded at this time

by the MS was one of 100 amu, consistent with the molecular formula of epoxyhexane ($C_{16}H_{12}O$). Additionally, the main fragmentation peaks are consistent with the proposed structure for these species: the fragment at 85.1 amu can be seen to correspond to a loss of a CH_3 group, the fragment with a mass of 71.1 amu can be correlated to a loss of a C_2H_5 group from the carbon backbone of the molecule, the peak at a mass of 58.1 amu can be attributed to the loss of a C_2H_2O fragment from the epoxy hexane, and finally the peak observed at 55.1 amu can be attributed to the loss of a CH_2O group from one end of the molecule and a CH_3 group from the other side of the molecule.

The high concentration of epoxyhexane present in the mixture (as seen by its relative peak intensity) indicates that this product is the primary partial photooxidation product of the reaction. This is a good indication that the rate of decomposition of 1-hexene on TiO_2 is very fast until the relatively stable epoxyhexane is formed. After reaching this compound the rate of photodecomposition decreases, thus favouring the accumulation of epoxyhexane in the system. This analysis is supported by previous academic studies which have demonstrated the tendency of 1-hexene to undergo photocatalytic epoxidation.[32,306,309]

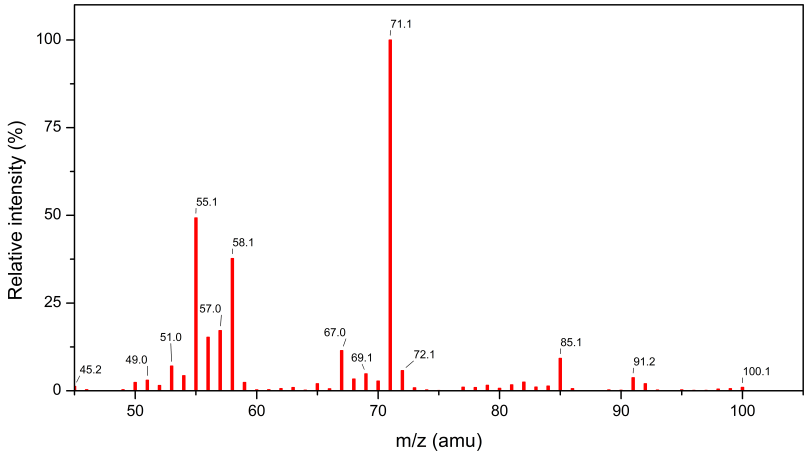

Fig. 8.4 Mass spectrum of the species eluted at 4.31 minutes from the gas chromatograph of the partial photooxidation products of 1-hexene, this spectrum correlates to that of epoxyhexane in the NIST database.

The two peaks observable with retention times of 5.39 and 5.52 minutes were identified as impurities present in the toluene trapping solution. The mass spectra of these peaks were correlated to the NIST database, allowing to identify them as ethylbenzene and xylene, respectively. A comparison with a GC-MS analysis of the pure toluene trapping solution revealed the presence of

these two species and allowed to establish their nature as contaminants in the toluene solution. The concentration of these impurities in the system wherein they become the second and third most prominent peaks in a GC-MS spectrum, gives a good indication of the low concentration of the trapped epoxyhexane. This shows that although there is a slowing down in 1-hexene decomposition rate at the point in which epoxyhexane is formed, this reduction in rate remains limited, causing the majority of the 1-hexene to undergo further decomposition beyond the formation of epoxyhexane.

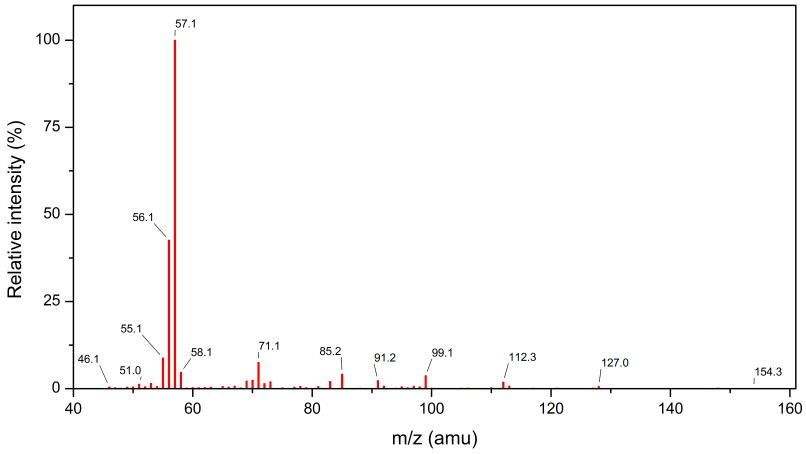

Fig. 8.5 Mass spectrum of the species eluted at 7.22 minutes from the gas chromatograph of the partial photooxidation products of 1-hexene.

By similarly contrasting the final peak in the GC-MS spectrum shown in Figure 8.3 against the GC-MS of the original toluene solution, it was possible to determine that this species originated from the photoepoxidation reactions. Unfortunately, the MS spectrum corresponding to the species eluted at this retention time (as shown in Figure 8.5) did not correlate with any known species on the NIST database. This inability to identify the molecule can be attributed in part to its very low concentration which led to the lack of strong MS signals. Nonetheless, from the MS in Figure 8.5 it is possible to see the traditional ionisation pattern of CH_3 groups (the m/z peaks at 57.1, 56.1, and 55.1 amu), this indicates that the studied species may be a branched alkane.

Finally, although the species eluted with a retention time of 5.26 minutes did not yield a sizeable peak in the GC-MS spectrum of the reaction, it was possible to identify its nature. By correlating with the NIST database, it was possible to determine that the eluate at 5.26 was 2-hexenal. The presence of this species in the trapping solution indicates the occurrence of a double

bond migration on the organic species during the photoepoxidation reactions. A similar bond migration was previously reported in literature by Pillai and Sahle-Demessie.[291]

Furthermore, it is important to remember that although it was seen during this series of experiments that the main partial photooxidation product was epoxyhexane, the observed GC-MS spectrum does not supply a full image of the photooxidation reaction. Indeed, the necessity of a 4 minute solvent delay (to eliminate the detection of toluene) signifies that a number of potentially more volatile eluates which may have been produced and captured in the system, remained unobserved. This lack of information is further exacerbated by the technical limitations of the mass spectrometer which rendered impossible the detection of small molecular species such as CO_2.

These limitations can be partially overcome through chemical reactions. By carrying out a reaction at the exhaust of the photoreactor it is possible to convert small and reactive molecules into larger, more stable, species. These larger molecules will inevitably display longer retention times and thus be analysable through GC-MS.

8.3.2 Tandem Reaction of Diisopropylamine With the Photoreactor Exhaust

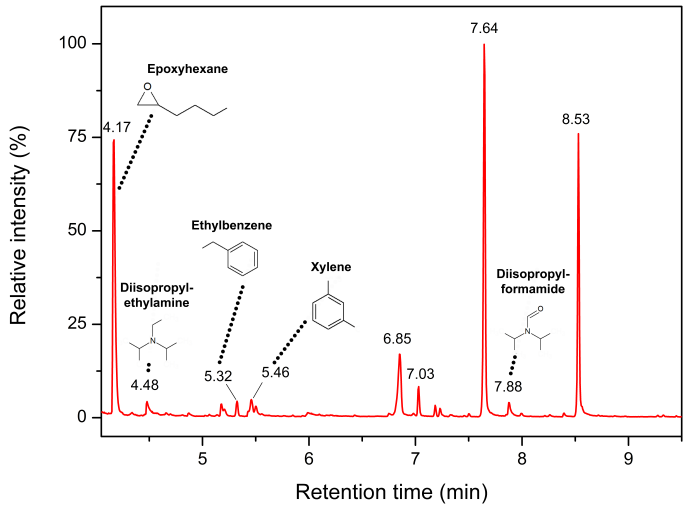

Fig. 8.6 Gas chromatogram of the diisopropylamine/toluene trap used for the tandem reaction of the partial photooxidation products of 1-hexene after 72 h of reaction time. The retention time of the main peaks in the spectrum has been marked above each peak. The nature of the peaks identifiable by correlating the MS of each peak with the NIST database (NIST 98) is also shown.

The gas chromatogram of the trapping mixture containing diisopropylamine after 72 hours of continuous hexene epoxidation reactions is shown in Figure 8.6. From this chromatogram it is possible to distinguish nine different peaks with relative retention times of 4.17, 4.48, 5.32, 5.46, 6.85, 7.03, 7.64, 7.88, and 8.53 minutes. This abundance of species in the gas chromatogram arises from four different sources: the toluene trapping solvent, the diisopropylamine reagent, the un-reacted partial oxidation products, and the products of the reaction between the reactor exhaust and the diisopropylamine. For clarity, the retention times, sources, and known identities of the different species are shown in Table 8.1.

Table 8.1 Identification of the main GC-MS signals observed in the chemical trap after the reaction of the 1-hexene photodecomposition products with diisopropylamine. The source and confirmed identity of each signal has been reported, the unidentifiable samples have been marked as unknown.

Retention time (min)	Origin	Identity
4.17	Photooxidation	Epoxyhexane
4.48	Diisopropylamine	Diisopropylethylamine
5.32	Toluene	Ethylbenzene
5.46	Toluene	Xylene
6.85	Reaction	Unknown
7.03	Photooxidation	Unknown
7.64	Reaction	**Unknown A**
7.88	Reaction	Diisopropylformamide
8.53	Reaction	**Unknown B**

The origin of the chemical impurities attributed to the toluene and diisopropylamine in Table 8.1 was established by comparing the GC-MS spectrum presented in Figure 8.6 with those of the two species independently. The nature of these impurities was further determined out by correlating the MS spectra of each peak with the NIST database. As such, it was possible to identify the two eluates with retention times of 5.32 and 5.46 as the ethylbenzene and xylene impurities present in the toluene. The eluate detected with a retention time of 4.48 was identified to be diisopropylethylamine. This latter compound is known as Hünig's base and is a common impurity in diisopropylamine formed by its alkylation.

The source of the two peaks attributed to the photooxidation reaction was determined by comparing the peaks in Figure 8.6 with those observed in the previous studies on the partial photooxidation products of this reaction (as shown in Figure 8.3). As such, by correlating the MS

spectra with the NIST database it was possible to identify the eluate with a retention time of 4.17 minutes as epoxyhexane. The retention time for this species is marginally smaller ($\sim$ 6 seconds) than that observed in Figure 8.3, this difference can be attributed to experimental error arising from a short cool down time in the GC method which left the GC oven slightly above the intended initial temperature from a previous GC-MS run at the time in which the analysis of the present sample was carried out. The eluate observed at a retention time of 7.03 minutes can also be attributed to the photooxidation reactions. This species can be seen to elute at 7.06 minutes in Figure 8.3. Unfortunately, due to the low concentration of this species, no positive correlation was achieved with the NIST database.

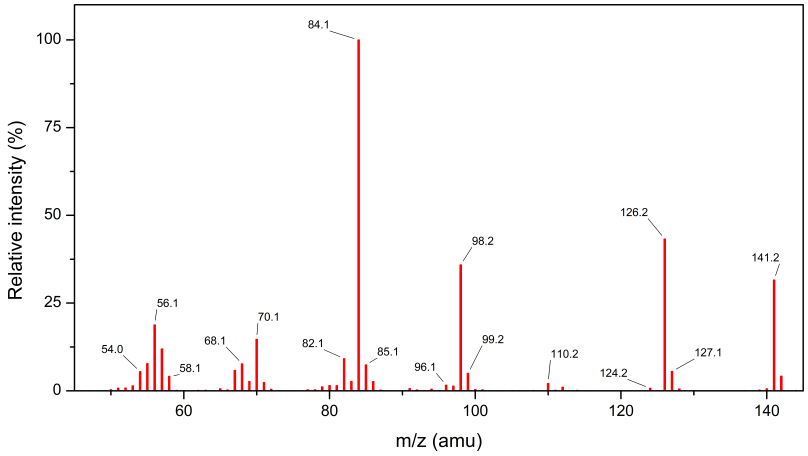

Fig. 8.7 Mass spectrum of the species eluted at 6.85 minutes from the gas chromatograph of the the reaction of diisopropylamine with the partial photoxidation products of 1-hexene.

A similar lack of correlation limited the identification of the main products of the diisopropylamine reaction. The species eluted with a retention time of 6.85 minutes was unique to the spectra containing the photooxidation products in combination with the diisopropylamine. Unfortunately, the MS of this species (shown in Figure 8.7) could not be correlated to any species present in the available NIST database. Nonetheless, it is possible to ascertain that this species is the product of a reaction of diisopropylamine by the odd-numbered m/z peak (141.2 amu) as well as the even-numbered fragments of the molecule which indicate the presence of nitrogen in the species.

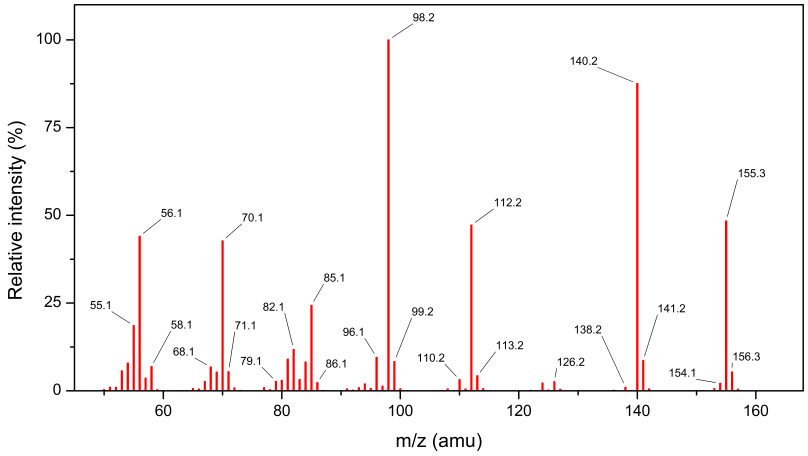

Fig. 8.8 Mass spectrum of one of the major products of the the reaction of diisopropylamine with the partial photoxidation products of 1-hexenespecies. This species is labelled as unknown A and was eluted with a retention time of 7.46 minutes.

In a similar fashion, the two major products of the diisopropylamine reaction (unknown A and unknown B in Table 8.1) did not correlate to any species present in the NIST database. However, by observing their respective MS traces (Figure 8.8 for unknown A and Figure 8.9 for unknown B) it is possible to suggest the molecular structures for these species. It can be seen from the odd m/z peak (155.3 amu) as well as the 14 amu difference between most fragments in Figure 8.8 that unknown A is a nitrogen containing species which fragments by losing CH_2 groups. A similar analysis can be made for the MS spectrum of unknown B in Figure 8.9 with the sole difference that unknown B is larger by 14 amu. This difference between unknown A and unknown B indicates that both molecules originate from species with similar structures but which differ from each other by a single CH_2 group.

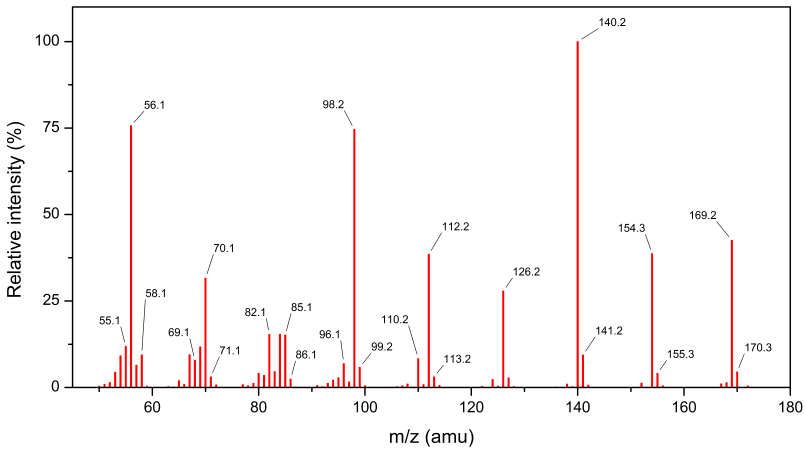

Fig. 8.9 Mass spectrum of one of the major products of the the reaction of diisopropylamine with the partial photoxidation products of 1-hexenespecies. This species is labelled as unknown B and was eluted with a retention time of 8.53 minutes.

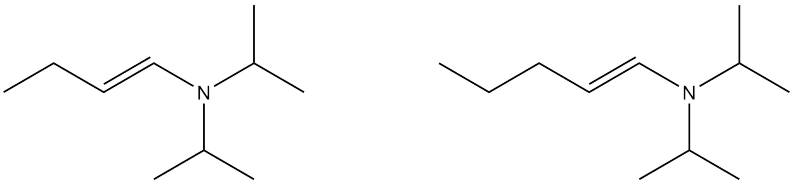

Unknown A Unknown B

Fig. 8.10 Proposed molecular structure for the two major unknown products formed during the reaction of the partial photodecomposition products of 1-hexene with diisopropylamine.

Based on the MS patterns of unknown A and unknown B, it becomes possible to suggest the structures of these two species as shown in Figure 8.10. By further taking into account the known reactivity of the diisopropylamine, it is plausible that the two unknown species were synthesised from the ring opening reactions of their respective epoxides, followed by rapid condensation reactions, as shown in Figure 8.11.

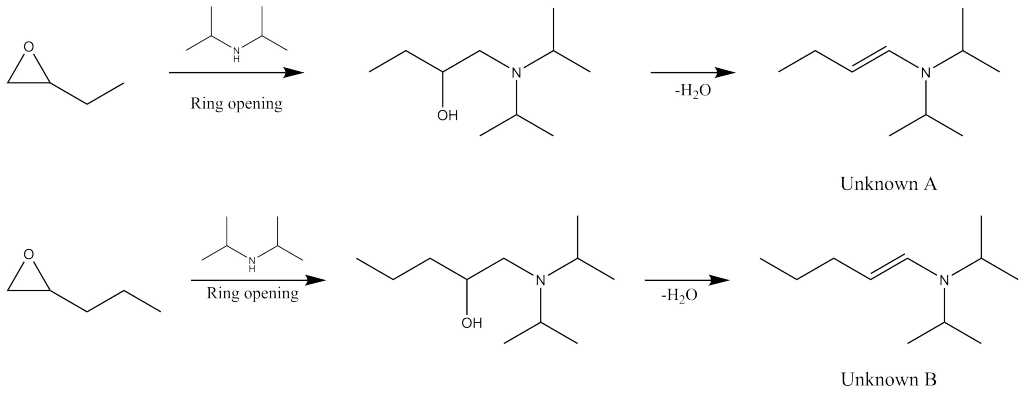

Fig. 8.11 Proposed scheme for the formation of unknown A and unknown B from ring opening reactions with diisopropylamine.

The difference of CH_2 group between the starting materials of the two unknown molecules is consistent with the known photoxidation processes on TiO_2 which occur through the gradual fragmentation of organic molecules. Figure 8.12 suggests a series of possible reaction pathways through which the starting products for unknown A and unknown B could have been created. It is nonetheless important to note that the process of organic photodecomposition on TiO_2 is a complicated one that proceeds through a large variety of different pathways. As such, the scheme proposed in Figure 8.12 can only be considered as a possible synthetic route until further evidence (such as the *in situ* analysis of the reactions) can be gathered.

Although attempts were made during this series of experiments in order to isolate both of the two unknown species, these approaches were unsuccessful and further work had to be postponed as a result of time constraints.

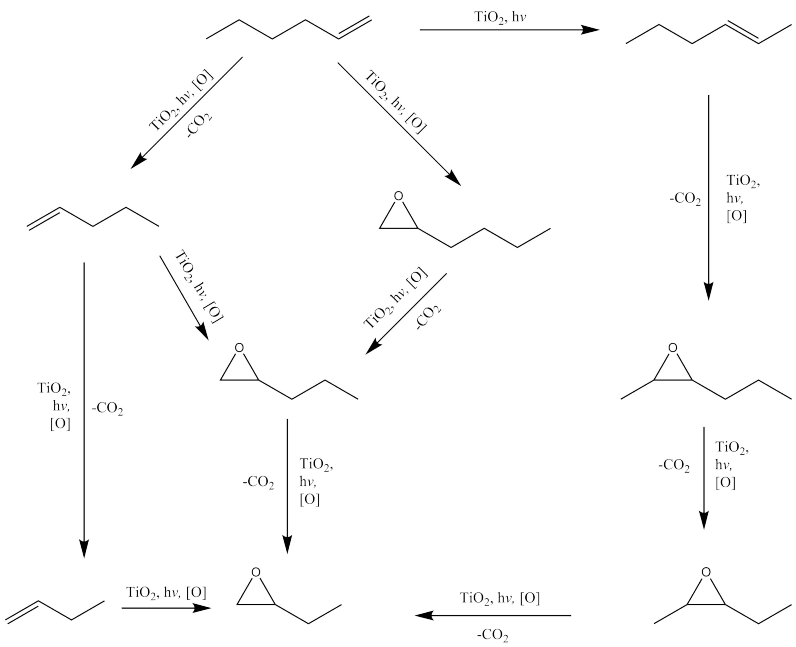

Fig. 8.12 Proposed scheme for the formation of the epoxide precursors to unknown A and unknown B from 1-hexene. [O] = oxidant/O_2.

8.4 Conclusions

During this series of experiments, it was possible to successfully demonstrate the potential for the photocatalytic reactor designed during this study as a technology whose use exceeds the simple photodecomposition of toxic contaminants in gas streams.

The photoepoxidation of 1-hexene into epoxyhexane was performed successfully. Although this reaction generated only limited quantities of epoxyhexane over extended periods of time, the conversion was achieved with only a cold cathode UV_a lamp as energy source. As such, this series of experiments shows the development of a system which allows to create highly useful chemical species whilst only using limited amounts of energy. This advantage in combination with the potential of photoreactor optimisation to increase the yield of epoxyhexane renders the developed technologies attractive at an industrial level. Furthermore, the production of a number of secondary partial photooxidation products was observed in the created system. Amongst these products it was postulated that there were species too volatile or too reactive to be successfully detected through traditional means.

In order to take advantage of these species, a chemical reaction was successfully performed at

the exhaust of the photoreactor, allowing to create two novel compounds. Due to limitations in the MS database, the ultimate identification of the newly created compounds was difficult. Nonetheless, it was possible to suggest the molecular structure of these species. Further literature studies demonstrated the rarity of these species which have been mentioned only briefly in literature[310,311] and whose use has been investigated as anti-tumour and analgesic agents, leading to the publication of two patents within the last 25 years.[310,312,313]

Information on the traditional synthesis procedures for the two structures created during this series of experiments is hard to achieve and few methods seem to exist.[311,312] These methods require complex catalysts and allow to yield the molecules only as metal complexes. As such, the technologies presented during this series of experiments offer the potential for a low cost synthesis of species whose creation remains problematic through non photocatalytic means.

In conclusion, through the present series of experiments it was possible to develop the technologies used for the decomposition of VOCs in gas streams and adapt them to become synthetic reactors. The presented technologies still require a significant amount of optimisation in order to achieve industrial viability. Nonetheless, the potential for the use of photoreactors as facile, energy-efficient, alternatives to traditional multi-stage organic syntheses, is readily apparent. As such, it is possible to see the developed reactors as an initial step towards the creation of a more powerful and more sustainable chemical industry.

9. Conclusions and Future Developments

Throughout this thesis a large number of novel developments were carried out in the field of TiO_2 mediated gas-phase photocatalysis. From these developments it becomes possible to envisage a significant amount of future work both at academic and industrial levels in order to achieve high efficiency, commercial, photocatalytic gas purification reactors.

9.1 Conclusions

During the present study a series of novel TiO_2 nanostructures were synthesised in order to develop a technique for the enhanced gas phase photodecomposition of organic pollutants. The application of these catalysts in the absorptive and photocatalytic removal of siloxanes from static environments allowed to determine an ideal candidate for the photodecomposition of contaminants in gas streams. As such, P25 was coated on glass beads by using a novel technique and used as the photocatalyst for the decomposition of both siloxanes and VOCs in gas streams. Further work on gas flow reactors allowed to demonstrate their potential to carry out functional group interconversions.

Initial synthetic experiments were focused on the development of high surface area nanostructures for the effective photodecomposition of siloxanes. Through the electrospinning technique, TiO_2, SiO_2, and WO_3 nanofibres were successfully created. Further templating studies allowed to create three novel nanostructures with enhanced surface areas: core/shell SiO_2/TiO_2 nanofibres, porous TiO_2 nanofibres, and hollow TiO_2 nanofibres. The morphological and electronic properties of these structures were successfully characterised in order to establish appropriate candidates for the photocatalytic purification of gases. Of the six created structures, both the core/shell and hollow nanofibres were discounted for applications in the industrial photodecomposition of contaminants. The core-shell nanofibres were discounted due to their complex preparation technique

which rendered them unsuitable for large scale industrial applications whilst the hollow nanofibres were discarded due to a high mechanical fragility inherent to the created architectures.

Following the selection of potential photocatalysts, studies were carried out to investigate their siloxane adsorption properties. These studies successfully compared the synthesised nanofibrous structures to the industrial standard adsorption media used by PpTek ltd. in order to achieve a benchmark for the removal of siloxanes through adsorption. The adsorption properties of the created nanofibrous catalysts were further compared to two additional materials with high surface areas synthesised during this study: silica aerogel granules, and modified silica gel beads. The commercially available silica gel was seen to be the ideal adsorbent for siloxanes, displaying an adsorption capacity 50 % larger than that of the PpTek media. The aerogel granules proved to be rapid adsorbents although they only displayed a limited siloxane adsorption capacity due to the presence of inaccessible internal pores. Similarly, the nanofibrous TiO_2 and SiO_2 structures were shown to be only mildly effective at removing gas-phase siloxanes by adsorption, with the SiO_2 nanofibres showing a greater affinity for siloxanes due to their chemical composition. From these studies, it was possible to establish a baseline for the removal of siloxanes and monitor the relative adsorption properties of the different nanostructured catalysts. It was further possible to gain an insight on the adsorption affinity of siloxanes with the created structures and the parameters which govern the catalyst-siloxane contact time.

After having established a baseline value for the removal of siloxanes in the gas phase, the photodecomposition properties of the created nanofibrous structures were determined in static environments in order to select one ideal photocatalyst for the purification of gas streams at industrial levels. These studies allowed to ascertain the rates of decomposition of the created structures and compare them with those of the commercially available nano-photocatalyst P25. From the decomposition studies it was successfully shown that the created porous TiO_2 nanofibres displayed the highest photodecomposition efficiency. The achieved siloxane decomposition kinetics were further improved by applying doping to the created nanostructures. WO_3 doped TiO_2 nanofibres were thus created and their siloxane decomposition properties studied. Eventually, it was possible to develop an ideal photocatalyst for the decomposition of gas-phase siloxanes through these studies. Indeed, TiO_2 nanofibres doped with 1 mol% of WO_3 demonstrated an effective increase in photodecomposition rate of 126 % with respect to P25.

The successful decomposition of siloxanes in static environments allowed to proceed further into developing the industrial applicability of the studied photocatalysts for the purification of gas streams. As such, a TiO_2 based gas stream photoreactor was developed. In order to ensure the industrial applicability of the created technologies, P25 was chosen as the photocatalyst due to its large scale commercial availability. A novel technique, the GIAC method, was developed in order to support the catalyst on glass bead substrates and ensure a maximum gas-catalyst contact time. The GIAC method allowed to achieve a mechanically stable catalyst coating on the glass substrates, thus further enhancing the industrial applicability of the developed techniques.

With an industrially compatible gas stream photoreactor, it was possible to investigate the siloxane photodecomposition properties of P25. As the photodecomposition of siloxanes led to the formation of SiO_2 residues on the catalysts surface, the catalyst's TON was investigated. From the TON of the photocatalytic reactor it was observed that the total amount of siloxane decomposed by the photoreactor was over twice that removed by the industrial adsorbents in static reaction conditions, demonstrating the effectiveness of photocatalytic purification techniques. Further flow degradation studies were carried out in order to achieve the regeneration of the TiO_2 catalysts. Two different techniques allowed to achieve full regeneration of catalytic activities: chemical recoating and mechanical recoating. Although both of the techniques provided a catalytic regeneration of ~ 100 % , mechanical recoating was observed to be the most appealing for industrial applications. This preference was determined based on the facilitation of industrial requirements as mechanical recoating proceeded through the GIAC method whilst chemical recoating required a separate *ad-hoc* procedure.

Having established the viability and potential of TiO_2 based photocatalytic reactors for the purification of biogas, the scope of the designed devices was expanded to include the purification of ambient environments. The photocatalytic reactor was further optimised and used to successfully decompose three common VOCs. Although it was possible to decompose IPA, acetone, and styrene to non-toxic levels in gas streams, the formation of carbonaceous deposits and partial photooxidation products was observed during these experiments. In particular, through GC-MS analysis it was possible to determine the main partial photodecomposition products of styrene and establish potential mechanistic pathways towards their formation.

The study of partial photocatalytic decomposition products was further pursued in the final

series of experiments presented during this thesis. In these experiments it was shown that, using the established photoreactor design, it was possible to carry out the photoepoxidation of hexene. Further experiments were carried out in order to directly react the less stable partial photooxidation products issued from the gas flow reactors. As such, it was possible to synthesise two particular molecular species. By analysing the GC-MS data for the two species it was possible to propose their molecular structure as well as a potential synthetic pathway for each molecule. The synthesised molecules are particularly important as their presence is only poorly recorded in literature and routes to their synthesis are complicated and expensive. This successful synthesis allowed to further expand the scope of the created devices from simple gas purification systems to synthetic molecular pipelines.

In conclusion, during the present thesis it was possible to study the photodecomposition properties of a variety of nanostructures which led to the development of highly efficient photocatalytic reactors for the photodecomposition of contaminants in the gas phase. The development of the presented technologies was performed in such a way as to retain and enhance their industrial applicability. In addition to their role as photocatalytic purification agents, it was further possible to demonstrate the potential of the developed reactors to act as sources of rare and novel organic synthesis precursors.

9.2 Future Developments

Two main avenues, one academic and the other industrial, can be pursued in order to further develop and expand on the work presented during this thesis.

Academic Prospects

From an academic perspective, future work developed from this thesis should focus primarily on furthering the photosynthetic research presented in Chapter 8. Initially, efforts should be made to isolate and identify the two novel synthetic products created in order to ascertain their mechanistic formation pathways. This could be performed through a variety of techniques amongst which liquid chromatography and cryogenic distillation. Once a solid understanding of the underlying processes is achieved, the photosynthetic reactor can be developed further in order to study its effectiveness as a synthetic flow reactor for the formation of rare organic molecules.

In parallel to these studies, the efficiency of the photosynthetic reactor could be further increased by modifying the used photocatalysts as well as the concentration of oxidising agents (such as O_2) in the gas streams. By changing the catalyst's specific properties it will be possible to modify the selectivity of the photocatalytic reactions and promote the formation of partial photooxidation products over that of CO_2. However, as the reduction of selectivity for CO_2 is often accompanied by a loss in conversion, studies will have to focus on the selection of a catalyst which will allow a minimal loss in overall conversion whilst maintaining a low CO_2 selectivity.

Further advancements to the photocatalytic efficiency of the reactor could also be achieved through the development of nanomaterials with increased surface area. It was shown during this study that nanomaterials with enhanced surface areas displayed improved photocatalytic decomposition properties. As such, further studies into the quantification of the surface area of the created catalysts through BET devices as well as the development of high surface area nanomaterials becomes essential.

Through these improvements it should be possible to develop a second generation of photocatalysts. These materials would allow to further expand the use of the presented technologies by enhancing the photocatalytic degradation of the reactors as well as developing a fine control over

the chemical output of these reactors. From this, further studies should be performed in order to lower the energetic requirements of the system by using lower band gap semiconductors and thus allow for the development of a solar-powered photocatalytic gas purification reactor.

Industrial Prospects

A number of industrial developments can be brought forward from the work presented during this thesis. Due to the effectiveness of the GIAC coating technique, intellectual protection has been sought for this method and, at the time of writing, is undergoing the patent application process under a revised name. Further work on this technique should focus on the scaling up of the coating procedure such that a large throughput of substrate coated catalysts can be achieved within reduced time-scales.

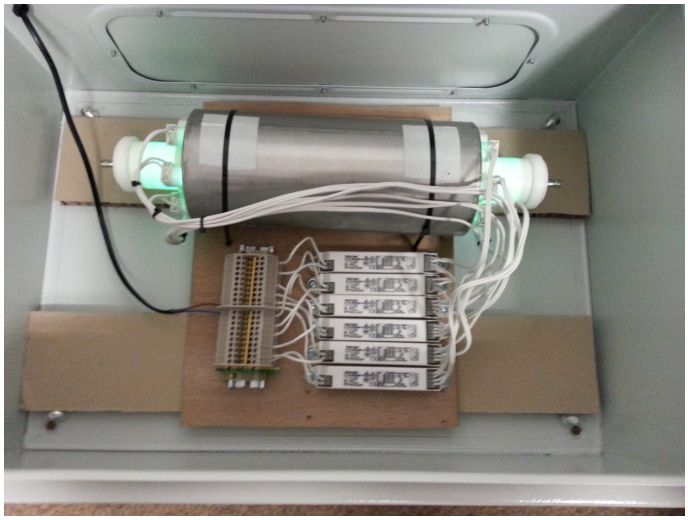

Fig. 9.1 Photograph of the prototype photoreactor developed for the industrial photodecomposition of siloxanes in biogas.

This enhancement of the GIAC coating procedure should be performed in combination with the industrial application of the photoreactors presented during this thesis. Recent progress in this field has allowed for the successful construction of the first photocatalytic purification reactor prototype. At the time of writing, a created photocatalytic reactor prototype (shown in Figure 9.1) is awaiting formal approval in order to be applied to industrial biogas flows. From the data gathered during these tests, it will be possible to establish the drawbacks of the technology and determine the required engineering and chemical improvements necessary to establish the developed technologies as commercially successful systems.

One of the major developments required by industrial systems on the technologies presented in this thesis will be to address the lifetime of the catalysts as well as their regeneration techniques. Indeed, in order to render the developed reactors competitive at an industrial scale, not only does the level of siloxane removal need to exceed that of the industrially used standards but the lifetime of the catalysts must also be long enough to require only a minimal level of regeneration. The lifetime of the catalysts can be extended through a variety of ways which range from the improvement of the photocatalysts at a chemical level (by using different semiconductors), to a modification in engineering which allows to optimise the interaction between the catalysts and the contaminant species through different reactor designs. The regeneration techniques presented in this study require further work in order to ascertain their potential over extended regeneration cycles as well as the ultimate financial costs of the recoating procedures.

By combining the proposed academic and industrial improvements, it is possible to see in the present thesis the first steps towards the development of cheap, energy efficient, and versatile photocatalytic gas purification and synthesis devices. Such devices would allow for a low-cost, solar-powered, air purification system aimed at the sterilisation of contained atmospheres in countries with emerging economies. In addition to this, photocatalytic reactors based on the presented technology could be used in developed economies for the production of specialised molecular species in both academic and pharmaceutical environments. In the long term, it is possible to envisage the ultimate development of a photocatalytic chemical pipeline which would allow for the synthesis of tailored chemicals through the simple use of solar energy, as dreamed of in the dawn of the 20th century:

"On the arid lands there will spring up industrial colonies without smoke and without smokestacks; forests of glass tubes will extend over the plains and glass buildings will rise everywhere; inside of these will take place the photochemical processes that hitherto have been the guarded secret of the plants, but that will have been mastered by human industry which will know how to make them bear even more abundant fruit than nature, for nature is not in a hurry and mankind is. ... If our black and nervous civilization, based on coal, shall be followed by a quieter civilization based on the utilization of solar energy, that will not be harmful to progress and to human happiness." - Giacomo Ciamician, Bologna, 1912.[314]

10. Bibliography

[1] P. Le Billon, *Polit. Geogr.*, 2001, **20**, 561–584.

[2] J. D. Colgan, *Energy Res. Soc. Sci.*, 2014, **1**, 198–205.

[3] International Energy Agency, *World Energy Outlook 2013*, International Energy Agency, Paris, 2013.

[4] *Climate Change 2013 - The Physical Science Basis*, ed. Intergovernmental Panel on Climate Change, Cambridge University Press, Cambridge, 2014, pp. 1–1552.

[5] United Nations, *Adoption of the Paris Agreement*, United Nations, Paris, 2015.

[6] D. J. MacKay, *Sustainable Energy - without the hot air*, UIT, Cambridge, England, 2009.

[7] M. Schweigkofler and R. Niessner, *J. Hazard. Mater.*, 2001, **83**, 183–196.

[8] B. Eklund, E. P. Anderson, B. L. Walker and D. B. Burrows, *Environ. Sci. Technol.*, 1998, **32**, 2233–2237.

[9] *GB Pat.*, 2440123, 2008.

[10] *Eu Pat.*, 2593211, 2013.

[11] P. Gislon, S. Galli and G. Monteleone, *Waste Manag.*, 2013, **33**, 2687–93.

[12] J. Huang and R. Crookes, *Fuel*, 1998, **77**, 1793–1801.

[13] R. Dewil, L. Appels and J. Baeyens, *Energy Convers. Manag.*, 2006, **47**, 1711–1722.

[14] S. O. Hay, T. N. Obee and C. Thibaud-Erkey, *Appl. Catal. B-Environmental*, 2010, **99**, 435–441.

[15] A. Antonello, G. Soliveri, D. Meroni, G. Cappelletti and S. Ardizzone, *Catal. Today*, 2014, **230**, 35–40.

[16] M. Ajhar, M. Travesset, S. Yuece and T. Melin, *Bioresour. Technol.*, 2010, **101**, 2913–2923.

[17] *US Pat.*, 7306652, 2007.

[18] L. Kaj, J. Andersson, A. P. Cousins, M. Remberger and E. Brorström-Lundén, *Results from the Swedish National Screening Programme 2004 - Subreport 4: Siloxanes*, IVL Report B1643, Stockholm, 2005.

[19] A. Einstein, *Ann. Phys.*, 1912, **342**, 832–838.

[20] S. Califano, *Pathways to Modern Chemical Physics*, Springer, Heidelberg, 2012, p. 288.

[21] S. Glasstone, *Textbook of Physical Chemistry*, Macmillan & Company, London, 2nd edn., 1947, p. 1155.

[22] A. Jabłoński, *Nature*, 1933, **131**, 839–840.

[23] M. Kasha, *Discuss. Faraday Soc.*, 1950, **9**, 14.

[24] P. Atkins and J. de Paula, *Atkins' Physical Chemistry*, OUP Oxford, 8th edn., 2006.

[25] A. Albini, *Photochemistry*, Springer, Heidelberg, 2016.

[26] J. D. Coyle, *Introduction to Organic Photochemistry*, John Wiley & Sons, London, 1986.

[27] N. J. Turro and G. Schuster, *Science*, 1975, **187**, 303–12.

[28] *Advances in Photochemistry*, ed. D. C. Neckers, D. H. Volman and G. von Bnau, John Wiley & Sons, Hoboken, NJ, USA, 1994.

[29] A. Cembran, F. Bernardi, M. Garavelli, L. Gagliardi and G. Orlandi, *J. Am. Chem. Soc.*, 2004, **126**, 3234–3243.

[30] E. Merino and M. Ribagorda, *Beilstein J. Org. Chem.*, 2012, **8**, 1071–1090.

[31] H. Yamazaki and R. J. Cvetanovic, *J. Am. Chem. Soc.*, 1969, **91**, 520–522.

[32] J. Clayden, G. Nick, W. Stuart and W. Peter, *Organic Chemistry*, Oxford University Press, Oxford, 2001, pp. 1017–1023.

[33] L. J. Johnston, *Chem. Rev.*, 1993, **93**, 251–266.

[34] *Handbook of Vinyl Polymers: radical polymerisation, process, and technology*, ed. M. K. Mishra and Y. Yagci, CRC Press, Boca Raton, 2nd edn., 2009.

[35] J. Mattay, *Angew. Chemie Int. Ed. English*, 1987, **26**, 825–845.

[36] S. Mishra, S. Daniele, S. Petit, E. Jeanneau and M. Rolland, *Dalt. Trans.*, 2009, 2569–2577.

[37] H. Togo, *Advanced Free Radical Reactions for Organic Synthesis*, Elsevier, Kidlington, 2004.

[38] W. D. Motherwell and D. Crich, *Free Radical Chain Reactions in Organic Synthesis*, Academic Press, London, 1992.

[39] B. D. A. Hook, W. Dohle, P. R. Hirst, M. Pickworth, M. B. Berry and K. I. Booker-Milburn, *J. Org. Chem.*, 2005, **70**, 7558–64.

[40] M. Fagnoni, D. Dondi, D. Ravelli and A. Albini, *Chem. Rev.*, 2007, **107**, 2725–2756.

[41] M. Grätzel, *Inorg. Chem.*, 2005, **44**, 6841–6851.

[42] S. Sakthivel, B. Neppolian, M. Shankar, B. Arabindoo, M. Palanichamy and V. Murugesan, *Sol. Energy Mater. Sol. Cells*, 2003, **77**, 65–82.

[43] L. Cermenati, A. Albini, L. Cermenati, C. Richter and A. Albini, *Chem. Commun.*, 1998, 805–806.

[44] J. M. R. Narayanam and C. R. J. Stephenson, *Chem. Soc. Rev.*, 2011, **40**, 102–113.

[45] T. P. Yoon, M. A. Ischay and J. Du, *Nat. Chem.*, 2010, **2**, 527–32.

[46] O. Carp, C. L. Huisman and A. Reller, *Prog. Solid State Chem.*, 2004, **32**, 33–177.

[47] *US Pat.*, 8791044 B2, 2014.

[48] *US Pat.*, 20120267321 A1, 2012.

[49] M. R. Hoffmann, S. T. Martin, W. Choi and D. W. Bahnemann, *Chem. Rev.*, 1995, **95**, 69–96.

[50] K. Pirkanniemi and M. Sillanpää, *Chemosphere*, 2002, **48**, 1047–1060.

[51] C.-Y. Hsiao, C.-L. Lee and D. F. Ollis, *J. Catal.*, 1983, **82**, 418–423.

[52] *Heterogeneous Photocatalysis: From Fundamentals to Green Applications*, ed. J. C. Colmenares and Y.-J. Xu, Springer, Berlin, 2015, pp. 297–299.

[53] W. C. Lee, G. E. Canciani, B. O. Alwhshe and Q. Chen, *Int. J. Hydrogen Energy*, 2016, **41**, 123–131.

[54] R. S. Kler, *PhD Thesis*, University of Sussex, 2013.

[55] H. Jiang, R. I. Gomez-Abal, P. Rinke and M. Scheffler, *Phys. Rev. B*, 2010, **81**, 085119.

[56] X. Zhang, Q. Han, Z. Dong, Y. Xu and H. Zhang, *J. Mater. Sci. Technol.*, 2008, **24**, 594–596.

[57] M. Y. Ghaly, T. S. Jamil, I. E. El-Seesy, E. R. Souaya and R. A. Nasr, *Chem. Eng. J.*, 2011, **168**, 446–454.

[58] N. Miranda-García, S. Suárez, B. Sánchez, J. Coronado, S. Malato and M. I. Maldonado, *Appl. Catal. B Environ.*, 2011, **103**, 294–301.

[59] O. Powell, D. Sweatman and H. B. Harrison, *Smart Mater. Struct.*, 2006, **15**, S81–S86.

[60] H. Zhang and J. F. Banfield, *J. Phys. Chem. B*, 2000, **104**, 3481–3487.

[61] K.-N. P. Kumar, K. Keizer, A. J. Burggraaf, T. Okubo, H. Nagamoto and S. Morooka, *Nature*, 1992, **358**, 48–51.

[62] H. Tang, K. Prasad, R. Sanjines, P. E. Schmid and F. Levy, *J. Appl. Phys.*, 1994, **75**, 2042–2047.

[63] A. Di Paola, M. Bellardita and L. Palmisano, *Catalysts*, 2013, **3**, 36–73.

[64] M. Grätzel and F. P. Rotzinger, *Chem. Phys. Lett.*, 1985, **118**, 474–477.

[65] A. L. Linsebigler, G. Lu and J. T. Yates Jr, *Chem. Rev.*, 1995, **95**, 735–758.

[66] A. Fujishima, X. Zhang and D. A. Tryk, *Surf. Sci. Rep.*, 2008, **63**, 515–582.

[67] K. Tennakone and J. Bandara, *Sol. Energy Mater. Sol. Cells*, 2000, **60**, 361–365.

[68] P. Christopher, H. Xin and S. Linic, *Nat. Chem.*, 2011, **3**, 467–472.

[69] I. S. McLintock and M. Ritchie, *Trans. Faraday Soc.*, 1965, **61**, 1007.

[70] G. N. Schrauzer and T. D. Guth, *J. Am. Chem. Soc.*, 1977, **99**, 7189–7193.

[71] J. Soria, J. C. Conesa, V. Augugliaro, L. Palmisano, M. Schiavello and A. Sclafani, *J. Phys. Chem.*, 1991, **95**, 274–282.

[72] F. Mahdavi, T. C. Bruton and Y. Li, *J. Org. Chem.*, 1993, **58**, 744–746.

[73] J. L. Ferry and W. H. Glaze, *Langmuir*, 1998, **14**, 3551–3555.

[74] IEA, *World Energy Outlook 2012*, OECD Publishing, Paris, 2012, pp. 544–547.

[75] A. J. Hamilton, R. M. May and E. K. Waters, *Nature*, 2015, **520**, 42–43.

[76] K. R. Thampi, J. Kiwi and M. Grätzel, *Nature*, 1987, **327**, 506–508.

[77] T. Inoue, A. Fujishima, S. Konishi and K. Honda, *Nature*, 1979, **277**, 637–638.

[78] S. Kaneco, H. Kurimoto, Y. Shimizu, K. Ohta and T. Mizuno, *Energy*, 1999, **24**, 21–30.

[79] S. S. Tan, L. Zou and E. Hu, *Catal. Today*, 2006, **115**, 269–273.

[80] S. Yanagida, T. Azuma, H. Kawakami, H. Kizumoto and H. Sakurai, *J. Chem. Soc., Chem. Commun.*, 1984, 21–22.

[81] L. Nie, K. K. Xin, W. S. Li and X. P. Zhou, *Catal. Commun.*, 2007, **8**, 488–492.

[82] Y. Ren, Y. Che, W. Ma, X. Zhang, T. Shen and J. Zhao, *New J. Chem.*, 2004, **28**, 1464.

[83] S. R. Taffarel, M. A. Lansarin and C. C. Moro, *J. Braz. Chem. Soc.*, 2011, **22**, 1872–1879.

[84] G. Odian, *Principles of Polymerization*, John Wiley & Sons, New York, 4th edn., 2004.

[85] M. A. Katkar, S. N. Rao and H. D. Juneja, *RSC Adv.*, 2012, **2**, 8071.

[86] V.-H. Nguyen, H.-Y. Chan and J. C. S. Wu, *J. Chem. Sci.*, 2013, **125**, 859–867.

[87] T. Ohno, T. Kigoshi, K. Nakabeya and M. Matsumura, *Chem. Lett.*, 1998, 877–878.

[88] S.-C. Jung, *Korean J. Chem. Eng.*, 2008, **25**, 364–367.

[89] J.-H. Lee, *Sensors Actuators B Chem.*, 2009, **140**, 319–336.

[90] Z. T. Y. Al-Abdullah, Y. Shin, R. Kler, C. C. Perry, W. Zhou and Q. Chen, *Nanotechnology*, 2010, **21**, 505601.

[91] J. S. Bedi, D. W. Lester, Y. X. Fang, J. F. Turner, J. Zhou, S. M. Alfadul, C. Perry and Q. Chen, *J. Polym. Eng.*, 2013, **33**, 453–461.

[92] M. Schmidt and F. Schwertfeger, *J. Non. Cryst. Solids*, 1998, **225**, 364–368.

[93] D. Gong, C. A. Grimes, O. K. Varghese, W. Hu, R. S. Singh, Z. Chen and E. C. Dickey, *J. Mater. Res.*, 2001, **16**, 3331–3334.

[94] Z. T. Al-Abdullah, *PhD Thesis*, University of Sussex, 2012.

[95] W. C. Lee, Y. Fang, R. Kler, G. E. Canciani, T. C. Draper, Z. T. Al-Abdullah, S. M. Alfadul, C. C. Perry, H. He and Q. Chen, *Mater. Chem. Phys.*, 2015, **149**, 12–16.

[96] S. Banerjee, M. Misra, S. K. Mohapatra, C. Howard, S. K. Mohapatra and S. K. Kamilla, *Nanotechnology*, 2010, **21**, 145201.

[97] A. C. Pierre and G. M. Pajonk, *Chem. Rev.*, 2002, **102**, 4243–4266.

[98] S. Cao, K. L. Yeung, J. K. Kwan, P. M. To and S. C. Yu, *Appl. Catal. B Environ.*, 2009, **86**, 127–136.

[99] P. B. Sarawade, J.-K. Kim, A. Hilonga and H. T. Kim, *Solid State Sci.*, 2010, **12**, 911–918.

[100] *US Pat.*, 20130137567, 2012.

[101] G. Taylor, *Proc. R. Soc. A Math. Phys. Eng. Sci.*, 1964, **280**, 383–397.

[102] G. Taylor, *Proc. R. Soc. A Math. Phys. Eng. Sci.*, 1966, **291**, 145–158.

[103] G. Taylor, *Proc. R. Soc. A Math. Phys. Eng. Sci.*, 1969, **313**, 453–475.

[104] S. Ramakrishna, *An introduction to electrospinning and nanofibers*, World Scientific, Singapore; Hackensack, NJ, 2005.

[105] N. Bhardwaj and S. C. Kundu, *Biotechnol. Adv.*, 2010, **28**, 325–347.

[106] C. L. Shao, H. Kim, J. Gong and D. Lee, *Nanotechnology*, 2002, **13**, 635–637.

[107] D. Li and Y. N. Xia, *Nano Lett.*, 2003, **3**, 555–560.

[108] Y. Fang, W. C. Lee, G. E. Canciani, T. C. Draper, Z. F. Al-Bawi, J. S. Bedi, C. C. Perry and Q. Chen, *Mater. Sci. Eng. B*, 2015, **202**, 39–45.

[109] G. He, Y. Cai, Y. Zhao, X. Wang, C. Lai, M. Xi, Z. Zhu and H. Fong, *J. Colloid Interface Sci.*, 2013, **398**, 103–111.

[110] A. Rezaee, M. T. Ghaneian, N. Taghavinia, M. K. Aminian and S. J. Hashemian, *Environ. Technol.*, 2009, **30**, 233–9.

[111] B. Ohtani, O. Prieto-Mahaney, D. Li and R. Abe, *J. Photochem. Photobiol. A Chem.*, 2010, **216**, 179–182.

[112] T. Ohno, K. Sarukawa, K. Tokieda and M. Matsumura, *J. Catal.*, 2001, **203**, 82–86.

[113] R. Su, R. Bechstein, L. Sø, R. T. Vang, M. Sillassen, B. Esbjörnsson, A. Palmqvist and F. Besenbacher, *J. Phys. Chem. C*, 2011, **115**, 24287–24292.

[114] D. O. Scanlon, C. W. Dunnill, J. Buckeridge, S. A. Shevlin, A. J. Logsdail, S. M. Woodley, C. R. A. Catlow, M. J. Powell, R. G. Palgrave, I. P. Parkin, G. W. Watson, T. W. Keal, P. Sherwood, A. Walsh and A. A. Sokol, *Nat. Mater.*, 2013, **12**, 798–801.

[115] D. C. Hurum, A. G. Agrios, K. A. Gray, T. Rajh and M. C. Thurnauer, *J. Phys. Chem. B*, 2003, **107**, 4545–4549.

[116] G. P. Mueller, *J. Eng. Gas Turbines Power*, 1995, **117**, 820.

[117] S. Bari, *Renew. Energy*, 1996, **9**, 1007–1010.

[118] T. Abbasi, S. M. Tauseef and S. A. Abbasi, *Biogas energy*, Springer, New York, NY, 2012.

[119] C. Stone and N. Ladommatos, *J. Inst. Energy*, 1991, **64**, 202–211.

[120] N. Macari and R. Richardson, *J. Eng. Gas Turbines Power-Transactions Asme*, 1987, **109**, 443–447.

[121] J. C. Martinez, F. Mendez and C. Trevino, *Open Chem. Eng. J.*, 2008, **2**, 42–50.

[122] N. Abatzoglou and S. Boivin, *Biofuels, Bioprod. Biorefining*, 2009, **3**, 42–71.

[123] J. S. Jang, H. G. Kim, P. H. Borse and J. S. Lee, *Int. J. Hydrogen Energy*, 2007, **32**, 4786–4791.

[124] X. M. Wang, S. C. Lee, G. Y. Sheng, L. Y. Chan, J. M. Fu, X. D. Li, Y. S. Min and C. Y. Chan, *Appl. Geochemistry*, 2001, **16**, 1447–1454.

[125] K. Oshita, Y. Ishihara, M. Takaoka, N. Takeda, T. Matsumoto, S. Morisawa and A. Kitayama, *Water Sci. Technol.*, 2010, **61**, 2003–2012.

[126] Sun R.-D., Nakajima A., Watanabe T. and Hashimoto K., *J. Photochem. Photobiol. A Chem.*, 2003, **154**, 203–209.

[127] H. Tada, *Langmuir*, 1996, **12**, 966–971.

[128] K. Ikeda, K. Hashimoto and A. Fujishima, *J. Electroanal. Chem.*, 1997, **437**, 241–244.

[129] C. Minero, V. Maurino and E. Pelizzetti, *Langmuir*, 1995, **11**, 4440–4444.

[130] H. de Lasa, B. Serrano and M. Salaices, *Photocatalytic Reaction Engineering*, Springer US, Boston, MA, 2005.

[131] M. Vezzoli, *Ph.D. thesis*, Queensland University of Technology, 2012.

[132] I. Langmuir, *J. Am. Chem. Soc.*, 1916, **38**, 2221–2295.

[133] M. Baudu, *Ph.D. thesis*, Université de Rennes 1, 1990.

[134] U. Diebold, *Surf. Sci. Rep.*, 2003, **48**, 53–229.

[135] S. Brosillon, L. Lhomme, C. Vallet, A. Bouzaza and D. Wolbert, *Appl. Catal. B Environ.*, 2008, **78**, 232–241.

[136] A. Rincón and C. Pulgarin, *Appl. Catal. B Environ.*, 2003, **44**, 263–284.

[137] G. Vincent, P. Marquaire and O. Zahraa, *J. Photochem. Photobiol. A Chem.*, 2008, **197**, 177–189.

[138] R. L. Romero, O. M. Alfano and A. E. Cassano, *Ind. Eng. Chem. Res.*, 1997, **36**, 3094–3109.

[139] M. I. Cabrera, O. M. Alfano and A. E. Cassano, *J. Phys. Chem.*, 1996, **100**, 20043–20050.

[140] G. Camera-Roda and F. Santarelli, *Catal. Today*, 2007, **129**, 161–168.

[141] A. Bogner, P.-H. Jouneau, G. Thollet, D. Basset and C. Gauthier, *Micron*, 2007, **38**, 390–401.

[142] R. E. Lee, *Scanning electron microscopy and x-ray microanalysis*, PTR Prentice Hall, Englewood Cliffs, 1993.

[143] *SEM Microcharacterization of Semiconductors*, ed. D. B. Holt and D. Joy, Academic Press, London, 1989.

[144] W. H. Zachariasen, *Acta Crystallogr.*, 1967, **23**, 558–564.

[145] W. L. Bragg, *Proc. R. Soc. A Math. Phys. Eng. Sci.*, 1914, **89**, 468–489.

[146] G. I. Waterhouse and M. R. Waterland, *Polyhedron*, 2007, **26**, 356–368.

[147] J. Tauc, *Mater. Res. Bull.*, 1968, **3**, 37–46.

[148] A. A. Tahir, M. A. Ehsan, M. Mazhar, K. G. U. Wijayantha, M. Zeller and A. D. Hunter, *Chem. Mater.*, 2010, **22**, 5084–5092.

[149] V. Kumar, S. Kr. Sharma, T. Sharma and V. Singh, *Opt. Mater. (Amst).*, 1999, **12**, 115–119.

[150] K. D. Bartle and P. Myers, *TrAC Trends Anal. Chem.*, 2002, **21**, 547–557.

[151] A. T. James and A. J. P. Martin, *Biochem. J.*, 1952, **50**, 679–690.

[152] B. H. Stuart, *Infrared Spectroscopy: Fundamentals and Applications*, John Wiley & Sons, Chichester, UK, 2004.

[153] E. Radeva, D. Tsankov, K. Bobev and L. Spassov, *J. Appl. Polym. Sci.*, 1993, **50**, 165–171.

[154] P. J. Launer, *Infrared analysis of organosilicon compounds: spectra-structure correlations*, Petrarch Systems, New York, 1987.

[155] *WO Pat.*, 2014016239 A1, 2014.

[156] *US Pat.*, 5835840 A, 1998.

[157] C. Liu, *Xiyou Jinshu Cailiao Yu Gongcheng/Rare Met. Mater. Eng.*, 2005, **34**, 17–18.

[158] S. Ullah, E. P. Ferreira-Neto, A. A. Pasa, C. C. Alcântara, J. J. Acuña, S. A. Bilmes, M. L. Martínez Ricci, R. Landers, T. Z. Fermino and U. P. Rodrigues-Filho, *Appl. Catal. B Environ.*, 2015, **179**, 333–343.

[159] L. Song, Q. Jiang, P. Du, Y. Yang and J. Xiong, *Mater. Lett.*, 2014, **123**, 214–216.

[160] B. Ding, H. Kim, C. Kim, M. Khil and S. Park, *Nanotechnology*, 2003, **14**, 532–537.

[161] F. O. Ochanda and M. R. Barnett, *J. Am. Ceram. Soc.*, 2010, **93**, 2637–2643.

[162] Z. Jiao, T. Chen, J. Xiong, T. Wang, G. Lu, J. Ye and Y. Bi, *Sci. Rep.*, 2013, **3**, 2720.

[163] F. Ruggieri, D. Camillo, L. Maccarone, S. Santucci and L. Lozzi, *J. Nanoparticle Res.*, 2013, **15**, 1982.

[164] S. Suphankij, W. Mekprasart and W. Pecharapa, *10th Eco-Energy Mater. Sci. Eng. Symp.*, 2013, **34**, 751–756.

[165] S. Zhang, X. Dong, S. Xu, J. Wang and G. Liu, *Xiyou Jinshu Cailiao Yu Gongcheng/Rare Met. Mater. Eng.*, 2008, **37**, 2196–2200.

[166] H. Y. Wang, Y. Yang, X. Li, L. J. Li and C. Wang, *Chinese Chem. Lett.*, 2010, **21**, 1119–1123.

[167] Q. Li, D. Sun and H. Kim, *Mater. Res. Bull.*, 2011, **46**, 2094–2099.

[168] B. Holland and J. Hay, *Polymer (Guildf).*, 2001, **42**, 4825–4835.

[169] B. Holland and J. Hay, *Polymer (Guildf).*, 2001, **42**, 6775–6783.

[170] M. Bognitzki, H. Hou, M. Ishaque, T. Frese, M. Hellwig, C. Schwarte, A. Schaper, J. H. Wendorff and A. Greiner, *Adv. Mater.*, 2000, **12**, 637–640.

[171] W. Stöber, A. Fink and E. Bohn, *J. Colloid Interface Sci.*, 1968, **26**, 62–69.

[172] G. H. Bogush, M. A. Tracy and C. F. Zukoski, *J. Non. Cryst. Solids*, 1988, **104**, 95–106.

[173] C. Wessel, R. Ostermann, R. Dersch and B. M. Smarsly, *J. Phys. Chem. C*, 2010, **115**, 362–372.

[174] N. Daude, C. Gout and C. Jouanin, *Phys. Rev. B*, 1977, **15**, 3229–3235.

[175] Y. Do, W. Lee, K. Dwight and A. Wold, *J. Solid State Chem.*, 1994, **108**, 198–201.

[176] S. P. Vattikuti, C. Byon and I.-L. Ngo, *Mater. Res. Bull.*, 2016, **84**, 288–297.

[177] M. El - Nouby, *Ph.D. thesis*, Osaka University, 2014.

[178] P. P. GonzaÌĄlez-Borrero, F. Sato, A. N. Medina, M. L. Baesso, A. C. Bento, G. Baldissera, C. Persson, G. A. Niklasson, C. G. Granqvist and A. Ferreira da Silva, *Appl. Phys. Lett.*, 2010, **96**, 061909.

[179] S. S. Nekrashevich and V. A. Gritsenko, *Phys. Solid State*, 2014, **56**, 207–222.

[180] I. T. Godmanis, A. N. Trukhin and K. Hübner, *Phys. status solidi*, 1983, **116**, 279–287.

[181] J. Cadet, E. Sage and T. Douki, *Mutat. Res. Mol. Mech. Mutagen.*, 2005, **571**, 3–17.

[182] S. Goswami, S. Sharma and C. Haldar, *J. Photochem. Photobiol. B.*, 2013, **125**, 19–25.

[183] J. Fan, R. Zamani, C. Fábrega, A. Shavel, C. Flox, M. Ibáñez, T. Andreu, A. M. López, J. Arbiol, J. R. Morante and A. Cabot, *J. Phys. D. Appl. Phys.*, 2012, **45**, 415301.

[184] E. J. W. Verwey, J. T. G. Overbeek and J. T. G. Overbeek, *Theory of the Stability of Lyophobic Colloids*, Courier Dover Publications, 1999, p. 205.

[185] M. R. Allen, A. Braithwaite and C. C. Hills, *Environ. Sci. Technol.*, 1997, **31**, 1054–1061.

[186] Z. M. Wang, G. Yang, P. Biswas, W. Bresser and P. Boolchand, *Powder Technol.*, 2001, **114**, 197–204.

[187] R. Huppmann, H. W. Lohoff and H. F. Schröder, *Fresenius. J. Anal. Chem.*, 1996, **354**, 66–71.

[188] M. Arnold, *Reduction and monitoring of biogas trace compounds*, VTT, Helsinki, 2009.

[189] S. C. Popat and M. A. Deshusses, *Environ. Sci. Technol.*, 2008, **42**, 8510–8515.

[190] *US Pat.*, 20060000352, 2006.

[191] *WO Pat.*, 2008024329, 2008.

[192] Y. Li and J. Shi, *Adv. Mater.*, 2014, **26**, 3176–205.

[193] Y. Kim, C. Kim and J. Yi, *Mater. Res. Bull.*, 2004, **39**, 2103–2112.

[194] N. Kawakami, Y. Fukumoto, T. Kinoshita, K. Suzuki and K. I. Inoue, *Jpn. J. Appl. Phys.*, 2000, **39**, L182–L184.

[195] N. Husing and U. Schubert, *Angew. Chemie - Int. Ed. English*, 1998, **37**, 22–45.

[196] E. Tan and C. Lim, *Compos. Sci. Technol.*, 2006, **66**, 1102–1111.

[197] S. Zong, W. Wei, Z. Jiang, Z. Yan, J. Zhu and J. Xie, *RSC Adv.*, 2015, **5**, 55579–55587.

[198] S. Nam, W. Namkoong, J.-H. Kang, J.-K. Park and N. Lee, *Waste Manag.*, 2013, **33**, 2091–8.

[199] G. B. Alexander, *J. Am. Chem. Soc.*, 1954, **76**, 2094–2096.

[200] K. Goto, *J. Phys. Chem.*, 1956, **60**, 1007–1008.

[201] E. A. Gorrepati, P. Wongthahan, S. Raha and H. S. Fogler, *Langmuir*, 2010, **26**, 10467–74.

[202] J. L. Gurav, A. V. Rao, A. P. Rao, D. Nadargi and S. Bhagat, *J. Alloys Compd.*, 2009, **476**, 397–402.

[203] S. H. Garofalini and G. Martin, *J. Phys. Chem.*, 1994, **98**, 1311–1316.

[204] G. R. Choppin, P. Pathak and P. Thakur, *Main Gr. Met. Chem.*, 2008, **31**, 53–71.

[205] R. Deshpande, D.-W. Hua, D. M. Smith and C. J. Brinker, *J. Non. Cryst. Solids*, 1992, **144**, 32–44.

[206] P. J. Davis, C. Jeffrey Brinker, D. M. Smith and R. A. Assink, *J. Non. Cryst. Solids*, 1992, **142**, 197–207.

[207] G. W. Scherer, *J. Non. Cryst. Solids*, 1988, **100**, 77–92.

[208] *CRC Handbook of Chemistry and Physics*, ed. W. M. Haynes, CRC Press, Boca Raton, 94th edn., 2013, pp. 6.182 – 6.185.

[209] S. D. Bhagat, Y.-H. Kim, Y.-S. Ahn and J.-G. Yeo, *Microporous Mesoporous Mater.*, 2006, **96**, 237–244.

[210] J. V. Alemán, A. V. Chadwick, J. He, M. Hess, K. Horie, R. G. Jones, P. Kratochvíl, I. Meisel, I. Mita, G. Moad, S. Penczek and R. F. T. Stepto, *Pure Appl. Chem.*, 2007, **79**, 1801–1829.

[211] D. R. Ortega and A. Subrenat, *Environ. Technol.*, 2009, **30**, 1073–1083.

[212] W. Urban, H. Lohmann and J. S. Gómez, *J. Power Sources*, 2009, **193**, 359–366.

[213] M. C. Canela, R. M. Alberici and W. F. Jardim, *J. Photochem. Photobiol. A Chem.*, 1998, **112**, 73–80.

[214] *US Pat.*, 7601670B2, 2009.

[215] *Ca Pat.*, 1165306 A1, 1984.

[216] M. Ratova, G. West and P. Kelly, *Coatings*, 2013, **3**, 194–207.

[217] K. Karthik, S. K. Pandian and N. V. Jaya, *Appl. Surf. Sci.*, 2010, **256**, 6829–6833.

[218] L. Liu, S. Chen, W. Sun and J. Xin, *J. Mol. Struct.*, 2011, **1001**, 23–28.

[219] X. Li, F. Wang, Q. Qian, X. Liu, L. Xiao and Q. Chen, *Mater. Lett.*, 2012, **66**, 370–373.

[220] V. Li and M. Wang, *Tungsten & Molybdenum Monthly*, Report No.31, Beijing Antaike Information Development Co., Beijing, 2014.

[221] A. Ivask, T. Titma, M. Visnapuu, H. Vija, A. Kakinen, M. Sihtmae, S. Pokhrel, L. Madler, M. Heinlaan, V. Kisand, R. Shimmo and A. Kahru, *Curr. Top. Med. Chem.*, 2015, **15**, 1914–29.

[222] J. H. Park, O. O. Park and S. Kim, *Appl. Phys. Lett.*, 2006, **89**, 163106.

[223] T. Putta, M.-C. Lu and J. Anotai, *J. Environ. Manage.*, 2011, **92**, 2272–2276.

[224] O. Lorret, D. Francová, G. Waldner and N. Stelzer, *Appl. Catal. B Environ.*, 2009, **91**, 39–46.

[225] M. Bellardita, M. Addamo, A. Di Paola and L. Palmisano, *Chem. Phys.*, 2007, **339**, 94–103.

[226] H. Song, H. Jiang, X. Liu and G. Meng, *J. Photochem. Photobiol. A Chem.*, 2006, **181**, 421–428.

[227] H. Aizawa and S. Tsuneyuki, *Surf. Sci.*, 1996, **363**, 223–228.

[228] S. Zhang, Z. Zheng, J. Wang and J. Chen, *Chemosphere*, 2006, **65**, 2282–8.

[229] P. Brimblecombe, *Herit. Sci.*, 2013, **1**, 3.

[230] Y. V. Pleskov, *Sov. Electrochem.*, 1981, **17**, 1–25.

[231] J. Gautron, P. Lemasson and J.-F. Marucco, *Faraday Discuss. Chem. Soc.*, 1980, **70**, 81.

[232] S. K. Choi, S. Kim, S. K. Lim and H. Park, *J. Phys. Chem. C*, 2010, **114**, 16475–16480.

[233] M. Schweigkofler and R. Niessner, *Environ. Sci. Technol.*, 1999, **33**, 3680–3685.

[234] E. Finocchio, T. Montanari, G. Garuti, C. Pistarino, F. Federici, M. Cugino and G. Busca, *Energy & Fuels*, 2009, **23**, 4156–4159.

[235] M. K. Chemweno, L. G. Cernohlavek and W. A. Jacoby, *J. Air Waste Manage. Assoc.*, 2008, **58**, 12–18.

[236] P. Reeves, R. Ohlhausen, D. Sloan, K. Pamplin, T. Scoggins, C. Clark, B. Hutchinson and D. Green, *Sol. Energy*, 1992, **48**, 413–420.

[237] C. H. Bartholomew, *Chem. Eng.*, 1984, **91**, 96–112.

[238] M. Lewandowski, *Appl. Catal. B Environ.*, 2003, **45**, 223–238.

[239] R. BAKER, *J. Catal.*, 1972, **26**, 51–62.

[240] C. H. Bartholomew, *Appl. Catal. A Gen.*, 2001, **212**, 17–60.

[241] Y. Minamoto and M. Fermin Fonseca, *Flowsquare (Version 4.0)*, 2013.

[242] Y. D. Lei, F. Wania and D. Mathers, *J. Chem. Eng. Data*, 2010, **55**, 5868–5873.

[243] L. Lamaa, C. Ferronato, S. Prakash, L. Fine, F. Jaber and J. Chovelon, *Appl. Catal. B Environ.*, 2014, **156-157**, 438–446.

[244] B. Kraeutler and A. J. Bard, *J. Am. Chem. Soc.*, 1978, **100**, 5985–5992.

[245] J. Bezares-Cruz, C. T. Jafvert and I. Hua, *Environ. Sci. Technol.*, 2004, **38**, 4149–4156.

[246] J. Peral and D. F. Ollis, *J. Mol. Catal. A Chem.*, 1997, **115**, 347–354.

[247] K. Chen, *Nucl. Eng. Des.*, 1973, **25**, 207–216.

[248] V. A. Patil and J. A. Liburdy, *Phys. Fluids*, 2013, **25**, 043304.

[249] Q. Qian, J. Ruiz-Martínez, M. Mokhtar, A. M. Asiri, S. A. Al-Thabaiti, S. N. Basahel, H. E. van der Bij, J. Kornatowski and B. M. Weckhuysen, *Chem. - A Eur. J.*, 2013, **19**, 11204–11215.

[250] D. L. Trimm, *Catal. Rev.*, 1977, **16**, 155–189.

[251] M. Argyle and C. Bartholomew, *Catalysts*, 2015, **5**, 145–269.

[252] D. Mores, E. Stavitski, M. H. F. Kox, J. Kornatowski, U. Olsbye and B. M. Weckhuysen, *Chem. - A Eur. J.*, 2008, **14**, 11320–11327.

[253] N. E. Klepeis, W. C. Nelson, W. R. Ott, J. P. Robinson, A. M. Tsang, P. Switzer, J. V. Behar, S. C. Hern and W. H. Engelmann, *J. Expo. Anal. Environ. Epidemiol.*, 2001, **11**, 231–52.

[254] J. D. Spengler and K. Sexton, *Science (80-.).*, 1983, **221**, 9–17.

[255] C. Dassonville, C. Mandin and S. Kirchner, *Arch. des Mal. Prof. l'Environnement*, 2014, **75**, 594–606.

[256] M. Wormuth, M. Scheringer, M. Vollenweider and K. Hungerbühler, *Risk Anal.*, 2006, **26**, 803–24.

[257] *Assessment of exposure to indoor air pollutants*, ed. M. Jantunen, J. J. K. Jaakkola and M. Krzyzanowski, World Health Organisation, Copenhagen, 1997.

[258] World Health Organisation, *Role of Human Exposure Assessment in Air Quality Management*, World Health Organisation, Copenhagen, 2003.

[259] A. Jones, *Atmos. Environ.*, 1999, **33**, 4535–4564.

[260] B. J. Finlayson-Pitts, *Science (80-.).*, 1997, **276**, 1045–1051.

[261] K. Ramanathan, V. L. Debler, M. Kosusko and L. E. Sparks, *Environ. Prog.*, 1988, **7**, 230–235.

[262] *US Pat.*, 5509946, 1996.

[263] *US Pat.*, 6280691, 1998.

[264] J.-C. Kim, *Radiat. Phys. Chem.*, 2002, **65**, 429–435.

[265] A. Gabelman and S.-T. Hwang, *J. Memb. Sci.*, 1999, **159**, 61–106.

[266] K. Urashima, *IEEE Trans. Dielectr. Electr. Insul.*, 2000, **7**, 602–614.

[267] *EU Pat.*, 2776137, 2014.

[268] *EU Pat.*, 0780150, 1997.

[269] *US Pat.*, 6372018, 2002.

[270] K. Hashimoto, H. Irie and A. Fujishima, *Jpn. J. Appl. Phys.*, 2005, **44**, 8269–8285.

[271] A. Fujishima and K. Honda, *Nature*, 1972, **238**, 37–38.

[272] S. N. Frank and A. J. Bard, *J. Am. Chem. Soc.*, 1977, **99**, 303–304.

[273] M. R. Nimlos, E. J. Wolfrum, M. L. Brewer, J. A. Fennell and G. Bintner, *Environ. Sci. Technol.*, 1996, **30**, 3102–3110.

[274] T. N. Obee and R. T. Brown, *Environ. Sci. Technol.*, 1995, **29**, 1223–1231.

[275] U. I. Gaya and A. H. Abdullah, *J. Photochem. Photobiol. C Photochem. Rev.*, 2008, **9**, 1–12.

[276] S. N. Frank and A. J. Bard, *J. Phys. Chem.*, 1977, **81**, 1484–1488.

[277] N. J. Peill, L. Bourne and M. R. Hoffmann, *J. Photochem. Photobiol. A Chem.*, 1997, **108**, 221–228.

[278] L. Cao, F. J. Spiess, A. Huang, S. L. Suib, T. N. Obee, S. O. Hay and J. D. Freihaut, *J. Phys. Chem. B*, 1999, **103**, 2912–2917.

[279] A. Mutti, P. P. Vescovi, M. Falzoi, G. Arfini, G. Valenti and I. Franchini, *Scand. J. Work. Environ. Health*, 1984, **10**, 225–8.

[280] D. Dietz, J. Leininger, E. Rauckman, M. Thompson, R. Chapin, R. Morrissey and B. Levine, *Fundam. Appl. Toxicol.*, 1991, **17**, 347–360.

[281] R. J. Slaughter, R. W. Mason, D. M. G. Beasley, J. A. Vale and L. J. Schep, *Clin. Toxicol.*, 2014, **52**, 470–8.

[282] S. W. Verbruggen, S. Ribbens, T. Tytgat, B. Hauchecorne, M. Smits, V. Meynen, P. Cool, J. A. Martens and S. Lenaerts, *Chem. Eng. J.*, 2011, **174**, 318–325.

[283] M. Henderson, *J. Catal.*, 2008, **256**, 287–292.

[284] H. Žabová and B. Dvořák, *React. Kinet. Catal. Lett.*, 2009, **98**, 165–175.

[285] J. M. Coronado, S. Kataoka, I. Tejedor-Tejedor and M. A. Anderson, *J. Catal.*, 2003, **219**, 219–230.

[286] Y. Ohko, K. Hashimoto and A. Fujishima, *J. Phys. Chem. A*, 1997, **101**, 8057–8062.

[287] N. R. Neti, G. R. Parmar, S. Bakardjieva and J. Subrt, *Chem. Eng. J.*, 2010, **163**, 219–229.

[288] W. Xu and D. Raftery, *J. Catal.*, 2001, **204**, 110–117.

[289] W. Xu, D. Raftery and J. S. Francisco, *J. Phys. Chem. B*, 2003, **107**, 4537–4544.

[290] M. El-Maazawi, A. Finken, A. Nair and V. Grassian, *J. Catal.*, 2000, **191**, 138–146.

[291] U. R. Pillai and E. Sahle-Demessie, *J. Catal.*, 2002, **211**, 434–444.

[292] S. K. Brown, M. R. Sim, M. J. Abramson and C. N. Gray, *Indoor Air*, 1994, **4**, 123–134.

[293] N. L. Nagda and H. E. Rector, *Indoor Air*, 2003, **13**, 292–301.

[294] W. Xu and D. Raftery, *J. Phys. Chem. B*, 2001, **105**, 4343–4349.

[295] J. B. Rawlings and J. G. Ekerdt, *Chemical Reactor Analysis and Design Fundamentals*, Nob Hill Publishing, Madison, 2nd edn., 2013.

[296] Q. Sun, L. Xiao, C. Zhao, Y. Wang, H. Ding and H. Wu, *Chinese J. Environ. Eng.*, 2015, **9**, 3387–3392.

[297] R. Su, R. Tiruvalam, Q. He, N. Dimitratos, L. Kesavan, C. Hammond, J. A. Lopez-Sanchez, R. Bechstein, C. J. Kiely, G. J. Hutchings and F. Besenbacher, *ACS Nano*, 2012, **6**, 6284–6292.

[298] X. Lang, X. Chen and J. Zhao, *Chem. Soc. Rev.*, 2014, **43**, 473–486.

[299] M. Ouzzine, M. Lillo-Ródenas and A. Linares-Solano, *Appl. Catal. B Environ.*, 2013, **134-135**, 333–343.

[300] V. I. Sobolev and K. Y. Koltunov, *Appl. Catal. A Gen.*, 2014, **476**, 197–203.

[301] V.-H. Nguyen, H.-Y. Chan, J. C. Wu and H. Bai, *Chem. Eng. J.*, 2012, **179**, 285–294.

[302] S. Murcia-López, V. Vaiano, D. Sannino, M. C. Hidalgo and J. A. Navío, *Res. Chem. Intermed.*, 2015, **41**, 4199–4212.

[303] Y. Shiraishi, M. Morishita and T. Hirai, *Chem. Commun.*, 2005, 5977.

[304] B. J. Aronson, C. F. Blanford and A. Stein, *Chem. Mater.*, 1997, **9**, 2842–2851.

[305] W. Qiu and Y. Zheng, *Appl. Catal. B Environ.*, 2007, **71**, 151–162.

[306] N. Azizi and M. R. Saidi, *Org. Lett.*, 2005, **7**, 3649–3651.

[307] E. Rohrmann and H. A. Shonle, *J. Am. Chem. Soc.*, 1944, **66**, 1640–1643.

[308] P. Klusener, L. Tip and L. Brandsma, *Tetrahedron*, 1991, **47**, 2041–2064.

[309] L. Shechter, J. Wynstra and R. P. Kurkjy, *Ind. Eng. Chem.*, 1956, **48**, 94–97.

[310] A. R. Khokhar, S. L. Doran, D. B. Brown and M. P. Hacker, *Inorganica Chim. Acta*, 1987, **135**, 81–83.

[311] S. L. Doran, D. B. Brown and C. W. Allen, *J. Organomet. Chem.*, 1988, **340**, 111–118.

[312] *EU Pat.*, 0 799 823 B1, 2007.

[313] *WO Pat.*, 1994012547 A2, 1994.

[314] G. Ciamician, *Science*, 1912, **36**, 385–394.

Exeunt Omnes